UNIVERSITAT DE
BARCELONA

Development of RTP processing for kesterite solar cells

Alejandro Hernández Martínez

Tesi doctoral

Development of RTP processing for kesterite solar cells

Alejandro Hernández Martínez

Dr. Edgardo Saucedo & Dr. Paul Pistor

UNIVERSITAT DE BARCELONA

Development of RTP processing for kesterite solar cells

Programa de doctorat en Nanociències

Autor: Alejandro Hernández Martínez

Directors: Dr. Edgardo Saucedo i Dr. Paul Pistor

Tutor: Prof. Dr. Alejandro Pérez Rodríguez

Lloc on s'ha dut a terme:

UNIVERSITAT DE BARCELONA

IREC
Shaping Energy for a Sustainable Future

In Loving Memory of Víctor Erenas Lobato,

Always loved, never forgotten

We will keep rocking for you, as promised

DESPRÉS

No serà falaguer, l'estiu, i la tardor
-saps prou com l'estimàvem-
serà potser en excés melangiosa.
Quan s'escurcin els dies te'm faràs més
present,
perquè el silenci fa més densos
els records, i més íntim el temps
que ens és donat per viure'ls.
A ulls clucs et veuré: tot serà tu
per la cambra, pels llibres, en la fosca.
Després passaran anys i esdevindràs
translúcida
i a través teu estimaré el futur
potser sense pensar-te ni sentir-te.
Arribaràs a ser una part tan íntima
de mi mateix, que al capdavall la mort
se t'endurà de nou quan se m'endugui.

Miquel Martí i Pol

Acknowledgments

Almost four years ago, I embraced the biggest challenge and adventure in my life so far. In those years, I've lived so many new experiences that I could have never ever dreamt about them. I've worked in a very cool lab, I've learnt about a topic that fascinates me, Photovoltaics, I've improved my background, I've learnt more about myself that probably I had prior done in my life. This adventure is reaching its end, but in contrast to previous stages in my life that I was looking forward to finish them and burn stages, in this one I've enjoyed it as it deserved but I feel like it's time to move on and keep walking through this one-way ticket in this path called life.

In this thesis there are two capital persons that helped me through these years, my thesis directors: Edgardo and Paul. Edgar, thanks a lot for trusting me and letting me embrace this challenge, thanks for all your wisdom, thanks for all your support, thanks for all your advices, thanks for all the laughs, thanks for the opportunities, thanks for all the scientific explanations, thanks specially for teaching me how to properly present stuff, thanks a lot also for the moments when I needed to be remarked that I wasn't working properly, in those moments it's where we learn more. I'm very proud to say that I've been able to perform my PhD under your direction. Finally, I would also want to thank you Edgar for always believing in me and my abilities, even in the moments when I doubted on myself, you never did and I strongly appreciate it. Paul, I've loved working with you, I believe that you and Edgar are an amazing tandem to work with. Thanks Paul, you have also always been there, I've loved working with you, it brought new ideas, different scopes, very wise advices for my presentations, for my articles, for my reports. I feel blessed because I got the opportunity to work with you. Also, I wanted to thank you for being my first close experience to your amazing country. It was incredible to get the chance to work back together in Germany. I loved our weekly meetings and being able to get to know your personal facet even more. I strongly believe that in our life we are able to meet a certain amount of people that strikes in your personality and I believe that I'm a better person thanks to have met you. Vielen Dank Paul.

I would also like to thank Alejandro for being always such an extremely kind and nice person whatever it happens, for his deep knowledge and advices not only about PV, but also about life and attitude towards life. Also, thanks for the incredible work done as our group leader and directing the group that has awarded us with the chance to work with you and to realize our thesis.

I have been awarded with the chance to work at IREC, my beloved institute. We might not be the biggest institute nor the richest one, but I strongly believe that we are the ones with the biggest motivation and illusion to show the best of everyone. I wanted to thank the amazing team that we all together become. I would like to specially thank Elisabeth Chulilla, for being someone simply special for me, your advices and wisdom are simply extremely clever and believe me if I tell you that you are one of the persons I pay more attention when comes to

advices in my life. I can't and I won't forget my dear Inés, what an incredible woman, thanks for all the support, all the laughs in our metro ways and for always listening, withstanding me in the bad and in the good moments in this thesis and your incredible help in the crazy Belarus Visa process. The whole administration team is always there and extremely supportive: thanks Jaume, Emili, Montse, Yolanda, Vanesa, Josep Maria, Francesc Torregrossa, Raquel, Víctor, Ramón, Alba, Marta (Maresme lliure i tropical sempre), Miguel and Francesc. I don't forget also the previous staff at IREC who were so supportive and friendly to me: Alexandra, Marta, Ferran and David.

Performing your PhD is also about learning how to work in a team, and about this, I've been extremely lucky. I specially need to thank the whole team in the SEMS group at IREC:

- **Nacho:** the person I've considered here my biggest friend and who has been almost all the time in this process working in parallel with me. So many, long days working together, so many lab hours, so many laughs, so many songs, so many nice moments, so many advices for science and for life, a true colleague and a true friend. Also, always listen carefully to him, he's able to say the coolest sentences such as: "*I've discovered I've the ability not to miss people, actually to be happy when they are missing".*
- **Yudenia:** half-time colleague and half-time mother for me. Thanks for all our beautiful moments in front of the CdS discussing about our stuff, your advices have always been great and I hope that I've also been able to help you a little bit raising that incredible diamond you've at home, take care of him, he's a very talented kid!
- **Marcel:** as I've always said my non-official Thesis director, thanks Marcel for such an incredible help in the lab, I owe you almost everything, without you this thesis wouldn't have been done. Thanks also for all the laughs and all your jokes, they made the long journeys way easier
- **Victor:** The Raman God. Thanks, for all the figures, the explanations, the teaching, the origin classes, the XRD, the Raman, the critics also, the laughs, the jokes and the crazy ideas. You have been capital in my thesis thanks Victor, I'll never forget all your help.
- **Sergio:** one of the best colleagues you can find. My other pal from Santa Coloma, we have also been together in this process since the very beginning, it has been really fun travelling together, partying together, working until late in the lab, our music, our jokes, our crazy ideas. Thanks a lot for everything mona and don't change.
- **Diouldé:** I strongly believe that if I'm able to properly work in a lab is thanks to you. Thanks for catching a young, barely experienced Alex and teaching him so, so, so many things. Thanks Diouldé, I appreciate so much how you took care of me, how many things you taught me, how much you worried about me and how much you withstood me. After, I was also lucky to get to know you and I saw even clearer how cool and clever you are, Merci.
- **Jacob:** my great tablemate. I loved our confidences next to each other at our tables. It has been great to work altogether, if they ask me about Jacob, I can say that he's someone you can trust in.
- **Макс:** The Raman Master. I've learnt a lot from your mastery in Raman and you helped me a lot when I started discovering this place that has so much to offer called the East. СПАСИбО)
- **Mohammed:** pure heart and nice guy. I can say that I've learnt a lot from you, specially about attitude towards life.

Jordi Lluís, Germà Giné, Juan Bracero and David Codina. Special thanks to Ainhoa, the first who saw my potential and has always been the best guidance I ever had. I also would like to acknowledge Joan F. Piniella for being the best teacher I had through my university studies and I'm very glad that we are still in touch, thanks for showing me that crystallography is indeed extremely interesting.

I would also like to thank my family for their unconditional support through all my studies, since the very beginning until this moment when I am submitting my Thesis. Biggest thanks also to: Mama, Papa, Carlos and Yaya for always supporting me, discussing with me about my ideas, withstanding me (especially in the end of the thesis) and of course working like hell to help me pay my studies. Gracias de corazón.

Finally, this Thesis is specially dedicated to: Xavier, Pau, Grau, Noa, Sigurd and Maia. You kids are our future and I hope that this Thesis will enlighten your path if you ever also decide to embrace this big adventure.

Gràcies, Gracias, Thanks, Danke, Спасибо, Дзякуй

Hernández Martínez, Alejandro

25/09/2019

Sant Adrià del Besòs

Table of Contents

List of Tables

List of Figures

Preface

Preface

The work presented in this thesis has been carried out at the Catalonia Institute for Energy Research (IREC) in Sant Adrià del Besòs (Barcelona, Spain) from 2015 until 2019. The main subject of this Thesis is the understanding and development of new annealing strategies via Rapid Thermal Processing (RTP) for Earth-abundant $Cu_2ZnSn(S_x,Se_{1-x})$ (CZTSSe) kesterite solar cells, which show a clear consensus amongst the scientific community as one of the most suitable production techniques for a posterior industrial implementation.

The thesis is structured into six chapters: the first chapter provides a general introduction to renewable energies and expounds the underlying motivation of this thesis. The second chapter provides details about the main experimental methodologies used throughout the thesis. The next three chapters cover the main experimental results obtained during the course of this Thesis, presenting the optimization of the RTP processing baseline at IREC, a comprehensive study about the kesterites formation pathways and an investigation of the robustness of the baseline developed at IREC. This is followed by a chapter highlighting the conclusions and outcomes of this work. A more detailed description of the different chapters that comprise the structure of the thesis is presented below:

- **The first chapter** is subdivided in well differentiated sections. It starts with an analysis of the problematic derived from greenhouse emissions and climate change and the measures that have been provided to deal with it. After that, an in order to justify why Renewable Energies are so important for mitigating it, it is also commented how the energy demand is increasing with time and how this increase still relies mostly on fossil fuels, even though the share of sources is every time more and more split. The chapter advances by introducing a short review about PV production and why the market is dominated mostly by Si technologies. Then, the fundamentals of solar cells are briefly commented with the aim to provide an understanding of the key concepts behind their operation and internal structure. This explanation is later followed by a description of the currently available commercial photovoltaic technologies comparing 1st generation (Si-based), 2nd generation (thin film) and third generation technologies (emerging, novel technologies and advanced concepts) are also introduced and provided with further discussion about strengths and drawbacks of the different PV technologies. The next sub-section aims to discuss the main advantages and current limitations of kesterite thin film technologies, upon which this Thesis is based on. Then, a review of the state-of-the-art about kesterites and their best results for the high amount of synthesis techniques employed is presented. Finally, this chapter also presents the objectives of this thesis.
- **The second chapter** covers the experimental methodology employed in the present work. This includes the general process for manufacturing kesterite solar cells at IREC, as well as the main characterization methods, mostly summarized into optoelectronic and Raman spectroscopy. As the development of an RTP process is the main objective of this work, the Magnetron Sputtering setup and the RTP equipment employed are presented in more detail.
- **The third chapter** explores the implementation of an RTP process into IREC's kesterite production baseline. First, most interesting capabilities that can be achieved by using RTP are introduced and then the evolution that the RTP annealing process underwent through this present Thesis is described. It starts by commenting the previously and long-time running established annealing procedure for conventional furnaces at IREC

and how the RTP annealing process ended up evolving towards a double-step RTP annealing procedure. It also depicts how the scope was set-up into obtaining an annealing procedure that would maximize the beneficial effects of RTP into the minimum possible processing time without compromising its efficiency. Moreover, it shows an RTP process that has been able to reach up to 8.3% (neither Anti-Reflective Coating nor metallic grids were applied) in a 12 min annealing process. Once this double-step RTP annealing procedure was established, it was of key importance to obtain a deep and comprehensive knowledge about the process ins and outs. In order to do so, a break-off experiment where the process was stopped in key parts of it and strongly characterized with several techniques was implemented. The main results of this Chapter have given rise to the following publication:

Hernández-Martínez, A.; Placidi, M.; Arqués, L.; Giraldo, S.; Sánchez, Y.; Izquierdo-Roca, V.; Pistor, P.; Valentini, M.; Malerba, C.; Saucedo, E. *Insights into the Formation Pathways of $Cu_2ZnSnSe_4$ Using Rapid Thermal Processes*. *ACS Appl. Energy Mater.* **2018**, *1* (5), 1981–1989. DOI: 10.1021/acsaem.8b00089 Impact factor: pending

The fourth chapter presents the analysis and understanding of the importance of the chalcogen availability to drive the kesterite formation pathways. The Chapter is focused on understanding the relationship between the intermediate phases and the possible formation routes in physical vapour deposition methodologies, together with a kinetic analysis of the system. In order to do so, innovative experiments were implemented to demonstrate the strong interrelationship between the reaction pathways for kesterites using sequential processes, depicting how crucial the chalcogen availability is for the kesterite synthesis. Furthermore, a kinetic analysis combined altogether with an extensive phase analysis of the selenization process is presented for the first time. This kinetic analysis shows the relationship between the chalcogen availability and the reaction order. Furthermore, it is also presented that the binary phases compounds, even being able to be driven to a marginal extent, they cannot be completely eliminated. The most relevant results of this Chapter have been submitted for publication with the following detail:

A. Hernández-Martínez, S. Giraldo, X. Alcobé, J. Andrade, M. Placidi, V. Izquierdo-Roca, P. Pistor, A. Pérez-Rodríguez, E. Saucedo. *Driving the kesterite formation pathway with the chalcogen availability: a kinetic and phase analysis. Angewandte Chemie (submitted)* Impact factor: 12.257(Q1).

- **The fifth chapter** deals with the reliability and trustiness on the RTP annealing baseline established in Chapter 3 by extending its use to other precursor synthesis techniques, in this case electrodeposition. First, the electrodeposition synthesis technique is introduced and reviewed in order to obtain a broad view of this technique that also possesses very interesting properties. Electrodeposited precursors were submitted to the new established RTP annealing baseline developed in order to check its efficiency and optoelectronic results, turning out into a very interesting result of 5.2% efficiency for co-electrodeposited precursors and RTP annealing, the highest reported in the literature so far under these synthesis conditions (to the best of my knowledge). This device has been strongly characterized and proves the reliability of the RTP annealing

baseline developed in this Thesis. The most important results of this Chapter have been published in the following paper.

Valdés, M.; **Hernández-Martinez, A.;** Sánchez, Y.; Oliva, F.; Izquierdo-Roca, V.; Perez Rodriguez, A.; Saucedo, E. *Cu$_2$ZnSnSe$_4$ based solar cells combining co-electrodeposition and rapid thermal processing*. *Sol. Energy* **2018**, *173* (June), 955–963. DOI: 10.1016/j.solener.2018.08.049 Impact factor: 4.674 (Q1).

- **The sixth chapter** summarizes the main results of this Thesis, providing the most relevant Conclusions, and putting them into a perspective for the future progresses of kesterite photovoltaic technology.

Prefacio

Prefacio

El trabajo presentado en esta tesis ha sido realizado en el *"Institut de Recerca en Energia de Catalunya"* (IREC) en Sant Adrià del Besòs (Barcelona, España) desde el 2015 hasta el 2019. El tema principal de la presente tesis es el desarrollo de nuevas estrategias de recocido por *Rapid Thermal Procesing* (RTP, Procesos de Recocido Rápidos) para celdas solares basadas en kesterita, $Cu_2ZnSn(S_x,Se_{1-x})$ (CZTSSe). Esta tecnología está siendo extensivamente estudiada gracias a que gracias a que su estructura está formada únicamente por elementos abundantes en la corteza terrestre y de baja toxicidad. Además, la síntesis del material incluyendo técnicas RTP es de gran interés para una posible aplicación industrial en el futuro cercano.

La tesis se estructura en seis capítulos. El primer capítulo provee una introducción general sobre las energías renovables y expone las motivaciones de la tesis. El segundo capítulo relata una descripción sobre los detalles experimentales y la metodología utilizada a lo largo de la tesis. Los tres capítulos siguientes presentan los resultados obtenidos más importantes incluye: la optimización de la línea de trabajo en RTP para la producción de celdas solares de kesteritas en IREC, un estudio exhaustivo sobre las vías de reacción para la formación de estos compuestos y un estudio sobre la robustez de la línea de trabajo desarrollada. Finalmente, se desarrolla un capítulo que resalta las conclusiones y resultados obtenidos por el trabajo realizado. A continuación, se presenta una descripción más detallada de cada uno de los diferentes capítulos que comprenden la estructura de la tesis:

- **El primer capítulo** se encuentra subdividido en secciones bien diferenciadas. Empieza con un análisis sobre la problemática derivada de las emisiones de gases de efecto invernadero y el cambio climático, comentando además las medidas emprendidas para mitigarlo. A continuación, y con la idea de justificar por qué las energías renovables son tan importantes en este sentido, se comenta cómo la demanda de energía está creciendo sosteniblemente, dependiendo enormemente aún hoy en día de los combustibles fósiles pese a que la generación de energía está cada vez más diversificada y tiende hacia la generación por renovables. El capítulo avanza mediante la introducción de una pequeña revisión sobre la producción fotovoltaica y cómo el mercado está dominado por la tecnología basada en el silicio. A continuación, se comentan brevemente los fundamentos en los que se basa la tecnología de las celdas solares con la intención de destacar los conceptos claves detrás de su operación y estructura interna. La explicación continúa con la descripción de las diferentes tecnologías fotovoltaicas: la primera generación (basada en tecnología de Silicio), la segunda generación (basada en tecnología de capa delgada) y la tercera generación (que engloba tecnologías emergentes, noveles y conceptos avanzados) proveyendo además con sus puntos fuertes y limitaciones. La siguiente subsección se enfoca en la tecnología de capa fina basada en kesterita remarcando sus ventajas y limitaciones, tecnología sobre la cual se centra la presente tesis. El primer capítulo presenta además una revisión del estado del arte de las diferentes tecnologías para la síntesis de kesterita compilando los mejores resultados obtenidos. Finalmente, el capítulo concluye presentando los objetivos de la tesis.
- **El segundo capítulo** engloba la metodología experimental utilizada en el presente trabajo. Esta metodología incluye el proceso completo de fabricación de las celdas solares de kesterita en IREC, junto con las técnicas de caracterización más relevantes incluyendo: caracterización optoelectrónica y espectroscopia Raman. Debido a que el desarrollo de un proceso de RTP es el objetivo primordial de la tesis, el equipo de

Magnetron Sputtering (evaporación catódica) y de *RTP* también son comentados detalladamente.

- **El tercer capítulo** explora la implementación de un proceso de RTP en la línea de producción de celdas solares de kesterita de alta eficiencia en IREC. Inicialmente, se introducen todas las características altamente interesantes que provee el trabajar con RTP y a continuación se describe la evolución experimentada por el proceso de RTP a lo largo de la presente tesis. Empieza por comentar el proceso de recocido previamente establecido basado en la utilización de hornos tubulares convencionales en IREC y cómo el proceso de RTP ha evolucionado hasta un proceso que cuenta con dos etapas. Además, comenta cómo el foco ha estado dirigido hacia la obtención de un proceso de RTP que maximizaría los puntos fuertes de esta técnica en el tiempo mínimo de proceso sin comprometer así la eficiencia. Por otra parte, se muestra un proceso capaz de obtener hasta un 8.3% de eficiencia (sin aplicar recubrimientos anti-reflexión o contactos metálicos) con un proceso de tan solo 12 minutos. Finalmente, el capítulo se enfoca en desarrollar un experimento novedoso donde el proceso de recocido se detiene y se analiza en etapas claves, para obtener una mayor comprensión de este. Los resultados más relevantes de este capítulo han dado lugar a la siguiente publicación:

Hernández-Martínez, A.; Placidi, M.; Arqués, L.; Giraldo, S.; Sánchez, Y.; Izquierdo-Roca, V.; Pistor, P.; Valentini, M.; Malerba, C.; Saucedo, E. *Insights into the Formation Pathways of $Cu_2ZnSnSe_4$ Using Rapid Thermal Processes*. *ACS Appl. Energy Mater.* **2018**, *1* (5), 1981–1989. DOI: 10.1021/acsaem.8b00089 Factor de Impacto: pending

- **El cuarto capítulo** se centra en comprender los aspectos termodinámicos y cinéticos del proceso de RTP, en función de la cantidad de calcogenuro (selenio) presente en el sistema. En primera instancia el estudio se centra en la comprensión de las fases intermediarias presentes en el mecanismo de formación de la kesterita. Para ello se ha implementado un estudio comparativo entre el proceso convencional de síntesis del material y el proceso RTP, intentando comprender y comparar los pasos que están determinados termodinámica y cinéticamente en ambos casos, en función de la cantidad de selenio presente en la atmósfera de recocido. Como resultado se presenta por primera vez un análisis combinado sobre la cinética y las fases presentes en el proceso de selenización. El análisis cinético en particular discierne sobre la relación entre la presencia de calcógeno y el orden de la reacción. Finalmente, se demuestra que los compuestos de fases binarias, pese a que pueden ser reducidos hasta niveles bajos, nunca pueden ser completamente eliminados. Los resultados más relevantes de este capítulo han sido enviados para publicación recientemente, con el siguiente detalle:

<u>A. Hernández-Martínez</u>, S. Giraldo, X. Alcobé, J. Andrade, M. Placidi, V. Izquierdo-Roca, P. Pistor, A. Pérez-Rodríguez, E. Saucedo. *Driving the kesterite formation pathway with the chalcogen availability: a kinetic and phase analysis. Angewandte Chemie (presentado)* Factor de Impacto: 12.257 (Q1)

- **El quinto capítulo** demuestra la versatilidad y robustez de la línea de síntesis desarrollada mediante RTP en el capítulo 3, estudiando su extensión hacia precursores obtenidos con otras técnicas de síntesis, en este caso electrodeposición. Primero, la técnica de recubrimiento de capas metálicas mediante electrodeposición es introducida y revisada con la intención de proveer con un conocimiento amplio sobre la misma, y su aplicación en el depósito de capas metálicas. Precursores metálicos obtenidos por electrodepósito fueron selenizados mediante la nueva línea de síntesis establecida con

RTP y caracterizados, obteniendo un dispositivo récord de 5,2%, probablemente el resultado más alto para esta combinación reportado hasta la fecha. Los resultados más relevantes han sido presentados en el siguiente artículo:

Valdés, M.; **Hernández-Martinez, A.;** Sánchez, Y.; Oliva, F.; Izquierdo-Roca, V.; Perez Rodriguez, A.; Saucedo, E. *Cu$_2$ZnSnSe$_4$ based solar cells combining co-electrodeposition and rapid thermal processing*. *Sol. Energy* **2018**, *173* (June), 955–963. DOI: 10.1016/j.solener.2018.08.049 Factor de Impacto: 4.674 (Q1).

- **El sexto capítulo** resume los principales resultados obtenidos en la Tesis, contextualizándose en el marco del desarrollo de energías renovables sostenibles y presenta las conclusiones generales de la Tesis.

List of Acronyms and Abbreviations

GHG: greenhouse gases

UNFCC: United Nations Framework Convention on Climate Change

KP: Kyoto Protocol

EU: European Union

NDC: Nationally Determined Contribution

VB, E_v: Valence Band

CB, E_c: Conduction Band

W: Work function

E_F: Fermi Level

E_{VAC}: Vacuum Level

E_{EA}: Electron Affinity

TCO's: Transparent Conductive Oxides

a-Si:H: amorphous Si

CdTe: Cadmium Telluride

CIS: $CuInSe_2$

CIGS: $Cu(_{In1-x}Ga_x)Se_2$

CPV: concentrator photovoltaics

MJ: multi-junction

OPV: organic photovoltaics

TPV: thermo-photovoltaics

CZTS: Cu_2ZnSnS_4

CZTSe: $Cu_2ZnSnSe_4$

CZTSSe: $Cu_2ZnSn(S_xSe_{1-x})_4$

SLG: Soda-Lime Glass

CBD: Chemical Bath Deposition

i-ZnO: intrinsic ZnO

ITO: $In_2O_3:SnO_2$

ARC: Anti-Reflective Coating

SEM: Scanning Electron Microscope

PVD: Physical Vapour Deposition techniques

PLD: Pulsed-laser Deposition

ED: Electrodeposited

FTO: Semi-transparent substrates

V_{oc}: Open-circuit Voltage

RTP: Rapid Thermal Processing

CVD: Chemical Vapour Deposition

DC: Direct current

RF: Radiofrequency

SEMS: Solar Energy Materials and Systems group

CL: Cathodoluminiscence

PAT: Pre-annealing treatments

CAZTSSe: $(Cu,Ag)_2ZnSn(S,Se)_4$

XRD: X-Ray Diffraction

RS: Raman Spectroscopy

XRF: X-ray Fluorescence spectroscopy

GDOES: Glow discharge optical emission spectrometer

J-V: Current Density-Voltage measurements

EQE: External Quantum Efficiency

CZT: Precursors (Cu, Zn, Sn)

ZT: Zn/Sn

CTSe: Cu_2SnSe_3

RT: Room Temperature

FWHM: Full Width at Half-Maximum

J_{sc}: short circuit current density

FF: Fill Factor

η: Efficiency

ChA: Chalcogen Availability

$t_{1/2}$: half-life time

SEL: Stacked elemental layer approach

R_S: Series Resistance

R_{SH}: Shunt Resistance

Chapter 1

Introduction

1   Introduction

Nowadays one of the main challenges that humanity is facing is the climate change due to the greenhouse gases (GHG) that increases the average temperature of the planet with consequences such as the thaw in polar areas and in mountain glaciers, the decrease of the humidity in the ecosystems and the increase of the desertification of the same, among others. Even though climate change is a natural process and in Earth's history it has already happened several times (i.e. the so-called ice age)[1], in this case the climate change due to anthropomorphic effects has never been so fast and with so many implications in a short period of time. The origin of this anthropomorphic strong impact into the climate change comes from one of the turning points in human history: The Industrial Revolution, as illustrated in **Figure 1.1**.
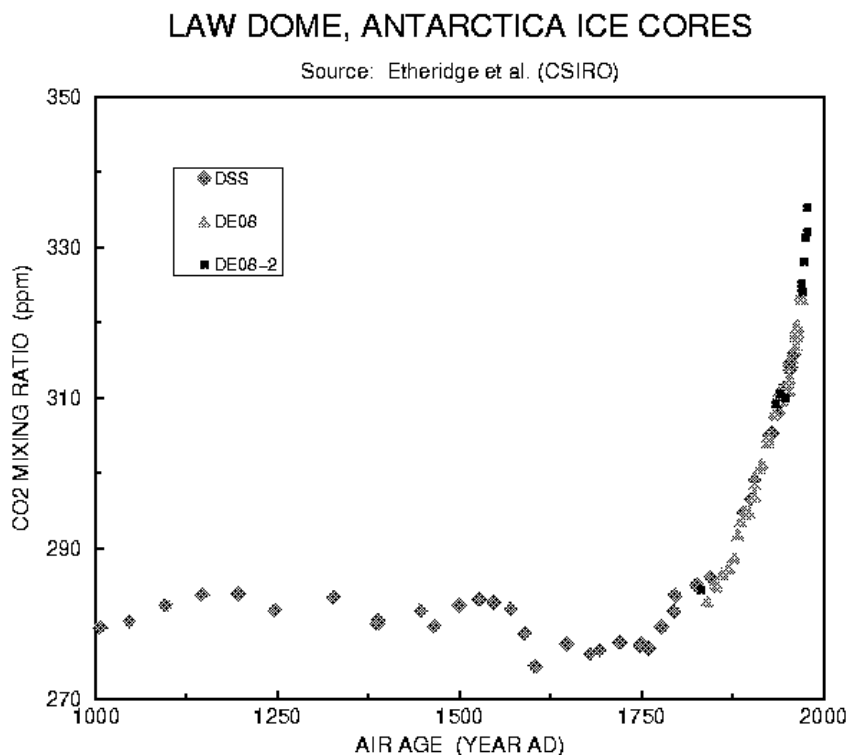
Figure 1.1 CO_2 evolution from the atmosphere as analysed in ice cores at LAW DOME showing pre-industrial levels and post-industrial levels[2]

Despite humanity was prior strongly depending on the world energy primary sources (mostly in form of biomass) it was not until the origin of The Industrial Revolution that a huge dependence on fossil fuels was originated and has not been overcome yet. The Industrial Revolution resulted into a massive change of our societies (social, technological, political, etc.) but also became a turning point for our climate.

1.1   Mitigating the Climate Change

Several efforts to fight this climate change have been attempted with different scopes and results: the first concerted effort was the creation of the United Nations Framework Convention

on Climate Change (UNFCC) in 1992 yet did not fully operate until 1994. The main UNFCC objective was: *"stabilize greenhouse gas concentrations in the atmosphere at a level that would prevent dangerous anthropogenic interference with the climate system"*[3]. Although it was a good and promising starting point it also contained several shortcomings, mostly summarized into it was not set a concentration level for the anthropomorphic GHG dangerous level for the climate system and it also suggested that the climate change was unstoppable. So, it recognized there was no scientific evidence about what might be hazardous. The UNFCC was also indicating to embrace preventive actions but moreover to take actions to adapt to the new situation that would arise from this climate change. In order to overpass these limitations in 1997, the UNFCC started its most important action up to date: The Kyoto Protocol. The main objective of the Kyoto Protocol (KP) was to reduce the onset of global warming by reducing GHG gas concentrations into the atmosphere, in a legally tied way: *"to a level that would prevent dangerous anthropogenic interference with the climate system"*[4]. One of the obvious successes of KP's was that for a first-time countries were tied in a legal way. Yet it was not completely effective as it is based on the principle of common problem but varying responsibilities.

Furthermore, these climate negotiations have faced the common problems of politics and international legislation, as not all the countries signed and ratified the protocols. The KP was based on the idea that all countries have different capabilities for combating climate change, so subsequently countries were indexed into annexes that would define their capabilities and responsibilities into fighting the climate change. As time passed by, it became clear that KP was not enough to effectively fight the climate change, another meeting was set up, the Paris Agreement in 2015. The Paris Agreement has been the most ambitious international plan to mitigate climate change so far. The main objectives for the Paris Agreement are[5]:

1. *"Holding the increase in the global average temperature to well below 2°C above pre-industrial levels and to pursue efforts to limit the temperature increase to 1.5°C above pre-industrial levels, recognizing that this would significantly reduce the risks and impacts of climate change"*
2. *"Increasing the ability to adapt to the adverse impacts of climate change and foster climate resilience and low greenhouse gas emissions development, in a manner that does not threaten food production"*
3. *"Making finance flows consistent with a pathway towards low greenhouse gas emissions and climate-resilient development"*.

The Paris Agreement has been considered the first comprehensive attempt to reduce climate change. In contrast to KP, the structure of the Paris Agreement arises from a bottom-up structure. The emphasize has consisted in finding common consensus that will end-up into voluntary and national targets, in contrast to Kyoto's where legally binding targets had legal force. The Paris Agreement has set more the scope into political targets than legal. In contrast to KP, The Paris Agreement has been able to overpass the differences into countries by following the motto: *"Common but Differentiated Responsibility and Respective Capabilities"*. The Paris Agreement negotiations shall keep going on in order to clarify the roles for each nation more specifically, as it will run since the beginning of 2020.

Moving the scope to European Union (EU) in Paris Agreement, EU has become one of the key actors in putting together the Paris Agreement. EU has been into the forefront of the international efforts for turning the Paris Agreement into a success. Currently, it is leading the Agreement with the higher targets on it. Also the EU was the first major economy to submit its intended contribution to the UNFCC to its new agreement by March 2015[6]. Speaking about

targets, EU has ratified the EU's Nationally Determined Contribution (NDC) for the Paris Agreement in order to reduce the GHG emissions in EU by at least 40% by 2030 in comparison to its emissions in 1990, as it will be all reported in the new 2030 climate and energy agreement framework replacing the HORIZON 2020 agreement.

1.2 Global Electricity Production

Figure 1.2 shows the increasing into the world energy generation between 1973 and 2016, depicting that humanity is demanding every day more and more energy. Still nowadays, this demand is mostly covered by non-renewable energies. By the year 2016, only an 8% of the total energy demand was supplied by non-hydro renewables energies. The gap between the source share for fossil fuels and renewables is still wide, implying that further measures should be taken into the near future and there is an enormous field to work in. In this commented scenario of climate change and the actions that should be considered to fight it, renewable energies appear as one of the most important actors for its mitigation.
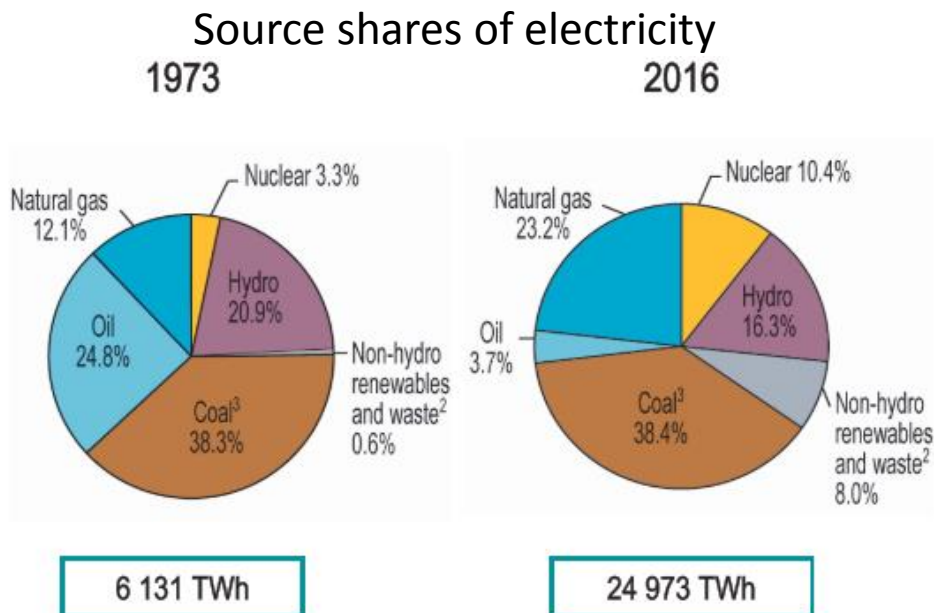
Figure 1.2 Comparison of the share of different generation types for the global electricity production between 1973 and 2016[7]

Figure 1.3 shows the global share of renewable energies production in 2015 depicting that the most advanced and consolidated technologies are hydropower and wind as altogether cope up to the 86% of the total share. On the other hand, solar PV only represents a 5% of the total production. Living in a planet where the Sun is the highest unlimited energy source further development into PV is required.
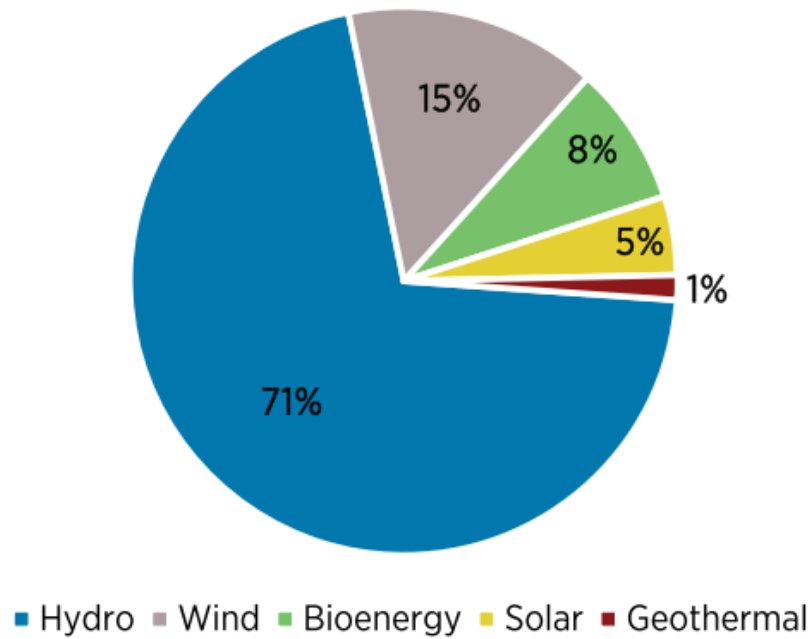
Figure 1.3. Global renewable electricity generation by energy source in 2015[8]

In the previous **Figure 1.3** it has been shown that the PV energy production is still in a very low market-share in comparison to other renewable energies. Whereas, this market-share is expected to increase due to the huge increasing rate that the PV electricity production has been showing. **Figure 1.4** shows the world solar PV electricity production from 2005 to 2016, where it is depicted how the growth on the production, which has been following a very high growing trend, almost exponential. It is of special interest the paper that China has played into the PV market, especially since in 2010 a new Feed-in-Tariff policy was introduced by the Chinese government acting, since then, as the leader of the PV increase. Currently, China operates up to nearly 1/3 of the world's solar power generator capacities[9].

World Solar PV electricity production from 2005 to 2016 by region (TWh)
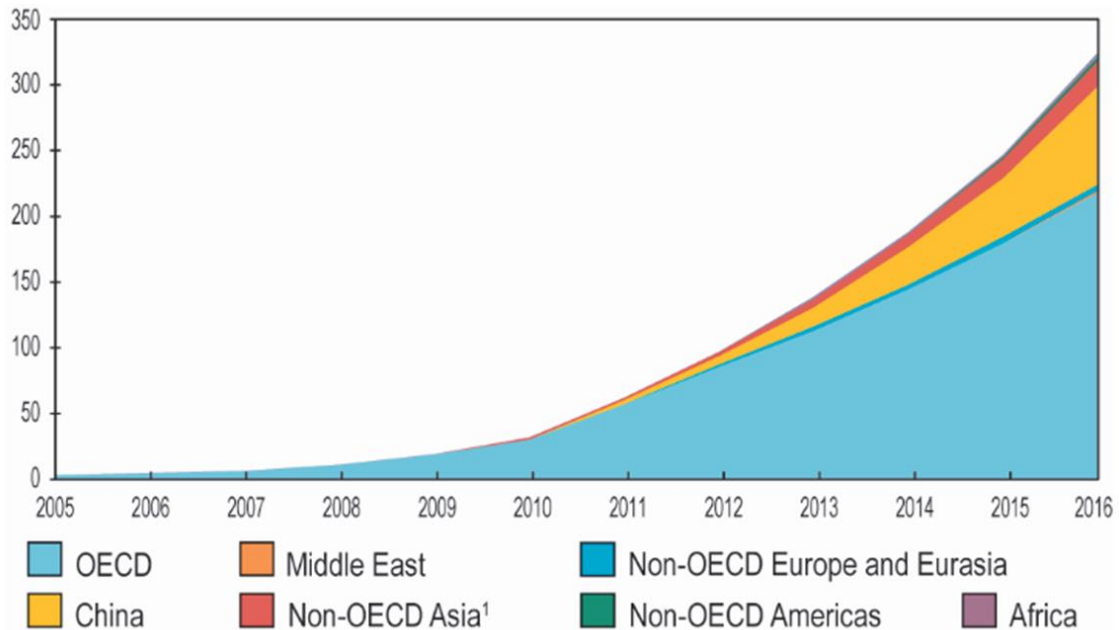
Figure 1.4 Increase into the World Solar PV electricity production[7]

China's incursion in the PV market has provoked an earthquake in the industry[10], as module-prices have gone down to their lowest levels in history (0.35 €/W, April 2019)[11]. This increase in the PV production has been supported by the lowering of the PV module prices predicted into the so-called Swanson's law (**Figure 1.5**). Swanson's law, usually related and compared to Moore's law, comments the observation of PV module prices which tend to drop by 20% for every doubling of cumulative shipped volume.
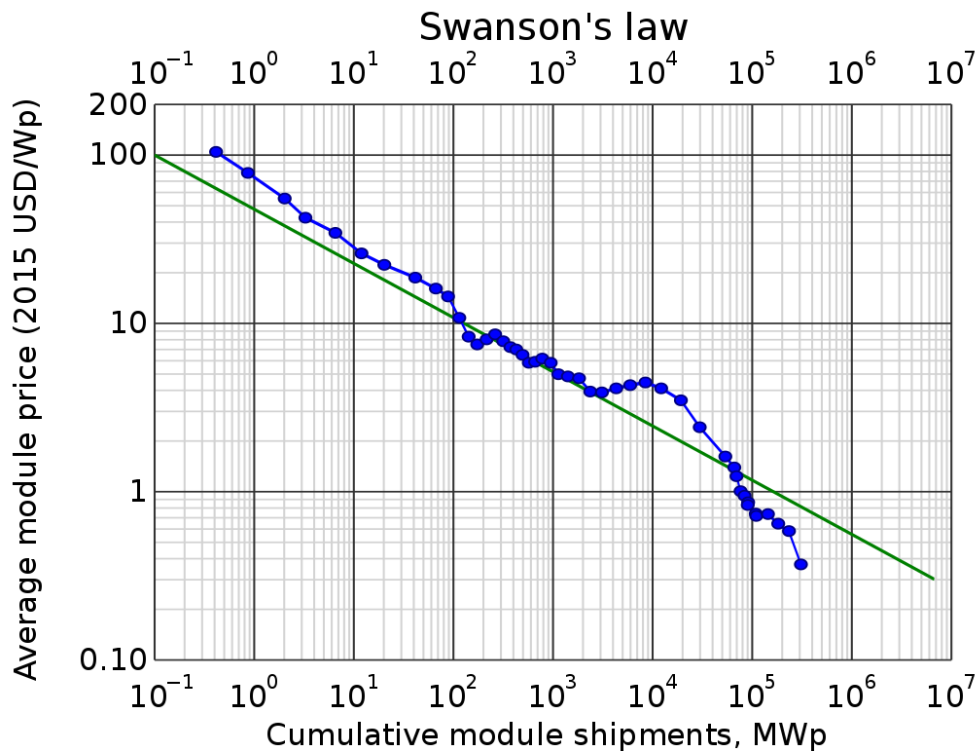
Figure 1.5 Swanson's law, the learning curve of PV[12]

Swanson's law and the huge reduction into the PV module prices can be observed in **Figure 1.6** which shows the evolution of module prices between 2010 and 2017. Module prices have been cut by over 80%, predicting a huge PV revolution. The next PV revolution will find its path in self-consumption. Self-consumption possesses unique features that can be summarized into[13]:

- Contributes to the decentralization of electricity production
- Provides the consumers with higher prominence
- Energy demand and energy production can be modulated
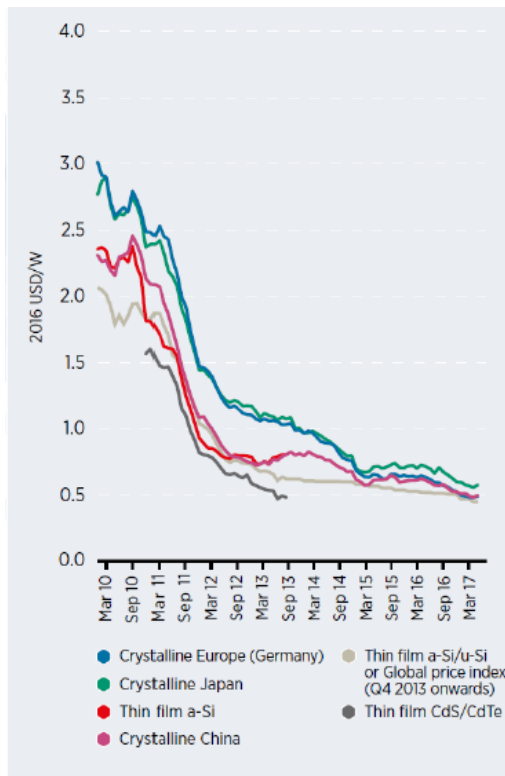
Figure 1.6 Price trends for Solar PV module during the period 2010-2017[14]

1.3   Photovoltaic technologies

PV allows a direct energy conversion from sun to electricity. When a photon with enough energy falls on a semiconductor material it gets absorbed. Then this energy will be transferred to an electron that will jump from a lower state (valence band, VB) to a higher state (conduction band, CB) where they can freely move. This absorption and transfer to a higher state are the key for the energy generation. This electron by jumping to the CB leaves behind it a "hole" (+ charge) in the VB, generating two charge carriers, the so-called "electron-hole pair". Almost all PV devices consist of p-n junctions where a p-type semiconductor material (excess of holes) and a n-type semiconductor material (excess of electrons) are joined.

In **Figure 1.7a** the standard solar cell structure is presented along with the band diagram of its p-n junction and its relevant electronic properties. The E_g or bandgap is the minimum amount of energy required to excite an electron from the VB towards the CB. The valence band (E_v) corresponds to the valence level of the isolated atom (hence its name), which determines its interactions with the outside and the energy level at which this electron is considered free to move, is called the conduction band (E_c). The difference in energy between the minimum energy of the conduction band and the maximum of the valence band in space E vs K, corresponds to the so-called forbidden energy band or Gap, which in representation E vs X is the one presented in **Figure 1.7.** The Work function (W) of the material is defined as the minimum required energy to transfer an electron from the Fermi level (E_F) to the vacuum level (E_{VAC}), while the electron affinity (E_{EA}) is the energy needed to transfer an electron from the conduction band to the vacuum level.

9
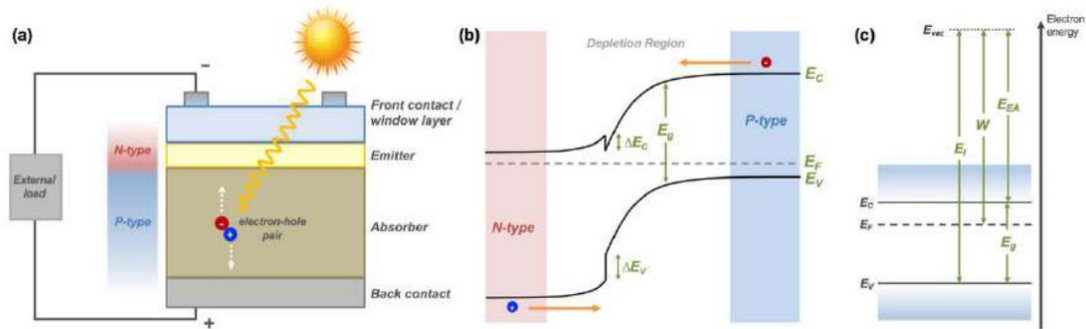
Figure 1.7a) Schematic of the standard solar cell structure. **b)** band diagram of the p-n junction (E_g: band-gap energy, E_c: conduction band energy, E_v: valence band energy, E_f: fermi level). **c)** relevant electronic properties of semiconductor materials in a p-n junction (E_{fa}: electron affinity, W: work function, E_I: Ionization energy)[15]

As previously commented the p-n junction consists of n-doped and p-doped semiconductor materials. In the first case, the main charge carriers are the electrons, while in the second case the holes and the p-doped are a high concentration of holes, so that in the p-n junction the electrons diffuse from the region of type n to the region of type p. This movement of the electrons and the holes towards the other side of the junction leave the exposed charges unbalanced and fixed charges on both sides (ionized donor and acceptors, respectively) with the consequent formation of an electric field (positive on the n side and negative on the p side). Because of that an internal electric field is formed between both sides in a zone called the "depletion region" or the "space charge region". The generated electric field favours the drift movement of minority carriers (holes in part n and electrons in part p) and opposes the diffusion of major carriers on both sides, so that total current through the junction has two components:

- The diffusion due to the majority carriers
- Drift current due to minority carriers

Under equilibrium conditions the total current through the junction must be zero.

P-n junctions can be obtained with different semiconductor and several different PV technologies have been developed in the past. These are historically classified into three categories: the first-generation PV consists mainly of crystalline and multi-crystalline silicon PV, the second generation of PV consists of the thin film PV and finally the third one that includes the emerging and novel concepts in PV. The main characteristics of the three PV technologies are summarized and presented into **Figure 1.8.** In the next pages, the different PV technologies will be presented.

Figure 1.8 Classification and main characteristics of the available PV technologies[15]

The First generation of PV is the one that englobes all the Si-based PV. It is the most mature and robust technology and when people think about PV, they are most probably thinking about Si-based PV. This technology includes mono-crystalline (single-crystal) and multi-crystalline (poly-crystalline) Si-based devices. Si PV relies on its maturity, as it has already been studied and optimized for decades. There is also a high amount of information about evaluating the reliability and robustness of its designs, as a result of those decade's research, crucial for a good final performance. Si PV also benefits from the huge microelectronics industry and about Si being one of the most abundant materials on Earth[16]. Si-based devices show a high operational reliability and stability as crystal silicon modules can reach lifetimes of more than 25 years and exhibit little long-term degradation. Si PV industry also employs industrial high-quality and purity Si wafers. All this interesting properties of Si PV have helped to obtain the highest performance for mass-produced single junction devices, which reduce the final cost installation[17]. Based on all those advantages Si-based devices are dominating the PV market and constituted 95% of the total PV production in 2018[18]. Despite all the advantages, Si-based PV also contain some challenges: Si PV is reaching the theoretical efficiency limit[19,20] for single junction devices (over 26% for mono-crystalline cells and over 21% for poly-crystalline cells)[21], so any new improvement is becoming more and more difficult. The other challenges when working with Si-based devices are its indirect band gap, which ends up with a low absorption coefficient, requiring a thicker absorber layer (around 200 µm) that increases the material cost and its usage. The required purity of the Si (99.9999%) and the problems derived from cutting the wafers from blocks might turn into a problem for Si PV. Despite Si is one of the most abundant materials in the world, it enters competition with the microelectronics industry that may develop into a second silicon crisis as in 2008.

The Second-generation PV is the one based on Thin Film PV. Thin film PV technologies are generally based on absorber materials with direct bandgaps, high absorber coefficients and in contrary to Si-based PV they do not require thick layers of semiconductor materials (around 100

times less material). This direct band-gap also allows for a higher throughput with less material as the required thickness for thin film PV is way smaller than for Si-based devices, so almost any semiconductor material is inexpensive enough to be considered as a suitable candidate[22]. By metal or chalcogenide substitutions it is also possible to tune their band-gap[23]. Furthermore, a very interesting benefit when comes to Thin Film PV is the wide range of physical, chemical, electrochemical, plasma based and hybrid techniques that are available for depositing thin films of one material[24]. Finally, another technological advantage is the possibility to deposit Thin Films directly onto almost any given substrate (glass, polyimide, stainless steel or ceramics).

The main commercial thin film PV technologies are: amorphous Si (a-Si:H) with efficiencies over 14%[21], Cadmium Telluride (CdTe) with efficiencies up to 21%[21] and the chalcopyrite materials family like CIS ($CuInSe_2$) or the most common and used CIGSe ($Cu(In_{1-x}Ga_x)Se_2$ with a top record amongst commercial thin film PV about 22.9% efficiency[21].

Amorphous Silicon was a very promising material based on its use of non-toxic abundant Si, but in contrast to crystalline silicon bearing the advantage of thin film deposition: direct band gap ranging from 1.4-1.6eV, flexible deposition, no bonding, no cutting losses[25]. However, the several advantages that a-Si:H has shown, its late low efficiencies have situated it in a decline trend.

CdTe is currently the second most common PV technology in the marketplace, only after c-Si, sharing a 5% of the marketplace. CdTe solar cells show direct-band gap on its structure (1.45eV)[26] and benefits from its ease and low cost manufacturing. The appearance of Cd on its structure it's the main culprit for CdTe solar cells. Despite being an abundant material its high toxicity might compromise the expansion of CdTe manufacturing[27].

On the other hand, CIGS has been the thin film PV that has reached the highest efficiencies (22.9%)[21]. Even though CIGS and CdTe are very interesting technologies with a high number of advantages, their limitations are also challenging for its relatively near future. CIGS and CdTe contain either toxic materials as Cd[28] or very scarce elements like In and Te[29]. This limitation may develop into a shortage of raw materials which could make it difficult to deploy beyond the Terawatt level[30,31].

In order to overpass this possible shortage scenario, the scientific community started to look for other PV materials where kesterite solar cells appeared as one of the most promising technologies to overpass these previously commented limitations.
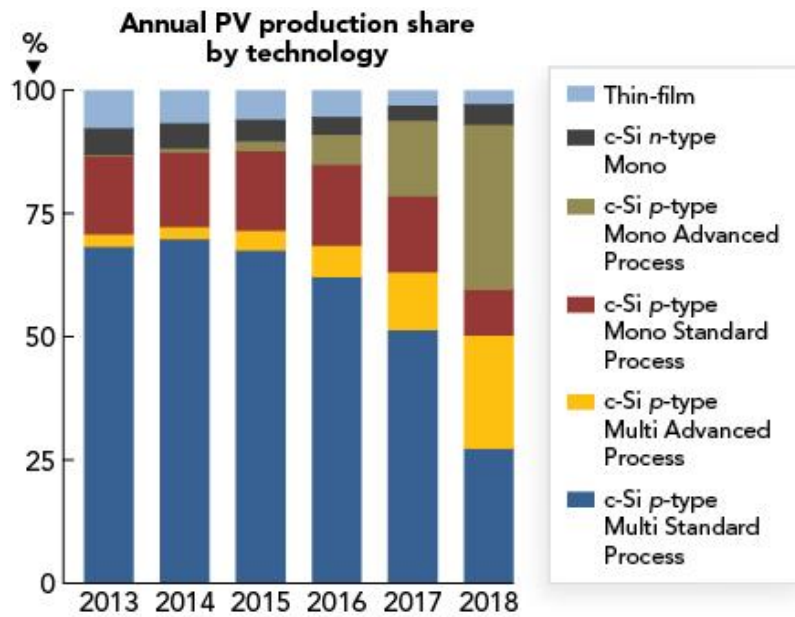
Figure 1.9 Annual PV production share by technology for the period 2013-2018[32]

Figure 1.9 shows a decrease in the PV market share of thin films. However, this decrease is by far not caused by declining production levels. To the contrary, the absolute module production levels of thin films have substantially increased (by 40%, 2500 MWp)[18] over the past 10 years, and are only outnumbered by tremendous increase in Si PV production over the past years, leading to the decreased market share.

The third generation of PV joins the most innovative and breakthrough ideas in the field of PV. Even aiming to overpassing the theoretical efficiency limits (Shockley-Queisser limit[20,33]) for single-junction solar cells. But always trying to maintain economic and environmental costs in line with thin film advantages. In third generation PV several technologies can be found such as: concentrator photovoltaics (CPV), multi-junction tandem solar cells (MJ) which are receiving an increasing attention, as they possess potential to achieve efficiencies over 50%[34]. Another huge research field into the third generation PV are: organic photovoltaics (OPV), advanced inorganic thin film, represented by technologies such as kesterite or Sb_2Se_3, and thermo-photovoltaics (TPV). Moreover, one of the most promising and representative are the perovskite-based solar cells with efficiencies over 25%[21] but with stability and reliability problems[35].
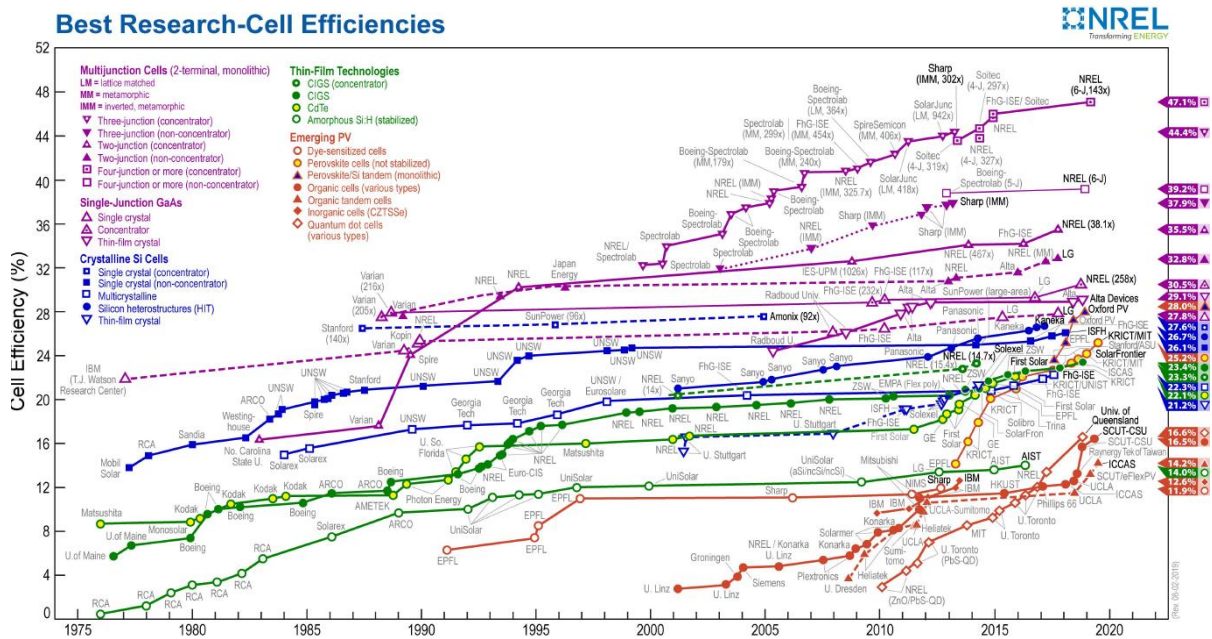
Figure 1.10 Best research-cell efficiencies for the different PV technologies (Reproduced from the National Renewable Energy Laboratory, Golden, CO)[36].

Figure 1.10 represents the best research-cell efficiencies for all the currently studied PV technologies. If MJ, tandem or GaAs are not taken into consideration because of being composed by more than one cell or their enormous costs as in GaAs, it is clear that by far crystalline Si is the most interesting technology thanks to the reasons previously commented. Yet, the comparison between novel and emerging technologies, as the kesterite that this present thesis is devoted to, should not be completely addressed as Si PV has been studied for a very long time (since the 50's[37]) in contrast to kesterite's whose first studied solar cells were only 20 years ago[38]. Si-based PV technologies are a mature technology, whereas kesterite it's only at its dawn.

1.4   Kesterite solar cells

Kesterite solar cells are composed of Cu_2ZnSnS_4 (CZTS). They replace the scarce elements In and Ga from CIGS with the Zn and Sn, two non-critical elements[16,30], overcoming the main limitation for CIGS. CZTS and its related compounds: $Cu_2ZnSnSe_4$ (CZTSe) and its solid solution $Cu_2ZnSn(S_xSe_{1-x})_4$ (CZTSSe) have been regarding increasing attention from the research community. As an example, in **Figure 1.11** the number of publications is depicted and shows a fast increase of research articles published on kesterite.
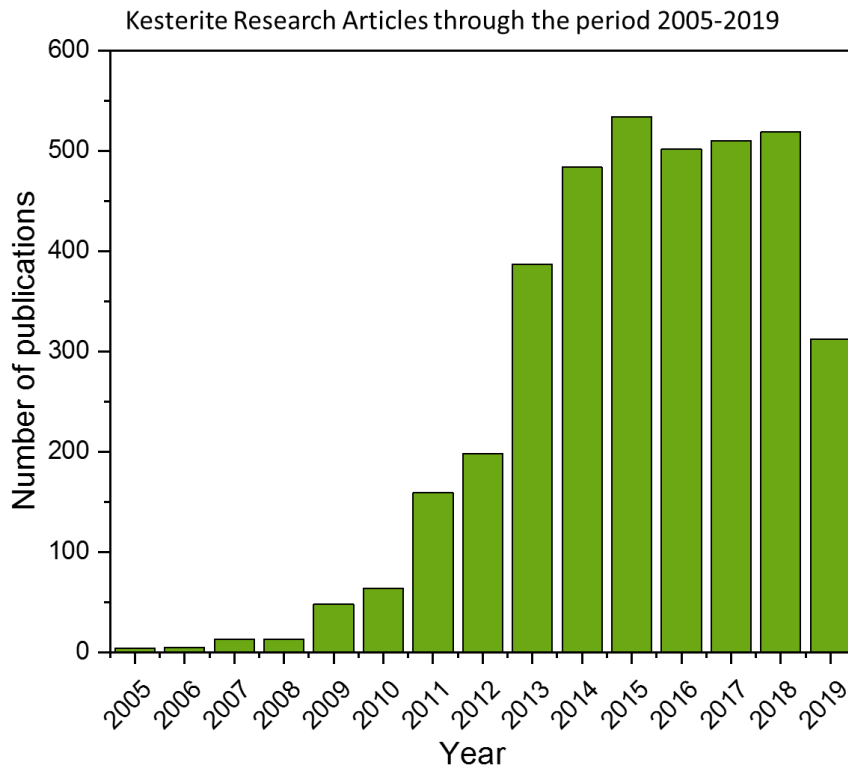
Figure 1.11 Kesterite increasing trend of Research Articles, when the words "kesterite or Cu$_2$ZnSnS$_4$ or Cu$_2$ZnSnSe$_4$ or CZTS or CZTSe" are searched published through the period 2005-2019. *Values obtained from Scopus[39].*

CZTS's history starts first in 1988 when it was suggested as a suitable alternative absorber material[40]. However, it was not until 1997 when *Katagiri et al.*[38] achieved fabricating the first CZTS solar cell that reached up to 0.66% efficiency[38]. This early solar cell set up the spark for an increasing research into kesterites. During the, next years, researchers were able to considerably increase the efficiency of kesterites solar cells. By the year 2008, kesterites demonstrated efficiencies of 6.77%[41] through subsequent optimizations of the materials and the deposition techniques, introducing in-line vacuum steps[42] and etchings to remove detrimental secondary phases[41]. In the following years, IBM laboratories developed a solution-based process and were able to increase the top efficiency by the year 2010, when IBM laboratories published a 9.66%[43] efficiency. This efficiency, only one year later, was increased up to 10.1%[44]. The current certified record stands for a CZTSSe 12.6%[45] cell efficiency that was reported in 2013 by Prof. Mitzi's group at IBM.

CZTS solar cells exhibit several advantages that can be summarized:

- It is composed by earth-abundant, non-critical and non-toxic materials.
- Because of intrinsic points defects, kesterites already show intrinsic p-type doping.
- It has a direct band-gap transition with a high absorption coefficient ($\approx 10^4$cm^{-1})[46].
- This direct band-gap can be tuned through varying the S/Se ratio, from 1.0eV for the pure Se kesterite CZTSe up to 1.5 eV for the pure S kesterite CZTS[47,48]. There are also other strategies available for an effective tuning of the band-gap via cation substitution like: Ge-alloying (Sn substitution)[49], Cd-alloying (in Zn position)[50], Ag-allowing (in Cu position)[51] or Li-alloying (also in Cu position)[52].

15

- Kesterite is usually commonly called a *"close cousin"* of CIGS; this implies knowledge obtained within the CIGS community can be directly transferred to and adopted by the kesterite technology.

The standard architecture of a CZTS solar cell is presented in **Figure 1.12.** For CZTS solar cells, soda-lime glass (SLG) is usually used as substrate, though a variety of alternative substrates such as polyimide[53], stainless steel[54] or ceramics[55] can also be used. On the SLG substrate, at first a Mo layer with around 800 nm thickness is deposited that serves as a back-contact. Afterwards, the ≈1.6µm thick kesterite absorber is synthesized by a sequential process (Sputtered metallic precursor stack + reactive annealing under S+Se atmosphere) that will act as the p part of the p-n junction. In order to finish the p-n junction a ≈50 nm thick layer of n-type CdS is deposited via Chemical Bath Deposition (CBD). Finally, in order to finish the solar cell, a conductive transparent window layer is sputtered as front contact consisting of: ≈50 nm intrinsic ZnO (i-ZnO) and ≈200 nm of In_2O_3:SnO_2 (ITO). Finally, an Ag or Ni/Al metallic contact grid can be deposited on top in order to facilitate charge extraction. Optionally, a MgF_2 anti-reflective coating (ARC) can be applied.
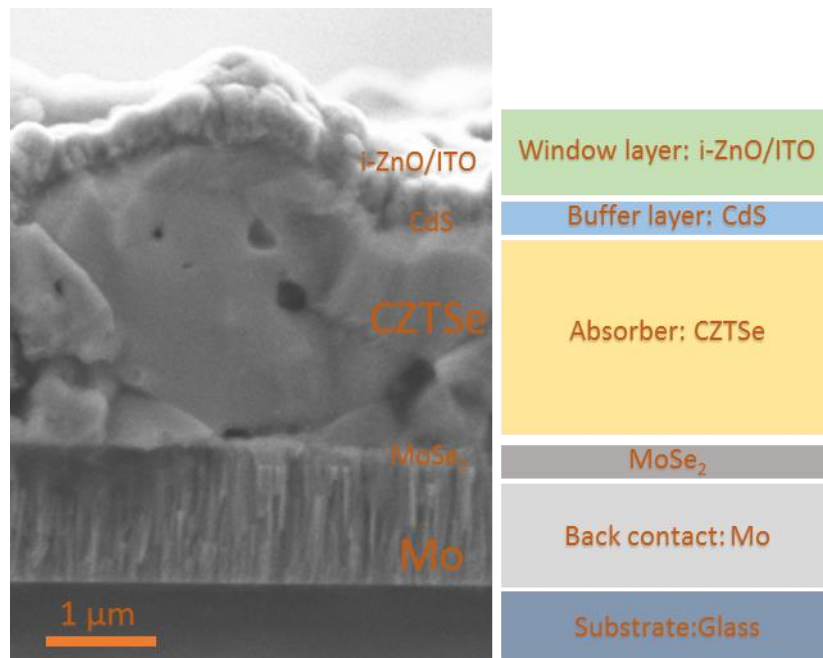
Figure 1.12 Cross-sectional scanning electron microscope (SEM) picture of a typical kesterite solar cell and a schematic drawing of the device architecture.

Several advantages for the kesterite solar cell devices have been commented and explained but one of the key points for its high implementation into research lines all over the world has been its high feasibility to be synthesized. Usually, its synthesis methods are summarized into two main groups: vacuum-based (mostly Physical Vapour Deposition techniques (PVD)) and non-vacuum-based techniques. Vacuum-based techniques include thermal evaporation, e-beam evaporation, sputtering or pulsed-laser deposition (PLD) being the most widespread techniques. Non-vacuum techniques include solution processing via spin-coating/dip coating/doctor-blade-coating/spraying of the precursor, chemically synthesizing CZTS nanoparticle solution or electrochemical deposition.

This high number of synthesis technologies with their pros and contra has generated a widespread of record efficiencies for each of these technologies that can be observed in **Table**

1. The record nowadays is set at 12.7%[56] by a solution-processed solar cell and several other synthesis techniques have proven efficiencies over 10%.

Table 1 Selection of the best reported kesterite solar cells, including pure selenium CZTSe, solid solution CZTSSe, pure Sulphur CZTS, Electrodeposited (ED) solar cells and over semi-transparent substrates (FTO).

	Material (Eg, eV)	Affiliation	Eff (%)	Voc(mV)	Jsc (mA/cm2)	FF (%)	Cell Area (cm²)	Technique	Further Details	Ref
	CZTSe(1.0)	IBM	11.6	423	40.6	67.3	0.43	Co-evap+Hot Plate	Na doping	a
	CZTSe(1.0)	IMEC	10.4	395	39.7	66.2	0.52	Sputtering + H$_2$Se	-	b
	CZTSe(1.03)	Nankai University	10.4	419	38.5	64.8	0.345	Sputtering + Se vapor	w/o ARC	c
Se	CZTSe(0.97)	NREL	9.8	380	37.5	68.9	0.42	Co-evaporation	Certified	d
	CZTSe (1.07)	AIST	9.6	425	34.9	64.5	0.519	Co-evaporation + CTP	Na doping	e
	CZTSe(1.06)	EMPA	9.4	440	34	63	0.346	Co-sputtering + RTP	Se capping layer, w/o ARC	f
	CZTSe(1.06)	Purdue University	9.3	400	35.2	66.2	0.47	Nanoparticle-based + RTP	-	g
	CZTSe(1.04)	IREC	10.1	453	33.3	66.8	0.09	Sputtering + CTP	Ge doping, w/o ARC	h
	CZTSe (1.05)	IREC	10.6	473	34.4	65.4	0.228	Sputtering + CTP	Ge doping	i
	CZTSe(1.04)	IREC	11.8	463	38.3	66.3	0.487	Sputtering + CTP	Ge doping	j
	CZTSSe (1.07)	IBM	12.7	466	38.9	69.8	0.45	Hydrazine-based	Hybrid In$_2$S$_3$/CdS buffer	k
	CZTSSe(1.13)	IBM	10.6	513	35.2	69.8	0.42	Hydrazine-based	Certified	l
	CZTSSe(1.04)	University of Washington	11.8	449	38.8	68.1	0.1	Spray	Li doping	m
S,Se	CZTSSe	Solar Frontier	11.8	503	35.1	66.8	10.6	Sputtering + SAS (Se-->S)	Hybrid In$_2$S$_3$/CdS buffer, submodule	n
	CZTSSe (1.11)	EMPA	11.5	496	35.2	65.8	0.3	Spin-coating + RTP	Li doping (high)	o
	CZTSSe(1.17)	IMRA	10.9	520	32.2	65	0.25	Spray + N$_2$-->Se	Hybrid In$_2$S$_3$/CdS buffer	p
	CZTSSe(1.07)	ZSW	10.3	471	31.6	69.6	0.25	Doctor-Blade coating	Certified	q
	CZTSSe(1.05)	NCK University	10.1	450	36.5	61.9	0.141	Spin coating + SBS(S-->Se)	w/o ARC	r
S	CZTS (1.5)	UNSW	11	731	21.7	69.3	0.234	Co-sputtering + RTP	(Zn,Cd)S buffer, Certified	s
ED	CZTS	Osaka University	8	719	17.7	62.9	0.03	Electrodeposit	Preheating treatment	t
	CZTSe(1.05)	NEXCIS	8.2	425	30.86	62.7		Electrodeposit	Etching + buffer optimization	u
FTO	CZTSSe	IREC	7.7	412.9	34.6	54.1		Sputtering + CTP	FTO/Mo	v

Corresponding references: a[57], b[58], c[59], d[60], e[61], f[62], g[63], h[64], i[65], j[66], k[56], l[45], m[67], n[68], o[69], p[70], q[71], r[72], s[73], t[74], u[75], v[76]. Partially reproduced and extended from: *Sergio Giraldo*[15]

Crystal structure and associated defects

The natural mineral kesterite belongs to the family of $A_2^I B^{II} C^{IV} X_4^{VI}$ compounds, which can be found in two main tetragonal crystal structure types: the kesterite type and the stannite type structure[77]. Those structures are closely related but differ in their cationic distribution (A^I and B^{II}). In their structures each anion X^{VI} is surrounded by two A^I, one B^{II}, and one C^{IV}. In addition, every cation is tetrahedral coordinated by XVI as can be observed in **Figure 1.13.** Both structures are quite similar and difficult to depict their differences only by applying crystallographic methods, which leads to the necessity of applying a careful crystal structural analysis with the aim to differentiate within structures. Nevertheless, several First-principle calculations predict the kesterite structure to be more stable than the stannite one, for both CZTS and CZTse[78–80]. Neutron power diffraction has proven to be, all together with high-resolution XRD studies, a good tool to support that both CZTS and CZTSe crystallize in the kesterite structure[81,82]. Quite recently, polarized Raman spectroscopy has also proven to distinguish kesterite and stannite structure and confirm the presence of kesterite in most compounds[83].
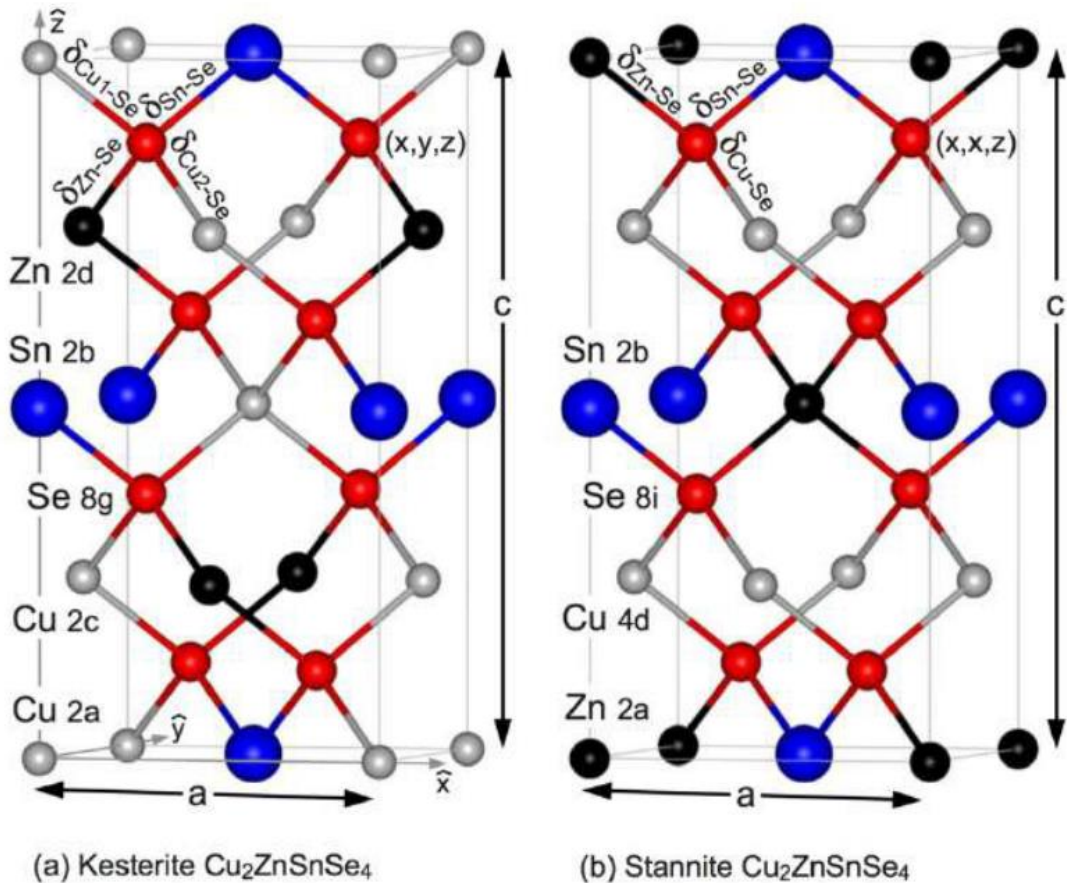
Figure 1.13 Conventional unit cells of the (a) kesterite structure and (b) the stannite structure for CZTSe, containing four Cu atoms (light grey), two Zn atoms (black) two Sn atoms (blue) and eight Se atoms (red) per conventional unit cell. Reproduced from *Persson*[84].

The kesterite structure and more specifically the arrangement of its atoms generates very interesting and challenging phenomena. The most important and recognized one is the Cu/Zn disorder[70,85]. This Cu/Zn disorder is originated by the presence of mixed Cu-Zn planes in the kesterite structure, the similar ionic radii of Cu and Zn and the fact that both are isoelectronic makes them very likely to interchange positions. This Cu/Zn disorder promotes the formation of common Cu_{Zn} and Zn_{Cu} antisites defects. Usually, those defects are tried to be compensated by applying Cu-poor Zn-rich composition as a target for high-efficiency devices[86,87]. However this synthesis conditions, not all the Cu/Zn disorder can be eliminated and it promotes an increase into the bad-tailing (formation of trap states that arise due to electrostatically potential fluctuations), which are detrimental for the open-circuit voltage (V_{oc}) and the final efficiency of the solar cells[88,89].
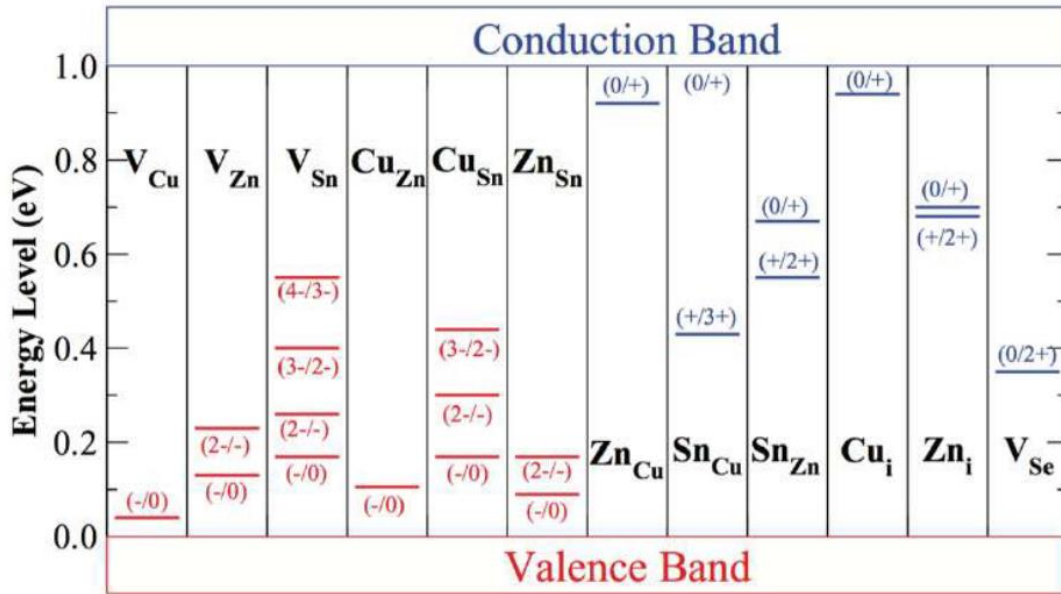
Figure 1.14 Ionization levels of intrinsic defects in the band-gap of CZTSe. Red bars contain acceptor levels, whereas blue bars contain donor levels, with initial and final charge states labelled in parenthesis. Reproduced from *Chen et al*[90].

In **Figure 1.14** theoretically calculated ionization levels of different intrinsic defects can be observed, e.g. cation anti-sites and vacancy defects. The most common and shallow acceptor defects are the V_{Cu} and Cu_{Zn} and they are expected to contribute to the p-type conductivity of the CZTSe. Deep defects are a striking issue into CZTSe solar cells as they act as recombination centres for hole-electron pairs, resulting detrimental for the solar cell final performance. Looking into detail in **Figure 1.14**, most of the Sn-related defects, (V_{Sn} and Sn-antisite defects) are located deep within the band-gap potentially detrimental for the device operation. Moreover, Sn atoms in the kesterite structure have been identified to adopt different oxidation states (+II or +IV) that may contribute to the formation of detrimental defects, in a more specific sight: Sn_{Zn} has proven to be a deep recombination centre when Sn adopts state +II[91].

A very interesting and promising research strategy in the kesterite community is doping (or alloying). Doping as mixing with small amounts (<1at%.) is a very interesting path to modify electrical properties, transport charge properties, interfaces characteristics, morphology or elemental distributions. Yet doping will not or only slightly affect the optical band-gap or structural parameters. On the other hand, alloying (typically >1at%.) is the most interesting path to tune the band-gap and achieve fundamental properties changes.

1.5   Objectives of the present thesis

The main objective of this thesis is to develop novel high efficiency thin film photovoltaic technologies based on sustainable kesterite ($Cu_2ZnSnSe_4$) absorbers. Taking as a basis IREC's previously established baseline: a sequential process (sputtering of metallic precursors followed by reactive annealing), it has been implemented a Rapid Thermal Processing (RTP) annealing. In order to fulfil this general objective, several sub-objectives are proposed:

1. Development, establishment and optimization of a sequential process for the synthesis of kesterite thin films, consisting on the sputtering deposition of Cu/Sn/Cu/Zn metallic stacks onto Mo-coated soda-lime glass substrates and its posterior annealing in a Se atmosphere via Rapid Thermal processing in a semi-closed system.
2. Study and establishment of the fastest possible RTP annealing process that maximize its efficiency without compromising the solar cell qualities.
3. Obtainment of a deep understanding on the formation pathways that run the kesterite synthesis through the annealing technologies present at IREC.
4. Acknowledge the synthesis conditions to drive the kesterite through the different formation pathways, depicting its pros and contras.
5. Study of the flexibility and reliability of the established Rapid Thermal Processing annealing baseline by extending it to other precursor synthesis techniques.

Chapter 2

Methodology and Experimental

2 Methodology and Experimental

Figure 2.1 Schematics of the typical fabrication and characterization process for CZTSe solar cells by Rapid Thermal Processing at IREC.

In **Figure 2.1** can be appreciated the sequential process developed at IREC for the synthesis of CZTSe absorber layers, as well as the fabrication and characterization of the corresponding solar cell devices. This include the following steps: metallic stack precursors deposition by DC-magnetron sputtering, absorber synthesis via Rapid Thermal Processing or Conventional Thermal Processing, detrimental secondary phases removal via chemical etching and finally buffer layer and window layer deposition via chemical bath deposition and pulsed DC-magnetron sputtering respectively. In more detail:

1. **Metallic precursor deposition.** Cu/Sn/Cu/Zn metallic precursors were deposited by DC-magnetron sputtering (Alliance Concept Ac-450) onto Mo coated soda lime glass (10 x 10 cm^2, 600-800 nm Mo + 3mm glass, $R_\square$ = 0.25-0.4 $\Omega/\square$). Precursors films were approximately 650 nm thick, with compositions range near of those reported as ideal for high-efficiency solar cell devices, namely, Cu-poor and Zn-rich conditions: Cu/(Zn+Sn) = 0.77, Zn/Sn = 1.21, Cu/Zn = 1.41 and Cu/Sn = 1.71.

2. **Absorber formation.** Precursors (2.5 x 2.5 cm^2 in area) were then selenized by RTP using an AnnealSys AS-ONE-100 furnace in a semiclosed system made up by a graphite box with a reaction volume of 3.8 cm^3. Approximately, 20 mg of elemental Se (Alfa Aesar, 99.999% purity) are placed into the box next to the substrates and after two vacuum and purge cycles (base vacuum of $3x10^{-2}$ mbar), the Ar flow was increased until obtaining 1 mbar total pressure inside the furnace. Then, the reactive annealing was conducted in a two-step process. (1) heating from room temperature up to 400 ^{o}C (ramp, 180°C/min; dwell time, 3 min) and (2) heating to 500 ^{o}C with an increasing in pressure up to 900 mbar (ramp, 60 ^{o}C/min; dwell time, 5 min). The temperatures during all the process are measured by a calibrated pyrometer located just below the sample holder, which consists of a specially designed graphite box. After the second step, the setup cools down naturally to below 80 ^{o}C (also at 900 mbar). The whole annealing process lasts for 12 min with additional 8 min for the cool down step. In RTP, the reaction process is so fast that no extra Sn in principle is required.

3. **Detrimental secondary phases removal.** The CZTSe absorbers are submitted to two etchings in order to remove mainly ZnSe and SnSe secondary phases. (1) $KMnSO_4$ etching in H_2SO_4 acidic media in order to transform ZnSe[92] into elemental Se and (2) $(NH_4)_2S$ etching was also realized in order to remove the previously formed elemental Se and also possible Sn-Se secondary phases[93].

4. **Buffer layer deposition.** CdS is grown by chemical bath deposition (CBD) in a vertical configuration at 75 ^{o}C for 40 min by a $Cd(NO_3)_2$ bath. The chemical bath is composed by

Cd(NO$_3$)$_2$, Na$_3$C$_6$H$_5$O, CH$_4$N$_2$S and NH$_4$OH with a pH = 9.5. The thickness of the CdS buffer layer is around 50 nm.

5. **Window layer deposition.** First an i-ZnO layer around 50 nm is deposited and then a 200 nm In$_2$O$_3$: SnO$_2$ (ITO) layer were deposited via DC pulsed magnetron sputtering (CT100 Alliance). The sheet resistance of the window layer is around 30-100 Ω/□.

Once the solar cells were finished, 3 x 3 mm^2 cells were mechanically scribed and indium was soldered onto Mo surface in order to complete device fabrication.

2.1 Physical Vapour Deposition: Sputtering

Sputtering deposition is englobed into the Physical Vapour Deposition (PVD) techniques. PVD are techniques that normally involve vaporized coating techniques, which rely on the material transfer up to atomic/molecular level. One of the main points for PVD is that in contrast to Chemical Vapour Deposition (CVD) techniques, the material that is going to be deposited starts initially already in solid state (gaseous for CVD). Sputtering deposition was originally thought to deposit refractory materials and has found a very interesting application in thin films depositions and most of the materials are able to be deposited by sputtering techniques[94].

The basic principle for sputtering deposition is:

- *"Bombardment and removal of the cathode material with positive ions from a rare gas discharge"*[95]

This principle can be depicted onto the basic schema for sputtering deposition, where it can be observed what is required for a sputtering deposition: a vacuum chamber, an external pumping system, sputter sources, vacuum gauges, a substrate holder and a gas flow supply.
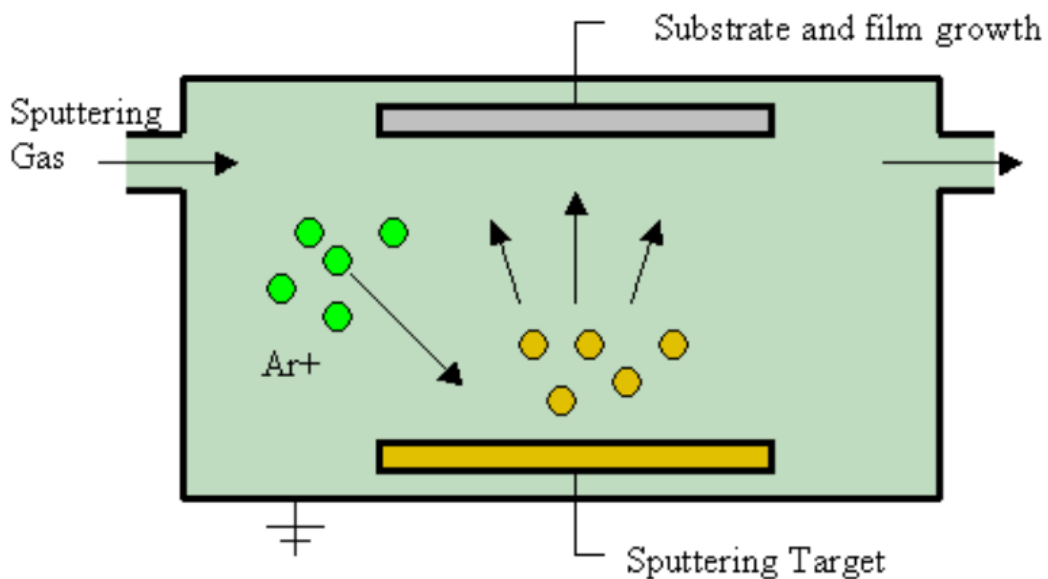
Figure 2.2 Sputtering schema[95]

In order to obtain the deposition of the sputtered element, the inert gas ions are accelerated onto the target and some of the surface atoms are sputtered off from the target, leading to the ejection of those atoms that can "flow" towards the substrate holder in order to finally obtain the grown thin film. Moreover, one of the most interesting points about sputtering deposition is that the deposited film will have the same stoichiometry as the target.
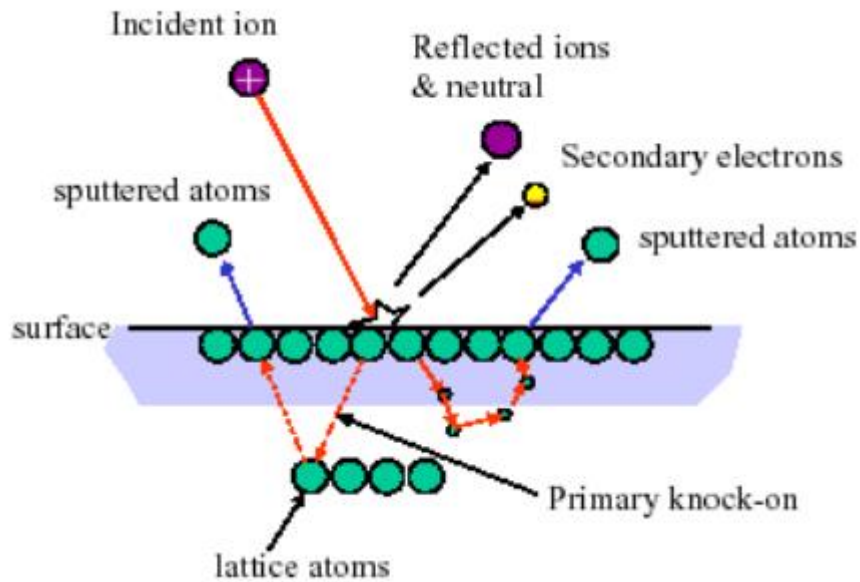
Figure 2.3 Sputtering mechanism[96]

The sputtering process is usually characterized by the sputtering yield S (see the definition of S in *Seah et al*[97]*)*. S most typically ranges from 0.01 to 4. This sputtering yield depends on[98]:

- The energy of the incident ions
- The masses of the ions and target atoms
- The binding energy of atoms in the solid
- The incident angle of ions

In summary the advantages of sputtering deposition can be summarized into:

- Elements, alloys and compounds can be sputtered and deposited onto substrates
- Employing sputtering targets provide a stable and a vaporization source with a long life.
- Also, reactive depositions can be obtained by using reactive species activated by a plasma.
- The source and substrates are spaced together in the same chamber
- The volume of the sputtering chamber can be chosen.

2.1.1 Magnetron Sputtering

There are several sputtering working conditions such as: DC (direct current) diode sputtering, RF (radiofrequency) sputtering, reactive sputtering and the one employed in this thesis: magnetron sputtering.
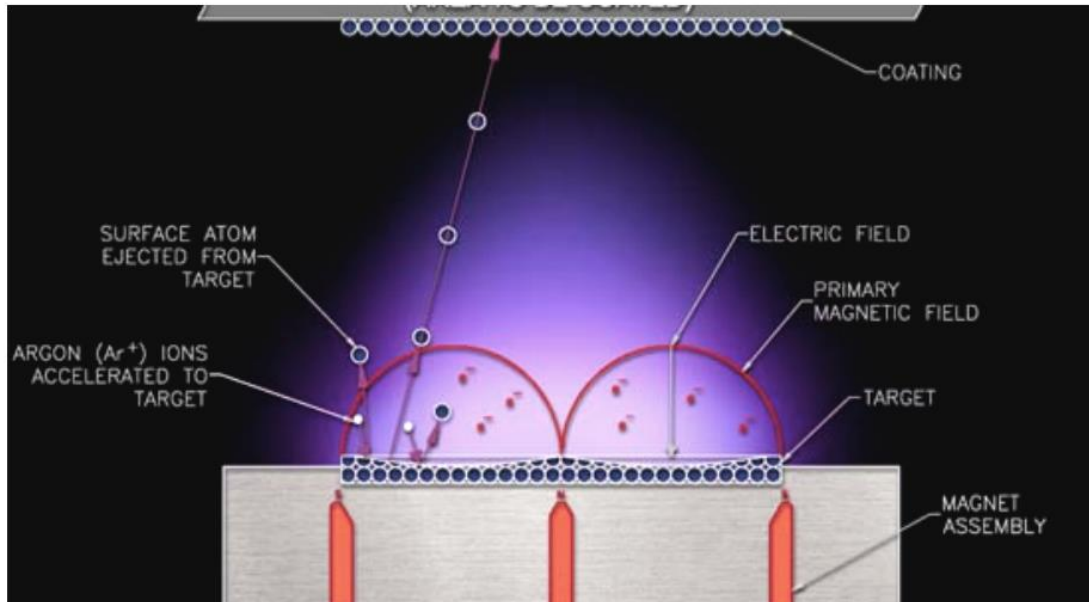
Figure 2.4 Magnetron sputtering principle[99]

The magnetron sputtering working mode is represented into **Figure 2.4** which shows how this technology employs powerful magnets with the aim to confine the glow discharge plasma to the closest region towards the target. This configuration helps to hugely improve the deposition rate just by maintaining a high density of ions, ending onto an electron/gas molecule collision process way more efficient. Magnetron sputtering is able to employ either DC or RF sources[100].

In summary, magnetron sputtering ensures a high deposition rate, helps reducing electron bombardment over the substrate and allows to extend the operating vacuum range. All those conditions commented previously have situated Magnetron Sputtering as the most widely commercially practiced sputtering method.

At IREC two main sputtering systems are fully operational into the kesterite solar cell processing baseline, being[101]:

- **Alliance Ac450** (**Figure 2.5**, left): This system is comprised by a load lock and a deposition chamber connected to a mechanical pump and a turbomolecular pump. Inside the deposition chamber there are three confocal cathodes located at the top where 101 mm diameter targets can be placed. The substrate is placed at the bottom. It is equipped with a DC generator (TRUMPF Truplasma DC 3002) for sputtering and a RF generator (TRUMPF PFG 300 RF) for plasma etching surface treatments. This system was used for the deposition of metallic layers (Cu, Zn and Sn). The depositions were performed using an Ar plasma.
- **Alliance CT100** (**Figure 2.5**, right): This system is comprised by a load lock and two deposition chambers each of them connected to independent mechanical and

turbomolecular pumps. There are two cathodes at the left chamber and three at the right chamber where 101 mm diameter targets can also be placed. It is equipped with a pulsed DC generator (Advanced Energy DC pinnacle plus). The left chamber was employed for Mo deposition and the right chamber for the deposition of oxides and TCOs (ZnO and In_2O_3 : SnO_2).

Figure 2.5 Magnetron sputterings present at IREC

2.2   Rapid Thermal Annealing

This section is devoted to the description of the Rapid Thermal Annealing (RTP) equipment available at IREC, due to the key relevance of this technique in the present Thesis.

2.2.1   The RTP set-up

The RTP set-up available at IREC consists of an ANNEALSYS-AS-ONE 100 furnace which has been specially designed to be able to perform in a wide range of laboratories such as: universities, research laboratories or small-scale production lines. The equipment contains a process chamber made out of stainless steel cold wall technology designed at ANNEAL-SYS, optimal for a fast cooling[102]. The substrate size accepted is up to 100 mm in diameter and the temperature range works up to 1300 $^{\circ}$C, however the one present at IREC has only been calibrated for temperatures below 750 $^{\circ}$C due to the kesterite annealing conditions. The RTP employs 4 gas lines: compressed air, Argon (Ar), argon: hydrogen (Ar:H$_2$) and Nitrogen (N$_2$) and a dry pump to reach the desired vacuum for the process. Thanks to the special low-volume design for the process chamber, a fast pumping and a very low process gases consumption can be easily obtained. The temperature is measured in three different points in the chamber by employing a pyrometer and two extra thermocouples being controlled by the fast PID for RTP employed in the present equipment, allowing a very accurate control of the process. Finally, this RTP process is directed by its own software that can include processes with up to 100 steps and a complete logging of the data processing and the historical process realized.

Physical specifications

- Voltage: 3x400V+N+Gr
- Power: 30 kW
- Water: 2 to 4 bars, pressure drop 1 bar, 10 l/min
- Compressed air: 6 bars (valve actuation)
- Process gas fittings: double ferrule $^1/_4$
- Width: 530 mm
- Depth: 800 mm
- Height: 1.425 mm
- Mass: 194 kg
- Temperature range up to 1300 $^{\circ}$C
- Ramp up rate up to 200 $^{\circ}$C/s (depending upon version)
- Cooling rate up to 100 $^{\circ}$C/s with special equipment
- Gas mixing capability with mass flow controllers
- Vacuum range: atmosphere to 10^{-6} Torr
- Full PC control with Windows compatibility

Figure 2.6 ANNEALSYS-AS-ONE 100[103]

2.2.2 RTP State of Art

RTP processing has become one of the hottest topics amongst the kesterite community as it employment has kept increasing over the years. First works reported into the literature date from 2011 by *Maeda et al.*[104] where the annealing temperature dependence for CZTS thin films was studied. On it, two-steps annealing procedures were also implemented with a first step at 250 °C for 10 min and a second step that ranged from 350 up to 600 °C that also lasted for 10 min, employing a ramp of 100 °C/min, double than the maximum possible ramp with CTP by IREC's furnaces. Despite this, and although no working devices were already obtained, interesting properties that RTP processing generates for the absorbers have been reported such as: improvements into the gran size, reduction of S defects and increase in the crystalline quality of the films with short cycle times and low thermal budgets. More research groups started working with RTP through the next years[105–108] and by the year 2013 CZTSSe devices with a 6.6% efficiency were already reported[108]. Unfortunately, only info about the processing temperature was reported (500 °C). An impressive 7.5% obtained by solution processes was also reported, yet once again very few details about the RTP processing were published.[109]

By the year 2014, first approaches to employ RTP with precursors obtained via sputtering were performed for CZTS by *Sousa et al.*[110] and for CZTSe by *Fairbrother et al.*[111] reaching up to 3.1% and 4.3%, respectively. Deep studies on the annealing properties and the conditions were carried on by *Sousa et al.*[110] studying: the heating rate, the maximum sulfurization temperature, the time at maximum temperature and the amount of evaporated sulphur. The amount of

evaporated sulphur proved that samples sulfurized at higher temperatures, shorter times and higher amount of it exhibited larger grain sizes. On the other hand, *Fairbrother et al.*[111] focused his studies onto the precursor stack order, which is of key importance for the films properties including alloys formation, composition and/or elemental losses, morphology and its secondary phases appearance and distribution. The most beneficial precursor ordering obtained was Sn/Zn/Cu thanks to its reduction into elemental losses. Furthermore, it must be pointed out that those were the first studies about RTP processing carried on at the Solar Energy Materials and Systems group (SEMS) at IREC.

The year 2015 came as a breakthrough for RTP processing as the number of publications related to it, widely increased. New techniques such as cathodoluminiscence (CL) started to be employed to characterize RTP annealed samples, focusing into the phases presented and the crystalline quality[112], yet it was proven that there was not enough database to report an exhaustive and detailed study. For the first time, spin-coated CZTS thin films were started to be annealed by RTP[113] but due to a low crystallinity it was not possible to obtain working devices. Also, Pre-annealing treatments (PAT) appeared and were included into processing baselines[114]. PAT helped to enhance CZTSSe overall parameters thanks to its fully developed micron-sized grains, without interfacial voids, in contrast to the cases where PAT was not applied. PAT also affected the elemental concentrations through the whole sample. The upper parts showed well-crystallized kesterite phases, whereas in films without PAT voids and zinc-segregations were also found. Thanks to this PAT, the CZTSSe efficiency was able to reach up to 6.77%. The major progress obtained in RTP processing came from the solution processed kesterite by *Haass et al.*[115] where an impressive 11.2% device was obtained. This device was synthesized via hydrazine-free DMSO approach, reporting a V_{oc} deficit of only 0.57 V. This V_{oc} improvement is attributed to the three-stage RTP annealing process, which allowed to obtain an increase into the incorporation of selenium and large-grained microstructure, generating a higher minority carrier lifetime, lower diode current saturation that are related to dispositive with a low concentration of recombination centres.
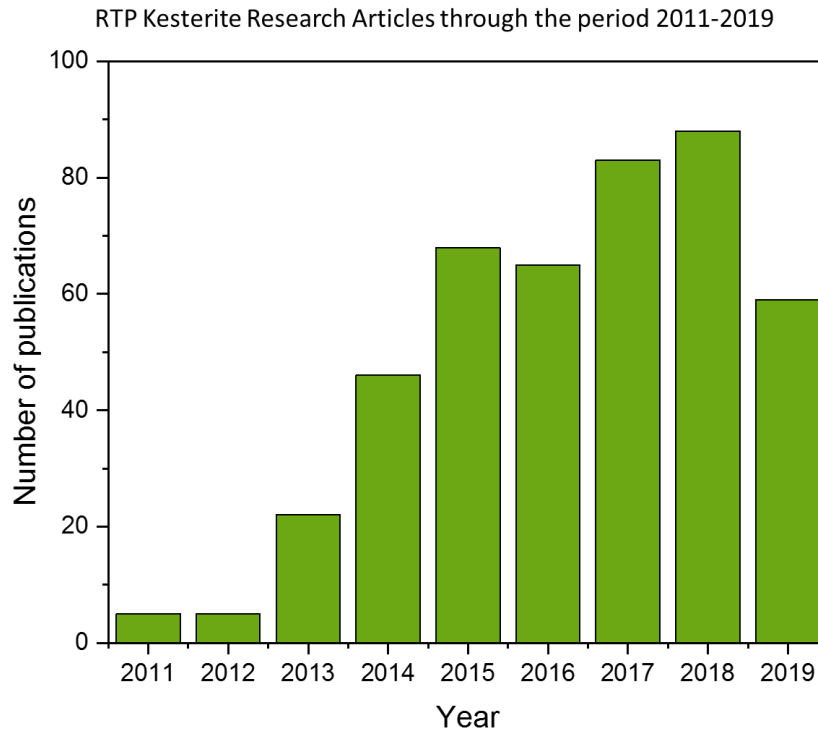
Figure 2.7 Evolution of the citations about Kesterite and RTP processing through the last years. *Values obtained from Scopus by searching "Kesterite or CZTS or CZTSe or Cu₂ZnSnSe₄ or Cu₂ZnSnS₄" and "RTP or RTA or Rapid Thermal Annealing or Rapid Thermal Processing"* [116].

In the year 2016, the scope moved even more towards obtaining highly efficient kesterite. In order to do so, several studies about the effects on the process to synthesize the kesterite were performed. One of the most remarkable and interesting was conducted by *Hages et al.*[117]. On it, it is studied how to tune and how critical are large grains for highly efficient devices. The role of liquid Selenium through the synthesis process at the RTP annealing was studied and a mechanism was proposed for a liquid assisted grain growth. Furthermore, a nanoparticle based dispositive of 9.3% was reported. Another pathway studied by the kesterite community in order to overcome the large V_{oc} deficit was the doping with other elements. In this research line, one of the most interesting was the one were Ag was introduced into the CZTSe structure[118]. By alloying Cu with Ag it was possible to address the absorber band tailoring, reducing the V_{oc} deficit up to 110 meV, reaching an efficiency of 10.2% for a CZTSe device, and also 9.4%[62] for co-sputtering plus RTP processing were obtained.

Other techniques introducing cost-efficient production methods with a high throughput started to be studied. Between them, one of the most promising was to obtain precursors by doctor blade methods and later submit them to RTP annealing processes, though non-working devices were obtained in 2016[119]. Finally, the highest record obtained for a CZTSSe solar cell by RTP was also obtained at 2016, by *Yang et al.* [120] who were able to obtain an impressive record-efficiency of 12.3% for a CZTSSe device, very close to the world record in Kesterite (12.6%). In their work, their scope was set into obtaining a band-gap grading and in order to so SeS₂ was employed. By using a SeS₂/Se ratio, they were able to obtain a graded band gap into the depletion region. Thanks to this band-gap grading a record V_{oc} deficit of 0.576 V was achieved.

By the year 2017, studies on Ag-alloying kept going on and the record efficiency for $(Cu,Ag)_2ZnSn(S,Se)_4$ (CAZTSSe) was increased up to 10.36%[121]. Doping/alloying with Ag allowed to impact on the reduction of the Cu-Zn disorder defects which helps to improve the quality of the thin film.

Further strategies to tackle the V_{oc} deficit problem, were investigated by stacking two CZTS layers with different doping level[122]. Thanks to this double stacking structure, it was possible to increase the V_{oc} around 70-80 mV, yet the J_{sc} decreased because of voids between layers and several tailoring problems. With this procedure efficiency up to 7.5% were able to be obtained.

Also, in 2017, as in CIGS, alkali doping was turning a hot topic for solar cells and very interesting reports about it started to appear in the literature[123]. It must be commented the one realized by *Haass et al.*[124] where by employing a potassium post deposition treatment, they were able to reduce the V_{oc} deficit, implying a decrease of interface recombination. On the other hand, this post deposition treatment implied also a decrease into the J_{sc}, the fill factor and the efficiency of the devices. However, it opened a very interesting path to help reducing one of the main drawbacks of the kesterite technology, the V_{oc} deficit.

In the year 2018, the quest for highly efficient kesterite devices remained open and alkali doping was increasing its presence more and more. Several elements were studied such as Na or Li. About Na doping it was studied via applying a NaF layer either before the RTP annealing or after it as a post-deposition treatment[125]. This Na doping helped to once again increase the acceptor concentration, which ended up into an improvement for the V_{oc} and the FF. Li doping also proved to be a booster for kesterite efficiency and helps to improve the overall electronic parameters. Furthermore, by tuning the ratio Li/(Li+Cu) it is possible to tune the band gap of the solar cell[126].

Also, studies on the Zn/Sn ratio were conducted by *Min et al.*[127] depicting once again, as through the last years, the importance and how challenging is to study the precursor composition for a highly efficient device. On their study, it was demonstrated that by increasing the Zn/Sn ratio it was possible to slightly narrow the energy band gap to extend the light absorption range and improving the photocurrent. Devices with efficiencies up to 10.1% were reported. All those works of course were performed using RTP annealing.

Table 2 Evolution of the RTP state of the art through the last years (2011-2018)

Ref	Year	Material	Annealing Process	Efficiency(%)	Remarkable info
a	2011	CZTS	(1)250 °C-10min-100°C/min (2) 300-600°C-10min-100°C/min	-	First processes applied
b	2013	CZTSSe	Sulfur containing atmosphere	6.6	First efficiencies reported
c	2013	CZTSSe	540°C for 6 minutes	7.5	Tri-layer structure with homogeneous structure
d	2014	CZTS	0.2 °C/s rate	3.1	Large gran sizes
e	2014	CZTSe	500 °C-180°C/min-3min	4.3	Sn/Zn/Cu Precursor Stack Order
f	2015	CZTSe	550 °C-5min	-	CL Characterization

g	2015	CZTS	500 °C-120 °C/min-10 min	-	Spin-coated films
h	2015	CZTSSe	600 °C-25°C/s-20 min	6.77	PAT study
i	2015	CZTSSe	300,500,550°C-100 min	11.2	Three stage process
j	2016	CZTSe	500°C-5°C/s	9.3	Nanoparticles
k	2016	CZTSe	450-600°C	10.2	ACZTSe
l	2016	CZTSe	550 °C-4°C/s- 5 min	9.4	Co-sputtering process
m	2016	CZTS	500°C -30 min	-	Ball-Milled precursors
n	2016	CZTSSe	300°C-25 min-510°C-18min	12.3	Bandgap grading
o	2017	CZTSe	480°C-9°C/s-20min	11.2	ACZTSe
p	2017	CZTS	9°C/min and 30°C/min	7.5	Double Stack Layer
q	2017	CZTSSe	300,500,550°C-100 min	9.7	KF PDT
r	2018	CZTSe	550°C-4°C/s-5min	7	NaF Pre orPDT
s	2018	CZTSSe	300,500,550°C-100 min	11.6	Li doping

References: a[104], b[108], c[109], d[110], e[111], f[112], g[113], h[114], i[115], j[117], k[118], l[128], n[120], o[129], p[122], q[124], r[125], s[126].

2.3 Characterizations

In this section, a very brief description of the main characterization techniques is presented, together with the typical parameters employed during this Thesis.

> **Scanning electron microscopy (SEM)**. The SEM images were obtained through a ZEISS Series Auriga microscope using accelerating voltage (5-10 kV), with a working distance of 5-8 mm and a magnification ranges from 10000 x to 50000.

> **X-ray diffraction (XRD).** XRD measurements were performed using a PANalyticial X'Pert ProMPD diffractometer with Cu Kα radiation (λ = 1.54056 Å) monochromated and a secondary graphite monochromator.

> **Raman spectroscopy (RS)**. Raman scattering measurements were performed in back scattering configuration using a Horiba Jobin Yvon fHR-640 spectrometer for the wavelengths 325nm, 442nm and 532nm and an iHR-320 spectrometer for the 785nm wavelength. Spectrometers are coupled with Raman probes developed at IREC and a low noise CCD detector cooled to -70°C. Excitation and light collection were made using a macro optic system with a laser spot diameter of the order of 50 μm. In order to avoid thermal effects in the spectra, the power density on the surface of samples was kept below 150 W/cm^2. The position of all spectra has been corrected taking into account the first order Raman spectrum of monocrystalline silicon as a reference measured before each acquisition and imposing its position at 520 cm^{-1}.

> **X-ray fluorescence spectroscopy (XRF).** A Fischerscope XVD system has been used for the measurement of the composition and the thickness of metallic precursors and kesterite absorbers. The system is calibrated with a set of standards whose composition was determined via inductively coupled plasma optical-emission spectroscopy (ICP-OES,

Perkin-Elmer Optima 3200 RL). Usually average values were obtained by measuring 9 or 16 points for each sample.

- ➢ **Glow discharge optical emission spectrometer (GDOES).** Depth profiling analysis were performed by GDOES using a Horiba Jobin Yvon GD Profiler 2 Spectrometer, equipped with an anode diameter of 4 mm and 19 element channels.
- ➢ **Current Density-Voltage measurements (J-V).** Dark and illuminated J-V curves have been obtained using an ABET Technologies Sun 3000 Class AAA solar simulator calibrated by a reference silicon solar cells at 1 sun, AM 1.5G and 25 ^{o}C.
- ➢ **External Quantum Efficiency (EQE).** The external quantum efficiency of the devices has been obtained on a Bentham PVE300 system, calibrated by Si and Ge photodetectors. The maximum measurement range is 300-1600 mm.

Chapter 3

Transferring and understanding the kesterite's annealing baseline towards RTP

3 Transferring and understanding the kesterite's annealing baseline towards RTP

3.1 Comparison of the optimized CTP and RTP process protocol and best device efficiencies

Obtaining a good quality kesterite absorbers remains still as one of the main challenges for kesterite technology. In order to do so at IREC, the baseline developed has been based on the so-called sequential process where the precursor and the absorber are synthesized in separated steps[130,131]. Sequential processes show a high number of advantages and are in possession of several of the highest efficiencies amongst the kesterite technology. They consist of the separate synthesis of the precursors (Cu, Zn, Sn) (CZT) and their reactive annealing in furnaces. Thanks to this separate synthesis process, it is possible to achieve a high accuracy of the thickness of the different layers allowing a precise control of the precursor's ratio obtained in order for them to be Cu-poor and Zn-rich. This region has been proven to be the one with the highest efficiency for kesterite compounds[132].

Employing sequential processes might seem more time consuming because of each layer for the precursor must be deposited successively. However, it allows a higher deposition rate than for co-evaporated processing as it is not necessary to balance all the deposition metals at once. Once the precursor is deposited, then it is submitted to the annealing step in order to synthesize the kesterite. This annealing step is commonly realized within CTP and this technology has shown the highest efficiencies amongst the kesterite technologies. CTP furnaces have been extensively employed into laboratory research and provide annealing routes with radiative heating generated from electrical resistances that last for several hours.

IREC's kesterite baseline production has not been an exception and an extensive research over CTP annealing routes has been carried out over the last years[64,130,133]. Usually, the absorber synthesis process consists of two steps: a first one about the synthesis of the kesterite at low temperature and a second one that consists on the crystallization of the kesterite grains in order to obtain a better absorber at a higher temperature. For the CTP annealing process it is necessary to include extra Sn, in powder form at IREC's baseline, in order to compensate the loss of highly volatile species through the process that would affect the final performance of the device[134]. The annealing process is driven by thermodynamic (temperature, total pressure and the chalcogen partial pressure) and kinetic parameters (ramp rate and dwelling time) that must be controlled and optimized in order to obtain highly efficient kesterite devices. At IREC's baseline a particular system that is composed of a semi closed graphite box has been specially designed which has allowed to improve the kesterite performance through the years until reaching 11.8% (Illuminated Area) for CZTSe as published in *Giraldo et al.*[66].

Previous studies over the CTP annealing have been conducted through the years at IREC until establishing a current annealing baseline process that consists of:

Annealing profile	Temperature (°C)	Se amount (mg)	Sn amount (Sn)	Pressure (mbar)	Ramp rate (°C/min)	Dwell time (min)
2 steps	1) 400°C 2) 550°C	100 mg	5 mg	1) 1.5 mbar 2) ≈1 bar	20 °C/min	1) 30 min 2) 15 min
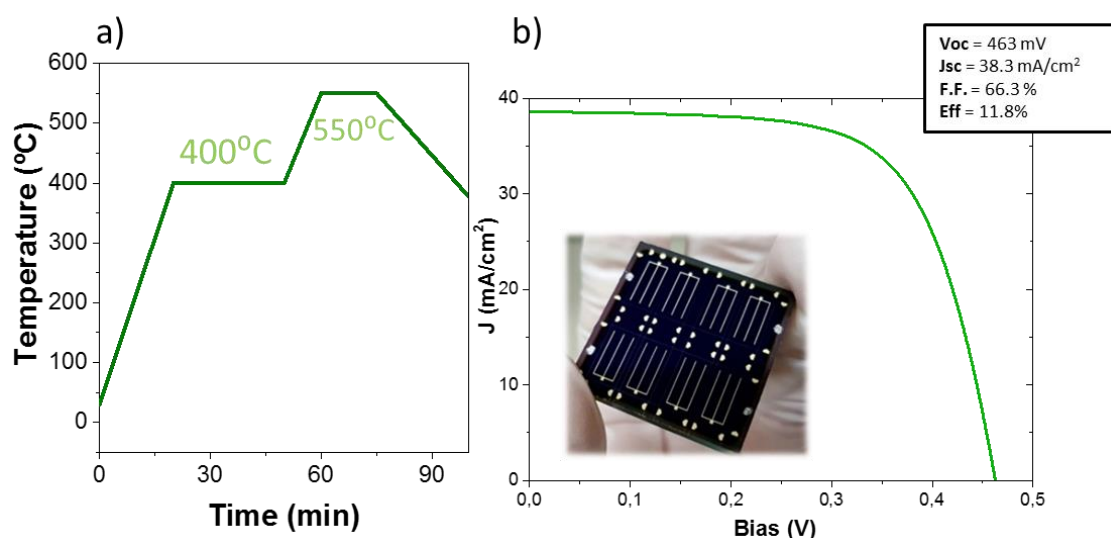
Figure 3.1 a) Temperature profile of the two-step CTP annealing process from IREC's baseline. **b)** Record efficiency CZTSe solar cell obtained at IREC and presented into *Giraldo et al.*[66]

Major progresses and advances, either at IREC or worldwide, have been carried out into CTP. If discussing about a possible posterior industrial application, CTP annealing it is not a very suitable candidate as the annealing routes usually take around 2-3h for each annealing, compromising its possible adaptation. Whereas, RTP appears as a very promising way to foresee a future industrial application for kesterite thanks to its many advantages:

- The use of fast heating through the halogen lamps is extensively employed into the conventional PV industry, helping for a future easier adaptation.
- RTP offers a substantial reduction of the time required for the synthesis and crystallization process, minimizing the processing time and energy consumption.
- The RTP setup allows obtaining a more precise control of thermal treatment parameters.
- In contrast to CTP that is governed by a thermodynamically control, RTP allows a kinetic control.
- RTP processing is better suited for the development of complex recrystallization processes involving several steps.
- RTP processing allows achieving higher chalcogen vapour pressures from its very beginning producing several changes that have been proven to be beneficial for the kesterite, which will be further presented and explained through this present chapter.

In order to establish a new baseline for kesterite annealing via RTP at IREC's sequential process, all the knowledge obtained at IREC in the CTP has been taken as a basis for the RTP baseline. A

new set up has been designed for the RTP annealing consisting of a specially designed semi-closed system of a graphite box with a volume of 3.8 cm^3, located at the centre of the chamber as can be observed in **Figure 3.1** using an AS-ONE-100 furnace. Approximately, 20 mg of elemental Se are placed into the graph box next to the substrates and submitted to the annealing process.
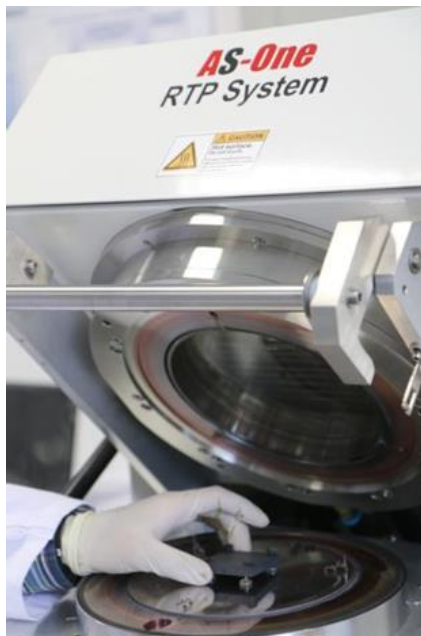
Figure 3.2 AS-ONE-100 RTP furnace showing the special set up designed at IREC.

The aim for the RTP process optimization has been set to obtaining the highest efficiency achievable for CZTSe employing the fastest possible process, as it would be most interesting for the industry.

3.1.1   First attempts: Single-step processing

Working with standard CZT precursors obtained at IREC, the first attempts were conducted with a single step process:
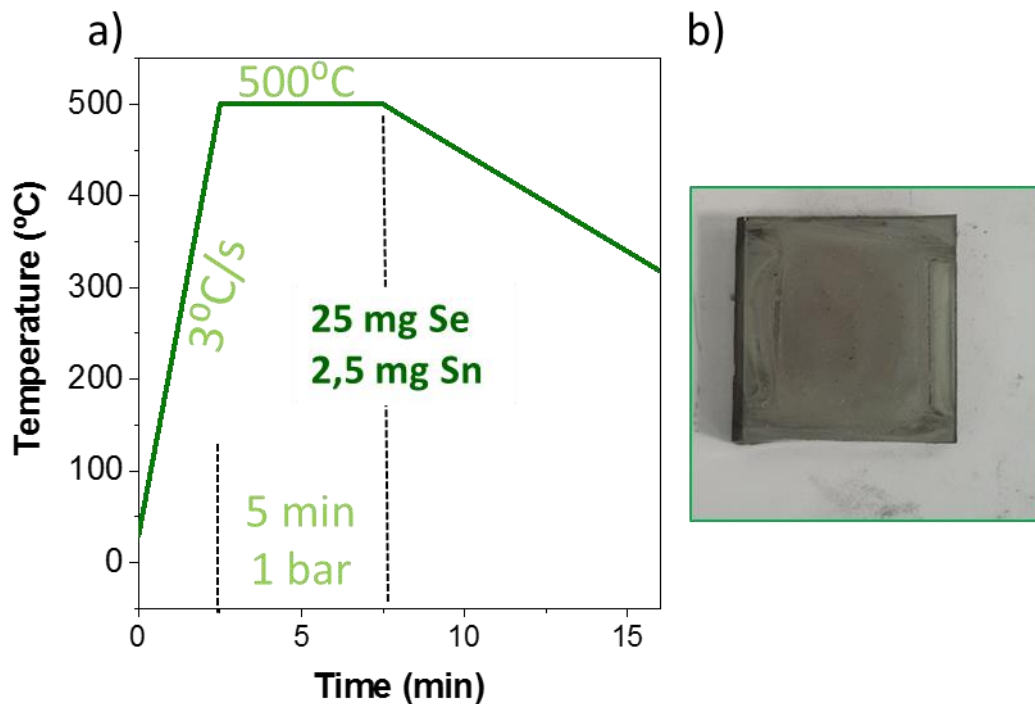
Figure 3.3 a) Single-step RTP annealing processing schema detailing the processing conditions. **b)** Example of a non-homogeneous sample obtained by single-step RTP annealing.

Table 4. Summary of the most relevant annealing parameters for the RTP single step annealing process at IREC's baseline

Annealing profile	Temperature (°C)	Se amount (mg)	Sn amount (Sn)	Pressure (mbar)	Ramp rate (°C/sec)	Dwell time (min)
1 step	500°C	25 mg	2,5 mg	≈1bar	3 °C/sec	5 min

Single-step RTP processes were able to provide already functionalizing devices reaching efficiencies up to 6.4%. Although, this was an acceptable starting point, single-step devices showed a very low homogeneity and uniformity. This shows the difficulty to properly control the selenization of the absorber with this approach. It became clear that although this was a very fast processing way, single-step RTP processing compromised the efficiency of the final device. So, two-step processes were started to be studied based on the previous knowledge obtained in the group for CTP. From the start of the two-stages RTP implementation, improvements in homogeneity and uniformity came clear even by bare eye.
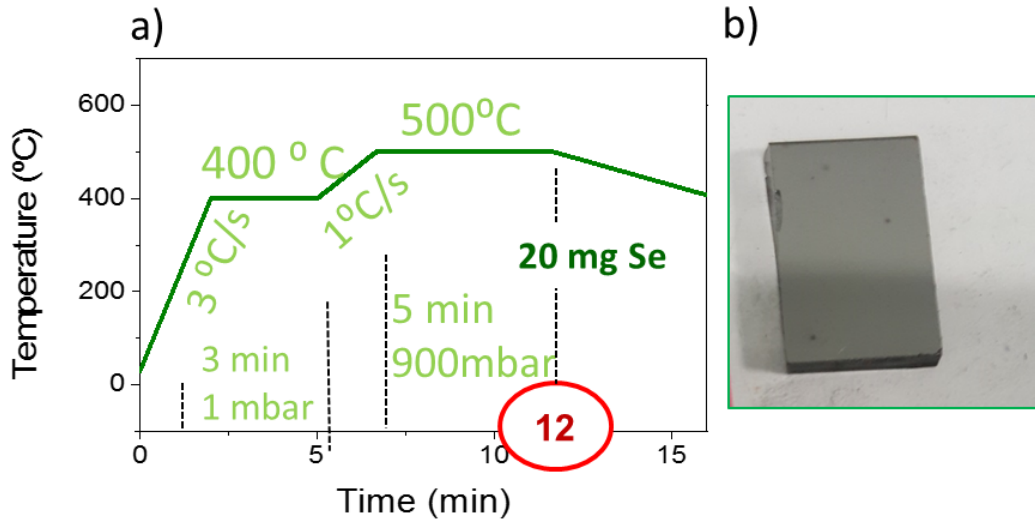
Figure 3.4 a) Two-step RTP annealing processing scheme detailing the processing conditions. **b)** Example of a homogeneous sample obtained by two-step RTP annealing.

3.1.2   Improvement: Two-step temperature profiling

For the two-step RTP annealing procedure two evacuation and purge cycles (base vacuum of 3×10^{-2} mbar) are realized, before the Ar flow is increased until obtaining 1 mbar total pressure inside the annealing chamber. Then, the reactive annealing is conducted in a two-step temperature profile: (1) heating from room temperature to 400 $^\circ$C (ramp, 180 $^\circ$C/min; dwell time, 3 min) and (2) heating to 500 $^\circ$C (ramp, 60 $^\circ$C/min; dwell time, 5 min). The temperatures through the whole process were measured by a calibrated pyrometer located just below the sample holder. During the second step the pressure is raised up to 900 mbar, once the second dwelling time finishes the process cools down naturally (also at 900 mbar) to below 80 $^\circ$C. The whole annealing process takes only 12 min, with an additional 8 min approximately for the cool down. This process is summarized into **Table 5:**

Table 5 Summary of the most relevant annealing parameters for the RTP annealing process at IREC's baseline

Annealing profile	Temperature (°C)	Se amount (mg)	Sn amount (Sn)	Pressure (mbar)	Ramp rate (°C/sec)	Dwell time (min)
2 steps	1) 400°C 2) 500°C	20 mg	-	1) 1.5 mbar 2) 900 mbar	1) 3°C/sec 2) 1°C/sec	1) 3 min 2) 5 min

As it can be observed in **Table 5**, for the RTP annealing process those no extra Sn in form of powder is added to the graphite box. This is thanks to RTP's so fast annealing processing that not even the volatile species are able to evaporate towards the atmosphere, as will be discussed in more detail throughout the chapter.

The champion cell obtained with this only 12 min (20 min including the cooling process) annealing has achieved an 8.3% efficiency, without Anti-reflective coating (ARC) nor metallic grid, comparable with the results obtained for the CTP and proving how promising RTP annealing

processing is. If we compare this device with others previously reported at our group using the CTP annealing (10.1%, 10.6%, 8.2% and 11.8%)[64–66,135] it can be concluded that the V_{oc} is at the same level, only J_{sc} and FF are slightly lower. Though, it should be noted that the RTP annealing devices have been prepared without any additional Ge doping layer. The J_{sc} is somehow lower than expected, a plausible cause is the rather small absorber thickness (1.2 μm) for these absorbers; also, no ARC has been applied. The lower FF can be related to the necessity to adapt and optimize the back and front contacts for the RTP absorbers and the fact that no metallic grids were applied.
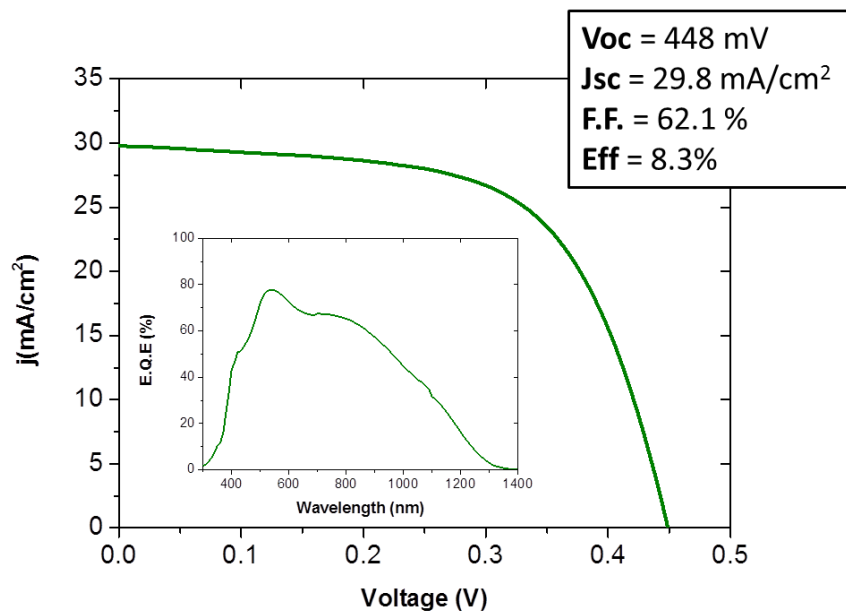
Figure 3.5 j-V illuminated curve (under AM1.5G conditions, no ARC nor metallic grid), and external quantum efficiency of the champion cell obtained by RTP.

3.2   Insights into the Formation Pathways of $Cu_2ZnSnSe_4$ Using Rapid Thermal Processes

In order to comprehend the mechanism that drives the kesterite formation in the RTP process at IREC, a break-off experiment was implemented. The results obtained will be subsequently discussed in this chapter and have been published in *Hernández-Martínez, et al.* [136] (DOI: 10.1021/acsaem.8b00089), also included into the Appendix of this thesis.

3.2.1   Design of the break-off experiment

Figure 3.6 summarizes the break-off experiment, where the process was interrupted at different times of the annealing protocol. The first five points (A-E) cover different temperatures during the first temperature ramp in stage one. Point F is after finishing the dwell time of the first stage. Points G-H-I finally cover different annealing times during the second dwell time at 500 °C (beginning, middle and end of the second stage). The resulting samples after interrupting the

process at times A-I were then thoroughly characterized in a comprehensive manner for their compositional, structural and morphological properties by SEM, XRF, XRD, Raman and GDOES.
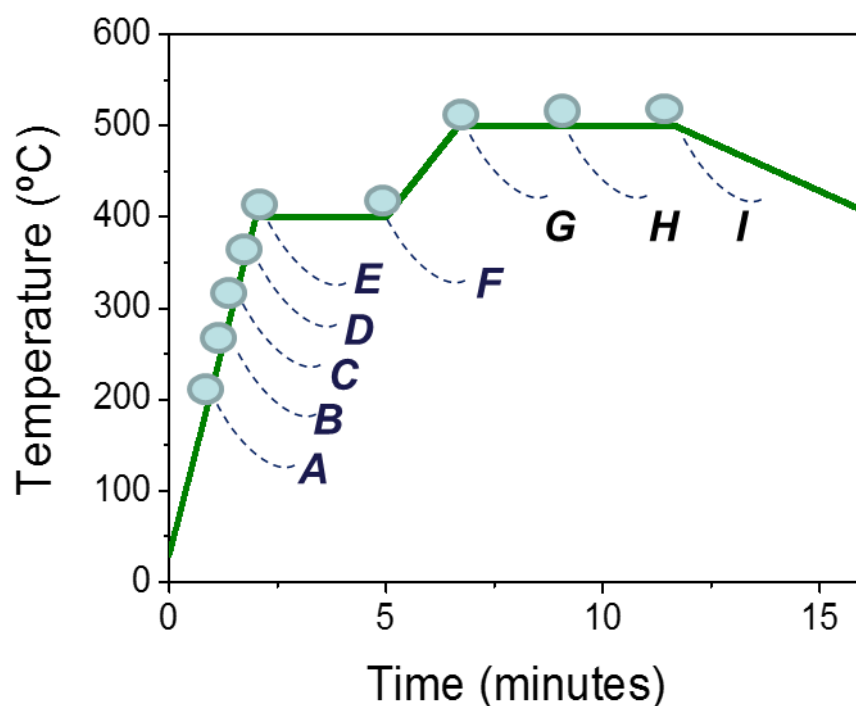
Figure 3.6 Temperature profile with the different stages where the annealing process was stopped. Points A-E are covering temperatures during the first temperature ramping, being 200, 250, 300, 350, and 400 °C, respectively. Points E-I are the different key points in the annealing process.

3.2.2 Selenium incorporation and morphology evolution

The selenium incorporation was studied via XRF analysis (**Figure 3.7**) which shows that the selenization of the metallic precursors is almost completed at point E (Se content approximately 50%). Before E, the selenization is uncompleted (Se content < 15%) and only rather small quantities of Se are further incorporated times later than E. It should also be noted that the Zn/Sn ratio is not severely increased during processing, indicating the mitigation of Sn loss for the fast RTP processes carried out at IREC.

Focusing on the morphology evolution of the samples during the annealing, it was analysed by comparing cross-sectional SEM images. The most relevant samples can be observed in **Figure 3.8**. At point E, the thickness of the precursor has already increased almost as twice with respect to the typical metallic stack obtained with IREC's baseline (**Figure A1** in **Appendix**). This huge increasing into the thickness, in line with the previously observed via XRF, confirms that most of the selenization has already taken place. The first step synthesizes the kesterite and the second one (steps F-I) helps to improve the crystallinity of the absorber. The grain size is clearly increased throughout E-H (first in the surface near region, afterward these grains grow towards the back interface) and rough superficial structures are reduced. Through this morphological analysis conducted the importance of applying a double-step annealing process became clear.
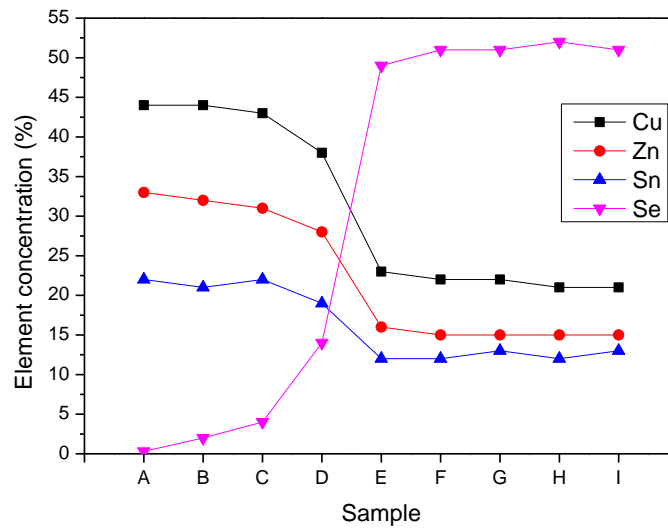
Figure 3.7 Evolution of the concentration of the different elements determined by XRF for the several stages at this experiment.
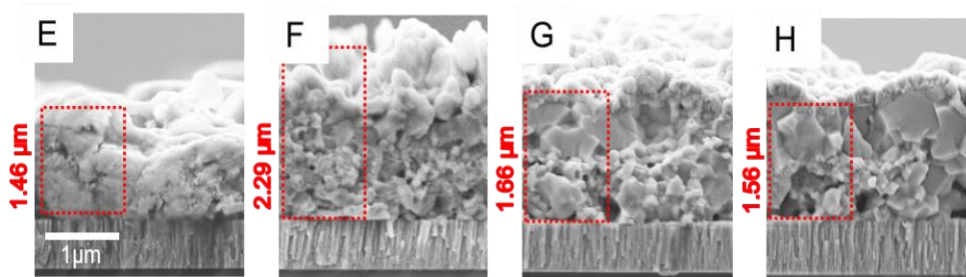
Figure 3.8 Cross-section SEM images of devices from the most relevant samples for the analysis (E-H).

3.2.3 Depth profiling

In order to illuminate the elemental distribution of the layered structures observed in the SEM cross sections and to support the previous statements by XRF, a GDOES depth profiling of the samples has been carried out. Characterization of the samples F-I can be observed in **Figure 3.9**, the depth profiles show a homogeneous elemental distribution already for the sample F, after the end of the first stage. This implies that despite starting with stacked metallic precursors, at the end of the first stage, all elements have intermixed and form a homogeneously mixed material. GDOES measurements with respect to the Na evolution through the process can be observed in **Figure A4** from the Appendix.

Other significant effects are the widening of the selenium depth profile, probably due to the molybdenum selenization, and the increasing of a shoulder in the Cu profile that should arise

from a copper diffusion inside the molybdenum. It is also visible a change in the surface element distribution: while the Se content at the surface seems almost constant during the process (after the step 2), Cu and Zn concentration seem to increase whereas an opposite trend is found for Sn.
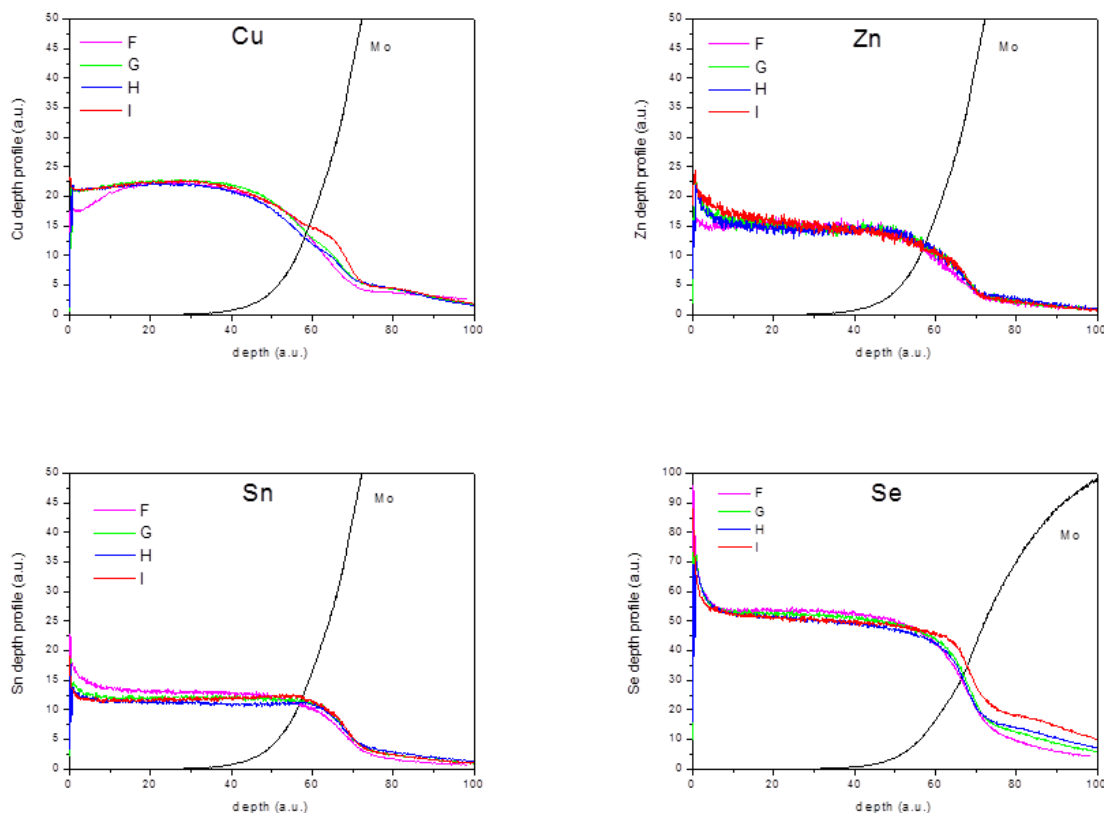
Figure 3.9 Comparison of Cu, Zn, Sn and Se depth profiles in different samples, measured after different RTP step processes

3.2.4   Phase analysis

RTP annealing clearly accelerates the Se incorporation thanks to the high Se vapour pressures present. As previously shown in **Figure 3.8**, this has a visible impact on the crystallization (large crystals are formed in very short times), but most likely this feature also has an impact on the phase evolution during the kesterite formation too.

In order to investigate this last assumption, a detailed phase analysis by XRD and Raman was performed of the complete set of samples. **Figure 3.10 a)** shows the series of diffractograms corresponding to all samples, while **Figure 3.11b)** shows the evolution of the relative XRD intensity for the different detected phases. This relative XRD intensity has been normalized with respect to the (110) reflection of Mo, which is supposed to be constant for all the samples. It is important to remark that the main XRD peaks of the ZnSe, Cu_2SnSe_3 (CTSe), and CZTSe phase almost coincide at room temperature, making the distinction extremely complicated.[137] While this impedes the detection of ZnS/CTSe secondary phases in a kesterite matrix, there are several

additional characteristics peaks with low intensity for the tetragonal kesterite phase, which allows to clearly identifying the latter. There are for example the peaks at 22.1⁰, 28.3⁰, 35.2⁰ and 36.1⁰ corresponding to diffraction planes (110), (103), (202) and (121), respectively. The first and major consequence came as already in point E, i.e., at the very beginning of the first dwell time at 400 ⁰C, it was already possible to detect peaks corresponding to the CZTSe tetragonal kesterites phase, all along with SnSe. There was no evidence of another phases.
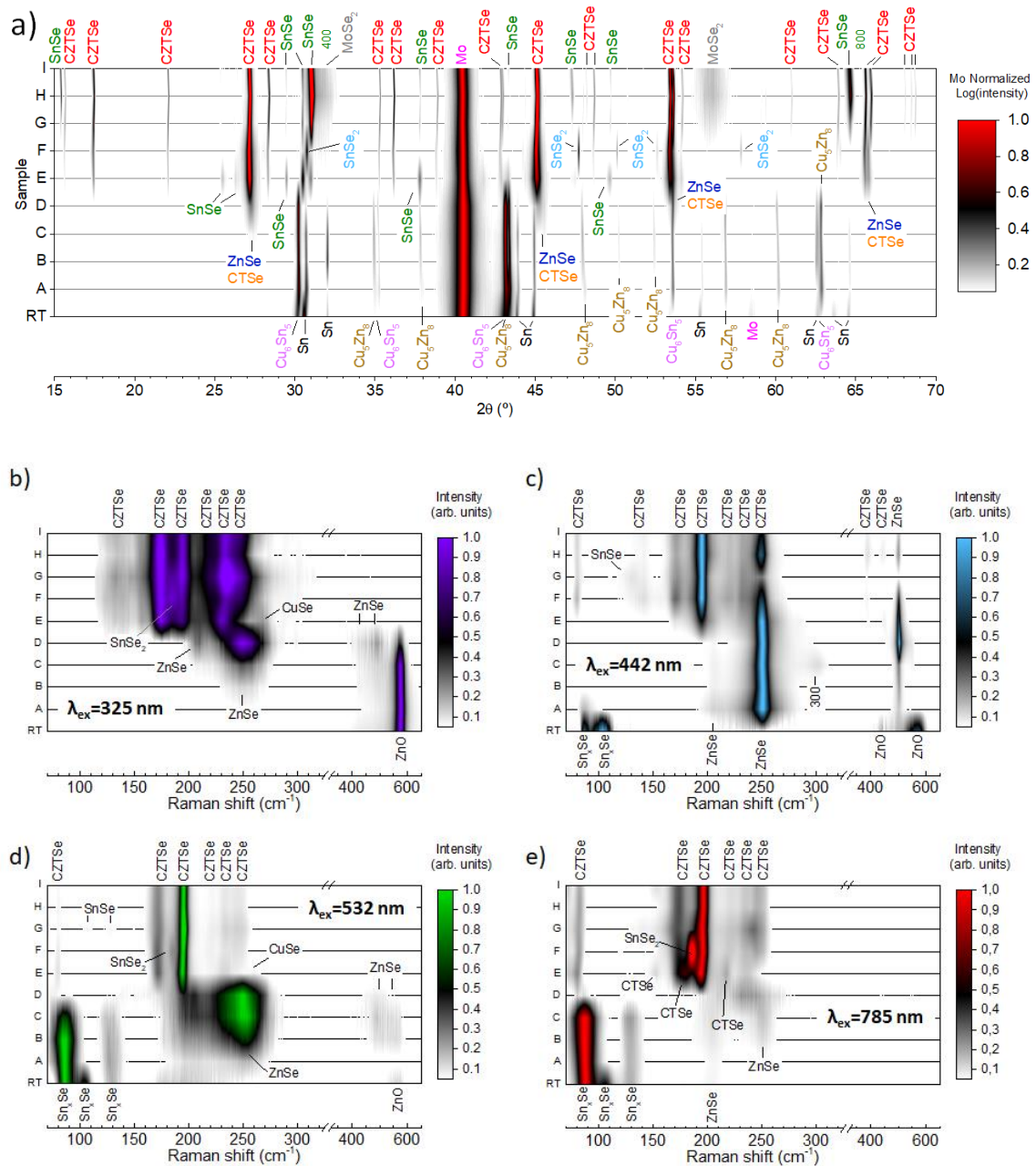
Figure 3.10 a) XRD diffractogram and **(b-e)** Raman spectra using four different excitation wavelengths (325, 442, 532, and 785 nm) of the different samples produced at the different stop points (A-I) (detailed diffractograms and Raman spectra are reported in **Figure A2 and Figure A3 in the Appendix**). Here and in the following, CTSe stands for the ternary Cu_2SnS_3 compound.

The early appearance of the CTZSe kesterite phase already at the point E turned out as a huge surprise as it contrasts with the samples prepared by the standard conventional thermal processing at IREC with very similar conditions (see **Figure A2** at the **Appendix**, point E), where no evidence of kesterite formation is found, although other groups have reported the possibility of also forming the kesterite at such low temperatures with standard annealing[138]. Whereas in the RTP annealing case, for the kesterite phase synthesis, i.e. point E, several secondary phases are observed, even including metallic ones. Once again, the appearance of those phases implies that in the RTP processing the formation of kesterite phases can occur faster at lower temperatures and/or lower times. This fast appearance of the kesterite phase is thought to be related to this high Se vapour pressure already achieved since the first's steps of the process. Although the RTP process seems to produce kesterite with acceptable crystalline quality even at 400 °C it is necessary a second step at higher temperature to enlarge grains in order to obtain working devices.
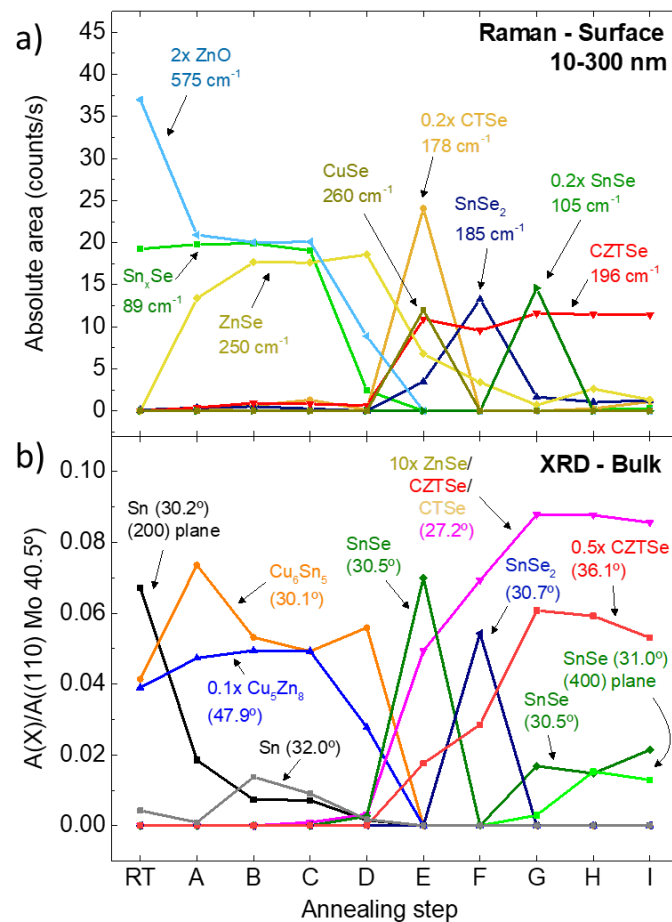
Figure 3.11 a) Evolution of the absolute area of most relevant peaks detected by Raman spectroscopy (surface analysis < 300 nm), corresponding to the different binary, ternary, and quaternary phases present in the system. **b)** Evolution of the XRD diffraction peaks area corresponding to the different binary, ternary and quaternary phases that have been normalized with respect to the total area of the 110 reflection of the Mo layer at 40.5°, extracted from **Figure A2.**

The evolution of the diffractograms of the different samples describes the phase formation in the bulk during the annealing process. From room temperature (RT) to point D, it can be observed the transformation of the metallic phases from a highly textured Sn phase and Cu-Sn,

Cu-Zn alloys toward a Cu-Sn alloy, accompanied by a reduction on the peaks of the Sn and Cu-Zn phases. The reduced intensities of the Zn related phase are attributed to the formation of ZnSe with low crystallinity. At point E and beyond (end of the first temperature ramp), no metallic phases are observed anymore. There are only slight differences between the diffractogram of point F to the one of point E, with a slight increase in the intensity of the CZTSe peaks, while the peaks corresponding to SnSe are decreased in favour of increasing $SnSe_2$ peaks. In this work, is postulated that the SnSe formed during the first dwell time gets further selenized to $SnSe_2$. Finally, for points G, H, and I (the last stages which correspond to the crystallization step at 500 °C), the intensity and the full width at half-maximum (FWHM) of the characteristic CZTSe peaks remain practically constant. Additionally, a thin $MoSe_2$ layer is formed, as expected in kesterite annealing. Highly [400] textured and nontextured SnSe is also detected, but its origin is most probably from the condensation of remaining gaseous Sn-Se during the user-forced cooling process.[139] In concordance with the previously stated arguments, the actual quaternary kesterite phase is already completely formed during the first dwell time at 400 °C (point E) and the second dwell time at 500 °C is predominantly necessary for an improved crystallization of the absorber.

In order to extend and complement the previous XRD analysis, Raman spectroscopy with four different excitation wavelengths (325, 442, 532, and 785 nm) was performed. The use of various excitation wavelengths leads to pre-resonant conditions for different compounds and enhances the ability to detect several secondary phases[140]. This helps to overcome the XRD limitations in forms of impossibilities to differentiate between several secondary phases. Panels b-e from **Figure 3.10** show the Raman spectra obtained in the different samples for the four excitation wavelengths. In particular, under UV excitation (325 nm) the ZnO phase is strongly enhanced[141], together with a non-bandgap resonant enhancement of the CZTSe.[142] Under blue excitation (442 nm) the detection of ZnSe is enhanced,[130,143] and with red excitation (785 nm) the detection of Sn-Se[53] and ternary Cu-Sn-Se phases[130](CTSe). **Figure 3.11a)** depicts the evolution of the absolute intensity for the Raman peaks evolution of the absolute intensity for the Raman recorded at the absorber surface (<300 nm) using the signal acquired with the most favourable excitation wavelength for each phase. During the first ramp (from point A up to point E) ZnO (appearing from the oxidation of the precursor), ZnSe, SnSe and Cu_2SnSe_3, are clearly detected. We find only traces of CuSe at point E. These results appeared as a surprise, as in literature the formation reaction is commonly reported to proceed via the reaction of binary compounds, and CuSe (S) is most frequently found along with SnSe (S) or SnSe (S) compounds[133]. Alternatively, $Cu_2SnSe(S)_3$ is found when the formation of kesterites proceeds via the reaction of this ternary phase with ZnSe[144]. The intimate mixing of all these phases and the presence of both Sn-Se and Cu-Sn-Se coexisting in the bulk of the same absorber suggest that most probably these two reactions pathways are competing and contributing both to the formation of kesterites under the studied conditions. We find that between point D (350 °C) and point E (400 °C) the kesterite formation starts, which is in agreement with the literature data[144,145]. However, when RTP is applied in our case the heating ramp is of 180 °C/min, i.e., to move from point D to point E only takes the very short time of 17 s. This fast ramp implies that once the minimum formation temperature is reached, the precursor phases react very quickly with selenium in the RTP and form the kesterite almost immediately.

At point E, even though the kesterite phase is already detected the kesterite synthesis has not been completed yet, as strong contributions from the ternary Cu-Sn-Se compounds and ZnSe are found altogether with few quantities of Cu-Se and Sn-Se. At point F, the reaction can be considered almost finished, the kesterites are completely formed, and only some small residues

of secondary phases still remain: ZnSe due to the Zn-rich composition and SnSe most probably into the $MoSe_2$/CZTSe interface[130] and the surface due to condensation during the cooling process from pre-evaporated material.[139] Also, a clear contribution from the $SnSe_2$ (under resonant conditions with 785 nm excitation) is observed and can be arguably correlated with the superficial structures observed in the corresponding SEM images (**Figure 3.8**). Interestingly, after point F, i.e., once the temperature is increased to 500 °C, no reduction of the Raman FWHM is observed for the CZTSe phase. This contrasts with CTP processes where in the last step a clear improvement of the crystal quality with the annealing time has been reported[66]. On the other hand, if compared with an accurate analysis (using the Raman nonbandgap resonant conditions with 325 nm excitation) a clear modification of the bands at 175, 233, and 250 cm^{-1} can be observed (**Figure 3.12**). Modifications of these peak intensities have been attributed to changes in the V_{Cu} and Zn_{Sn} point defect concentrations which have shown a strong impact in the final optoelectronic properties.[142]
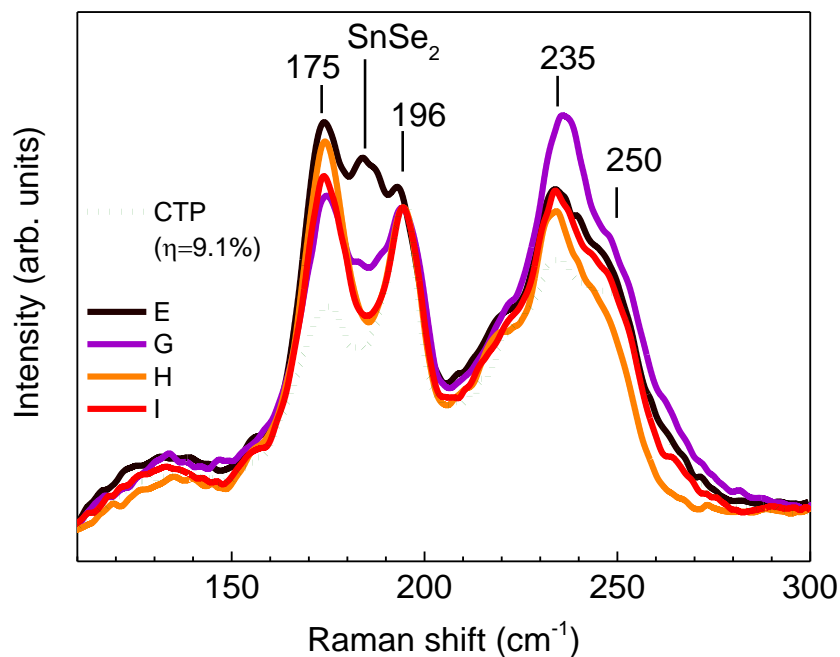
Figure 3.12 Raman spectra under UV non-bandgap resonant conditions (325nm) for samples E to I together with a reference sample annealed using an optimized conventional thermal process.

These first results raised the question about the possible kesterite formation mechanisms for our RTP annealing process and how it may be altered. With start our considerations, with an extensive analysis of the formation mechanisms reported in the literature summarized in **Table 6**:

Ref.	Material	Process	Precursor	Annealing process	Reaction pathway	T_F (°C)*
a	CZTSSe	Chemical: Hydrazine based slurries	Cu_2S-S/$SnSe_2$-Se/Zn slurries Spin coating	Hot Plate at 540 °C	$Cu + Sn + Zn + X$ or alloys $\rightarrow$ Binary chalcogenides $\rightarrow Cu_2ZnX_3 + ZnX$ $\rightarrow Cu_2ZnSnS_4, X = S, Se$	350
b	CZTS	Physical: Sputtering (metallic stacks)	Sn/Cu/Zn metallic stacks	Graphite box (S+Sn) at 550 °C	$[Cu_2S + SnS]_{(liq)} + ZnS + S_{2(gas)}$ $\rightarrow Cu_2ZnSnS_4$	480
c	CZTSe	Chemical: Ethanol based inks	Cu (II) and Zn nitrates, Sn (IV) chloride. Knife coating. Se top capping layer.	Graphite dome with enough Se at 550 °C	$(Cu, Zn, Sn) \xrightarrow{\sim190ºC} CuSe_x \xrightarrow{\sim340ºC} Cu_2SnSe_3 + Cu_2ZnSnSe_4 \xrightarrow{\sim420ºC} Cu_2ZnSnSe_4$	340
d	CZTS	Chemical: electro-deposition of metals	Cu and Zn metallic electrodeposited.	Graphite box with S and Sn at 550 °C as maximum T	$2ZnS_{(s)} + Cu_{2-x}S_{(s)} + SnS_{(g)} + 1/2S_{2(g)}$ $\rightarrow Cu_2ZnSnS_{4(s)} + ZnS_{(s)}$	>500
e	CZTS	Physical: sputtering (sulphides)	ZnS, SnS_2 and Cu by sputtering	Tubular furnace (N_2/H_2S 95%/5%) at 550ºC as maximum T	$Cu_2S + SnS_2 \xrightarrow{350ºC} Cu_2SnS_3$ $Cu_2SnS_3 + ZnS \xrightarrow{500ºC} Cu_2ZnSnS_4$	500
f	CZTSe	Physical: sputtering (metals)	Cu, Zn and Sn metals by co-sputtering	Graphite box with elemental Se at a maximum T of 600 °C	$\alpha Cu + \beta Cu_xSn_y + Zn + 2Se_2$ $\rightarrow Cu_2ZnSnSe_4$	>350
f	CZTSe	Physical: sputtering (metals)	Cu, Zn and Sn metals by co-sputtering	Three zones furnace using elemental Se with a cracking zone at a maximum T of 600 °C	$\alpha'Cu_{2-z}Se + ZnSe + SnSe + \gamma'Se_2$ $\rightarrow Cu_2ZnSnSe_4$	300

Table 6 Summary of some of the most relevant papers published in the literature analyzing the formation mechanisms of kesterites.

Ref: a[146], b[147], c[144], d[148], e[149], f[145]

Amongst the kesterite research community there is a general agreement that the synthesis route of kesterites proceeds either via the formation of binary metal selenides such as: Cu-X, Zn-X, and Sn-X, X = S and/or Se) or ternary (mainly Cu-Sn-X phase, X = S and/or Se) compounds, which react at a given temperature to form the corresponding kesterite quaternary phase with Zn-X. From **Table 6** the formation of the pure Se-based kesterite compound seems to proceed at lower temperatures ($\approx$350 ^{o}C) than the formation of the pure S-based counterpart ($\approx$500 ^{o}C). The mechanism including the ternary compound (CTSe) has a clear advantage over the one based on three binary selenides: it has a simplified, formation scheme, with less phases involved in the synthesis which potentially can resist reaction and form detrimental secondary phases after the end of the synthesis process. When compared our first RTP results with those reported in the literature a few observations can be done. For low chalcogen vapour pressures and/or low availability of chalcogens (e.g., no chalcogen in the precursors), the formation of kesterites is likely to proceed via the binary compound. On the other hand, under high chalcogen vapor pressure, such as in this work, or high availability of chalcogens from the very beginning of the annealing (i.e. if the precursors already contain chalcogen in their composition), the reaction preferably proceeds via the formation of ternary compounds. In the case of our RTP annealing processing both mechanisms are present and compete between them. **Figure 3.13** sketches the hypothesized competition between both reaction pathways:
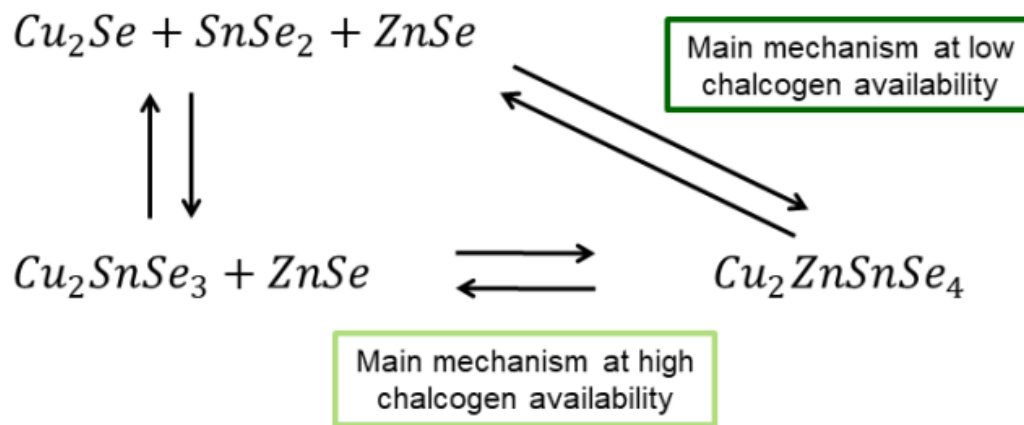
Figure 3.13 Schematic representation of the two competing formation mechanism for the RTP annealing.

3.2.5 Devices

Finally, in order to study the impact of the different stages on the properties and characteristics of the devices, solar cells were prepared with the most relevant samples. As expected, devices prepared with absorbers from A up to F (end of the first dwell time) do not produce any working solar cell. All of them were shunted, most probably because of the presence of very large amounts of secondary phases as has been observed with Raman and XRD altogether with a very poor crystallization or uncompleted reaction of the kesterite phase. However, with samples G, H and I working solar cells could be obtained, as presented in **Figure 3.14**. In this figure, the short circuit current density (J_{sc}), open circuit voltage (V_{oc}), the fill factor (FF) and efficiency (η) are presented. The solar cells prepared with absorber G exhibit low efficiencies mainly due to the low V_{oc} and FF. However, the slight differences between F and G (only 100 s and 100 ^{o}C) seem to be enough to pass from non-working devices to working ones. This change implies that the

crystallization/defect reordering observed previously by Raman spectroscopy under 325 nm excitation wavelength (**Figure 3.12**) is also very fast for the RTP process with relatively high Se pressures. Nevertheless, at point G, the absorber properties (defects concentration or type and presence of a residual $SnSe_2$ phase) are still not good enough to ensure a high performance, implying the necessity of a longer dwell time into this second step. Also, this low V_{oc} and FF might be related with the relatively small grains observed by SEM. A large number of grain boundaries which are not well passivated might lead to an increased density of defects. All of those, could severely deteriorate the charge transport properties of the absorber and explain the bad performance.

After only 150 additional seconds at 500 °C, both the V_{oc} and the FF are largely improved (and in consequence the efficiency). The J_{sc} is also slightly increased. This large improvement can be explained by a healing of defects within the crystal structure, an improved crystalline quality with larger grains of the absorber, as well as the complete consumption or minimization of detrimental secondary phases. Longer crystallization times seem to have a limited impact on the improvement of the performance of the devices, suggesting that times as short as 150 s (point H) at relatively high temperatures can be enough to crystallize the CZTSe absorber and fully exploit the potential of the RTP annealing.
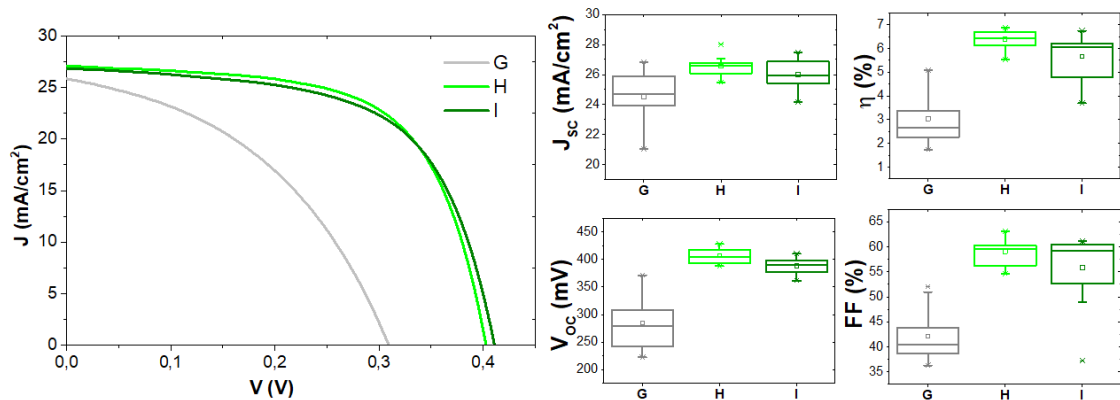
Figure 3.14 J-V illuminated curve of devices obtained from absorbers produced during the break-off experiments (points G, H and I). Evolution of the different optoelectronic parameters of the same three points.

3.3 Summary

In this chapter the advantages of employing an RTP process have been presented. The set-up designed specifically for this purpose at IREC was introduced, consisting of a semi-closed graphite box with a volume of 3.8 cm^3. This set-up allows to achieve very high chalcogen vapour pressures from the very beginning of the kesterite synthesis. For the RTP processes, 20 mg of Se, and no extra Sn are applied. First attempts showed the necessity of adopting a two-step temperature profile because of the homogeneity of single step processes. The final optimized annealing parameters studied for IREC's RTP baseline can be revisited in **Table 5.**

In order to understand the mechanisms underlying the fast selenization during the RTP kesterite synthesis, a detailed experimental analysis of the phase formation and evolution has been conducted. For this a series of break-off experiments is presented, which allows to study morphology and composition of the resulting samples as well as the phase present by applying a detailed SEM, XRF, Raman, XRD and GDOES analysis of all involved samples. In continuation, the main results of this break-off experiments are summarized:

- The second step at 500 °C is necessary in order to obtain working solar cells due to improvements in phase purity and crystal quality, even if the formation reaction of the kesterite phase seems to be completed without it.
- The higher vapour pressures achieved with the RTP annealing at IREC have shown to have a very strong impact on the formation pathways of the kesterite absorber.
- In contrast to conventional CTP annealing, where the selenization of metallic precursors precedes predominantly via binary metal selenide compounds, in RTP a competition between two distinct mechanisms (binaries and ternaries) is observed.
- Literature shows that a pathway involving binary selenides is preferred for relatively low Se availability during the annealing and a pathway involving the CTSe ternary compound predominates for relatively high Se availability. In between apparently both mechanisms can compete.

Finally, a champion device of 8.3% (No ARC nor metallic grid) from a process only lasting 12 minutes' is obtained, comparable with devices obtained by CTP at IREC. This proves that RTP processing is a very promising way to obtain highly efficient kesterite devices.
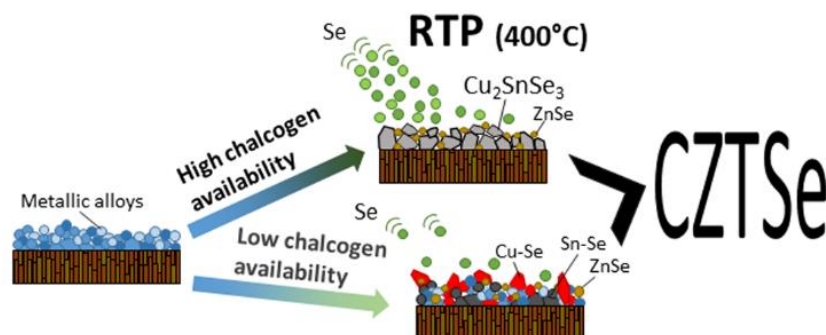
Figure 3.15 Summary of the dependence on the kesterite formation pathways for IREC's RTP annealing baseline.

Chapter 4

Driving the kesterite formation pathway with the chalcogen availability: a kinetic and phase analysis

4 Driving the kesterite formation pathway with the chalcogen availability: a kinetic and phase analysis

Previous results obtained in Chapter 3 depicted the differences into the formation pathways for the kesterite synthesis. Two main routes are present: one ruled by binary compounds and a second one by the ternary compound. In this chapter a deep and comprehensive study about driving the kesterite formation pathway to one or another option through a kinetic analysis altogether with an extensive phase analysis is going to be presented. Furthermore, the results presented in this chapter have been summarized into a manuscript already submitted for publication.

4.1 The importance about studying the kesterite formation pathways

This Thesis is centred in sequential processes for the synthesis of the kesterite absorber, whereas it is of key importance for obtaining highly efficient solar cell devices to deeply understand all the intermediates species participating into the formation routes of the absorber layer. In fact, as has started to be commented in the previous chapter, the formation mechanisms are directed either via binary compounds, or between ternary and binary ones[66,150]. It can be foreseen that when the precursor already contains chalcogen on its structure, the route involving the ternary compound is the preferred one, whereas when the precursor is chalcogen free the route involving binary compounds is the most commonly reported, as can be observed in **Table 6** and in *Hernandez et al.*[136] Nevertheless, most of the present literature deals with thermodynamic and phase analysis aspects about those systems[151–155], because kinetically aspects had been very difficult to be evaluated.

When discussing about kinetics aspects related to sequential processes for chalcogenides, even for CIGS there is very little available bibliography, depicting only general studies using mainly precursors that already contain chalcogen or are limited to theoretical analysis[156–161]. About kesterite, as has been previously noted, the different possible formation systems have been prior studied in some extent, yet from the thermodynamic point of view and once again only very limited and qualitatively kinetic information is available. *Bodeaux et al.*[162] studied the selenization of co-sputtered Cu-Zn-Sn precursors, suggesting that the kinetics of the reaction between Sn and Se is slower than the corresponding one between Cu and Se, indicating that this is probably a limiting factor for the CZTSe formation rate. On the other hand, *Qu et al.*[163] studied the sulfurization kinetics of CZTSSe nanoparticles using the parabolic grain growth and Avrami models. These methodologies are mainly useful for understanding grain growth processing or chalcogen diffusion yet provides limited information about the reaction kinetic types and the corresponding kinetic parameters that might be very relevant at early stages of the compound formation. The correlation between the kinetic aspects at the very beginning of the kesterite formation, combined with a thermodynamic phase analysis can be very helpful to understand and overcome possible synthesis limitations inside the systems.

In order to do so, this chapter is devoted to study the kinetic and phase aspects of the formation reaction of kesterite at very early stages. For it, the formation reaction of the kesterites must be stopped employing the sequential process in IREC's baseline (sputtering of metallic stacks

followed by reactive annealing either in CTP or in RTP) at different temperatures, studying both fast and slow ramping processes, and moreover introducing the chalcogen availability factor as the most relevant annealing parameter (see definition below). By only employing a relatively simple compositional measurement a first kinetic analysis of the pure selenide kesterite formation extracting important parameters such as the reaction order, kinetic constant and reaction half-time will be proposed. Also, thanks to the combination of multi-wavelength RS and XRD to perform a complete and deep phase analysis, it will be correlated this kinetic regime with the phases formed.

The samples for this study were prepared following IREC's standard baseline up to the annealing process that was extend for two reactive annealing types: CTP and RTP, in order to obtain either a slow or a fast ramping process respectively. The most important parameter to study in this chapter is related to the chalcogen vapour pressure, defined as chalcogen availability (ChA). For all the samples studied in this chapter: the area, the thickness and the maximum temperature were kept constant, in the defined set-up only the chalcogen mass and reactor volume were varied.

Accordingly, for the different annealing performed, the chalcogen availability has been defined as: $ChA = m_{Ch}(g)/V_{GB}(cm^3)$, where m_{Ch} is the mass of chalcogen (S or Se) used during the experiments performed in grams and V_{GB} is the volume of the graphite box in cubic centimetres.

The RTP samples were annealed following the special set-up designed at IREC where a 3.8 cm^3 semi-closed graphite box is employed. However, the annealing process was not the complete process, commented and studied in deepness in Chapter 3, yet consisted on heating from room to maximum temperature (400 °C, 350 °C, 300 °C, 250 °C and 200 °C) with a fast ramp (180 °C/min) and a total pressure of 1 mbar of Ar, being also stopped after 20s, 50s, 80s, 110s, 140s and 200s. When the RTP process reaches the desired temperature is immediately stopped and the system quickly cooled down as fast as possible in a natural way. The set of samples obtained with different Se availabilities were split into three types of regimes: low, medium and high Se availability. More concretely, the following six quantities were employed: 2.6×10^{-4} g_{Se}/cm^3 (low availability); 1.32×10^{-3}, 2.64×10^{-3} and 5.26×10^{-3} g_{Se}/cm^3 (medium availability); and 1.32×10^{-2} and 2.6×10^{-2} g_{Se}/cm^3 (high availability). The employment of six quantities responds to the necessity of having statistics and intermediate points to validate the presented kinetic models.

Additionally, a set of samples was also studied under slow ramping annealing conditions with the CTP in a Se(S) + Sn atmosphere. Once again, a semi-closed system specially designed at IREC made up by a graphite box with a reaction volume of 69 cm^3 was employed at 1 mbar of Ar as total pressure, being heated from room temperature up to 400 °C (either for S and Se) with a ramp of 20 °C/min and for the following Se or S availabilities: 7.2×10^{-5} g_{Se}/cm^3 and 7.2×10^{-4} g_{Se}/cm^3 (low availability); 1.45×10^{-3}, 2.90×10^{-3} and 7.2×10^{-3} g_{Se}/cm^3 (medium availability); and 1.45×10^{-2} g_{Se}/cm^3 (high availability).

4.2 Introducing a kinetic and phase analysis for the selenization of the kesterite under slow or fast ramping conditions

In the next sections of this Chapter, a complete kinetic model and phase analysis of samples prepared with different chalcogen availabilities (from low to high) using fast ramps (for Se by RTP, kinetically controlled), and slow ramps (for S and Se, thermodynamically controlled by CTP), will be presented.

The first scope of the study presented here is to obtain the fundamental kinetic parameters of the selenization process which depend on the chalcogen availability. Once they are obtained, it is of key importance to detect and identify the intermediate species present through the kesterite formation at the different regimes. Finally, and as a summary, a kinetic model of metallic stacks chalcogenization for the pure selenide kesterite compound and a first extension for the pure sulphide compound will also be presented.

4.2.1 $Cu_2ZnSnSe_4$ formation reaction kinetic and phase analysis with different chalcogen availabilities

Figure 4.1 presents the evolution of the elemental composition of Cu, Zn, Sn and Se as a function of the ChA parameter covering the three studied regimes, as well as for two types of processes, either with fast (180 $^{\circ}$C/min) or slow ramping (20 $^{\circ}$C/min), which are defined as:

- Low availability: $[Se] < 1\times10^{-3}$ g/cm^3
- Medium availability: $1\times10^{-3} \leq [Se] \leq 1\times10^{-2}$ g/cm^3
- High availability: $[Se] > 1\times10^{-2}$ g/cm^3

The temperature was decided to be stopped at 400 $^{\circ}$C based on previous results from Chapter 3 and bibliography[66,136,147] depicting that the kesterite formation has already started at such temperature. Only by changing the processing ramp, it is possible to, in principle, investigate two type of processes, being one kinetically controlled (RTP, fast ramping) and the other one thermodynamically controlled (CTP, slow ramping). Applying this strategy can be very useful to depict and understand differences and similarities between slow and fast processing, separating the kinetic and thermodynamic factors which may play a major role through the formation of these compounds.
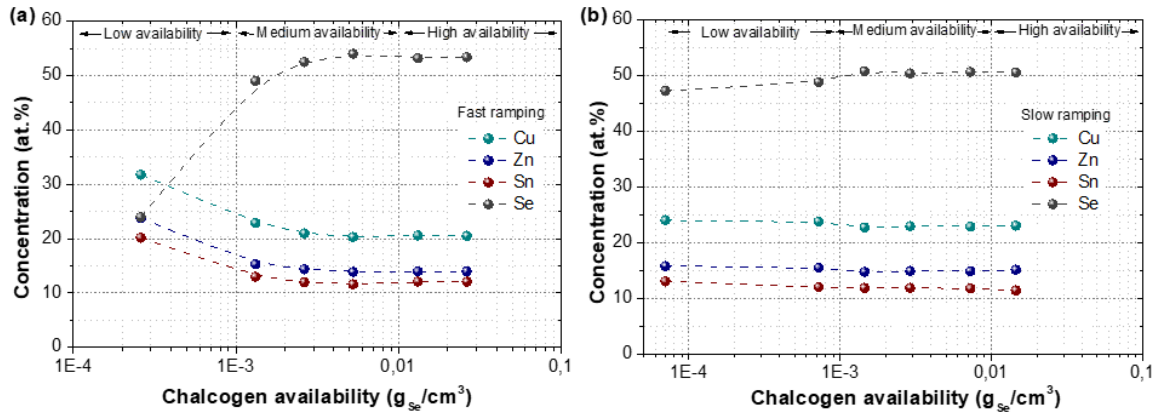
Figure 4.1 Evolution of the concentration of the different elements as determined by XRF for CZTSe samples prepared with fast ramping (180 °C/min) **(a)** and slow ramping (20 °C/min) **(b).**

When it comes to a detailed study of **(a)** (fast ramping process) it can be observed that only partial Se incorporation takes place for low and even for medium-low chalcogen availabilities. Only when high chalcogen availabilities are approached, all the possible Se is then incorporated into the layer. On the other hand, this situation changes drastically when it comes to applying slower ramps, where almost all the Se is already included even for very low chalcogen availabilities **(b)**, suggesting that the chalcogenization process has prior achieved the equilibrium and is almost completed in a relatively short time, in good agreement with reports[164].

Those results clearly indicate that for the case of fast ramping the system is still out of equilibrium and probably under kinetic control, which opens very interesting possibilities to perform a kinetic analysis of the system. In order to study the kinetic of the metallic phases chalcogenization reaction, several appreciations must be taken care of, such as the possible order of the selenization reaction and to do so, it is necessary to define a generic reaction which is:

$$mM_{(s)} + nSe_{2(g)} \overset{T,t}{\leftrightarrow} xCh_{(s)}$$
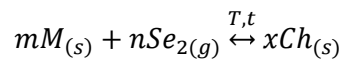
Equation 1. Generic kesterite formation mechanism.

Where *M* represents all the metals together in the precursor layer and *m* is their stoichiometric factor in the reaction, Se_2 is the selenium presented in the atmosphere and *n* is it stoichiometric factor, and Ch represents the formed chalcogens and *x* is the corresponding stoichiometric factor. T is temperature and t is time.

If we start from the general reaction, the simplest kinetic rate equation that can be used for the chalcogenization of metals based on the law of mass action is[165]:

$$\frac{d[Ch]}{dt} = xk[M]^m[Se_2]^n$$

Where *k* is the kinetic constant. Two reasonable assumptions can be introduced in order to simplify this present model. Firstly, by considering that *M* is a solid specie and it can be considered that the concentration will remain constant into our system, implying that is not affecting the reaction rate. Secondly, *Ch* corresponds to the total chalcogen introduced in the precursor layer as measured by XRF, which is going to be represented as $[Se]_k$. Lastly, the Se concentration into the atmosphere corresponds to the selenium availability defined at the beginning of the study minus the reacted Se.

In this case:

$$[Se_2] = [Se]_{ChA} - [Se]_K$$

So, then the kinetic rate equation can be further simplified as:

$$\frac{d([Se]_K)}{dt} = xk([Se]_{ChA} - [Se]_K)^n$$

In this study, it has been supposed three types of kinetic orders for the chalcogenization of metallic stacks, applying a differential method[166] and are represented by the following equations:

$$-d([Se]_K) = k_0 dt \Rightarrow [Se]_K = ([Se]_{ChA} - [Se]_K)_0 - k_0 t \; \textbf{\textit{Zero order kinetic}}$$

$$\frac{-d([Se_K])}{([Se_{ChA}] - [Se_K])} = k_1 dt \Rightarrow \ln([Se_{ChA}] - [Se_K]) = ln([Se_{ChA}] - [Se_K])_0 - k_1 t \; \textbf{\textit{First order}}$$
$$\textbf{\textit{kinetic}}$$

$$\frac{-d([Se_{ChA}] - [Se_K])}{([Se_{ChA}] - [Se_K])^2} = k_2 dt \Rightarrow \frac{1}{([Se_{ChA}] - [Se_K])} = \frac{1}{([Se_{ChA}] - [Se_K])_0} - k_2 t \; \textbf{\textit{Second order kinetic}}$$

Where k_0, k_1 and k_2 are the kinetic constants corresponding to zero, first and second order reactions respectively. With the obtained knowledge and considering the vapour pressure of selenium, it can be considered that no or very few chalcogen is going to be available below 200 ºC[66,136]. In this sense, it can be estimated t starting when the heating up process is just above 200 ºC and finishing when the cooling down process is just below 200 ºC in order to estimate the reaction times.

By employing the previous equations, altogether with info from **Figure 4.2** the experimental values can be fitted to the supposed kinetic orders with the aim to identify which one adjusts better to them. In the present model there are made two important assumptions:

1. There are no competing reactions, implying that chalcogen is preferably introduced by a single reaction
2. Even if T was not constant for each experiment, and *k* as well as the chalcogen concentrations depends on T, it is supposed that most of the chalcogenization reactions happen in a narrow T range where the system can be considered constant.

Once those two issues have been taken into consideration, *k* values for the different kinetic models have been estimated and are going to be presented in this Chapter. Moreover, depending on the kinetic order it can be estimated a kinetic parameter called half-life time ($t_{1/2}$), which represents the time required for the system to complete half of the reaction. It is normally considered that the reaction is completed after six times the half-life value. The $t_{1/2}$ presented have been calculated as follows:

$$t_{1/2} = \frac{([Se]_{ChA} - [Se]_K)_0}{2k_0} \; \text{For a } \textbf{zero-order reaction}$$

$$t_{1/2} = \frac{ln2}{k_1} \; \text{For a } \textbf{first order reaction}$$

Obviously, an in-situ analysis of the chalcogenization process would be the ideal strategy, but is rather complicate with this sequential annealing process due to the harsh processing conditions. In most cases of analysis in dedicated *in situ* characterization setups, the processes can not be reproduced exactly as used for the general absorber synthesis. In addition, the chalcogenization reaction is a relatively fast process, much faster than the typical times necessary for a complete annealing process (of the order of several tens of minutes), even under fast ramping conditions. Therefore, the application of the differential method for the determination of the reaction-order is very challenging, requiring some assumptions.

Figure 4.2 shows the Se concentration obtained for different layers where the RTP chalcogenization process has been stopped at different temperatures (nominally 200 °C, 250 °C, 300 °C, 350 °C and 400 °C; for this last temperature in another different run than the one presented in **Figure 4.1**) and employing four different chalcogen availabilities (low, medium-low, medium and high regimes). If the temperature is below 250 °C the chalcogenization reaction does not proceed, or partially proceeds only under high chalcogen availabilities. When the temperature is equal or above 400 °C, the reaction is almost completed at the very beginning, even under low ChA values. This last affirmation leaves only the temperature range between 250-350 °C useful for the kinetic analysis. 300 °C has been selected as the most suitable temperature for a deep kinetic analysis, considering that common differential methods for kinetic analysis require isotherm conditions[166].

The methodology employed for approaching the kinetic model of CZT metallic stacks selenization is based on the following assumptions:

1. In the working limited range of temperature employed (in most of the cases from 250-350 °C), the most stable phases in the kesterite system does not change[133,164].
2. Most of the phases involved into the system are solid (and their concentrations can be considered independent of temperature) apart from Se vapour which temperature variation is being considered with the measurement of chalcogen incorporation into the layers.
3. The diffusion of Se can be considered fast in the chalcogenide system even at relative low temperature and is enhanced by sodium's presence[167,168].
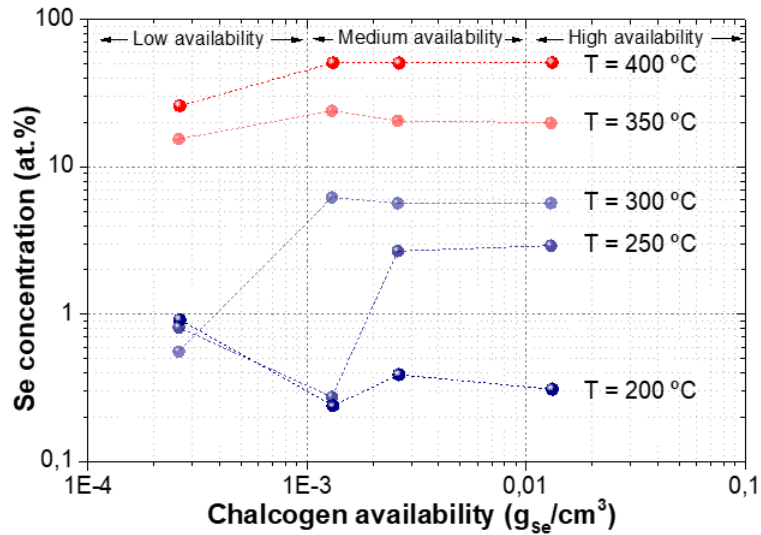
Figure 4.2 Se concentration for the experiments performed stopping the reaction at different temperatures (RTP) and using different Ch_A values

Taking the previous assumptions into consideration, it is possible to develop a simplified kinetic model for Equation 1. This way a qualitative estimation of the kinetic constants can be obtained as well as the kinetic order of the reaction determined. The simplified kinetic model for the reaction presented in Equation 1 can be simplified as:

$$\frac{d([Se]_{sat} - [Se]_K)}{dt} = k_n([Se]_{sat} - [Se]_K)^n$$ Equation 2. General kinetic model for metallic stacks selenization.

Where *[Se]$_{sat}$* is the Se concentration (or number of moles) for an infinite-time reaction, *[Se]$_K$* is the Se concentration (or number of moles) in the kesterite compound, and *K_n* is the kinetic constant corresponding to a reaction-order *n*. In fact, (*[Se]$_{sat}$* - *[Se]$_K$*) is the Se quantity required to end the reaction or, equivalent, the metallic phases consumed during the selenization. Using this general kinetic expression, the data with reactions of zero-, first- and second kinetic can be fitted as described previously. **Figure 4.3** presents the kinetic results obtained for medium-low and medium-high chalcogen availabilities, at 300 °C. It is worth to mention that for high chalcogen availabilities the reaction is very fast, so then the metallic layers are almost completely selenized in very short times, impeding reliable kinetic analysis with our set-up.
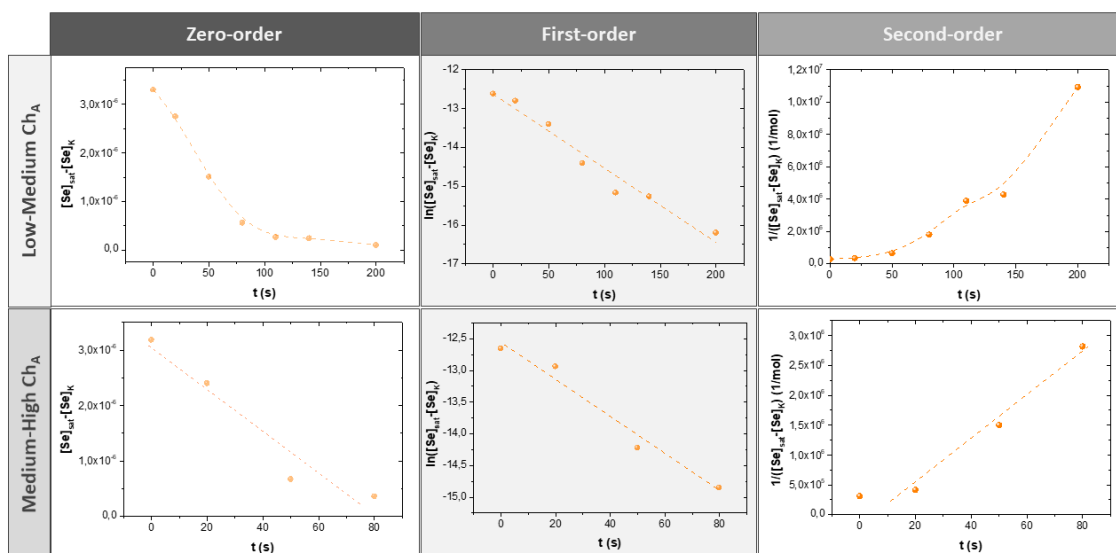
Figure 4.3 Complete kinetic analysis of the selenization of metallic stacks using fast ramping. The fittings are presented for three different kinetic orders (zero, first and second order), as well as for two different chalcogen availabilities (medium-low and medium-high).

For medium-low ChA ($\approx 1\times10^{-3}$ g_{Se}/cm^3, the three different kinetic orders are contemplated and fitted (see upper part of **Figure 4.3**) being the best obtained fitting for a first-order kinetic (**Table A1** in the **Annex**). Most probably this is the reaction-order, although a zero-order kinetic cannot be discarded at the very beginning of the reaction. Nevertheless, this type of kinetic is often considered as a pseudo-state because it cannot continue after one of the involved reactants is exhausted. Normally, before going to zero, the reaction rate will change to another rate law[166], ins this case a first-order one. Two conditions can lead to a zero-order kinetic at the very beginning: 1) when only a small part of the reactants are in the state required to react but this small fraction is continually supported from the reactive source; and 2) when the concentration of one reactant is orders of magnitudes greater than the others. In the present case, it can be considered that the first condition better represents the system at the very beginning due to the Se quantity available for the reaction is limited in the range of medium-low ChA, yet the Se is continuously supplied during the reaction time. Despite this, it can be considered that in overall the selenization reaction proceed via a first order reaction whose kinetic parameters are summarized in **Table 7**.

The situation only slightly changes when the ChA is increased to medium-high values as can be observed in the lower part of **Figure 4.3.** In this case an only for the first four times, it can be used because the system saturates for longer annealing times. Best fitting is obtained again supposing a first order kinetic, implying that the selenization rate is directly proportional to the ChA. This is the most expected situation, depicting that by controlling the ChA value it can be controlled the selenization reaction rate. Whereas, higher reaction orders (second order) do not fit well with any condition, suggesting that the selenization process proceeds via a relatively simple mechanism. **Table 7** summarizes also the main kinetic parameters extracted from **Figure 4.3** for the different chalcogen availabilities, including the half-life time ($t_{1/2}$) determined as explained previously in this present Chapter. As already commented, it can be considered a reaction finished after 6 times the $t_{1/2}$, implying that for a complete selenization approximately 30-40 s are required even for medium-low chalcogen availabilities, confirming that the chalcogenization of the metallic stacks is a very fast process, which typically would require only few minutes to be completed[64,66,136].

Table 7 Estimation of the kinetic parameters for the identified reaction-orders and for the different chalcogen availabilities.

Chalcogen availability	More probable reaction order	k_1 (s^{-1})	$t_{1/2}$ (s)
Medium-Low	First	$k_0 = (1.9 \pm 0.2) \times 10^{-2}$	37
Medium-High	First	$k_1 = (2.9 \pm 0.4) \times 10^{-2}$	24

Summarizing, in this chapter are presented, for the first time to the best of my present knowledge, kinetic parameters for the selenization of metallic precursor stacks, observing that this type of synthetic route follows a first-order kinetic for a wide range of chalcogen availability values, implying that this process depends mainly on this parameter (ChA). This means that the chalcogen either reacts with the metal matrix indistinctly of the alloys that are formed (mainly bronzes and brasses), or that the selenization of one of these metal alloys is remarkably slower than the others, controlling the reaction kinetic. Additionally, it is expected that this does not depend on the type of ramping and this analysis could be transferred to slow ramping processes.

In order to further study and characterize the system, a complete morphology and phase analysis of samples whose composition has been presented in **Figure 4.1** was performed. **Figure 4.4.** shows SEM top view images for the two types of ramping processes under study, and for the whole range of chalcogen availabilities present (the complete set of SEM images is presented in **Figure A5** at the **Annex**). When a fast ramping is applied, the samples surface morphology prepared at low Se availability is very similar to the typical metallic precursor surface[169], confirming a low Se incorporation. As expected, morphology changes when increasing the Se availability as the Se is more and more incorporated into the metallic layers. For all the cases, the layers look either amorphous or nanocrystalline, suggesting that crystallization has not started under these conditions. Those appreciations reinforce the kinetic model presented before because they imply that all the Se incorporated into the samples has been mainly used to diffuse into the metallic layer to form the kesterite and not to crystalize it.
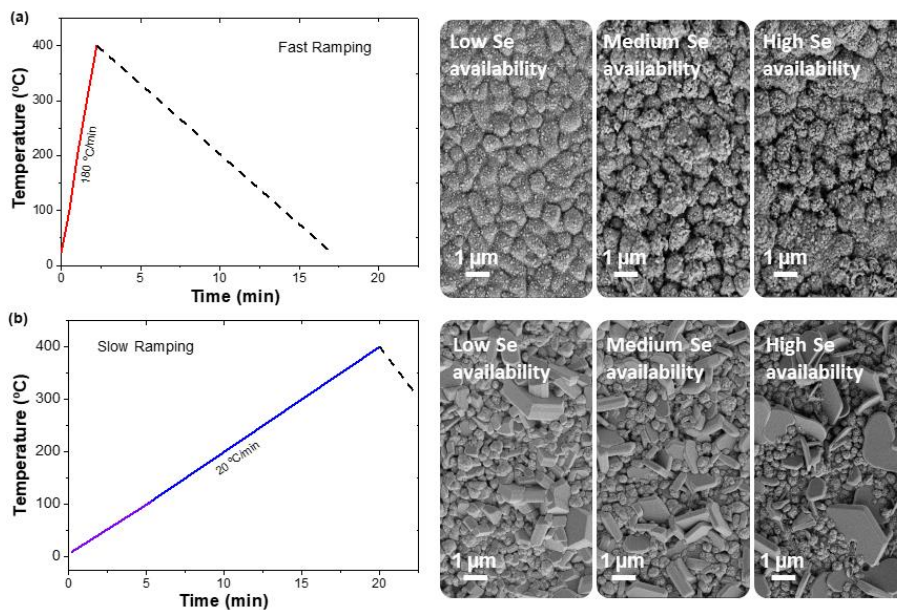
Figure 4.4 Thermal profile and top view SEM images of absorbers generated with a fast ramp at different chalcogen availabilities **(a).** Thermal profile and top view SEM images of absorbers generated slow ramp at different chalcogen availabilities **(b).**

Figure 4.5 presents a schematic representation of the different phases identified by XRD and Raman spectroscopy for fast and slow ramps. The data plotted has been obtained from the characterizations presented in the **Figure A7-10** at the **Annex**. In the **Figure 4.5** the chalcogen availability for whom the maximum intensity for each phase is obtained and represented by a vertical white line. The intensity of the Raman signal corresponding to each phase is plotted by the colour graduation. In addition, and with the aim to help clarifying the discussion, in **Table 8** all the detected phases under the different experimental conditions are summarized.
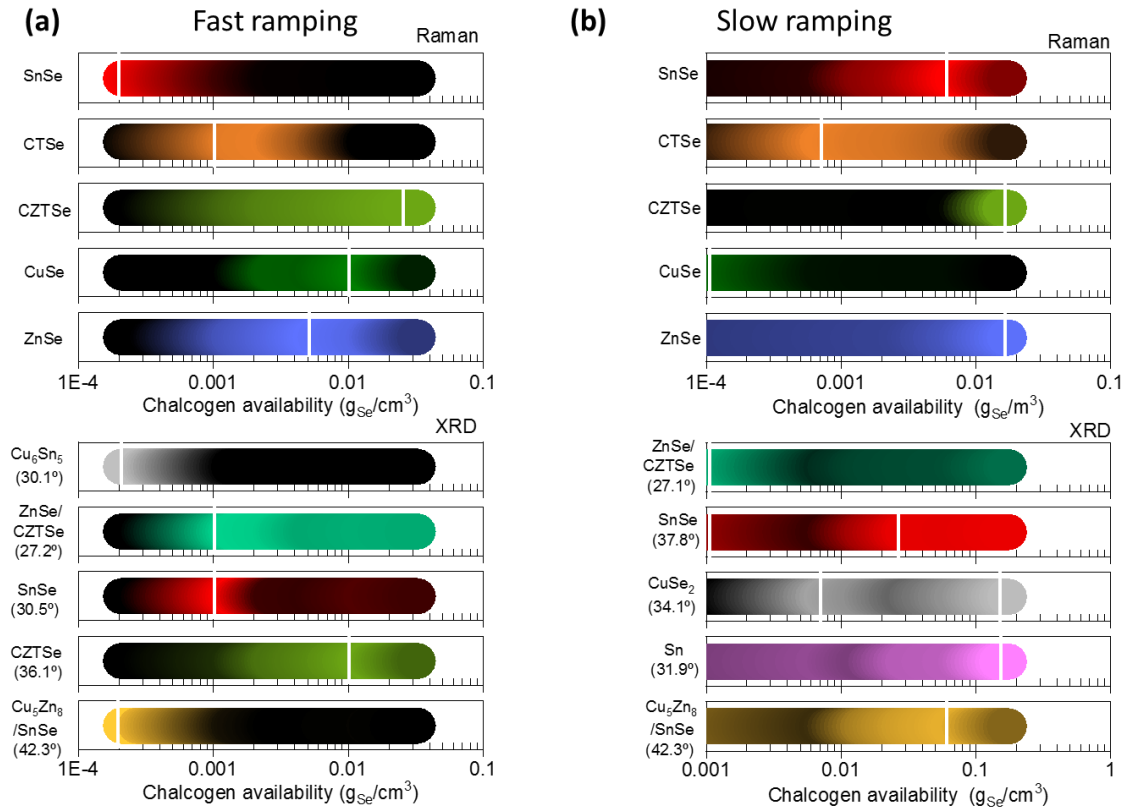
Figure 4.5 Schematic representation of the phase analysis performed using Raman spectroscopy and XRD for the whole chalcogen availability range, for fast ramp **(a)**, and slow ramp **(b)** processes. Vertical white lines represent the chalcogen availability where the maximum signal intensity corresponding to this particular phase is detected. The intensity of the colour correlates with the quantity of each phase.

Table 8 Summary of the detected phases extracted from **Figure 4.5**. **(-)** – Not detected. **(+)** – Present but in small quantities. **(++)** – Present in high quantities. **(?)** – Not clear.

Thermal process	Chalcogen availability (mg/cm³)		
	Low (ChA < 1x10⁻³)	Medium (1x10⁻³ ≤ ChA ≤ 1x10⁻²)	High (ChA > 1x10⁻²)
Fast ramping (kinetic control)	• Cu-Se: **(-)** • ZnSe: **(++)** • Sn-Se: **(++)** • Cu-Sn-Se: **(-)** • Cu₂ZnSnSe₄: **(+)** • Metals: **(+)** (bronze), **(?)** (brasses)	• Cu-Se: **(-)**, or **(?)** • ZnSe: YES • Sn-Se: **(+)** • Cu-Sn-Se: **(++)** • Cu₂ZnSnSe₄: **(+)** • Metals: **(-)**	• Cu-Se: **(-)** • ZnSe: **(++)** • Sn-Se: **(+)** • Cu-Sn-Se: **(+)** • Cu₂ZnSnSe₄: **(++)** • Metals: **(-)**

Slow ramping (thermodynamic control)	• Cu-Se: (++)	• Cu-Se: (++)	• Cu-Se: (++)
	• ZnSe: (++)	• ZnSe: (++)	• ZnSe: (++)
	• Sn-Se: (++)	• Sn-Se: (++)	• Sn-Se: (+)
	• Cu-Sn-Se: (-)	• Cu-Sn-Se: (++)	• Cu-Sn-Se: (++)
	• Cu$_2$ZnSnSe$_4$: (-), or (?)	• Cu$_2$ZnSnSe$_4$: (+)	• Cu$_2$ZnSnSe$_4$: (++)
	• Metals: (++) (Sn)	• Metals: (++) (Sn)	• Metals: (++) (Sn)

In the case of medium-low chalcogen availabilities, where probably a pseudo-zero-order kinetic is the most likely selenium-incorporation mechanism at the very beginning, which later evolves towards a first-order kinetic, only a mix of metallic and binary-chalcogenide phases are observed for both, fast and slow ramping. This strongly suggests that the preferred pathway formation for kesterite under such conditions is the one based on the reaction of binary phases. This reaction is fully compatible with the zero- or first- order kinetics, because in that case Se is limited reagent onto the precursor surface, so it reacts indistinctly with the immediate available metal forming the simplest and fastest species (binaries). It can be affirmed that main differences between fast or slow processes are only related to the type of metallic phases present in the system. Apparently, when fast ramping annealing is applied only complex metallic phases (bronzes and maybe brasses) are presented, due to shorter time annealing that is not enough to allow further phase transformation, implying that Se reacts directly with them by following Equation 3 and Equation 4. Nevertheless, for slow ramping processes, metallic Sn is also observed suggesting that when the system is thermodynamically driven, bronzes tend to be transformed during the selenization through Equation 5, releasing some free metallic Sn[170]. This result agrees with previous reports where metallic Sn has frequently been observed for slow ramping annealing during early stages of the kesterite synthesis[147]. Then, the resulted Cu-rich bronze is directly selenized as is shown in Equation 6. Basically, it can be inferred that for fast ramping processes the bronze metallic phases seem to be directly selenized, whilst when there is enough time in slow ramping cases and thermodynamics have enough time to play a major role over kinetics, bronzes first decompose and then the elemental metals are selenized. In the case of brasses, reliable information cannot be extracted from XRD because this phase as well as Zn and Cu metallic phases are hardly observed, so it can be supposed that even at very low chalcogen availabilities, the Cu-Zn alloys are directly selenized.

$$Cu_6Sn_{5(s)} + \frac{11}{2}Se_{2(g)} \xrightarrow[Fast\ ramp]{T=400ºC} 6CuSe_{(s)} + 5SnSe_{(s)}$$ Equation 3. Possible selenization of bronzes under fast ramping and low chalcogen availability.

$$Cu_5Zn_{8(s)} + \frac{13}{2}Se_{2(g)} \xrightarrow{T=400ºC} 5CuSe_{(s)} + 8ZnSe_{(s)}$$ Equation 4. Possible selenization of brasses under low chalcogen availability independently on the ramp.

$$Cu_6Sn_{5(s)} \xrightarrow[Slow\ ramp]{T=400ºC} 2Cu_3Sn_{(s)} + 3Sn_{(s)}$$ Equation 5. Possible decomposition of bronzes under slow ramping and low chalcogen availability.

$$Cu_3Sn_{(s)} + 2Se_{2(g)} \xrightarrow[Slow\ ramp]{T=400ºC} 3CuSe_{(s)} + SnSe_{(s)}$$ Equation 6. Possible selenization of bronzes under slow ramp and low chalcogen availability.

$$2CuSe_{(s)} + SnSe_{(s)} + ZnSe_{(s)} \xrightarrow{T=400ºC} Cu_2ZnSnSe_{4(s)}$$ Equation 7. Most probable formation reaction for kesterite at low chalcogen availability.

This implies that the only way to form kesterite under such conditions is through the reaction of the binary chalcogenide compounds, appearing Equation 7 as one possibility. It must be pointed out, when considering the complex Cu-Se and Sn-Se phase diagrams the competence with other possible binary compounds coming from these systems shall not be discarded, yet the general schema will not change and the possible competing reactions will always be those of a complex solid state reaction.

In summary, it can be concluded that when low amounts of chalcogen atoms are available in the system, the kesterite is formed mainly via binary phases reactions independently on the type of heating ramps. The only difference lies in the fact that bronzes are (at least partially) decomposed before being selenized when slow ramps are introduced, which is not the case for fast ramping. All these metallic phases are indistinctly selenized most probably via a zero-order reaction at the very beginning that immediately evolves towards a first order kinetic. Obviously, working under low chalcogen availabilities it is not recommended at all, due to the high risk to end up having unreacted binary-selenide and even metallic phases, altogether with the complexity of the mechanisms involved into the formation of the kesterite phase.

When the chalcogen availability is increased to values considered either medium or high, the situation drastically changes. As has been shown previously, the kinetic mechanism is better explained by a first order reaction with a relatively high kinetic constant and relatively low $t_{1/2}$ values. This implies that the reaction is accelerated and Se reacts very fast with any kind of metallic phase available in the system. It is clear in **Figure 4.5.** and **Table 8** that the Cu_2SnSe_3 ternary phase becomes the most relevant so far and no metallic phases are observed at all for fast ramping annealing, while only Sn is detected for slow ramping. So, in principle it can be considered that for this case bronzes and brasses react directly with selenium to form the intermediates. For fast ramping the selenization of bronze occurs most likely through Equation 8, where the ternary Cu_2SnSe_3 is directly formed, but inevitably altogether with Sn-Se phases at the same time. These results are very relevant, because they indicate that binary Sn-Se phases are necessarily always formed, independently on the selenization route followed by the bronze alloy. Brasses only have the possibility to react via Equation 4, where Cu-Se and ZnSe are the resulting phases. This allows to the first general conclusion that for medium-high chalcogen availabilities and fast ramping: even if in such conditions, the synthesis route of CZTSe involving in this case more complex phases like the ternary compound can be transformed, yet it is impossible to avoid the presence of simpler binary compounds as competitors.

On the other hand, this situation does not change too much when slow ramps are used. Still, elemental Sn is always observed for very high chalcogen availabilities implying that Equation 5 (i.e. transformation of Cu_6Sn_5 into Cu_3Sn) is in general faster than the selenization of bronzes. Then, Cu_3Sn is directly selenized forming the ternary compound as shown in Equation 9. Then, for that case and due to the presence of high quantities of ternary Cu_2SnSe_3 compound the formation of kesterite can proceed via the reaction of the ternary compound with ZnSe as described in Equation 10.

$$Cu_6Sn_{5(s)} + \frac{11}{2}Se_{2(g)} \xrightarrow[Fast\ ramp]{T=400^{\circ}C} 3Cu_2SnSe_{3(s)} + 2SnSe_{(s)}$$ Equation 8. Most probable reaction between bronzes and selenium under medium or high chalcogen availability and fast ramping.

$$Cu_3Sn_{(s)} + 2Se_{2(g)} \xrightarrow[Slow\ ramp]{T=400^{\circ}C} CuSe_{(s)} + Cu_2SnSe_{3(g)}$$ Equation 9. Possible selenization of bronzes under medium or high and slow ramping.

68
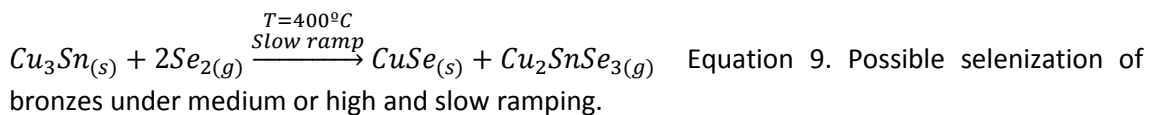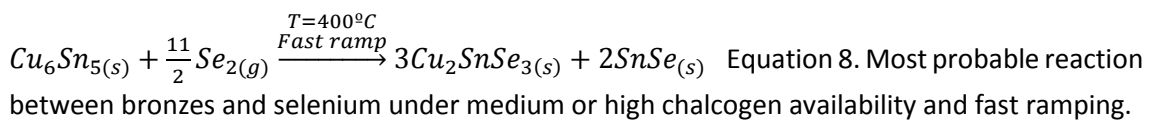
$$Cu_2SnSe_{3(s)} + ZnSe_{(s)} \xrightarrow{T=400^{\circ}C} Cu_2ZnSnSe_{4(s)}$$ Equation 10. Most probable formation reaction for kesterite at medium-high chalcogen availability.

Nevertheless, as can be observed from Equation 8, Equation 9, **Figure 4.5** and **Table 8.**, the presence of binary phases including Cu-Se and Sn-Se ones is almost unavoidable and have been detected at some time in all the possible kesterite formation pathways independently on the chalcogen availability and the type of kinetic reaction. This implies that, for medium and high chalcogen availability reaction in Equation 10 is the prevalent mechanism for kesterite formation. However, the reaction via Equation 7 is always present and competing, although probably to lesser extents as the chalcogen availability increases. As a summary, it is demonstrated that for low chalcogen availabilities the binary route with a pseudo-zero-order kinetics evolving to a first-order one for longer times is largely preferred, and for medium-high chalcogen availabilities the synthesis route via ternaries with a first-order kinetic is the prevalent, but competing with the binary route seems to be inevitable.

The results presented open very important perspectives for the synthesis of kesterites employing sequential processes where the precursors are metallic stacks. Independently on the precursor type and/or the chalcogenization conditions, the presence of undesired binary phases (Cu-Se and Sn-Se) even if it can be minimized, yet it cannot be 100% eliminated. At high chalcogen availabilities, the quantity of theses phases seems to be strongly reduced, although never eliminated. This has been considered the better condition to synthesize homogeneous absorbers. Nevertheless, and in order to ensure the lowest possible quantity of secondary phases at the end of the synthesis process it is strongly recommended to take additional measures such as: 1) ensure a high degree of intermixture between the metallic precursors, 2) ensure enough annealing time to let the reaction finish, and 3) post-deposition treatments are probably useful for the diffusion and termination of the reaction of these unreacted phases.

Finally, all the presented results in this section, strongly suggest that, despite the latest impressive progresses achieved with this type of synthetic routes, it is still nowadays impossible to obtain kesterite absorbers free of secondary phases with the chalcogenization of elemental metallic precursors. Further improvements are still required in future that might come by using precursors with a better mix of the different metals, i.e. complex alloyed precursors, better control of the chalcogen availability (temperature, pressure) and/or combination with precursors that already contain chalcogen.

4.2.2   First extension to Cu_2ZnSnS_4 case

With the aim to further develop this previous kinetic analysis to other types of kesterites, it was extended to the case of sulphur-based kesterites. For this study, the reactive annealing was also stopped at 400 °C, yet and due to technological reasons only a slow ramp (20 °C/min was applied), once again covering the full chalcogen availability range. **Figure 4.6** presents the evolution of the different elemental concentrations with increasing chalcogen availability, being analogue to **Figure 4.1.** It must be pointed out that even for high S amounts, the reaction is not completed after the investigated temperature, suggesting that the sulfurization process is a much slower process than the selenization one. This affirmation comes as a contradictory intuition to the expected trend: sulphur has a much higher vapour pressure and usually, sulphur vapours are more reactive than the selenium ones. Even at very high chalcogen availabilities

(>0.01 g_S/cm^3), the sulphur content in the layer tends to saturate at 42% under the studied conditions.
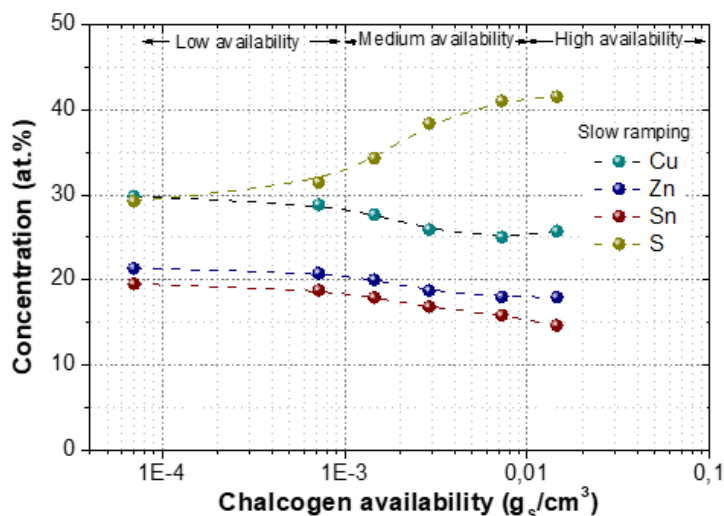
Figure 4.6 Evolution of the concentration of the different elements as determined by XRF for samples sulfurized under slow ramping conditions (20 °C/min).

As for the CZTSe study, these CZTS samples produced with different chalcogen availabilities, have also been characterized by Raman Spectroscopy and XRD. The complete Raman spectra with different excitation wavelengths as well as the XRD patterns are presented in **Figure A11** and **A12** at the **Annex**. The evolution of the different phases is graphically schematized in **Figure 4.7** and summarized in **Table 9.** In the case of the sulphur compound, when low chalcogen availabilities are applied a complex mix of metallic phases (bronzes, brasses and free Sn) are mainly present, altogether with remarkable amounts of ZnS. Those results corroborate the previous affirmation about the lower reactivity of sulphur with respect to Se and that this chalcogen reacts very selectively with Zn in order to form ZnS, which is the most stable phase in this system. Most probably kesterite is not formed due to the absence of Cu-S and Sn-S binary phases, because it is expected that for these synthesis conditions the binaries route for the formation of kesterite prevails.

When medium chalcogen availabilities are reached, the quantity of metallic phases starts to be drastically reduced. Other sulphide phases different than ZnS are observed including SnS and Cu_2SnS_3 and also small amounts of kesterite. This, once again, suggests that for medium chalcogen availability the formation pathway involving the ternary compound is the preferred route similarly to the observed for the selenide compound. By increasing the chalcogen availabilities to high values, an early kesterite formation is promoted with a strong reduction on the Cu_2SnS_3 and ZnS signals. This depicts an accelerated formation of CZTS under such conditions, but again both possible pathways including binaries and ternary compounds are most likely to be competing as in the case of the selenides.

The data presented in this chapter indicates that the formation pathways of sulphur and selenium compounds are very similar, although some differences are observed mainly in the processes dynamics, suggesting that the kinetic of the sulfurization of metallic stacks is somehow different and slower that the one observed for the selenides.
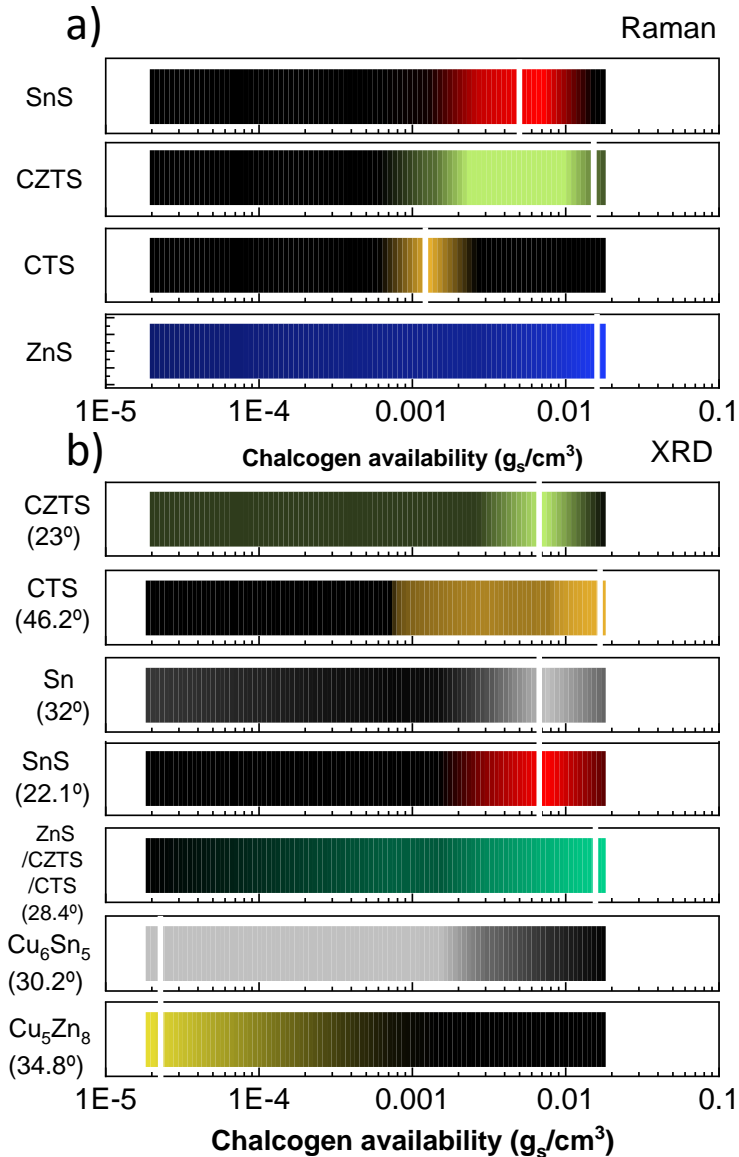
Figure 4.7 Schematic representation of the phase analysis performed using Raman spectroscopy and XRD for the whole chalcogen availability range for CZTS. Vertical white lines represent the chalcogen availability where the maximum intensity of this particular phase is obtained.

Table 9 Summary of the detected phases extracted from **Figure 4.7**. depending on the chalcogen availability regime. (-) – Not detected. (+) – Present but in small quantities. (++) – Present in high quantities. (?) – Not clear.

Thermal process	**Chalcogen availability (mg/cm³)**		
	Low (ChA < $1x10^{-3}$)	Medium ($1x10^{-3} \leq$ ChA $\leq 1x10^{-2}$)	High (ChA > $1x10^{-2}$)
Fast ramping (kinetic control)	• Cu-S: **(-)** • ZnS: **(++)** • Sn-S: **(-)** • Cu-Sn-S: **(-)** • Cu_2ZnSnS_4: **(-)**	• Cu-S: **(-)** or few • ZnS: **(++)** • Sn-S: **(+)** • Cu-Sn-S: **(++)** • Cu_2ZnSnS_4: **(+)**	• Cu-S: **(-)** • ZnS: **(++)** • Sn-S: **(+)** • Cu-Sn-S: **(+)** • Cu_2ZnSnS_4: **(++)**

	• Metals: **(+)** (bronze), **(+)** (brasses), **(-)** (Sn)	• Metals: **(+)** (bronze), **(+)** (brasses), **(+)** (Sn)	• Metals: **(-)** or **(?)** (Sn)

4.3 Summary

In this chapter it has been once again depicted and commented the high interest that physical vapour deposition methodologies have reached for the synthesis of kesterites. In those processes and specially for sequential processes based on metallic stacks, it is of key importance to deeply understand and comprehend the intermediate phases and possible formation routes on them for their future progress. In between those formation routes, one parameter identified that has turned out crucial is the chalcogen availability. In this present chapter a combined kinetic and phase analysis of the selenization process that includes slow and fast ramped annealing steps has been presented. On the study performed, it has been observed that for a medium-low chalcogen availability situation the kesterite is formed through a pseudo-zero order kinetic reaction, with a constant equal to $k_0 = (1.9 \pm 0.2) \times 10^{-2}$ s^{-1} and a $t_{1/2} = 37$ s, which evolves towards a first-order reaction for relatively long annealing times, mainly controlled by the reaction of Cu-Se, Sn-Se, and ZnSe binary phases. When the chalcogen availability is increased towards medium-high values, the kinetic of the selenization process is then identified as a first-order, with a kinetic constant about $k_1 = (2.9 \pm 0.4) \times 10^{-2}$ s^{-1}, and a $t_{1/2} = 24$ s. Finally evolving towards a simpler pathway involving the ternary Cu-Sn-Se compounds with ZnSe, simplifying the formation route of CZTSe. This is a clear advantage, as it reduces the occurrence of unreacted secondary phases after the selenization is finished. Nevertheless, it has also been commented that in spite of the high chalcogen availability, the synthesis route involving binary compounds is always observed and cannot be completely eliminated yet reduced to a much lower extent. With those conclusions in mind, it has also been affirmed that additional strategies for ensuring high quality absorbers free of secondary phases using this approach are still required.

Also, a first extension towards the sulphide kesterites has been developed through the chapter showing similarities in terms of phases observed, depicting the route involving binaries being the preferred one for low ChA, and the one involving the Cu_2SnS_3 ternary compound for high ChA. Finally, even though the sulfurization process still would require a more detailed analysis, it can be affirmed that the sulfurization process is slower than the selenization one.
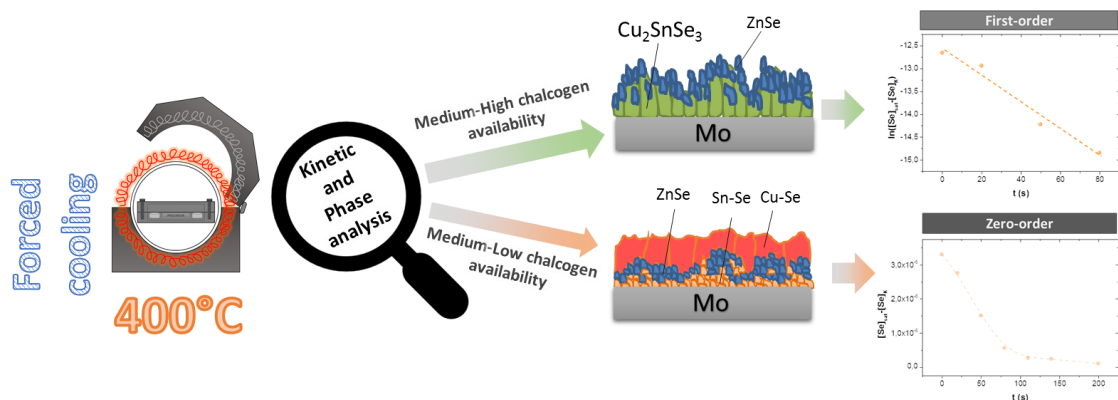
Figure 4.8 Summary of the dependence on the kinetic regime for the RTP annealing process at IREC.

Chapter 5

Kesterite solar cells combining Electrodeposition and RTP

5 Kesterite solar cells combining Electrodeposition and RTP

After optimizing the RTP and contrasting it to CTP employing standard sputtered metallic precursor layers from the IREC baseline (Chapter 3) and unravelling the fundamental mechanisms underlying rapid kesterite synthesis and film formation (Chapter 4), now the RTP versatility will be tested using different precursor layers. For this purpose, electrodeposited precursor layers are used with the optimized RTP procedure from Chapter 2. In this Chapter, we introduce the precursor electrodeposition process and fully characterize the finished absorbers with detailed Raman mapping at different wavelengths, X-ray diffraction, SEM and optoelectronic. First solar cell devices with electrodeposited precursor applying an RTP selenization are presented opening promising perspectives for this kind of processing and showing the versatility of the developed RTP process. The work presented in this chapter is summarized in a research article, also found in the appendix, *M. Valdés, A. Hernández-Martínez, et al.* [171] (DOI: 10.1016/j.solener.2018.08.049).

5.1 Electrodeposition of kesterite thin film

During this Thesis, sequential processes where metallic precursors are first deposited and then reacted into kesterites have been studied. Until now, the scope has been set onto the annealing step by implementing, optimizing and understanding a new annealing via RTP processing. In the next step, the versatility and robustness of the new RTP process should be tested. In order to so, the focus moves now towards a variation of the precursor deposition. Amongst the techniques to deposit kesterite precursors, electrodeposition (ED) appears as one of the most important routes because of several distinct advantages:

- Allows to deposit large-area thin films with a high throughput
- The ED method takes place at atmospheric pressure at low temperatures
- ED is a low-cost technique
- High quality films can be obtained with a very low capital investment
- The bath where the reaction occurs can be reused for many cycles if the solutions are refilled (reduced waste production, high material yield).
- A high-grade recycling of the materials used can be applied
- ED methods have already successfully been implemented into industry[172]

ED methods involve electron transfer reactions between electrodes and dissolved reactant ions, which are usually dissolved in an aqueous solution. Despite the previously mentioned advantages ED also presents challenges that must be overcome. The main challenge for ED is to ensure a uniform lateral distribution both at microscopic scale (morphology of the electro-deposited material) and also at the macroscopic scale (thickness/density of coverage of substrate area)[173]. In order to address both problems several strategies can be implemented: the microscopic uniformity is mostly influenced by the deposition potential and the interactions between the solution and the substrate. On the other hand, the macroscopic uniformity can be ensured by applying a uniform current to ensure the mass transport in an isotropic convection, in order not to limit mass transport[174].

When it comes to efficient ED processes for kesterites, there are two main techniques employed nowadays: Stacked elemental layer approach (SEL) and Cu-Sn-Zn metal alloy electrodeposition.

5.1.1 Stacked elemental layer approach for electrodeposition

Currently the best efficiencies achieved for ED kesterites have been obtained by SEL processing, as reported for CZTSe by *Vauche et al.*[75] reaching efficiencies up to 8.2% and in the case of CZTS by *Jiang et al*[74] up to 8%. Employing SEL it is very interesting thanks to its high feasibility and it is also very easy to variate the composition of the precursors just by independently changing the deposition parameters of each electrodeposited layer individually. The precursor composition can be easily tuned by changing the thickness of each layer present on it, e.g. by a variation of the deposition time.

The main drawbacks of this technique are a limitation of the available precursor designs. In ED the standard reduction potentials of the elements play a determinant role for deposition of an elemental layer on top of another. Because of this only the sequence Mo/Cu/Sn/Zn is able to behave correctly; it must be pointed out that the best efficiencies were obtained with this sequence.[174–179]

5.1.2 Cu-Sn-Zn metal alloy Electrodeposition

In contrast to the SEL routes where three separate electrolytes, baths and depositions are needed to obtain the metallic stack, for co-electrodeposition only one single electrolyte and one-electrodeposition step to form a precursor film is required. However, as in previous cases it also contains culprits related to difficulties to deposit homogeneous layers and problems with bath stability that might explain why up to now co-electrodeposition routes have shown lower efficiencies than SEL. Furthermore, obtaining an accurate control of the precursor metallic composition is challenging.

In terms of efficiencies ranges from 2-6% have been reported in the literature employing for co-electrodeposition followed by selenization or sulfurization treatments.[180–184] Most of these publications, report a low temperature thermal treatment on the CZT precursors prior the annealing. The highest efficiency achieved for co-electrodeposited precursors via ED was of 8.0% by *Jeon et al.*[185] and for the case of CZTS a 7.4% efficiency was reported by *Ge et al.*[186]

5.1.3 Quaternary Electrodeposition

The simultaneous electrodeposition of four elements (Cu, Sn, Zn and S (e)) is interesting as it consists of only one single deposition step, reducing enormously time and costs as less equipment and process steps are implied. Also, it could be expected that by depositing all the elements in a single step the precursor will be more uniformly intermixed at atomic scale. The deposition of all those elements altogether has proven to be extremely challenging and very few works have produced working devices, the best device obtained 5.5% efficiency and was reported by *Ge et al.*[187]

The different ED deposition options are summarized with their strengths and weaknesses in **Figure 5.1.** For this work, co-electrodeposited metallic precursor layers have been selected as most promising approach to be pursued.
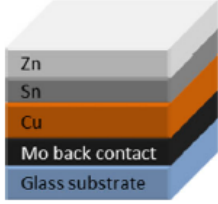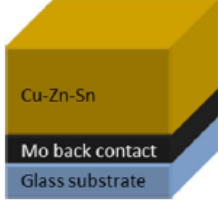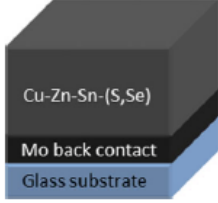
process	strengths	weaknesses	opportunities	threats
Section 3.2 Stacked elemental layer (SEL) electrodeposition	+ dense layers + easy control of stoichiometry + different stack orderings possible + short deposition times + stable electrolytes	− 3 steps − in-depth inhomo-geneity (need for interdiffusion/mixing) − one preferred stack order (Cu/Sn/Zn)	+ more degrees of freedom (stoichiometry, stack ordering, density…) + process more easily adaptable for industry	− if the precursor is required to contain chalcogen for the highest quality semiconductor material this process may need co-deposition of metal chalcogen for at least one layer
Section 3.3 metal alloy co-electrodeposition	+ single bath + minimum of equipment + short deposition times	− multiple diffusion coefficients and deposition potentials mean homogeneous deposition on cm^2 areas is difficult	+ control of as-deposited Cu-Sn and Cu-Zn alloys and alloy particle size	− electrolyte bath chemistry difficult to control to give uniform compositions over large areas
Section 3.4 chalcogenide co-electrodeposition	+ single bath + minimum of equipment	− as for alloy deposition and additionally: − no stable or reple-nishable chalcogen source − long deposition times	+ if a precursor containing sulfur or selenium shows superior semiconductor properties after annealing	− too many technical difficulties to surmount to provide uniform material even on areas of cm^2

Figure 5.1 Strengths, weaknesses, opportunities and threats analysis of the three main electrodeposition routes used to form kesterite precursors. *Reproduced from Colombara et al.*[173]

5.2 CZTSe solar cells combining co-electrodeposition and Rapid Thermal Processing

In this chapter, CZTSe thin films prepared by a sequential process combining a short-time co-electrodeposited CZT precursor deposition and a selenization step in the RTP baseline implemented at IREC will be presented.

In this work, we succeed in fabricating a 5.2% efficiency solar cell synthesized by this preparation route, which is about twice the efficiency of previous kesterite solar cells with co-electrodeposited precursors and conventional thermal annealing fabricated from IREC[188] previously. When compared to the literature, only one work has been published that also combines co-electrodeposition and RTP treatments reaching 4.5% efficiency[189]. In the work presented with IREC's RTP baseline, the final efficiency is increased, and the processing times are reduced by 4 times, if compared to the 4.5% device reported.

As throughout this whole thesis, CZTSe solar cells are prepared on SLG substrates, following the procedure commented in Chapter 2 until the Mo deposition step. Once the back contact was deposited, the CZT precursors alloy was co-electrodeposited employing a three-electrode cell in collaboration with PhD. Valdés. In order to obtain the best adherence for the ED layer, the Mo was immersed into a 20% NH_4OH solution for 3 min to remove native MoO_x. A platinum (purity 99.999%) mesh composed of much larger dimensions than the working electrode was used as an auxiliary electrode. Also, a silver chloride electrode (Ag/AgCl, KCl saturated) was employed as a reference.

The electrolyte solutions for the ED were prepared using deionized water containing milli molar concentrations of $CuSO_4 \cdot 5H_2O$ (ACS reagent ≥98% Sigma-Aldrich); $ZnSO_4 \cdot 7H_2O$ (ReagentPlus®, ≥99.0% Sigma-Aldrich) and $SnSO_4$ (≥95% Sigma-Aldrich). Sodium citrate tribasic ($Na_3C_6H_5O_7$, ACS reagent, ≥99.0% Sigma-Aldrich) was used as complexing agent in the electrolyte solution for the co-deposition of CZT as was previously reported by *Valdés et al.*[190] The molar ratios of Cu:Zn:Sn:Na-cit in the electrolyte were fixed to 1.3:1.2:1:20 with a copper concentration of $13 \cdot 10^{-3}$ mol/L. The final pH of the solution was close to 6 without any addition of acids or bases. CZT precursor films were co-electrodeposited at room temperature in potentiostatic mode applying a potential of -1.2 V (vs. Ag/AgCl) during 15 min employing a VSP Electrochemical Workstation (Biologic). Once the CZT precursors were deposited by ED, the samples were submitted to the same RTP annealing process as summarized in **Table 5.** The samples were then etched and further completed to solar cell devices and characterized as previously reported in Chapter 2.

5.2.1 Effects and results obtained on RTP annealing over co-electrodeposited precursors

In line with the rest of this Thesis, putting a strong emphasis on revealing the formation pathways of the kesterite synthesis process we proceed to analyse the phases present on the reacted absorbers. For this, an XRD analysis was also carried out for the non-annealed and the RTP annealed samples, as can be observed in **Figure 5.2:**
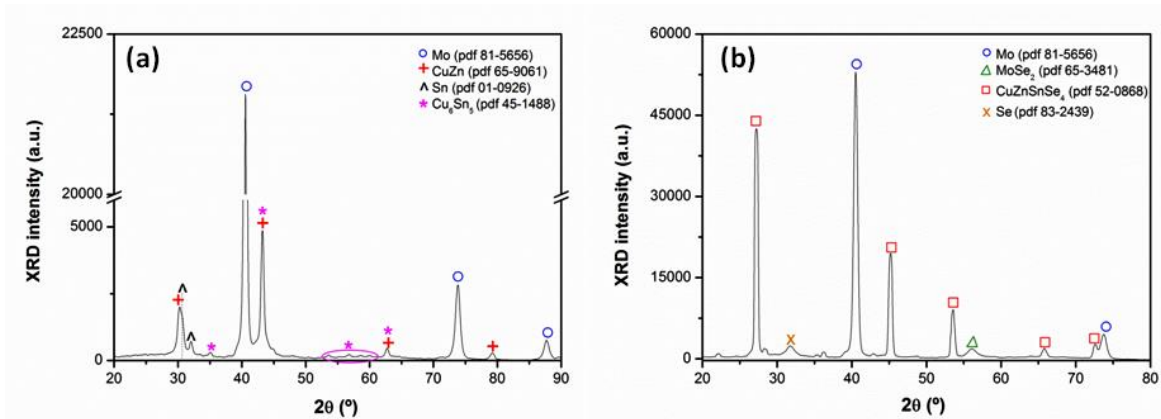
Figure 5.2 XRD pattern of (a) CZT precursor electrodeposited at -1.2 V (vs Ag/AgCl) during 15 min ad (b) CZTSe thin film obtained after RTP treatment.

The precursor obtained by co-electrodeposition is mainly composed of binary phases such as: CuZn, Zn-rich Cu_5Zn_8 and Cu_6Sn_5. Furthermore, weak signals related to Sn phases are found in the diffractogram. When compared to bibliography, those alloy phases are common and have been reported by several authors[180,191–193]. As a result of the co-electrodeposition routes, the formation of alloys instead of pure metals is observed. The presence of intermetallic CuZn has also been related to a Cu-poor composition of the CZT precursor[191] and it is suspected that the concentration of Cu ions regulates the formation of intermetallic compounds[193].

After RTP selenization, the diffractogram of the film presents intense and sharp peaks of the main crystallographic planes of the CZTSe phase. Furthermore, also $MoSe_2$ and elemental Se phases are also detected. This Se phase is suspected to arise from the cooling down of the annealing process where residual selenium on the samples can be deposited by condensation of Se vapour[194].

Besides the crystal structure, the chemical composition is of key importance to achieve highly efficiency devices, particularly the Cu/ (Zn + Sn) (CZT) and Zn/Sn (ZT) ratios. More specifically, ideal values for the absorber composition are Cu-poor and Zn-rich compositions with a CZT of around 0.8-0.9 and a ZT of 1.2[132].

Table 10 Chemical composition and elements ratios in selected CZT and CZTSe films[1].

Sample	Thickness [nm]	%Cu	%Zn	%Sn	%Se	Cu/(Zn+Sn)	Zn/Sn
CZT	480.5 ± 95. 2	44.2 ± 1.1	27.9 ± 1.5	27.8 ± 1.1	-	0.79	1.00

Sample	Thickness [μm]	%Cu	%Zn	%Sn	%Se	Cu/(Zn+Sn)	Zn/Sn
CZTSe	1.65 ± 0.21	22.7 ± 1.2	14.1 ± 1.0	10.4 ± 0.3	52.8 ± 1.5	0.94	1.38
CZTSe + KMnO$_4$	1.62 ± 0.15	22.5 ± 0.9	12.9 ± 0.6	12.5 ± 0.5	52.1 ± 1.0	0.88	1.03
CZTSe + KMnO4 + (NH$_4$)S	1.55 ± 0.1	22.8 ± 0.6	13.2 ± 1.1	11.4 ± 0.4	52.6 ± 1.3	0.93	1.16
CZTSe + KMnO$_4$ + (NH$_4$)S + KCN[2]	1.53 ± 0.15	21.4 ± 0.8	13. 6 ± 0.8	11.2 ± 0.6	53.8 ± 1.8	0.86	1.21

[1]Chemical composition and film thicknesses were determined using XRF. For CZT and CZTSe films the mean value and the error were calculated from six individual point measurements, while for the etched films not less than four individual measurements were taken.

[2]Composition of the best device reported in this thesis by co-electrodeposition and RTP.

In this work, the composition of the co-electrodeposited precursor as well as the finished absorber layer have been analysed by XRF. The results are presented in **Table 10.** As can be observed, the precursors obtained via ED are Cu-poor and contain equal amounts of zinc and tin atoms. It must be noted that one of the main drawbacks[173] about applying ED techniques is its difficulty to obtain homogeneously thick layers. This problem is also present here, as the thickness is around 0.5 µm, with a standard deviation around 100nm. However, the final deviation on the chemical composition for each element is below 5% for a 2.5 x 2.5 cm^2 electrodeposited film, which is a sign of good uniformity. After RTP annealing, the final composition approaches the desired Cu-poor Zn-rich stoichiometry. Finally, the excess of Se (above 50%) is thought to belong either to the MoSe$_2$ layer which is formed during the selenization and this phase is condensed elemental Se, as previously observed by XRD.

Furthermore, **Table 10** also includes the variation of the composition of the CZTSe film after etching it, with the standard etching treatment used at IREC to remove secondary phases like ZnSe, Sn-Se and Cu$_x$Se[93,195]. After complete etchings are performed, the composition of the best CZTSe absorber possesses a Cu/ (Zn + Sn) ratio of approx. 0.85 and Zn/Sn ≈1.2. As common for CZTSe absorber its thickness is approximately three times the one of the precursor layers.
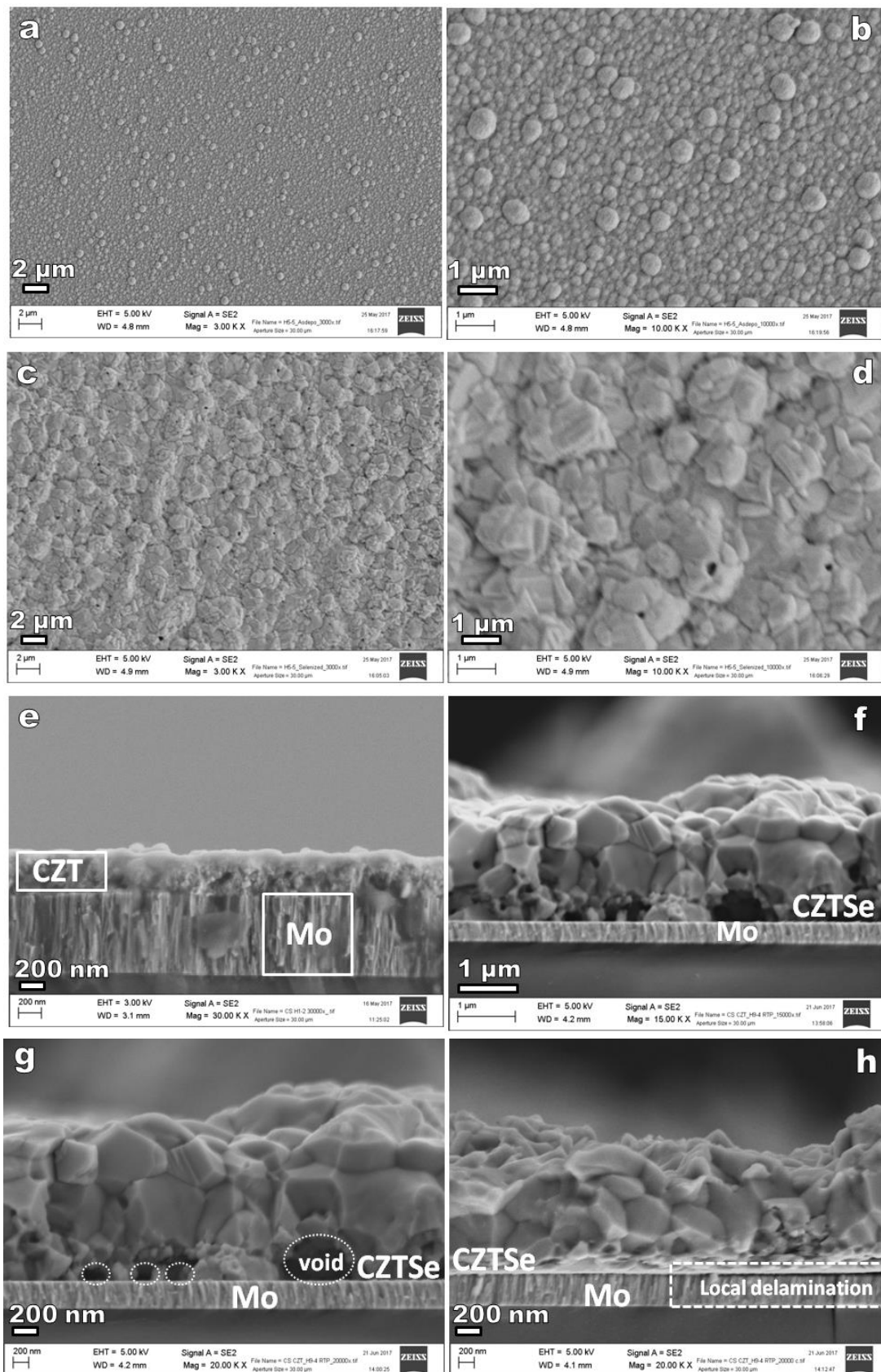
Figure 5.3 Top-view FESEM pictures of (a-b) co-electrodeposited CZT precursor (c-d) CZTSe thin film obtained after RTP selenization. Cross-section view of (e) CZT precursor and (f-h) CZTSe thin films (no etching). Pictures (g-h) show defects at Mo/CZTSe interface using higher magnification.

In order to characterize the differences in morphology, SEM analysis were conducted and are presented in **Figure 5.3.** At low magnification, **Figure 5.3(a),** all the films seem to be correctly and homogeneously deposited as no voids or cracks can be observed. When the magnification is increased **(b)** round particles within the nanometer range are noticed, with some dispersion of bigger agglomerates at the top surface. Once the RTP annealing is realized, **(c)**, the films keep showing a high degree of homogeneity, but the morphology completely changes towards planar particles with an irregular shape. After selenization, CZTSe absorbers depict a greyish and opaque film. When increasing the magnification, **(d)**, smalls voids start appearing at the surface.

Those present voids might appear as a result of partial evaporations from volatile compounds formed at high temperatures such as $SnSe_x$[134,196,197]. This evaporation of volatile $SnSe_x$, would also explain the increase of the Zn/Sn ratio from 1 to 1.38 after RTP selenization. A similar behaviour has also been reported by *Unveroglu et al.*[198]

Finally, cross section pictures for CZT in **(e)** and CZTSe **(f)** also help to corroborate the previous XRF thickness measurements presented and provide additional evidences about the increase on the film's thickness after RTP annealing. The CZT precursor shows compactness and high adherence to the Mo substrate. On the other hand, the CZTSe absorber, obtained via RTP, exhibits void at the Mo/CZTSe interface. Furthermore, localized delamination (partial detachment of the kesterite from the substrate) is observed, which is expected to be highly detrimental for the final device performance, as a low-quality Mo/CZTSe interface will strongly influence the overall solar performance. The formation of this voids and the local delamination is a common problem throughout the kesterite technology as it is reported for several synthesis techniques like sputtering[197,199] or chemical deposition methods[200,201].
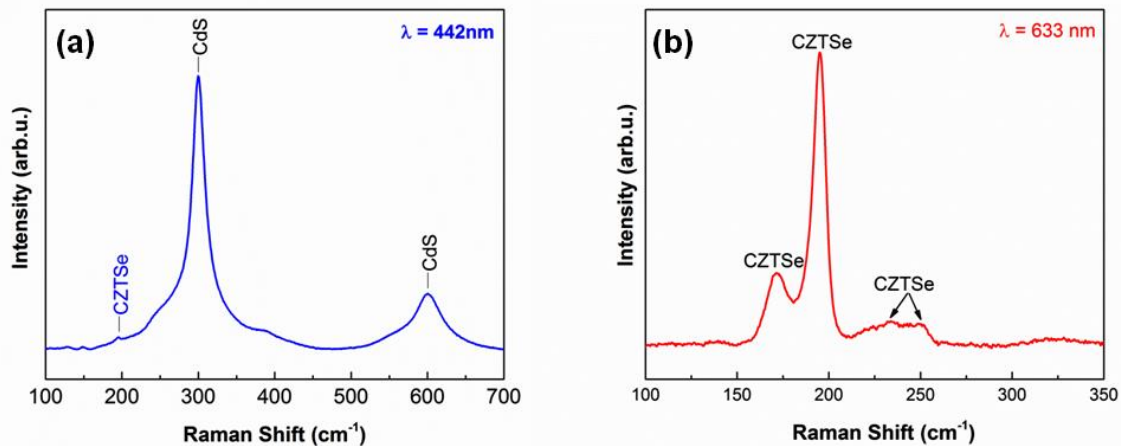
Figure 5.4 Raman spectra of a finished solar cell under different excitation wavelengths: (a) 442 nm and (b) 633 nm.

In order to further analyse the phases, present in our samples, Raman spectroscopy with several wavelengths was carried out. **Figure 5.4** depicts the spectra obtained for wavelengths 442 and 633 nm. Several wavelengths have been applied in order to take into account resonant excitation. When studying CZTSe, resonant effects are usually detected in binary compounds like ZnSe or Sn-Se, at excitation wavelengths of 442 or 663 nm respectively[202].

Once the chemical etching procedures developed at IREC and commented in Chapter 2 were implemented, no traces of $SnSe_2$ and/or ZnSe secondary phases were detected. In **Figure 5.4a** the spectrum of a complete device for the 442 nm wavelength is presented. Here, we observe a

dominant band at 300 cm^{-1} identified as A$_1$(LO) and weaker contributions at around 195 and at 600 cm^{-1} that can be identified as Se-Se vibrations of the CZTSe and the second order of the A$_1$ (LO) CdS mode. Resonant effects of CdS for this wavelength may explain the remarkable difference in Raman intensities between CdS and CZTSe layers[203]. Moreover, the absence of contributions at 250 and 500 cm^{-1} which are characteristic of ZnSe under resonant conditions (488 nm) suggest the absence of this phase in the CZTSe[204].

When a laser excitation of 633 nm is applied (**Figure 5.4b**) only Raman signals coming from the CZTSe layer are present in the spectrum without interference from the upper layers[203]. No contribution from further secondary phases can be detected. The spectrum obtained shows the main modes of CZTSe at 195 cm^{-1} and at 170 cm^{-1}, both of them containing A symmetry; and other two minor signals at 235 and 250 cm^{-1} with E and B symmetry, as has been reported into literature[205]. Under these excitation conditions the absence of Raman signals between 110 and 180 cm^{-1} might be taken as an indication of the absence of Sn-Se related secondary phases on the surface of the film[206].

With the aim to deeply analyse these samples, Raman micro-mapping was employed. Raman micro-mapping is considered nowadays a very powerful tool to study the homogeneity of thin films and their properties. Raman maps have been recorded for the sample present in **Figure 5.5a** following the grid depicted in **(a)**, using 20 μm steps in the x and y directions. Raman maps performed at excitation wavelengths of 532 **(b and c)** and 786 nm **(d and e)** showing a homogenous distribution of kesterite Raman signals along the analysed area (80 x 80 μm) altogether with a weak and broad signal from the CdS buffer layer, which is only visible when the excitation wavelength applied is 514 nm (close to the resonant effect). The broad appearance of the CdS Raman mode can be explained by its nanocrystalline dimensions. Also, the even distributions of Raman signals and a more statistical representation can be visualized by showing the maps in the form of colours contours. Those are represented for each wavelength in **(c and d)** respectively. In both figures narrows and high intensity colour bands around the main A mode (195 cm^{-1}) of the CZTSe, which is an indication of high crystallinity and homogeneity of the CZTSe absorber throughout the whole sample.
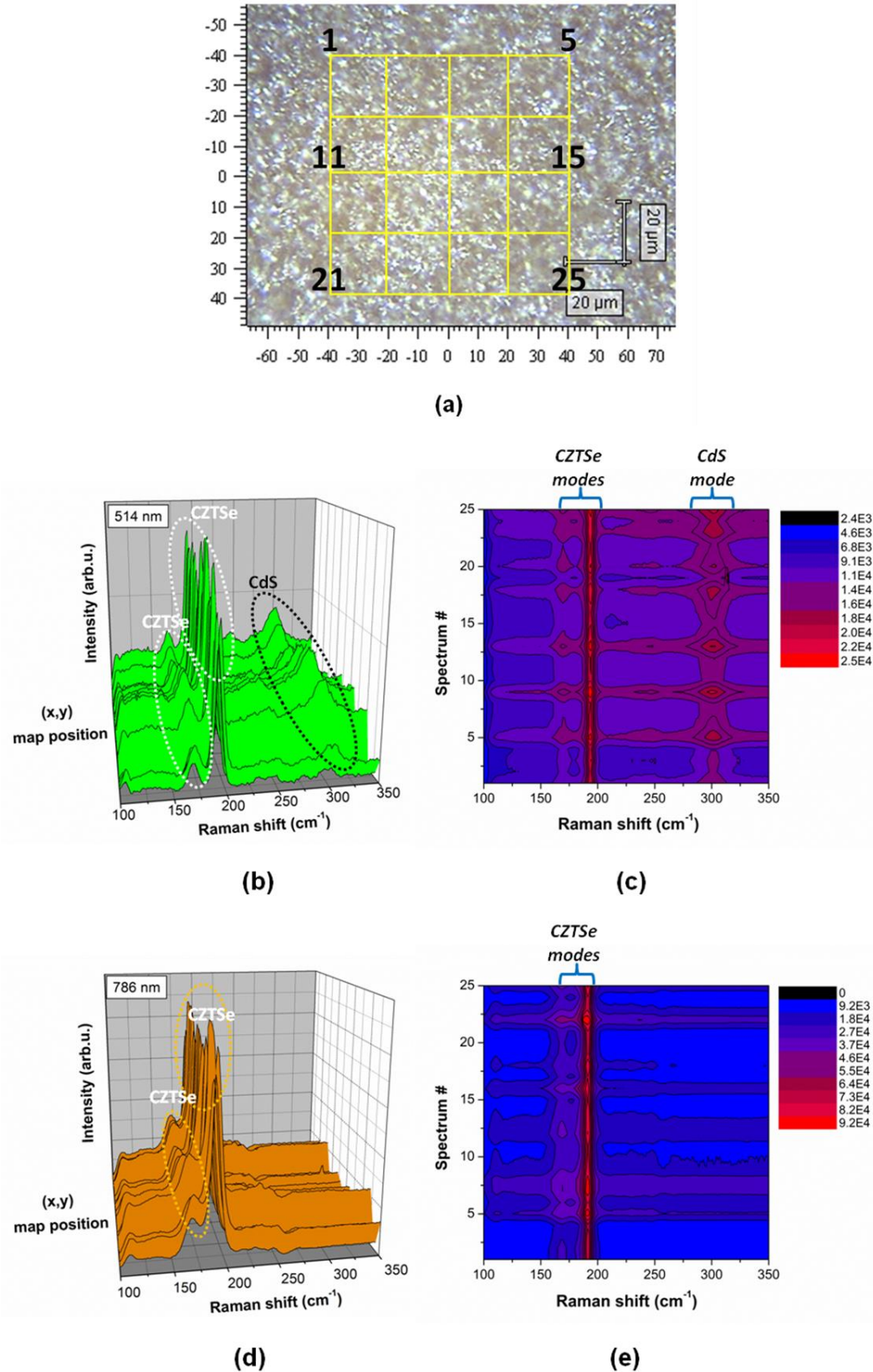
Figure 5.5 Raman μ-maps of the best CZTSe sample obtained by co-electrodeposition and RTP; (a) microscopy image and grid used to record the maps; (b) 514 nm Raman map; (c) 514 nm colour contour of Raman intensity signals; (d) 786 nm Raman map and (e) 786 nm colour contour of Raman intensity signals.

The optoelectronic parameters of the best solar cell obtained by co-electrodeposition and RTP are presented into **Figure 5.6.** Moreover, the solar cell parameters for the best cell and statistical values for the full sample can be found in **Table 11**. As commented previously, a solar cell with a maximum efficiency of 5.2% has been achieved doubling the previous results at IREC[188]. TO the best of my knowledge and this is also the highest value presented in the literature for co-electrodeposited precursors annealed by an RTP. Shunt and series resistance for the record cell were R_{shunt} = 67.4 Ω cm² and R_s = 0.2 Ω cm² respectively. In concordance with the observation from the Mo/CZTSe interface, the R_{shunt} of the solar is quite low in comparison to higher efficiency cells (around 10 times higher)[64].

It must be commented that there is no cross-over between dark and illuminated I-V curves. Usually, the cross-over has been explained by to the generation of photogenerated carrier trapping in the CdS layer[135,207,208]. In conclusion, the absence of a cross-over is a hint towards a good CZTSe/CdS interface quality and proper band alignment.
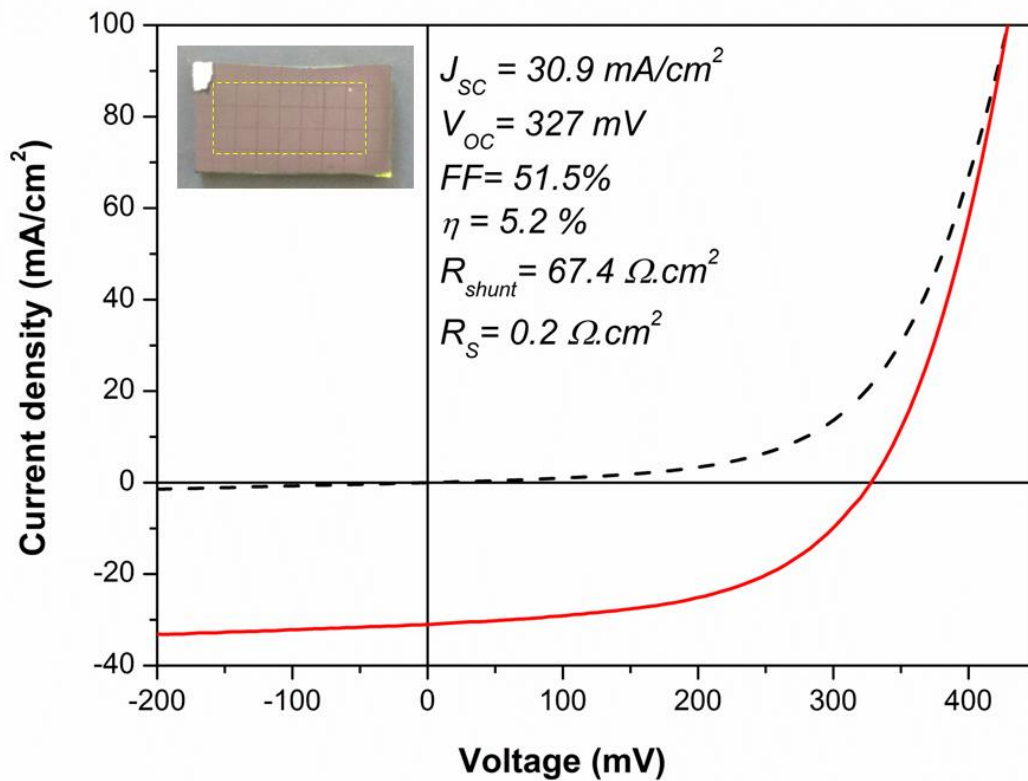
Figure 5.6 I-V voltage curves obtained under simulated AM1.5G for the best CZTSe solar cell obtained. The insert shows an image of the full sample and the statistical values are presented into **Table 11.**

Table 11 CZTS best device optoelectronic parameters[1]

η (best) [%]	η (mean) [%]	RSD [%]	J_{sc} (best) [mA cm^{-2}]	J_{sc} (mean) [mA cm^{-2}]	RSD [%]	V_{oc} (best) [mV]	V_{oc} (mean) [mV]	RSD [%]	FF [%]	R_{SH} [Ω.cm^2]	R_S [Ω.cm^2]
5.2	4.5	11.7	30.9	30.8	4.7	327	309.9	5.4	46.7	48.5	0.8

RSD, relative standard deviation.

[1]Main optoelectronic parameters (η, V_{OC}, J_{SC}) are reported as best value at cell size (active area: 0.087 cm^2), average value for the full sample (21 cells, see insert in **Figure 5.5a**), and its relative standard deviation. The reported values for fill factor (FF), series resistance (R_S), and shunt resistance (R_{SH}) are average for the full sample.
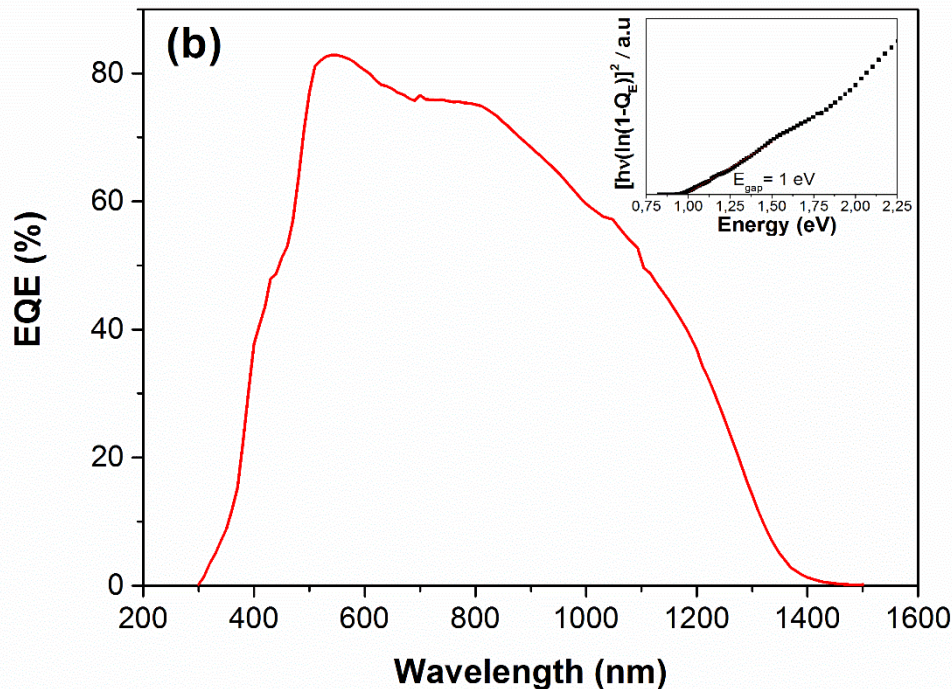
Figure 5.7 External Quantum Efficiency (EQE) of the best device obtained. The inset shows the calculated BG of the CZTSe absorber from the EQE data.

Finally, an EQE spectrum of the best cell is shown in **Figure 5.7.** The EQE reaches 70-80% between 500 and 800 nm indicating quite good carrier collection for the p-n junction. Below 500 nm absorption of the CdS buffer layer reduces the EQE in this region. Finally, from 900 nm, the decay in EQE is probably related to the deep absorption and low diffusion length of charge carriers generated at these wavelengths.

5.3   Summary

In this Chapter, the potential of fast, low-cost ans large area compatible processes for the preparation of earth-abundant kesterite solar cell technologies has been further expanded. For this, the previously developed RTP process for the reactive annealing of metallic precursors is applied to a new set of metallic precursor layers fabricated by electrodeposition. Electrodeposition (ED) offers fast and industrially compatible processing on large areas. From the different electrodeposition of metallic alloys from one electrolyte solution has been selected because of its simplicity.

Following the main emphasis of this Thesis, the layer properties and phases present in the precursor and final absorber films have been analysed. We find that the metallic CZT films synthesized by co-electrodeposition consist of mainly binary CuZn and CuSn alloys. The composition of the films, after the RTP annealing reached the desired Cu-poor Zn-rich stoichiometry. The investigation of the morphology by SEM showed a homogeneous coverage of the ED films composed of round particles with nanometric size. The deposited metallic precursor alloys showed a pronounced thickness variation of roughly 20% over 2.5 x 2.5 cm^2 sized substrates. While this is a common problem for ED, the thickness homogeneity should be improved in future optimizations. After RTP annealing, film thickness roughly triples and the film morphology changed to a large extent, showing now platelet-shaped grains. Cross-sectional micrographs revealed voids located in the Mo/CZTSe interface partial film delamination.

The XRD analysis conducted presented sharp and intense peaks of the main crystallographic planes of the kesterite phase, altogether with $MoSe_2$ and elemental Se. This elemental Se is thought to come from re-condensation of Se vapour in the chamber. The Raman spectroscopy analysis performed showed that after the chemical etchings procedures applied, no contribution from secondary phases was detected. Also, a Raman micro-mapping study was applied to the films, depicting homogeneous distributions of the signals, which are signs of high crystallinity and homogeneity of the CZTSe absorber.

Finally, absorbers made from co-electrodeposited precursor films selenized with optimized RTP recipe developed in this Thesis were completed to solar cell devices. The best device reached a promising 5.2% with no roll-over effect. This is twice as much as previously obtained at IREC with electrodeposited absorbers and conventional thermal annealing. It shows the versatility and applicability of the newly developed RTP process for different precursors and opens new horizons for industrially viable earth-abundant thin film PV technologies.
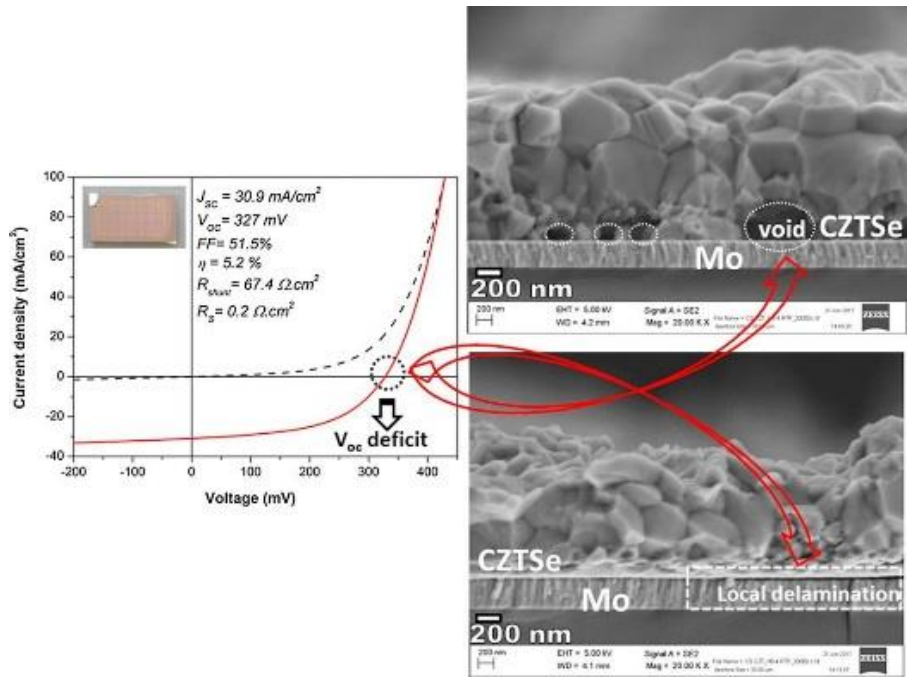
Figure 5.8 I-V curves of champion cell summarizing the main causes for its V_{oc} deficit.

Chapter 6

Conclusions and Outlook

6   Conclusions and Outlook

The first objective of this present Thesis was to develop, establish and optimize a RTP annealing process for the synthesis of CZTSe absorbers in the IREC's baseline. Special focus has been set on the obtainment of the fastest possible RTP annealing process without compromising its later efficiency, achieving remarkable values up to 8.3% for a CZTSe device submitted to an annealing process which lasts only 12 minutes. This is one of the highest efficiency for such a fast reaction so far. The second objective consisted in a comprehensive analysis of the reaction kinetics during the selenization process as a function of processing conditions and in comparison with slow standard slow processes developed for conventional tube furnaces. Finally, the technology transfer of the stablished RTP process to another set of precursor layers by co-electrodeposition was tested successfully. Most of the results of this thesis have been already published as research articles in high impact peer-reviewed journals or are in process to be published.

In the first part of this thesis, previously established baselines for conventional tubular furnaces at IREC were presented and the key points contrasted to RTP processing. It was demonstrated that a two-step temperature profile of the annealing process was necessary in order to properly control the homogenization of the selenization and to obtain uniform absorbers. The optimized two-step RTP process stablished at IREC through this thesis consists of a first stage at 400 $^{\circ}$C at 1 mbar that lasts for 3 minutes, using a 180 $^{\circ}$C/min ramp and a second stage at 500 $^{\circ}$C at 900 mbar that lasts in this case for 5 minutes, employing a 60 $^{\circ}$C/min ramp.

After technological process optimization, the question of how the reaction kinetics and phase formation pathways are influenced by the dynamics of the annealing procedure appeared. In order to do so, a break-off experiment where the process was interrupted at different times of the annealing protocol was implemented. It has been proven that the high vapour pressures obtained with RTP have a strong impact on the formation pathways of the kesterite absorber. In the RTP case, a competition between two mechanisms was found, one driven by binary metal selenide compounds and a second one driven by the ternary Cu-Sn-Se and Zn-Se compounds. While the selenium is already completely incorporated into the absorber after the first annealing step, the necessity of the second annealing step also came clear. In order to obtain high quality absorbers and efficient solar cells, the crystal quality still needs to be enhanced with the second annealing step.

The next part of this thesis, has provided evidences that the kesterite formation pathway critically depends on the chalcogen availability. It has been studied how to drive the formation mechanism with the chalcogen availability to a formation pathway based on the ternary compound Cu_2SnSe_3, which possesses a lower risk of secondary phases. A comprehensive analysis was carried with a combined kinetic and phase analysis for slow and fast ramping conditions. These studies confirmed that the formation pathways depend on the chalcogen availability and for medium-low chalcogen availabilities ($1x10^{-3} \leq [Se] \leq 1x10^{-2}$ g/cm^3) the kesterite is formed through a pseudo-zero order kinetic reaction, with a constant equal to $k_0 = (1.9 \pm 0.2) x10^{-2}$ s^{-1} and a $t_{1/2}$ = 37 s, which evolves to a first-order reaction when annealing times are long enough. On the other hand, when the chalcogen availability is increased to medium-high conditions the kesterite formation reaction follows a first-order type, with a kinetic constant about $k_1 = (2.9 \pm 0.4) x10^{-2}$ s^{-1}, and a $t_{1/2}$ = 24 s. Therefore, we were able to prove that the chalcogen availability allows to change the kesterite formation pathway. However, we could also show that the formation of binary compounds cannot be completely eliminated, but only

be diminished until marginal extents. Moreover, it has also been demonstrated that the sulfurization process is a slower process than the selenization.

In the last part of the Thesis, the reliability and feasibility of the stablished RTP process has been tested. In order to do so, the RTP annealing process was extended to precursors synthesized by other techniques, in this case co-electrodeposited Cu-Sn-Zn metals. This co-electrodeposited precursor layers consisted mainly on binary CuZn and CuSn alloys. After the RTP annealing was carried on, the composition of the films became the desired Cu-poor Zn-rich. The XRD analysis depicted sharp and intense peaks for the kesterite phase and also showed the appearance of elemental Se, most probable from condensation of Se reminiscences in the chamber. On the other hand, the Raman analysis proved that after the etching procedures no contribution from secondary phases was detected. Cross-sectional micrographs revealed voids located in the Mo/CZTSe interface. Finally, with this co-electrodeposition technique altogether with RTP processing, a very promising and remarkable efficiency of 5.2% was reached, being the highest result reported with this combination so far.

On the whole, the work presented in this Thesis provides extensive and comprehensive results about the development, establishment and optimization of an RTP annealing process for kesterite solar cells. The presented RTP annealing process has led to efficiencies which can withstand the comparison with the ones obtained by conventional furnace. It also has clarified how to drive the kesterite formation pathway by the chalcogen availability and the kinetics involved, providing a comprehensive picture of the kesterite synthesis and the turning knob that enable fine-tuning it. Overall, this has added a new kesterite production baseline option to IREC opening a wide new field of promising research possibilities.

In spite of the huge amount of research already performed in kesterite, there is still room for improvement. Research on kesterite has been mostly relying on what has been prior done to its "close cousin" CIGS, driving kesterite until nowadays where all the previous work has reached a limit, as can be observed in the no-improvement of the world record. Now is the time for kesterite to "leave the nest". New strategies specifically for kesterite must be addressed and RTP processing, thanks to all the interesting skills that provides such as: faster processing time, the possibility to achieve a high Se vapour since the early beginning of the annealing or its easy adaptation to work with process including several steps, appears as one of the most interesting paths for improving kesterite research. Paraphrasing Richard P. Feynman, *"there is plenty of room at the bottom",* several strategies must still be addressed to improve the now established kesterite RTP processing baseline at IREC, such as: alkali doping such as Li or Ge, study on the layers engineering by introducing new precursors containing bronze on its structure instead of pure Sn, studying the Na dynamics on the absorbers obtained by RTP, introducing an elemental Se layer prior to the annealing step, introducing anti-reflective coatings and metallic grids, start working on a band-gap grading and finally to follow modern trends in thin film research like the use of semi-transparent contacts.

References

7   References

(1)   Petit, J. R.; Jouzel, J.; Raynaud, D.; Barkov, N. I.; Barnola, J.-M.; Basile, I.; Bender, M.; Chappellaz, J.; Davisk, M.; Delaygue, G.; et al. *Climate and Atmospheric History of the Past 420,000 Years from the Vostok Ice Core, Antarctica The Recent Completion of Drilling at Vostok Station in East*; 1999.

(2)   *A History of Atmospheric CO_2 and Its Effects on Plants, Animals, and Ecosystems*; Baldwin, I. T., Caldwell, M. M., Heldmaier, G., Jackson, R. B., Lange, O. L., Mooney, H. A., Schulze, E.-D., Sommer, U., Ehleringer, J. R., Denise Dearing, M., et al., Eds.; Ecological Studies; Springer New York: New York, NY, 2005; Vol. 177.

(3)   UNFCCC. Report of the Conference of the Parties on Its Twenty-First Session. Part Two: Action Taken by the Conference of the Parties at Its Twenty-First Session. **2016**, *01194* (January), 36.

(4)   Ki-moon, B. *Climate Change Is the Defining Challenge of Our Age*.

(5)   Unidas, N. Acuerdo de París Naciones Unidas 2015. **2015**, 29.

(6)   EC. Green Paper - A 2030 Framework for Climate and Energy Policies COM(2013). **2013**, 1–16.

(7)   *World Energy Statistics 2018*; World Energy Statistics; OECD, 2018.

(8)   IRENA. Renewable Energy Highlights. **2017**, No. July, 1–2.

(9)   Gaetan, M.; Sinead, O.; Manoel, R. Global Market Outlook. *EPIA - Eur. Photovolt. Ind. Assoc.* **2018**, 60.

(10)   Sichao, K. Chinese Photovoltaic Market and Industry Outlook (Part 1). **2010**, No. April.

(11)   PV Module Index https://www.pv-magazine.com/features/investors/module-price-index/.

(12)   By Delphi234 - Own work, CC0, https://commons. wikimedia. org/w/index. php?curid=4038765. Swanson's Law.

(13)   Self-consumption the cornerstone of the new PV revolution https://www.pv-magazine.com/press-releases/self-consumption-the-cornerstone-of-the-pv-revolution/.

(14)   Ralon, P. Global Renewable Energy Cost Trends. **2018**, 27.

(15)   Muñoz, S. G. Advanced Strategies for High Efficiency Kesterite Thin Film Solar Cells. **2018**, No. January.

(16)   Yaroshevsky, A. A. Abundances of Chemical Elements in the Earth's Crust. *Geochemistry Int.* **2006**, *44* (1), 48–55.

(17)   Si PV research https://www.energy.gov/eere/solar/crystalline-silicon-photovoltaics-research.

(18)   Ise, F. *PHOTOVOLTAICS REPORT*.

(19)   Smith, D. D.; Cousins, P.; Westerberg, S.; Jesus-Tabajonda, R. De; Aniero, G.; Shen, Y.-C. Toward the Practical Limits of Silicon Solar Cells. *IEEE J. Photovoltaics* **2014**, *4* (6), 1465–1469.

(20)   Rühle, S. Tabulated Values of the Shockley–Queisser Limit for Single Junction Solar Cells. *Sol. Energy* **2016**, *130*, 139–147.

(21)   Green, M. A.; Hishikawa, Y.; Dunlop, E. D.; Levi, D. H.; Hohl-Ebinger, J.; Yoshita, M.; Ho-Baillie, A. W. Y. Solar Cell Efficiency Tables (Version 53). *Prog. Photovoltaics Res. Appl.* **2019**, *27* (1), 3–12.

(22)   Green, M. A. Recent Developments in Photovoltaics. *Sol. Energy* **2004**, *76* (1–3), 3–8.

(23)   Schock, H. W. *Thin Film Photovoltaics*; 1996; Vol. 92.

(24)   Chopra, K. L.; Paulson, P. D.; Dutta, V. Thin-Film Solar Cells: An Overview. *Prog. Photovoltaics Res. Appl.* **2004**, *12* (23), 69–92.

(25)   Arno smets. Solar Energy- The Physics and Engineering of Photovoltaic Conversion. **1970**, *13* (April), 1970.

(26)   CdTe info https://www.energy.gov/eere/solar/cadmium-telluride.

(27)   The Lowdown on the Safety of First Solar's CdTe Thin Film https://www.greentechmedia.com/articles/read/how-safe-is-first-solars-cdte-thin-film#gs.2w44dn.

(28)   Fthenakis, V. M.; Moskowitz, P. D. Photovoltaics: Environmental, Health and Safety Issues and Perspectives. *Prog. Photovoltaics Res. Appl.* **2000**, *8* (1), 27–38.

(29)   Phipps, G.; Mikolajczak, C.; Guckes, T. *Indium and Gallium: Long-Term Supply*.

(30)   Andersson, B. A. Materials Availability for Large-Scale Thin-Film Photovoltaics. In *Prog. Photovolt: Res. Appl.*; 2000; Vol. 8, pp 61–76.

(31)   Green, M. A. Estimates of Te and in Prices from Direct Mining of Known Ores. *Prog. Photovoltaics Res. Appl.* **2009**, *17* (5), 347–359.

(32)   Annual PV production share by technology https://www.industrial-lasers.com/articles/print/volume-33/issue-2/features/solar-manufacturing-moves-into-the-100-gw-plus-era.html.

(33)   Shockley, W.; Queisser, H. J. Detailed Balance Limit of Efficiency of P-n Junction Solar Cells. *J. Appl. Phys.* **1961**, *32* (3), 510–519.

(34)   Yamaguchi, M.; Takamoto, T.; Araki, K. Super High-Efficiency Multi-Junction and Concentrator Solar Cells. *Sol. Energy Mater. Sol. Cells* **2006**, *90* (18–19), 3068–3077.

(35)   Wang, D.; Wright, M.; Elumalai, N. K.; Uddin, A. Stability of Perovskite Solar Cells. *Sol. Energy Mater. Sol. Cells* **2016**, *147*, 255–275.

(36)   NREL. Best Research-Cell Efficiencies Chart. *Best Res. Effic. Chart* **2019**, 1.

(37)   Chapin, D. M.; Fuller, C. S.; Pearson, G. L. A New Silicon P-n Junction Photocell for Converting Solar Radiation into Electrical Power. *J. Appl. Phys.* **1954**, *25* (5), 676–677.

(38)   Katagiri, H.; Sasaguchi, N.; Hando, S.; Hoshino, S.; Ohashi, J.; Yokota, T. *Preparation Films by and Evaluation of Cu2ZnSnS4 Thin Sulfurization of E-B Evaporated Precursors*; 1997; Vol. 49.

(39)   Scopus. Kesterite citations https://www.scopus.com (accessed Sep 19, 2019).

(40)   Ito, Kentaro, T. N. *Electrical and Optical Properties of Stannite-Type Quaternary Semiconductor Thin Films*; 1988; Vol. 27.

(41) Katagiri, H.; Jimbo, K.; Yamada, S.; Kamimura, T.; Maw, W. S.; Fukano, T.; Ito, T.; Motohiro, T. Enhanced Conversion Efficiencies of Cu_2ZnSnS_4 -Based Thin Film Solar Cells by Using Preferential Etching Technique. *Appl. Phys. Express* **2008**, *1*, 041201.

(42) Jimbo, K.; Kimura, R.; Kamimura, T.; Yamada, S.; Maw, W. S.; Araki, H.; Oishi, K.; Katagiri, H. Cu_2ZnSnS_4-Type Thin Film Solar Cells Using Abundant Materials. *Thin Solid Films* **2007**, *515* (15), 5997–5999.

(43) Todorov, T. K.; Reuter, K. B.; Mitzi, D. B. High-Efficiency Solar Cell with Earth-Abundant Liquid-Processed Absorber. *Adv. Mater.* **2010**, *22* (20), E156–E159.

(44) Barkhouse, D. A. R.; Gunawan, O.; Gokmen, T.; Todorov, T. K.; Mitzi, D. B. Device Characteristics of a 10.1% Hydrazine-Processed $Cu_2ZnSn(Se,S)_4$ Solar Cell. *Prog. Photovoltaics Res. Appl.* **2012**, *20* (1), 6–11.

(45) Wang, W.; Winkler, M. T.; Gunawan, O.; Gokmen, T.; Todorov, T. K.; Zhu, Y.; Mitzi, D. B. Device Characteristics of CZTSSe Thin-Film Solar Cells with 12.6% Efficiency. *Adv. Energy Mater.* **2014**, *4* (7), 1301465.

(46) Seol, J.; Lee, S.; Lee, J.; Nam, H.; Kim, K. Electrical and Optical Properties of CuZnSnS Thin Films Prepared by Rf Magnetron Sputtering Process. *Sol. Energy Mater. Sol. Cells* **2003**, *75* (1–2), 155–162.

(47) He, J.; Sun, L.; Chen, S.; Chen, Y.; Yang, P.; Chu, J. Composition Dependence of Structure and Optical Properties of $Cu_2ZnSn(S,Se)_4$ Solid Solutions: An Experimental Study. *J. Alloys Compd.* **2012**, *511* (1), 129–132.

(48) Ahn, S.; Jung, S.; Gwak, J.; Cho, A.; Shin, K.; Yoon, K.; Park, D.; Cheong, H.; Yun, J. H. Determination of Band Gap Energy (Eg) of $Cu_2ZnSnSe_4$ Thin Films: On the Discrepancies of Reported Band Gap Values. *Appl. Phys. Lett.* **2010**, *97* (2), 021905.

(49) Ford, G. M.; Guo, Q.; Agrawal, R.; Hillhouse, H. W. Earth Abundant Element $Cu_2Zn(Sn_{1-x}Ge_x)S_4$ Nanocrystals for Tunable Band Gap Solar Cells: 6.8% Efficient Device Fabrication. *Chem. Mater.* **2011**, *23* (10), 2626–2629.

(50) Xiao, Z.-Y.; Li, Y.-F.; Yao, B.; Deng, R.; Ding, Z.-H.; Wu, T.; Yang, G.; Li, C.-R.; Dong, Z.-Y.; Liu, L.; et al. Bandgap Engineering of $Cu_2Cd_xZn_{1-x}SnS_4$ Alloy for Photovoltaic Applications: A Complementary Experimental and First-Principles Study. *J. Appl. Phys.* **2013**, *114* (18), 183506.

(51) Hages, C. J.; Koeper, M. J.; Agrawal, R. Optoelectronic and Material Properties of Nanocrystal-Based CZTSe Absorbers with Ag-Alloying. *Sol. Energy Mater. Sol. Cells* **2016**, *145*, 342–348.

(52) Lafond, A.; Guillot-Deudon, C.; Vidal, J.; Paris, M.; La, C.; Jobic, S. Substitution of Li for Cu in Cu_2ZnSnS_4 : Toward Wide Band Gap Absorbers with Low Cation Disorder for Thin Film Solar Cells. *Inorg. Chem.* **2017**, *56* (5), 2712–2721.

(53) Becerril-Romero, I.; Acebo, L.; Oliva, F.; Izquierdo-Roca, V.; López-Marino, S.; Espíndola-Rodríguez, M.; Neuschitzer, M.; Sánchez, Y.; Placidi, M.; Pérez-Rodríguez, A.; et al. CZTSe Solar Cells Developed on Polymer Substrates: Effects of Low-Temperature Processing. *Prog. Photovoltaics Res. Appl.* **2018**, *26* (1), 55–68.

(54) López-Marino, S.; Sánchez, Y.; Espíndola-Rodríguez, M.; Alcobé, X.; Xie, H.; Neuschitzer, M.; Becerril, I.; Giraldo, S.; Dimitrievska, M.; Placidi, M.; et al. Alkali Doping Strategies for Flexible and Light-Weight Cu 2 ZnSnSe 4 Solar Cells. *J. Mater. Chem. A* **2016**, *4* (5), 1895–1907.

(55) Becerril-Romero, I.; Giraldo, S.; López-Marino, S.; Placidi, M.; Sánchez, Y.; Sylla, D.; Pérez-Rodríguez, A.; Saucedo, E.; Pistor, P. Vitreous Enamel as Sodium Source for Efficient Kesterite Solar Cells on Commercial Ceramic Tiles. *Sol. Energy Mater. Sol. Cells* **2016**, *154*, 11–17.

(56) Kim, J.; Hiroi, H.; Todorov, T. K.; Gunawan, O.; Kuwahara, M.; Gokmen, T.; Nair, D.; Hopstaken, M.; Shin, B.; Lee, Y. S.; et al. High Efficiency Cu$_2$ZnSn(S,Se)$_4$ Solar Cells by Applying a Double In 2 S 3 /CdS Emitter. *Adv. Mater.* **2014**, *26* (44), 7427–7431.

(57) Lee, Y. S.; Gershon, T.; Gunawan, O.; Todorov, T. K.; Gokmen, T.; Virgus, Y.; Guha, S. Cu 2 ZnSnSe 4 Thin-Film Solar Cells by Thermal Co-Evaporation with 11.6% Efficiency and Improved Minority Carrier Diffusion Length. *Adv. Energy Mater.* **2015**, *5* (7), 1401372.

(58) Oueslati, S.; Brammertz, G.; Buffière, M.; ElAnzeery, H.; Touayar, O.; Köble, C.; Bekaert, J.; Meuris, M.; Poortmans, J. Physical and Electrical Characterization of High-Performance Cu$_2$ZnSnSe$_4$ Based Thin Film Solar Cells. *Thin Solid Films* **2015**, *582*, 224–228.

(59) Li, J.; Wang, H.; Wu, L.; Chen, C.; Zhou, Z.; Liu, F.; Sun, Y.; Han, J.; Zhang, Y. Growth of Cu 2 ZnSnSe 4 Film under Controllable Se Vapor Composition and Impact of Low Cu Content on Solar Cell Efficiency. *ACS Appl. Mater. Interfaces* **2016**, *8* (16), 10283–10292.

(60) Choi, S. G.; Kim, T. J.; Hwang, S. Y.; Li, J.; Persson, C.; Kim, Y. D.; Wei, S.-H.; Repins, I. L. Temperature Dependent Band-Gap Energy for Cu$_2$ZnSnSe$_4$: A Spectroscopic Ellipsometric Study. *Sol. Energy Mater. Sol. Cells* **2014**, *130*, 375–379.

(61) Tampo, H.; Min Kim, K.; Kim, S.; Shibata, H.; Niki, S. Improvement of Minority Carrier Lifetime and Conversion Efficiency by Na Incorporation in Cu$_2$ZnSnSe$_4$ Solar Cells ARTICLES YOU MAY BE INTERESTED IN. *J. Appl. Phys* **2017**, *122*, 23106.

(62) Andres, C.; Haass, S. G.; Romanyuk, Y. E.; Tiwari, A. N. 9.4% Efficient Cu$_2$ZnSnSe$_4$ Solar Cells from Co-Sputtered Elemental Metal Precursor and Rapid Thermal Annealing. *Thin Solid Films* **2017**, *633*, 141–145.

(63) Hages, C. J.; Carter, N. J.; Agrawal, R. Generalized Quantum Efficiency Analysis for Non-Ideal Solar Cells: Case of Cu$_2$ZnSnSe$_4$. *J. Appl. Phys.* **2016**, *119* (1), 014505.

(64) Giraldo, S.; Neuschitzer, M.; Thersleff, T.; López-Marino, S.; Sánchez, Y.; Xie, H.; Colina, M.; Placidi, M.; Pistor, P.; Izquierdo-Roca, V.; et al. Large Efficiency Improvement in Cu 2 ZnSnSe 4 Solar Cells by Introducing a Superficial Ge Nanolayer. *Adv. Energy Mater.* **2015**, *5* (21), 1501070.

(65) Giraldo, S.; Thersleff, T.; Larramona, G.; Neuschitzer, M.; Pistor, P.; Leifer, K.; Pérez-Rodríguez, A.; Moisan, C.; Dennler, G.; Saucedo, E. Cu$_2$ZnSnSe$_4$ Solar Cells with 10.6% Efficiency through Innovative Absorber Engineering with Ge Superficial Nanolayer. *Prog. Photovoltaics Res. Appl.* **2016**, *24* (10), 1359–1367.

(66) Giraldo, S.; Saucedo, E.; Neuschitzer, M.; Oliva, F.; Placidi, M.; Alcobé, X.; Izquierdo-Roca, V.; Kim, S.; Tampo, H.; Shibata, H.; et al. How Small Amounts of Ge Modify the Formation Pathways and Crystallization of Kesterites. *Energy Environ. Sci.* **2018**, *11* (3), 582–593.

(67) Xin, H.; Vorpahl, S. M.; Collord, A. D.; Braly, I. L.; Uhl, A. R.; Krueger, B. W.; Ginger, D. S.; Hillhouse, H. W. Lithium-Doping Inverts the Nanoscale Electric Field at the Grain Boundaries in Cu$_2$ZnSn(S,Se)$_4$ and Increases Photovoltaic Efficiency. *Phys. Chem. Chem. Phys.* **2015**, *17* (37), 23859–23866.

(68)   Hiroi, H.; Sakai, N.; Iwata, Y.; Kato, T.; Sugimoto, H. Impact of Buffer Layer on Kesterite Solar Cells. In *2015 IEEE 42nd Photovoltaic Specialist Conference (PVSC)*; IEEE, 2015; pp 1–4.

(69)   Haass, S. G.; Andres, C.; Figi, R.; Schreiner, C.; Bürki, M.; Romanyuk, Y. E.; Tiwari, A. N. Complex Interplay between Absorber Composition and Alkali Doping in High-Efficiency Kesterite Solar Cells. *Adv. Energy Mater.* **2018**, *8* (4), 1701760.

(70)   Bourdais, S.; Choné, C.; Delatouche, B.; Jacob, A.; Larramona, G.; Moisan, C.; Lafond, A.; Donatini, F.; Rey, G.; Siebentritt, S.; et al. Is the Cu/Zn Disorder the Main Culprit for the Voltage Deficit in Kesterite Solar Cells? *Adv. Energy Mater.* **2016**, *6* (12), 1502276.

(71)   Schnabel, T.; Abzieher, T.; Friedlmeier, T. M.; Ahlswede, E. Solution-Based Preparation of $Cu_2ZnSn(S,Se)_4$ for Solar Cells—Comparison of SnSe 2 and Elemental Se as Chalcogen Source. *IEEE J. Photovoltaics* **2015**, *5* (2), 670–675.

(72)   Wu, S.-H.; Chang, C.-W.; Chen, H.-J.; Shih, C.-F.; Wang, Y.-Y.; Li, C.-C.; Chan, S.-W. High-Efficiency $Cu_2ZnSn(S,Se)_4$ Solar Cells Fabricated through a Low-Cost Solution Process and a Two-Step Heat Treatment. *Prog. Photovoltaics Res. Appl.* **2017**, *25* (1), 58–66.

(73)   Kim, S.; Kim, K. M.; Tampo, H.; Shibata, H.; Niki, S. Improvement of Voltage Deficit of Ge-Incorporated Kesterite Solar Cell with 12.3% Conversion Efficiency. *Appl. Phys. Express* **2016**, *9* (10), 102301.

(74)   Jiang, F.; Ikeda, S.; Harada, T.; Matsumura, M. Pure Sulfide Cu_2ZnSnS_4 Thin Film Solar Cells Fabricated by Preheating an Electrodeposited Metallic Stack. *Adv. Energy Mater.* **2014**, *4* (7), 1301381.

(75)   Vauche, L.; Risch, L.; Sánchez, Y.; Dimitrievska, M.; Pasquinelli, M.; Goislard de Monsabert, T.; Grand, P.-P.; Jaime-Ferrer, S.; Saucedo, E. 8.2% Pure Selenide Kesterite Thin-Film Solar Cells from Large-Area Electrodeposited Precursors. *Prog. Photovoltaics Res. Appl.* **2016**, *24* (1), 38–51.

(76)   Espindola-Rodriguez, M.; Sylla, D.; Sánchez, Y.; Oliva, F.; Grini, S.; Neuschitzer, M.; Vines, L.; Izquierdo-Roca, V.; Saucedo, E.; Placidi, M. Bifacial Kesterite Solar Cells on FTO Substrates. *ACS Sustain. Chem. Eng.* **2017**, *5* (12), 11516–11524.

(77)   Hallt, S. R.; Szyma, J. T.; Stewart, J. M. *KESTERITE, $Cu_2(Zn,Fe)SnS_4$, AND STANNITE, $Cu2(FeZn)SnS4$, STRUCTURALLY SIMILAR BUT DISTINCT MINERALS*; 1978.

(78)   Nakamura, S.; Maeda, T.; Wada, T. Phase Stability and Electronic Structure of In-Free Photovoltaic Materials: $Cu_2ZnSiSe_4$, $Cu_2ZnGeSe_4$, and $Cu_2ZnSnSe_4$. *Jpn. J. Appl. Phys.* **2010**, *49* (12), 121203.

(79)   Camps, I.; Coutinho, J.; Mir, M.; Cunha, A. F. da; Rayson, M. J.; Briddon, P. R. Elastic and Optical Properties of $Cu_2ZnSn(Se_xS_{1-x})_4$ Alloys: Density Functional Calculations. *Semicond. Sci. Technol.* **2012**, *27* (11), 115001.

(80)   Zhang, Y.; Sun, X.; Zhang, P.; Yuan, X.; Huang, F.; Zhang, W. Structural Properties and Quasiparticle Band Structures of Cu-Based Quaternary Semiconductors for Photovoltaic Applications. *J. Appl. Phys.* **2012**, *111* (6), 063709.

(81)   Schorr, S. The Crystal Structure of Kesterite Type Compounds: A Neutron and X-Ray Diffraction Study. *Sol. Energy Mater. Sol. Cells* **2011**, *95* (6), 1482–1488.

(82)   Schorr, S.; Hoebler, H.-J.; Tovar, M. A Neutron Diffraction Study of the Stannite-Kesterite Solid Solution Series. *Eur. J. Mineral.* **2007**, *19* (1), 65–73.

(83)   Nam, D.; Kim, J.; Lee, J.-U.; Nagaoka, A.; Yoshino, K.; Cha, W.; Kim, H.; Hwang, I. C.; Yoon, K. B.; Cheong, H. Polarized Raman Spectroscopy of Cu-Poor and Zn-Rich Single-Crystal $Cu_2ZnSnSe_4$. *Appl. Phys. Lett.* **2014**, *105* (17), 173903.

(84)   Persson, C. Electronic and Optical Properties of Cu_2ZnSnS_4 and $Cu_2ZnSnSe_4$. *J. Appl. Phys.* **2010**, *107* (5), 053710.

(85)   Paris, M.; Choubrac, L.; Lafond, A.; Guillot-Deudon, C.; Jobic, S. Solid-State NMR and Raman Spectroscopy To Address the Local Structure of Defects and the Tricky Issue of the Cu/Zn Disorder in Cu-Poor, Zn-Rich CZTS Materials. *Inorg. Chem.* **2014**, *53* (16), 8646–8653.

(86)   Kobayashi, T.; Jimbo, K.; Tsuchida, K.; Shinoda, S.; Oyanagi, T.; Katagiri, H. Investigation of Cu_2ZnSnS_4 -Based Thin Film Solar Cells Using Abundant Materials. *Jpn. J. Appl. Phys.* **2005**, *44* (1B), 783–787.

(87)   Fairbrother, A.; Dimitrievska, M.; Sánchez, Y.; Izquierdo-Roca, V.; Pérez-Rodríguez, A.; Saucedo, E. Compositional Paradigms in Multinary Compound Systems for Photovoltaic Applications: A Case Study of Kesterites. *J. Mater. Chem. A* **2015**, *3* (18), 9451–9455.

(88)   Shin, D.; Saparov, B.; Mitzi, D. B. Defect Engineering in Multinary Earth-Abundant Chalcogenide Photovoltaic Materials. *Adv. Energy Mater.* **2017**, *7* (11), 1602366.

(89)   Gokmen, T.; Gunawan, O.; Todorov, T. K.; Mitzi, D. B. Band Tailing and Efficiency Limitation in Kesterite Solar Cells. *Appl. Phys. Lett.* **2013**, *103* (10), 103506.

(90)   Chen, S.; Walsh, A.; Gong, X.-G.; Wei, S.-H. Classification of Lattice Defects in the Kesterite Cu_2ZnSnS_4 and $Cu_2ZnSnSe_4$ Earth-Abundant Solar Cell Absorbers. *Adv. Mater.* **2013**, *25* (11), 1522–1539.

(91)   Biswas, K.; Lany, S.; Zunger, A. The Electronic Consequences of Multivalent Elements in Inorganic Solar Absorbers: Multivalency of Sn in Cu_2ZnSnS_4. *Appl. Phys. Lett.* **2010**, *96* (20), 201902.

(92)   López-Marino, S.; Sánchez, Y.; Placidi, M.; Fairbrother, A.; Espindola-Rodríguez, M.; Fontané, X.; Izquierdo-Roca, V.; López-García, J.; Calvo-Barrio, L.; Pérez-Rodríguez, A.; et al. ZnSe Etching of Zn-Rich $Cu_2ZnSnSe_4$: An Oxidation Route for Improved Solar-Cell Efficiency. *Chem. - A Eur. J.* **2013**, *19* (44), 14814–14822.

(93)   Xie, H.; Sánchez, Y.; López-Marino, S.; Espíndola-Rodríguez, M.; Neuschitzer, M.; Sylla, D.; Fairbrother, A.; Izquierdo-Roca, V.; Pérez-Rodríguez, A.; Saucedo, E. Impact of Sn(S,Se) Secondary Phases in $Cu_2ZnSn(S,Se)_4$ Solar Cells: A Chemical Route for Their Selective Removal and Absorber Surface Passivation. *ACS Appl. Mater. Interfaces* **2014**, *6* (15), 12744–12751.

(94)   PVD advantages https://www.azom.com/article.aspx?ArticleID=1558.

(95)   A, K. Synthesis and Characterization of Titanium Titanium Nitride Thin Films Prepared by DC Reactive Magnetron Sputtering with Supported Discharge, Anna University, 2017.

(96)   Sputtering mechanism http://www.utdallas.edu/~goeckner/plasma_sci_class/Plasma Process 3 Types.pd.

(97)   Seah, M. P.; Nunney, T. S. Sputtering Yields of Compounds Using Argon Ions. *J. Phys. D. Appl. Phys.* **2010**, *43* (25), 253001.

(98)   Sputtering yield https://www.azom.com/article.aspx?ArticleID=1558.

(99)   Phys.sinica.edu.tw. Thin film deposition review https://www.phys.sinica.edu.tw.

(100)   Magnetron sputtering http://www.angstromsciences.com/technology/sputtering.htm.

(101)   Concept, A. Thin film coating by magnetron sputtering http://www.alliance-concept.com.

(102)   ANNEAL-SYS. RTP - System.

(103)   ANNEAL-SYS https://www.annealsys.com/products/annealsys-products/rtp-and-rtcvd/as-one.html.

(104)   Maeda, K.; Tanaka, K.; Fukui, Y.; Uchiki, H. Dependence on Annealing Temperature of Properties of Cu_2ZnSnS_4 Thin Films Prepared by Sol–Gel Sulfurization Method. *Jpn. J. Appl. Phys.* **2011**, *50*, 01BE10.

(105)   Hong, S.; Kim, C.; Park, S.-C.; Rhee, I.; Kim, D.-H.; Kang, J.-K. Characteristics of $Cu_2ZnSnSe_4$ Film Formed by Using Co-Sputtered Precursors and Selenization. *Mol. Cryst. Liq. Cryst.* **2012**, *565* (1), 147–152.

(106)   Wibowo, R. A.; Yoo, H.; Hölzing, A.; Lechner, R.; Jost, S.; Palm, J.; Gowtham, M.; Louis, B.; Hock, R. A Study of Kesterite $Cu_2ZnSn(Se,S)_4$ Formation from Sputtered Cu–Zn–Sn Metal Precursors by Rapid Thermal Processing Sulfo-Selenization of the Metal Thin Films. *Thin Solid Films* **2013**, *535* (1), 57–61.

(107)   Romanyuk, Y. E.; Fella, C. M.; Uhl, A. R.; Werner, M.; Tiwari, A. N.; Schnabel, T.; Ahlswede, E. Recent Trends in Direct Solution Coating of Kesterite Absorber Layers in Solar Cells. *Sol. Energy Mater. Sol. Cells* **2013**, *119*, 181–189.

(108)   Lechner, R.; Jost, S.; Palm, J.; Gowtham, M.; Sorin, F.; Louis, B.; Yoo, H.; Wibowo, R. A.; Hock, R. $Cu_2ZnSn(S,Se)_4$ Solar Cells Processed by Rapid Thermal Processing of Stacked Elemental Layer Precursors. *Thin Solid Films* **2013**, *535* (1), 5–9.

(109)   Schnabel, T.; Löw, M.; Ahlswede, E. Vacuum-Free Preparation of 7.5% Efficient $Cu_2ZnSn(S,Se)_4$ Solar Cells Based on Metal Salt Precursors. *Sol. Energy Mater. Sol. Cells* **2013**, *117*, 324–328.

(110)   Sousa, M. G.; da Cunha, A. F.; Fernandes, P. A.; Teixeira, J. P.; Sousa, R. A.; Leitão, J. P. Effect of Rapid Thermal Processing Conditions on the Properties of Cu_2ZnSnS_4 Thin Films and Solar Cell Performance. *Sol. Energy Mater. Sol. Cells* **2014**, *126*, 101–106.

(111)   Fairbrother, A.; Fourdrinier, L.; Fontané, X.; Izquierdo-Roca, V.; Dimitrievska, M.; Pérez-Rodríguez, A.; Saucedo, E. Precursor Stack Ordering Effects in $Cu_2ZnSnSe_4$ Thin Films Prepared by Rapid Thermal Processing. *J. Phys. Chem. C* **2014**, *118* (31), 17291–17298.

(112)   Künecke, U.; Hetzner, C.; Möckel, S.; Yoo, H.; Hock, R.; Wellmann, P. Characterization of Kesterite Thin Films Fabricated by Rapid Thermal Processing of Stacked Elemental Layers Using Spatially Resolved Cathodoluminescence. *Thin Solid Films* **2015**, *582*, 387–391.

(113)   Majula, L.; Mlyuka, N. R.; Samiji, M. E.; Bryce, R. S.; Kim, D. Y.; Kim, S. H.; Lee, H. J.; Choi, H. J. Spin-Coated Kesterite CZTS Thin Films for Photovoltaic Applications. *J. Korean Phys. Soc.* **2015**, *67* (6), 1078–1081.

(114)   Hwang, S.; Kim, D.-H.; Son, D.-H.; Yang, K.-J.; Nam, D.; Cheong, H.; Kang, J.-K.; In, S. Effects of a Pre-Annealing Treatment (PAT) on $Cu_2ZnSn(S,Se)_4$ Thin Films Prepared by Rapid Thermal Processing (RTP) Selenization. *Sol. Energy Mater. Sol. Cells* **2015**, *143*, 218–225.

(115) Haass, S. G.; Diethelm, M.; Werner, M.; Bissig, B.; Romanyuk, Y. E.; Tiwari, A. N. 11.2% Efficient Solution Processed Kesterite Solar Cell with a Low Voltage Deficit. *Adv. Energy Mater.* **2015**, *5* (18), 1500712.

(116) Scopus. RTP Kesterite research articles https://www.scopus.com (accessed Sep 19, 2019).

(117) Hages, C. J.; Koeper, M. J.; Miskin, C. K.; Brew, K. W.; Agrawal, R. Controlled Grain Growth for High Performance Nanoparticle-Based Kesterite Solar Cells. *Chem. Mater.* **2016**, *28* (21), 7703–7714.

(118) Bishop, D.; Gershon, T.; Lee, Y. S.; Antunez, P.; Mankad, R.; Singh, S.; Gunawan, O.; Haight, R. Optimization of Silver-Alloying for Improved Photovoltaic Properties of CZTSSe. In *2016 IEEE 43rd Photovoltaic Specialists Conference (PVSC)*; IEEE, 2016; Vol. 2016-Novem, pp 0173–0178.

(119) Pani, B.; Pillai, S.; Singh, U. P. Kesterite Based Thin Film Absorber Layers from Ball Milled Precursors. *J. Mater. Sci. Mater. Electron.* **2016**, *27* (12), 12412–12417.

(120) Yang, K.-J.; Son, D.-H.; Sung, S.-J.; Sim, J.-H.; Kim, Y.-I.; Park, S.-N.; Jeon, D.-H.; Kim, J.; Hwang, D.-K.; Jeon, C.-W.; et al. A Band-Gap-Graded CZTSSe Solar Cell with 12.3% Efficiency. *J. Mater. Chem. A* **2016**, *4* (26), 10151–10158.

(121) Qi, Y.; Tian, Q.; Meng, Y.; Kou, D.; Zhou, Z.; Zhou, W.; Wu, S. Elemental Precursor Solution Processed $(Cu_{1-x}Ag_x)_2ZnSn(S,Se)_4$ Photovoltaic Devices with over 10% Efficiency. *ACS Appl. Mater. Interfaces* **2017**, *9* (25), 21243–21250.

(122) Yan, C.; Sun, K.; Liu, F.; Huang, J.; Zhou, F.; Hao, X. Boost Voc of Pure Sulfide Kesterite Solar Cell via a Double CZTS Layer Stacks. *Sol. Energy Mater. Sol. Cells* **2017**, *160*, 7–11.

(123) Giraldo, S.; Jehl, Z.; Placidi, M.; Izquierdo-Roca, V.; Pérez-Rodríguez, A.; Saucedo, E. Progress and Perspectives of Thin Film Kesterite Photovoltaic Technology: A Critical Review. *Adv. Mater.* **2019**, 1806692.

(124) Haass, S. G.; Diethelm, M.; Andres, C.; Romanyuk, Y. E.; Tiwari, A. N. Potassium Post Deposition Treatment of Solution-Processed Kesterite Solar Cells. *Thin Solid Films* **2017**, *633*, 131–134.

(125) Andres, C.; Schwarz, T.; Haass, S. G.; Weiss, T. P.; Carron, R.; Caballero, R.; Figi, R.; Schreiner, C.; Bürki, M.; Tiwari, A. N.; et al. Decoupling of Optoelectronic Properties from Morphological Changes in Sodium Treated Kesterite Thin Film Solar Cells. *Sol. Energy* **2018**, *175*, 94–100.

(126) Cabas-Vidani, A.; Haass, S. G.; Andres, C.; Caballero, R.; Figi, R.; Schreiner, C.; Márquez, J. A.; Hages, C.; Unold, T.; Bleiner, D.; et al. High-Efficiency $(Li_xCu_{1-x})_2ZnSn(S,Se)_4$ Kesterite Solar Cells with Lithium Alloying. *Adv. Energy Mater.* **2018**, *8* (34), 1801191.

(127) Min, X.; Shi, J.; Guo, L.; Yu, Q.; Zhang, P.; Tian, Q.; Li, D.; Luo, Y.; Wu, H.; Meng, Q.; et al. Regulation of Zn/Sn Ratio in Kesterite Absorbers to Boost 10% Efficiency of $Cu_2ZnSn(S, Se)_4$ Solar Cells. *Chinese Phys. B* **2018**, *27* (1), 016402.

(128) Andres, C.; Haass, S. G.; Romanyuk, Y. E.; Tiwari, A. N. 9.4% Efficient $Cu_2ZnSnSe_4$ Solar Cells from Co-Sputtered Elemental Metal Precursor and Rapid Thermal Annealing. *Thin Solid Films* **2017**, *633*, 141–145.

(129) Qi, Y.-F.; Kou, D.-X.; Zhou, W.-H.; Zhou, Z.-J.; Tian, Q.-W.; Meng, Y.-N.; Liu, X.-S.; Du, Z.; Wu, S.-X. Engineering of Interface Band Bending and Defects Elimination via Ag-Graded

Active Layer for Efficient (Cu,Ag)$_2$ZnSn(S,Se)$_4$ Solar Cells. *Energy Environ. Sci.* **2017**, 0–29.

(130) Fairbrother, A.; Fontané, X.; Izquierdo-Roca, V.; Placidi, M.; Sylla, D.; Espindola-Rodríguez, M.; Lopez-Marino, S.; Andrés-Pulgarín, F.; Vigil-Galán, O.; Perez-Rodriguez, A.; et al. Secondary Phase Formation in Zn-Rich Cu$_2$ZnSnSe$_4$- Based Solar Cells Annealed in Low Pressure and Temperature Conditions. *Prog. Photovoltaics Res. Appl.* **2014**, *22*, 479–487.

(131) Fairbrother, A.; Fontané, X.; Izquierdo-Roca, V.; Espindola-Rodriguez, M.; Lõpez-Marino, S.; Placidi, M.; Lõpez-García, J.; Pérez-Rodríguez, A.; Saucedo, E. Single-Step Sulfo-Selenization Method to Synthesize Cu$_2$ZnSn(S$_y$Se$_{1-y}$)$_4$ Absorbers from Metallic Stack Precursors. *ChemPhysChem* **2013**, *14* (9), 1836–1843.

(132) Platzer-Björkman, C.; Scragg, J.; Flammersberger, H.; Kubart, T.; Edoff, M. Influence of Precursor Sulfur Content on Film Formation and Compositional Changes in Cu$_2$ZnSnS$_4$ Films and Solar Cells. *Sol. Energy Mater. Sol. Cells* **2012**, *98*, 110–117.

(133) Fairbrother, A.; Fontané, X.; Izquierdo-Roca, V.; Espíndola-Rodríguez, M.; López-Marino, S.; Placidi, M.; Calvo-Barrio, L.; Pérez-Rodríguez, A.; Saucedo, E. On the Formation Mechanisms of Zn-Rich Cu$_2$ZnSnS$_4$ Films Prepared by Sulfurization of Metallic Stacks. *Sol. Energy Mater. Sol. Cells* **2013**, *112*, 97–105.

(134) Redinger, A.; Berg, D. M.; Dale, P. J.; Siebentritt, S. The Consequences of Kesterite Equilibria for Efficient Solar Cells. *J. Am. Chem. Soc* **2011**, *133*, 3320–3323.

(135) Neuschitzer, M.; Sanchez, Y.; López-Marino, S.; Xie, H.; Fairbrother, A.; Placidi, M.; Haass, S.; Izquierdo-Roca, V.; Perez-Rodriguez, A.; Saucedo, E. Optimization of CdS Buffer Layer for High-Performance Cu$_2$ZnSnSe$_4$ Solar Cells and the Effects of Light Soaking: Elimination of Crossover and Red Kink. *Prog. Photovoltaics Res. Appl.* **2015**, *23* (11), 1660–1667.

(136) Hernández-Martínez, A.; Placidi, M.; Arqués, L.; Giraldo, S.; Sánchez, Y.; Izquierdo-Roca, V.; Pistor, P.; Valentini, M.; Malerba, C.; Saucedo, E. Insights into the Formation Pathways of Cu$_2$ZnSnSe$_4$ Using Rapid Thermal Processes. *ACS Appl. Energy Mater.* **2018**, *1* (5), 1981–1989.

(137) Redinger, A.; Hönes, K.; Fontané, X.; Izquierdo-Roca, V.; Saucedo, E.; Valle, N.; Pérez-Rodríguez, A.; Siebentritt, S. Detection of a ZnSe Secondary Phase in Coevaporated Cu2ZnSnSe4 Thin Films. *Appl. Phys. Lett.* **2011**, *98* (10), 101907.

(138) Juškėnas, R.; Niaura, G.; Mockus, Z.; Kanapeckaitė, S.; Giraitis, R.; Kondrotas, R.; Naujokaitis, A.; Stalnionis, G.; Pakštas, V.; Karpavičienė, V. XRD Studies of an Electrochemically Co-Deposited Cu–Zn–Sn Precursor and Formation of a Cu$_2$ZnSnSe$_4$ Absorber for Thin-Film Solar Cells. *J. Alloys Compd.* **2016**, *655*, 281–289.

(139) Xie, H.; Sánchez, Y.; López-Marino, S.; Espíndola-Rodríguez, M.; Neuschitzer, M.; Sylla, D.; Fairbrother, A.; Izquierdo-Roca, V.; Pérez-Rodríguez, A.; Saucedo, E. Impact of Sn(S,Se) Secondary Phases in Cu$_2$ZnSn(S,Se)$_4$ Solar Cells: A Chemical Route for Their Selective Removal and Absorber Surface Passivation. *ACS Appl. Mater. Interfaces* **2014**.

(140) Fontane, X.; Izquierdo-Roca, V.; Fairbrother, A.; Espindola-Rodriguez, M.; Lopez-Marino, S.; Placidi, M.; Jawhari, T.; Saucedo, E.; Perez-Rodriguez, A. Selective Detection of Secondary Phases in Cu$_2$ZnSn(S, Se)$_4$ Based Absorbers by Pre-Resonant Raman Spectroscopy. In *2013 IEEE 39th Photovoltaic Specialists Conference (PVSC)*; IEEE, 2013; pp 2581–2584.

(141) Rousset, J.; Tsin, F.; Guc, M.; Vidal, J.; Le Bris, A.; Thomere, A.; Izquierdo-Roca, V.; Lincot, D. Perchlorate-Induced Doping of Electrodeposited ZnO Films for Optoelectronic Applications. *J. Phys. Chem. C* **2016**, *120* (34), 18953–18962.

(142) F. Oliva, S. Giraldo, M. Dimitrievska, P. Pistor, A. Martinez-Perez, L. Calvo-Barrio, E. Saucedo, A Perez-Rodriguez, V. I.-R. Raman Scattering Assessment of Point Defects in Kesterite Semiconductors: UV Resonant Raman Characterization for Advanced Photovoltaics. *IEEE 44th Photovolt. Spec. Conf. (PVSC), Washington, DC, (accepted Press.* **2017**.

(143) Dimitrievska, M.; Xie, H.; Jackson, A. J.; Fontané, X.; Espíndola-Rodríguez, M.; Saucedo, E.; Pérez-Rodríguez, A.; Walsh, A.; Izquierdo-Roca, V. Resonant Raman Scattering of ZnS_xSe_{1-x} Solid Solutions: The Role of S and Se Electronic States. *Phys. Chem. Chem. Phys.* **2016**, *18* (11), 7632–7640.

(144) Fella, C. M.; Uhl, A. R.; Hammond, C.; Hermans, I.; Romanyuk, Y. E.; Tiwari, A. N. Formation Mechanism of $Cu_2ZnSnSe_4$ Absorber Layers during Selenization of Solution Deposited Metal Precursors. *J. Alloys Compd.* **2013**, *567*, 102–106.

(145) Bodeux, R.; Mollica, F.; Delbos, S. Growth of $Cu_2ZnSnSe_4$ by Cosputtering and Reactive Annealing Atmosphere. *Sol. Energy Mater. Sol. Cells* **2015**, *132*, 67–73.

(146) Hsu, W.-C.; Bob, B.; Yang, W.; Chung, C.-H.; Yang, Y. Reaction Pathways for the Formation of $Cu_2ZnSn(Se,S)_4$ Absorber Materials from Liquid-Phase Hydrazine-Based Precursor Inks. *Energy Environ. Sci.* **2012**, *5* (9), 8564.

(147) Fairbrother, A.; Fontané, X.; Izquierdo-Roca, V.; Espíndola-Rodríguez, M.; López-Marino, S.; Placidi, M.; Calvo-Barrio, L.; Pérez-Rodríguez, A.; Saucedo, E. On the Formation Mechanisms of Zn-Rich Cu_2ZnSnS_4 Films Prepared by Sulfurization of Metallic Stacks. *Sol. Energy Mater. Sol. Cells* **2013**, *112*, 97–105.

(148) Berg, D. M.; Crossay, A.; Guillot, J.; Izquierdo-Roca, V.; Pérez-Rodriguez, A.; Ahmed, S.; Deligianni, H.; Siebentritt, S.; Dale, P. J. Simplified Formation Process for Cu_2ZnSnS_4-Based Solar Cells. *Thin Solid Films* **2014**, *573*, 148–158.

(149) Rim Jung, H.; Wook Shin, S.; Gurav, K.; Suryawanshi, M.; Woo Hong, C.; Seung Yang, H.; Yong Lee, J.; Ha Moon, J.; Hyeok Kim, J. CERAMICS Phase Evolution of Cu_2ZnSnS_4 (CZTS) Kesterite Thin Films during the Sulfurization Process. *Ceram. Int.* **2015**, *41*, 13006–13011.

(150) Taskesen, T.; Neerken, J.; Schoneberg, J.; Pareek, D.; Steininger, V.; Parisi, J.; Gütay, L. Device Characteristics of an 11.4% CZTSe Solar Cell Fabricated from Sputtered Precursors. *Adv. Energy Mater.* **2018**, *8* (16), 1703295.

(151) Grini, S.; Ross, N.; Persson, C.; Platzer-Björkman, C.; Vines, L. Low Temperature Incorporation of Selenium in Cu_2ZnSnS_4: Diffusion and Nucleation. *Thin Solid Films* **2018**, *665*, 159–163.

(152) Englund, S.; Saini, N.; Platzer-Björkman, C. $Cu_2ZnSn(S,Se)_4$ from Annealing of Compound Co-Sputtered Precursors – Recent Results and Open Questions. *Sol. Energy* **2018**, *175*, 84–93.

(153) Ren, Y.; Ross, N.; Larsen, J. K.; Rudisch, K.; Scragg, J. J. S.; Platzer-Björkman, C. Evolution of Cu_2ZnSnS_4 during Non-Equilibrium Annealing with Quasi-in Situ Monitoring of Sulfur Partial Pressure. *Chem. Mater.* **2017**, *29* (8), 3713–3722.

(154) Fairbrother, A.; Fontané, X.; Izquierdo-Roca, V.; Espíndola-Rodríguez, M.; López-Marino,

S.; Placidi, M.; Calvo-Barrio, L.; Pérez-Rodríguez, A.; Saucedo, E. On the Formation Mechanisms of Zn-Rich Cu_2ZnSnS_4 Films Prepared by Sulfurization of Metallic Stacks. *Sol. Energy Mater. Sol. Cells* **2013**, *112*, 97–105.

(155) Scragg, J. J.; Ericson, T.; Kubart, T.; Edoff, M.; Platzer-Björkman, C. Chemical Insights into the Instability of Cu_2ZnSnS_4 Films during Annealing. *Chem. Mater.* **2011**, *23* (20), 4625–4633.

(156) Oikkonen, L. E.; Ganchenkova, M. G.; Seitsonen, A. P.; Nieminen, R. M. Formation, Migration, and Clustering of Point Defects in $CuInSe_2$ from First Principles. *J. Phys. Condens. Matter* **2014**, *26* (34), 345501.

(157) Zweschke, A.; Wellmann, P. J. Numerical Reactive Diffusion Modeling of Stacked Elemental Layer Rapid Thermal Annealed Chalcopyrite Absorber Layer Formation. *Thin Solid Films* **2015**, *582*, 397–400.

(158) Hsiang, H.-I.; Lu, L.-H.; Chang, Y.-L.; Ray, D.; Yen, F.-S. $CuInSe_2$ Nano-Crystallite Reaction Kinetics Using Solid State Reaction from Cu2Se and In2Se3 Powders. *J. Alloys Compd.* **2011**, *509* (24), 6950–6954.

(159) Kim, W. K.; Kim, S.; Payzant, E. A.; Speakman, S. A.; Yoon, S.; Kaczynski, R. M.; Acher, R. D.; Anderson, T. J.; Crisalle, O. D.; Li, S. S.; et al. Reaction Kinetics of α-$CuInSe_2$ Formation from an In_2Se_3/CuSe Bilayer Precursor Film. *J. Phys. Chem. Solids* **2005**, *66* (11), 1915–1919.

(160) Kim, W. K.; Payzant, E. A.; Kim, S.; Speakman, S. A.; Crisalle, O. D.; Anderson, T. J. Reaction Kinetics of $CuGaSe_2$ Formation from a GaSe/CuSe Bilayer Precursor Film. *J. Cryst. Growth* **2008**, *310* (12), 2987–2994.

(161) Selvaraj, M.; Venkatachalapathy, V.; Mayandi, J.; Karazhanov, S.; Pearce, J. M. Preparation of Meta-Stable Phases of Barium Titanate by Sol-Hydrothermal Method. *AIP Adv.* **2015**, *5* (11), 117119.

(162) Bodeux, R.; Mollica, F.; Delbos, S. Growth of $Cu_2ZnSnSe_4$ by Cosputtering and Reactive Annealing Atmosphere. *Sol. Energy Mater. Sol. Cells* **2015**, *132*, 67–73.

(163) Qu, Y.; Zoppi, G.; Beattie, N. S. Selenization Kinetics in $Cu_2ZnSn(S,Se)_4$ Solar Cells Prepared from Nanoparticle Inks. *Sol. Energy Mater. Sol. Cells* **2016**, *158*, 130–137.

(164) Weber, A.; Mainz, R.; Unold, T.; Schorr, S.; Schock, H.-W. In-Situ XRD on Formation Reactions of Cu_2ZnSnS_4 Thin Films. *Phys. status solidi* **2009**, *6* (5), 1245–1248.

(165) Xu, Z.; Sun, X.; Khaleel, M. A. A Generalized Kinetic Model for Heterogeneous Gas-Solid Reactions. *J. Chem. Phys.* **2012**, *137* (7), 074702.

(166) Soustelle, M. *An Introduction to Chemical Kinetics*; John Wiley & Sons, Inc: Hoboken, NJ, USA, 2011.

(167) von Bardeleben, H. J. Selenium Self-diffusion Study in the 1-3-6 2 Semiconductor: $CuInSe_2$. *J. Appl. Phys.* **1984**, *56* (2), 321–326.

(168) Ross, N.; Larsen, J.; Grini, S.; Vines, L.; Platzer-Björkman, C. Practical Limitations to Selenium Annealing of Compound Co-Sputtered Cu_2ZnSnS_4 as a Route to Achieving Sulfur-Selenium Graded Solar Cell Absorbers. *Thin Solid Films* **2017**, *623*, 110–115.

(169) Giraldo, S.; Kim, S.; Andrade-Arvizu, J. A.; Alcobé, X.; Malerba, C.; Valentini, M.; Tampo, H.; Shibata, H.; Izquierdo-Roca, V.; Pérez-Rodríguez, A.; et al. Study and Optimization of Alternative MBE-Deposited Metallic Precursors for Highly Efficient Kesterite CZTSe:Ge

Solar Cells. *Prog. Photovoltaics Res. Appl.* **2019**, No. April, 1–10.

(170) Panchenko, I.; Mueller, M.; Wiese, S.; Schindler, S.; Wolter, K.-J. Solidification Processes in the Sn-Rich Part of the SnCu System. In *2011 IEEE 61st Electronic Components and Technology Conference (ECTC)*; IEEE, 2011; pp 90–99.

(171) Valdés, M.; Hernández-Martinez, A.; Sánchez, Y.; Oliva, F.; Izquierdo-Roca, V.; Perez Rodriguez, A.; Saucedo, E. Cu$_2$ZnSnSe4 Based Solar Cells Combining Co-Electrodeposition and Rapid Thermal Processing. *Sol. Energy* **2018**, *173* (June), 955–963.

(172) Deligianni, H.; Ahmed, S.; Romankiw, L. T. The Next Frontier: Electrodeposition for Solar Cell Fabrication. *Interface Mag.* **2011**, *20* (2), 47–53.

(173) Colombara, D.; Crossay, A.; Vauche, L.; Jaime, S.; Arasimowicz, M.; Grand, P.-P.; Dale, P. J. Electrodeposition of Kesterite Thin Films for Photovoltaic Applications: Quo Vadis? *Phys. status solidi* **2015**, *212* (1), 88–102.

(174) Abermann, S. Non-Vacuum Processed next Generation Thin Film Photovoltaics: Towards Marketable Efficiency and Production of CZTS Based Solar Cells. *Sol. Energy* **2013**, *94*, 37–70.

(175) Ahmed, S.; Reuter, K. B.; Gunawan, O.; Guo, L.; Romankiw, L. T.; Deligianni, H. A High Efficiency Electrodeposited Cu$_2$ZnSnS$_4$ Solar Cell. *Adv. Energy Mater.* **2012**, *2* (2), 253–259.

(176) Scragg, J. J.; Berg, D. M.; Dale, P. J A 3.2% Efficient Kesterite Device from Electrodeposited Stacked Elemental Layers. *J. Electroanal. Chem.* **2010**, *646* (1–2), 52–59.

(177) Jiang, F.; Ikeda, S.; Harada, T.; Ide, A.; Mochihara, A.; Yoshino, K.; Matsumura, M. Fabrication of an Efficient Electrodeposited Cu$_2$ZnSnS$_4$ -Based Solar Cells with More than 6% Conversion Efficiency Using a Sprayed Ga-Doped ZnO Window Layer. *RSC Adv.* **2014**, *4* (46), 24351–24355.

(178) Lin, Y.; Ikeda, S.; Septina, W.; Kawasaki, Y.; Harada, T.; Matsumura, M. Mechanistic Aspects of Preheating Effects of Electrodeposited Metallic Precursors on Structural and Photovoltaic Properties of Cu$_2$ZnSnS$_4$ Thin Films. *Sol. Energy Mater. Sol. Cells* **2014**, *120*, 218–225.

(179) Guo, L.; Zhu, Y.; Gunawan, O.; Gokmen, T.; Deline, V. R.; Ahmed, S.; Romankiw, L. T.; Deligianni, H. Electrodeposited Cu$_2$ZnSnSe$_4$ Thin Film Solar Cell with 7% Power Conversion Efficiency. *Prog. Photovoltaics Res. Appl.* **2014**, *22* (1), 58–68.

(180) Gougaud, C.; Rai, D.; Delbos, S.; Chassaing, E.; Lincot, D. Electrochemical Studies of One-Step Electrodeposition of Cu-Sn-Zn Layers from Aqueous Electrolytes for Photovoltaic Applications. *J. Electrochem. Soc.* **2013**, *160* (10), D485–D494.

(181) Khalil, M. I.; Bernasconi, R.; Pedrazzetti, L.; Lucotti, A.; Donne, A. Le; Binetti, S.; Magagnin, L. Co-Electrodeposition of Metallic Precursors for the Fabrication of CZTSe Thin Films Solar Cells on Flexible Mo Foil. *J. Electrochem. Soc.* **2017**, *164* (6), D302–D306.

(182) Li, Y.; Yuan, T.; Jiang, L.; Su, Z.; Liu, F. Growth and Characterization of Cu$_2$ZnSnS$_4$ Photovoltaic Thin Films by Electrodeposition and Sulfurization. *J. Alloys Compd.* **2014**, *610*, 331–336.

(183) Kondrotas, R.; Juškėnas, R.; Naujokaitis, A.; Selskis, A.; Giraitis, R.; Mockus, Z.;

Kanapeckaitė, S.; Niaura, G.; Xie, H.; Sánchez, Y.; et al. Characterization of $Cu_2ZnSnSe_4$ Solar Cells Prepared from Electrochemically Co-Deposited Cu–Zn–Sn Alloy. *Sol. Energy Mater. Sol. Cells* **2015**, *132*, 21–28.

(184) Yeong Kim, G.; Jo, W.; Doo Lee, K.; Choi, H.-S.; Young Kim, J.; Shin, H.-Y.; Thi Thu Nguyen, T.; Yoon, S.; Soo Joo, B.; Gu, M.; et al. Optical and Surface Probe Investigation of Secondary Phases in Cu_2ZnSnS_4 Films Grown by Electrochemical Deposition. *Sol. Energy Mater. Sol. Cells* **2015**, *139*, 10–18.

(185) Jeon, J.-O.; Lee, K. D.; Seul Oh, L.; Seo, S.-W.; Lee, D.-K.; Kim, H.; Jeong, J.; Ko, M. J.; Kim, B.; Son, H. J.; et al. Highly Efficient Copper-Zinc-Tin-Selenide (CZTSe) Solar Cells by Electrodeposition. *ChemSusChem* **2014**, *7* (4), 1073–1077.

(186) Ge, J.; Yan, Y. Controllable Multinary Alloy Electrodeposition for Thin-Film Solar Cell Fabrication: A Case Study of Kesterite Cu_2ZnSnS_4. *iScience* **2018**, *1*, 55–71.

(187) Ge, J.; Jiang, J.; Yang, P.; Peng, C.; Huang, Z.; Zuo, S.; Yang, L.; Chu, J. A 5.5% Efficient Co-Electrodeposited $ZnO/CdS/Cu_2ZnSnS_4$/Mo Thin Film Solar Cell. *Sol. Energy Mater. Sol. Cells* **2014**, *125*, 20–26.

(188) Kondrotas, R.; Juškėnas, R.; Naujokaitis, A.; Selskis, A.; Giraitis, R.; Mockus, Z.; Kanapeckaitė, S.; Niaura, G.; Xie, H.; Sánchez, Y.; et al. Characterization of $Cu_2ZnSnSe_4$ Solar Cells Prepared from Electrochemically Co-Deposited Cu–Zn–Sn Alloy. *Sol. Energy Mater. Sol. Cells* **2015**, *132*, 21–28.

(189) Zhang, Y.; Liao, C.; Zong, K.; Wang, H.; Liu, J.; Jiang, T.; Han, J.; Liu, G.; Cui, L.; Ye, Q.; et al. $Cu_2ZnSnSe_4$ Thin Film Solar Cells Prepared by Rapid Thermal Annealing of Co-Electroplated Cu–Zn–Sn Precursors. *Sol. Energy* **2013**, *94*, 1–7.

(190) Valdés, M.; Di Iorio, Y.; Castañeda, K.; Marotti, R. E.; Vázquez, M. Cu_2ZnSnS_4 Thin Films Prepared by Sulfurization of Co-Electrodeposited Metallic Precursors. *J. Appl. Electrochem.* **2017**, *47* (6), 755–765.

(191) Schurr, R.; Hölzing, A.; Jost, S.; Hock, R.; Voβ, T.; Schulze, J.; Kirbs, A.; Ennaoui, A.; Lux-Steiner, M.; Weber, A.; et al. The Crystallisation of Cu_2ZnSnS_4 Thin Film Solar Cell Absorbers from Co-Electroplated Cu–Zn–Sn Precursors. *Thin Solid Films* **2009**, *517* (7), 2465–2468.

(192) Juškėnas, R.; Kanapeckaitė, S.; Karpavičienė, V.; Mockus, Z.; Pakštas, V.; Selskienė, A.; Giraitis, R.; Niaura, G. A Two-Step Approach for Electrochemical Deposition of Cu–Zn–Sn and Se Precursors for CZTSe Solar Cells. *Sol. Energy Mater. Sol. Cells* **2012**, *101*, 277–282.

(193) Hreid, T.; Li, J.; Zhang, Y.; Spratt, H. J.; Wang, H.; Will, G. Effects of Metal Ion Concentration on Electrodeposited CuZnSn Film and Its Application in Kesterite Cu_2ZnSnS_4 Solar Cells. *RSC Adv.* **2015**, *5* (80), 65114–65122.

(194) Wei, Y.; Zhuang, D.; Zhao, M.; Gong, Q.; Sun, R.; Zhang, L.; Lyu, X.; Peng, X.; Ren, G.; Wu, Y.; et al. Effects of Selenium Atmosphere on Grain Growth for CZTSe Absorbers Fabricated by Selenization of As-Sputtered Precursors. *J. Alloys Compd.* **2018**, *755*, 224–230.

(195) López-Marino, S.; Sánchez, Y.; Placidi, M.; Fairbrother, A.; Espindola-Rodríguez, M.; Fontané, X.; Izquierdo-Roca, V.; López-García, J.; Calvo-Barrio, L.; Pérez-Rodríguez, A.; et al. ZnSe Etching of Zn-Rich $Cu_2ZnSnSe_4$: An Oxidation Route for Improved Solar-Cell Efficiency. *Chem. - A Eur. J.* **2013**, *19* (44), 14814–14822.

(196) López-Marino, S.; Placidi, M.; Pérez-Tomás, A.; Llobet, J.; Izquierdo-Roca, V.; Fontané, X.; Fairbrother, A.; Espíndola-Rodríguez, M.; Sylla, D.; Pérez-Rodríguez, A.; et al. Inhibiting the Absorber/Mo-Back Contact Decomposition Reaction in $Cu_2ZnSnSe_4$ Solar Cells: The Role of a ZnO Intermediate Nanolayer. *J. Mater. Chem. A* **2013**, *1* (29), 8338.

(197) Márquez, J.; Stange, H.; Hages, C. J.; Schaefer, N.; Levcenko, S.; Giraldo, S.; Saucedo, E.; Schwarzburg, K.; Abou-Ras, D.; Redinger, A.; et al. Chemistry and Dynamics of Ge in Kesterite: Toward Band-Gap-Graded Absorbers. *Chem. Mater.* **2017**, *29* (21), 9399–9406.

(198) Unveroglu, B.; Zangari, G. Towards Phase Pure Kesterite CZTS Films via Cu-Zn-Sn Electrodeposition Followed by Sulfurization. *Electrochim. Acta* **2016**, *219*, 664–672.

(199) Malerba, C.; Valentini, M.; Azanza Ricardo, C. L.; Rinaldi, A.; Cappelletto, E.; Scardi, P.; Mittiga, A. Blistering in Cu_2ZnSnS_4 Thin Films: Correlation with Residual Stresses. *Mater. Des.* **2016**, *108*, 725–735.

(200) Larramona, G.; Bourdais, S.; Jacob, A.; Choné, C.; Muto, T.; Cuccaro, Y.; Delatouche, B.; Moisan, C.; Péré, D.; Dennler, G. Efficient Cu_2ZnSnS_4 Solar Cells Spray Coated from a Hydro-Alcoholic Colloid Synthesized by Instantaneous Reaction. *RSC Adv.* **2014**, *4* (28), 14655–14662.

(201) Todorov, T. K.; Tang, J.; Bag, S.; Gunawan, O.; Gokmen, T.; Zhu, Y.; Mitzi, D. B. Beyond 11% Effi Ciency: Characteristics of State-of-the-Art $Cu_2ZnSn(S,Se)_4$ Solar Cells. *Adv. Energy Mater.* **2013**, *3* (1), 34–38.

(202) Fontané, X.; Calvo-Barrio, L.; Izquierdo-Roca, V.; Saucedo, E.; Pérez-Rodriguez, A.; Morante, J. R.; Berg, D. M.; Dale, P. J.; Siebentritt, S. In-Depth Resolved Raman Scattering Analysis for the Identification of Secondary Phases: Characterization of Cu_2ZnSnS_4 Layers for Solar Cell Applications. *Appl. Phys. Lett.* **2011**, *98* (18), 181905.

(203) Oliva, F.; Kretzschmar, S.; Colombara, D.; Tombolato, S.; Ruiz, C. M.; Redinger, A.; Saucedo, E.; Broussillou, C.; de Monsabert, T. G.; Unold, T.; et al. Optical Methodology for Process Monitoring of Chalcopyrite Photovoltaic Technologies: Application to Low Cost $Cu(In,Ga)(S,Se)_2$ Electrodeposition Based Processes. *Sol. Energy Mater. Sol. Cells* **2016**, *158*, 168–183.

(204) Dimitrievska, M.; Giraldo, S.; Pistor, P.; Saucedo, E.; Perez-Rodriguez, A.; Izquierdo-Roca, V. Raman Scattering Analysis of the Surface Chemistry of Kesterites: Impact of Post-Deposition Annealing and Cu/Zn Reordering on Solar Cell Performance. *Sol. Energy Mater. Sol. Cells* **2016**, *157*, 462–467.

(205) Guc, M.; Levcenko, S.; Izquierdo-Roca, V.; Fontané, X.; Arushanov, E.; Pérez-Rodríguez, A. Polarized Raman Scattering Analysis of $Cu_2ZnSnSe_4$ and $Cu_2ZnGeSe_4$ Single Crystals. *J. Appl. Phys.* **2013**, *114* (19), 193514.

(206) Dimitrievska, M.; Fairbrother, A.; Fontané, X.; Jawhari, T.; Izquierdo-Roca, V.; Saucedo, E.; Pérez-Rodríguez, A. Multiwavelength Excitation Raman Scattering Study of Polycrystalline Kesterite Cu_2ZnSnS_4 Thin Films. *Appl. Phys. Lett.* **2014**, *104* (2), 021901.

(207) Ben Messaoud, K.; Buffière, M.; Brammertz, G.; ElAnzeery, H.; Oueslati, S.; Hamon, J.; Kniknie, B. J.; Meuris, M.; Amlouk, M.; Poortmans, J. Impact of the Cd^{2+} Treatment on the Electrical Properties of $Cu_2ZnSnSe_4$ and $Cu(In,Ga)Se_2$ Solar Cells. *Prog. Photovoltaics Res. Appl.* **2015**, *23* (11), 1608–1620.

(208) Khadka, D. B.; Kim, S.; Kim, J. Effects of Ge Alloying on Device Characteristics of

Kesterite-Based CZTSSe Thin Film Solar Cells. *J. Phys. Chem. C* **2016**, *120* (8), 4251–4258.

Appendix

8 Appendix

8.1 Section 1- Appendix related to Chapter 3
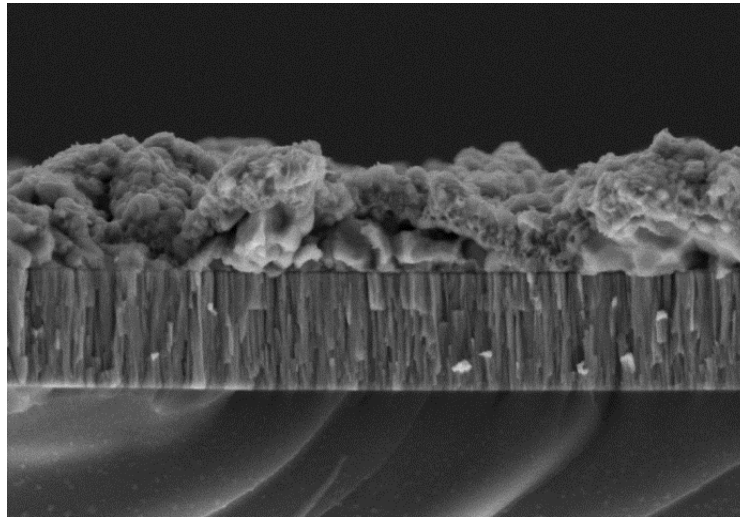
Figure A1. Cross sectional image of a kesterite precursor obtained via Sputtering.
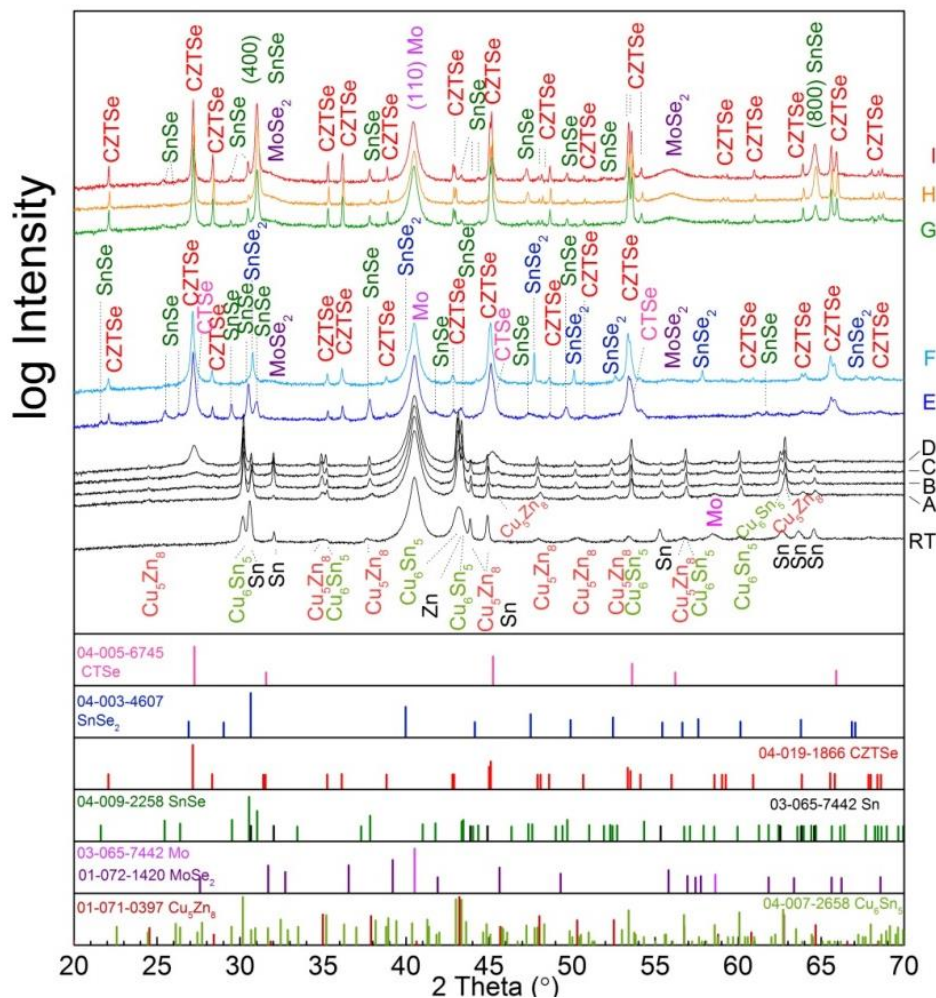
Figure A2. Samples studied in Chapter 3 ranging from RT up to 500 °C
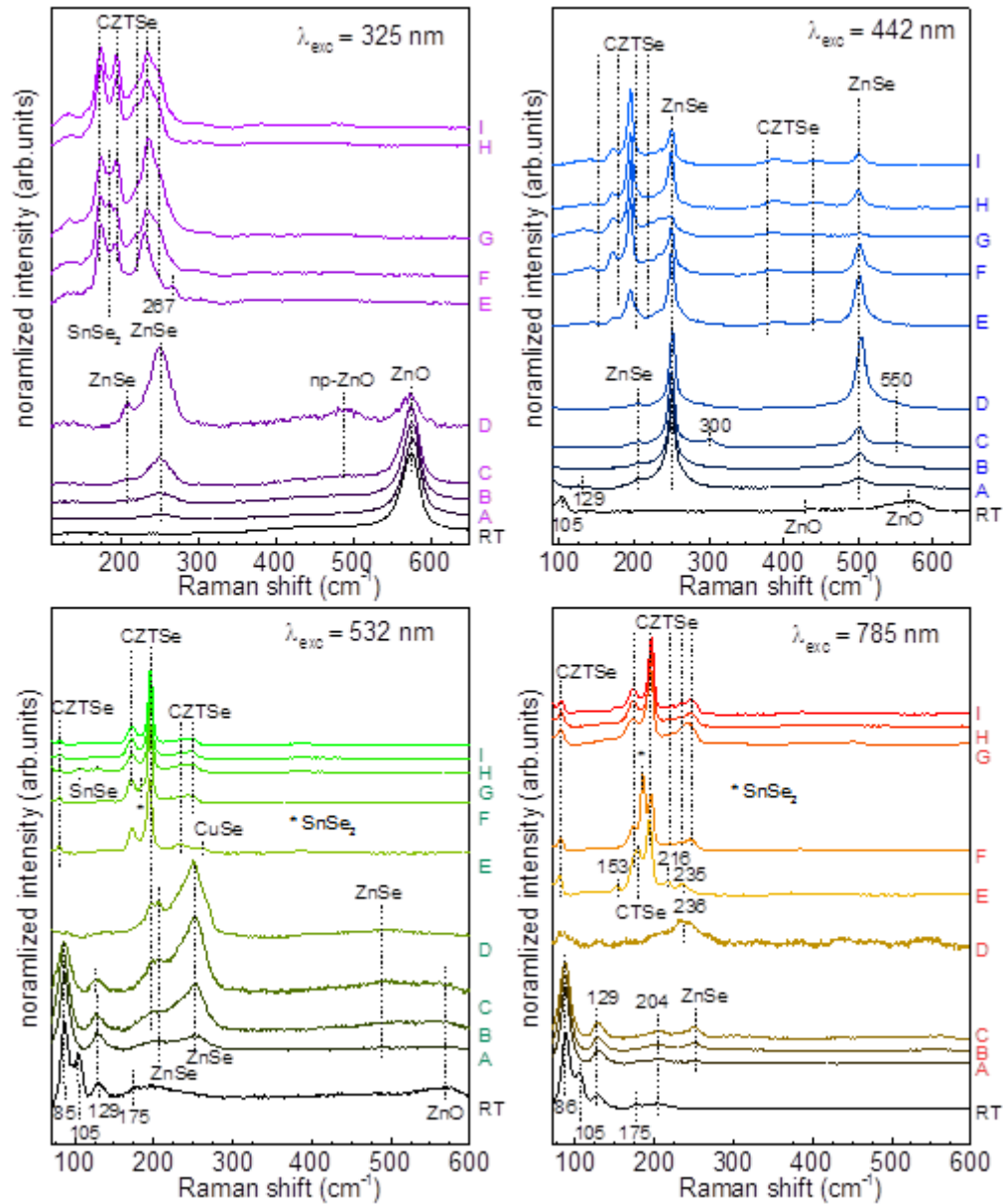
Figure A3. Raman analysis of the samples studied in Chapter3 from RT up to 500 °C under 4 different excitation wavelengths (325 nm, 442 nm, 532 nm and 785 nm)
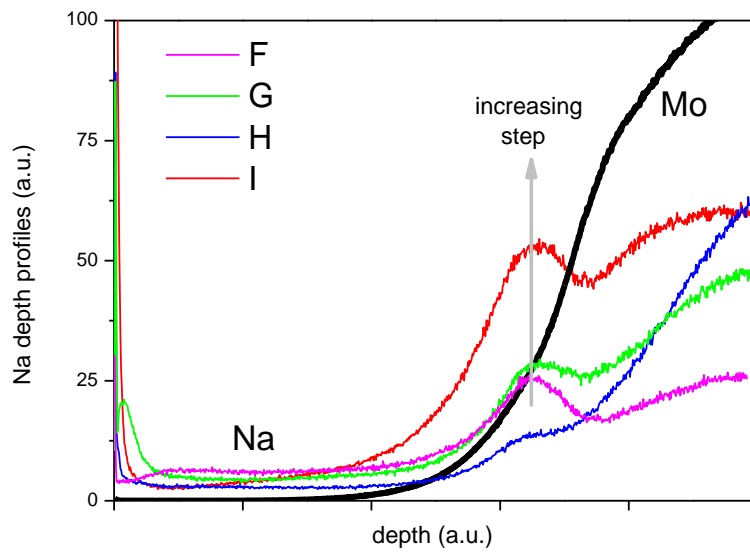
Figure A4. Sodium depth-profile evolution through RTP processing

It can be observed that the typical sodium segregation at the interfaces (CZTSe/Mo and CZTSe/air) increases with increasing process steps. Sample H shows a sodium profile out of trend, probably due to an anomalous sodium content in the glass substrate.

8.2 Section 2- Appendix related to Chapter 4

Complete SEM analysis of samples prepared under different chalcogen availabilities and EDX of selected samples
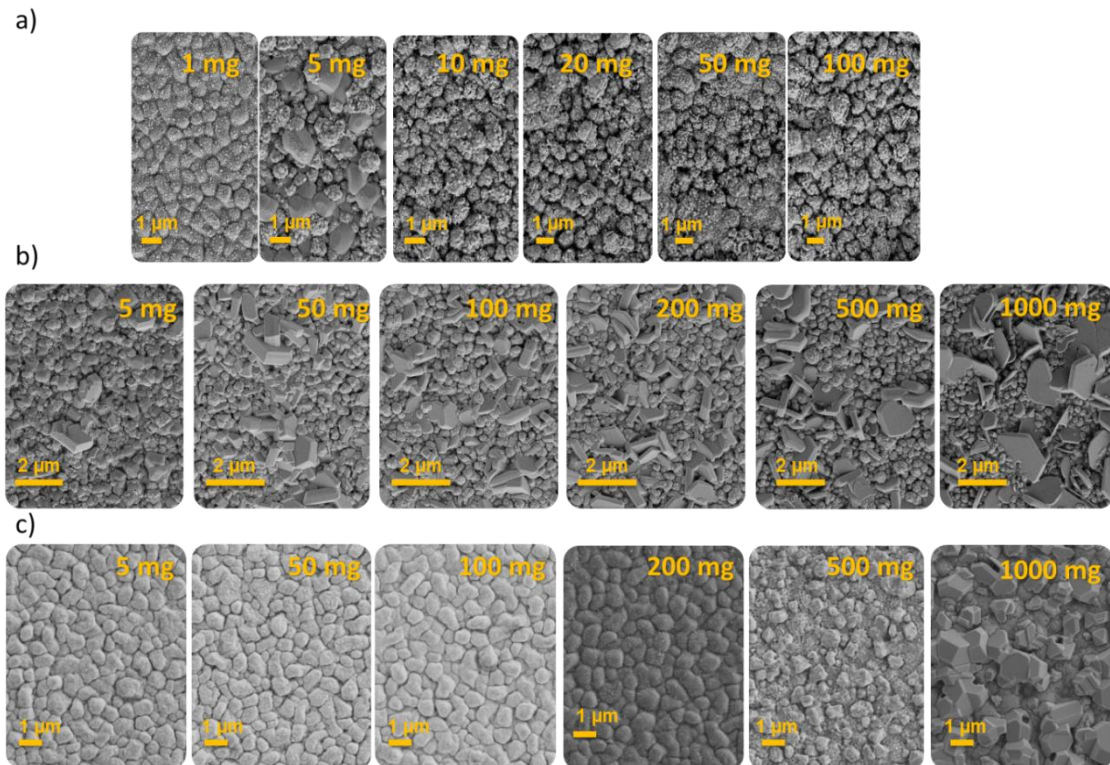
Figure A5. a) Top view SEM images of absorbers generated by RTP at different Se vapor pressures. b) Top view SEM images of absorbers generated by CTP at different Se vapor pressures. c) Top view SEM images of absorbers generated by CTP at different S vapor pressures.
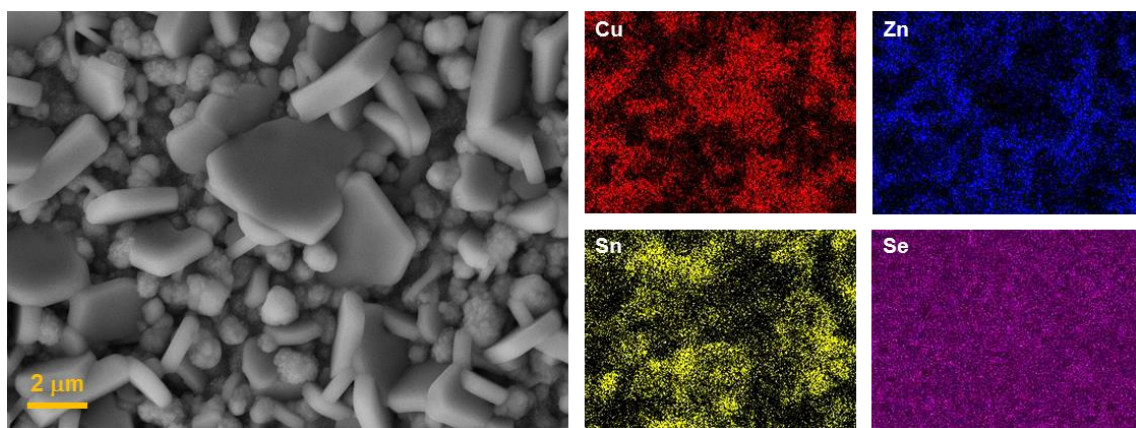
Figure A6. SEM top-view image of sample prepared under high chalcogen availability (low ramp), and corresponding elemental distribution.

Table A1. Equations employed for the order fitting

Kinetic Order	General Equation	Fitted Equation
Zero Order	$-\dfrac{d[Se]}{dt} = k$	$[Se]_t = [Se]_{t_0} - kt$
First Order	$-\dfrac{d[Se]}{dt} = k[Se]$	$\ln\left[\dfrac{[Se]_t}{[Se]_{t_0}}\right] = -kt$
Second Order	$-\dfrac{d[Se]}{dt} = k[Se]^2$	$\dfrac{1}{[Se]} = \dfrac{1}{[Se]_{t_0}} + kt$

- The [Se] has been extracted from the XRF measurements
- t_0: has been considered by [Se] at 250 ⁰C

Fast ramping selenization-
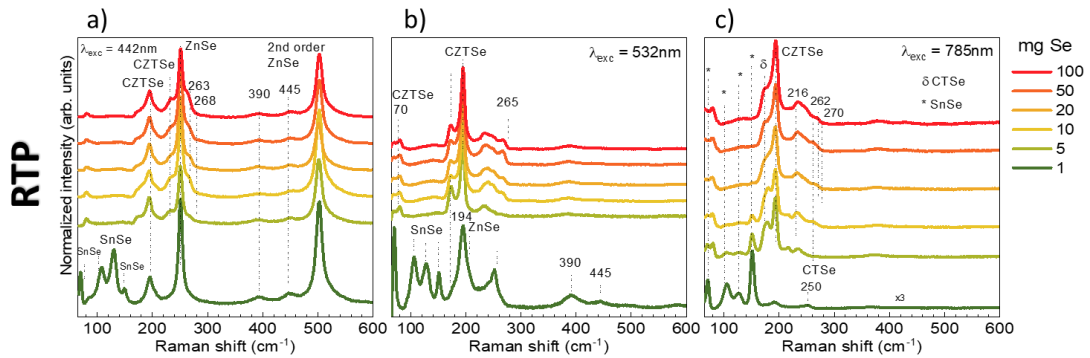
Figure A7. Raman spectra for absorbers prepared using fast ramping process under different chalcogen availabilities, with the following excitation wavelengths: 442 nm (a), 532nm (b) and 785nm (c).
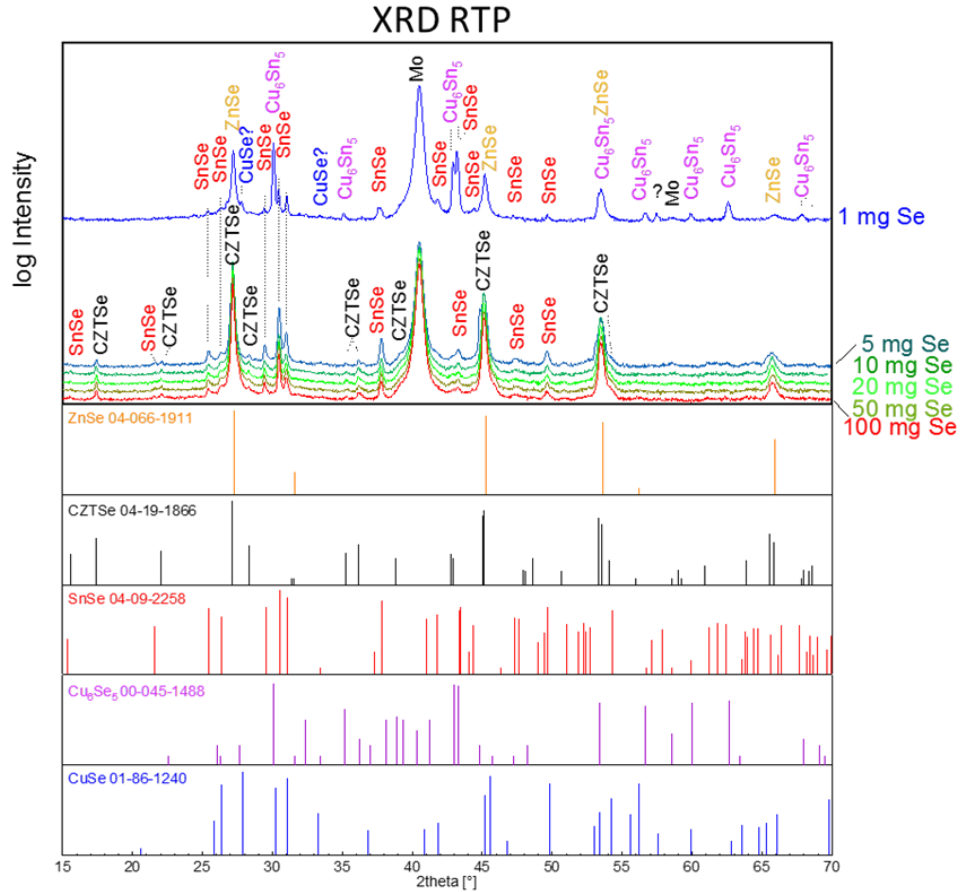
Figure A8. XRD diffractogram of the different samples studied varying the ChA with fast ramping.

Slow ramping selenization-
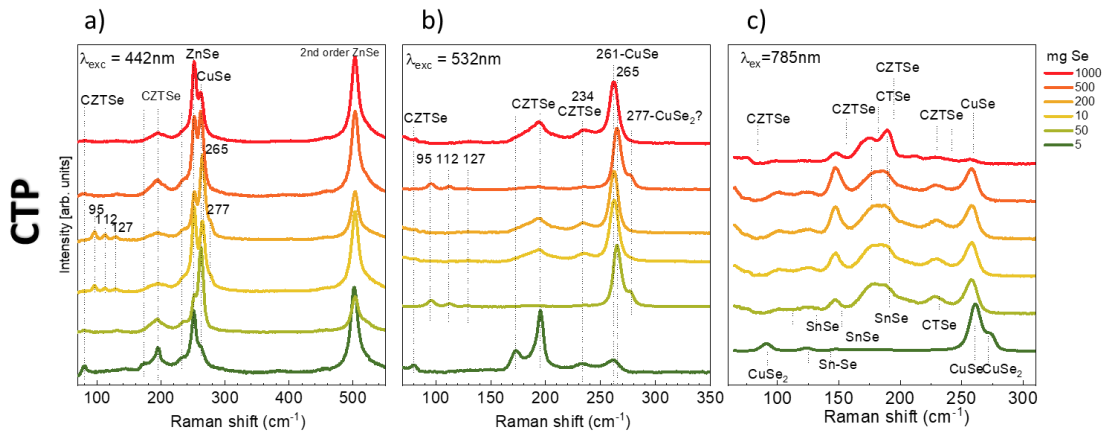
Figure A9. Raman spectra for absorbers prepared using slow ramping process under different chalcogen availabilities, with the following excitation wavelengths: 442 nm (a), 532nm (b) and 785nm (c).
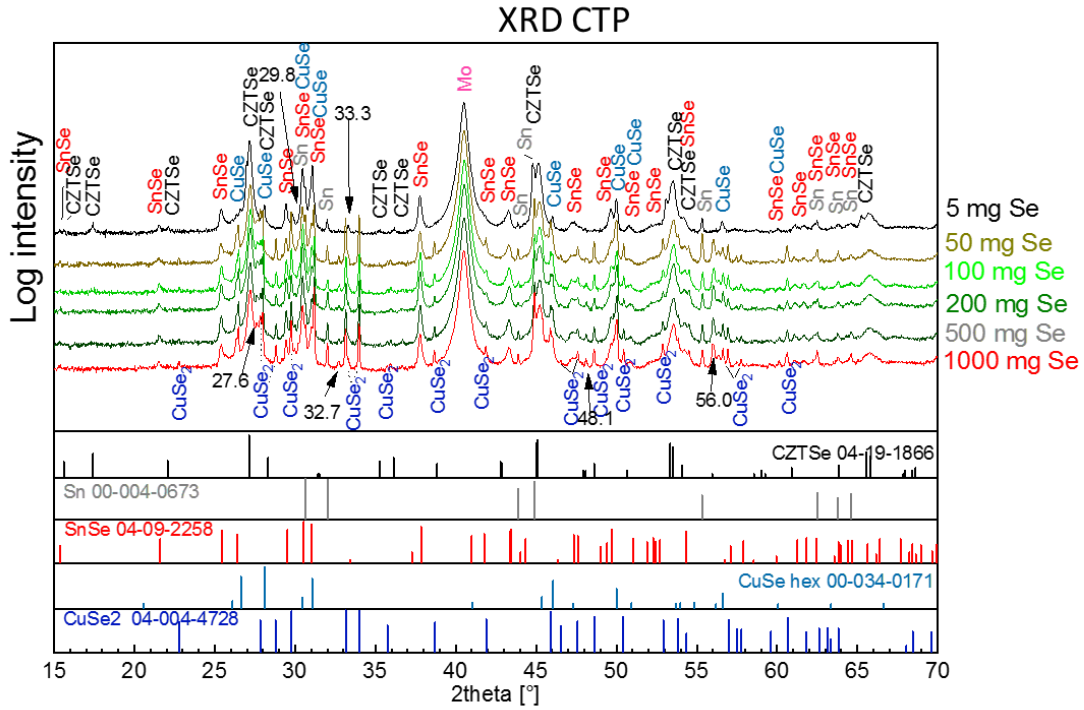
Figure A10. XRD diffractogram of the different samples studied varying the ChA with fast ramping.

Slow ramping sulfurization-

Figure A11. Raman spectra for absorbers prepared using slow ramping process under different chalcogen availabilities, with the following excitation wavelengths: 325 nm (a), 532nm (b) and 785nm (c).

Figure A12. XRD diffractogram of the different samples studied varying the ChA with fast ramping. * relates to unidentified peaks.

Insights into the Formation Pathways of Cu₂ZnSnSe₄ Using Rapid Thermal Processes
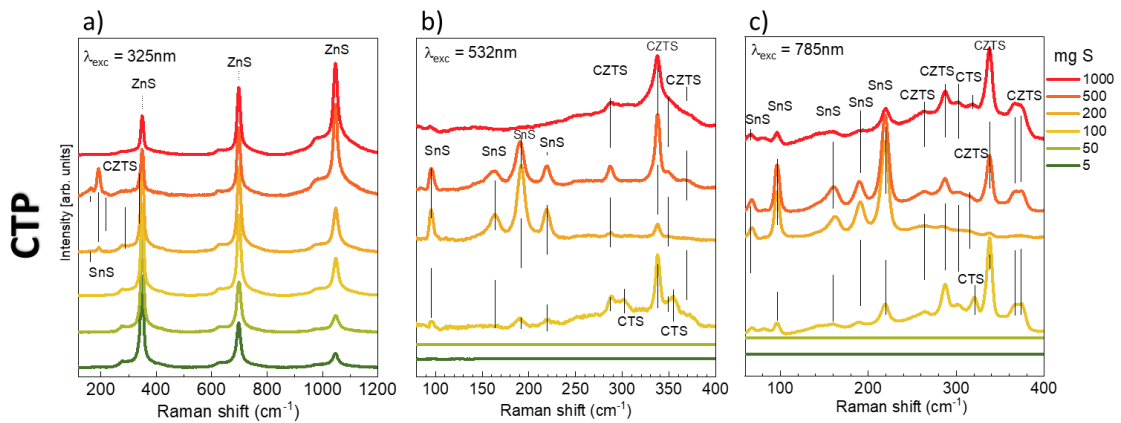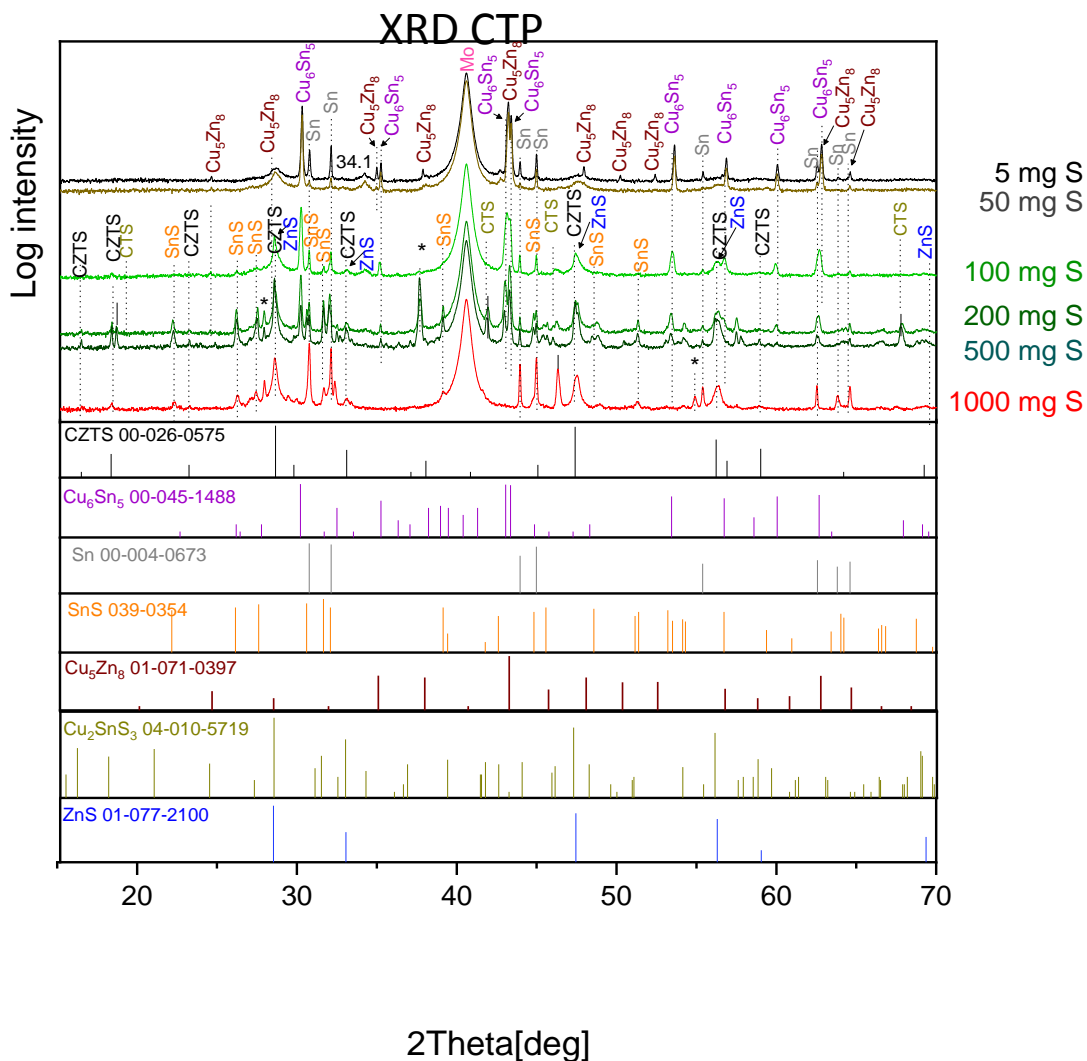
A. Hernández-Martínez,*[†] M. Placidi,[†] L. Arqués,[†] S. Giraldo,[†] Y. Sánchez,[†] V. Izquierdo-Roca,[†]
P. Pistor,[†,‡] M. Valentini,[§,∥] C. Malerba,[∥,⊥] and E. Saucedo[†]

[†]Catalonia Institute for Energy Research (IREC), 08930 Sant Adrià de Besòs (Barcelona), Spain

[‡]Martin Luther University Halle-Wittenberg, Universitätsplatz 10, 06108 Halle (Saale), Germany

[§]Rise Technology Srl, Lungomare Toscanelli 170, 00121 Roma, Italy

[∥]ENEA, Casaccia Research Center, via Anguillarese 301, 00123 Roma, Italy

[⊥]Department of Civil, Environmental, and Mechanical Engineering (DICAM), University of Trento, via Mesiano 77, 38123 Trento, Italy

Ⓢ *Supporting Information*

ABSTRACT: Recent advances in Cu₂ZnSn(S,Se)₄ (CZTSe) thin film photovoltaics open the possibility for the future industrialization of this technology. Nevertheless, major progresses in CZTSe have been achieved using conventional thermal processing annealing routes (CTP), which rely on time-consuming processes with tubular furnaces, incompatible with the requisites of fast methodologies for the Industry. Changing from conventional to rapid thermal processes (RTP) using halogen lamps as heating method is not at all obvious, since the system becomes kinetically controlled, and the CZTSe formation mechanisms as well as crystallization pathways can drastically change. In this work we present the transfer of our kesterite production baseline (Cu₂ZnSnSe₄:Ge) from a conventional thermal process using a tubular furnace toward a rapid thermal process using an adapted system, by comparing them and analyzing the differences between both processes in terms of formation mechanisms as well as photovoltaic absorber properties. For this purpose, the rapid annealing process is stopped at different steps, analyzing the compositional, structural, and morphological properties of the CZTSe absorber at these different stages. Using a combination of XRF, SEM, Raman spectroscopy, and XRD characterization techniques, it is demonstrated that, in contrast to CTP routes, when RTP is used, kesterite is being formed in large amounts in the very early stages. This suggests a fast formation of CZTSe promoted by the higher Se vapor pressure that can be quickly achieved with this methodology. The formation of kesterite seems to proceed via two competitive reactions (binaries vs ternary compound). Additionally, the fast reaction observed in the system avoids the possible Sn loss in an efficient way. Through the optimization of this RTP treatment a device with 8.3% efficiency has been obtained (the total time of the thermal process is 12 min), comparable with the efficiencies obtained so far with CTP routes. Finally, the consequences of all these changes for the future interpretation of the formation reaction mechanisms of kesterites are discussed.

KEYWORDS: *kesterite, Cu₂ZnSnSe₄, thin film solar cell, rapid thermal process, reaction mechanism*
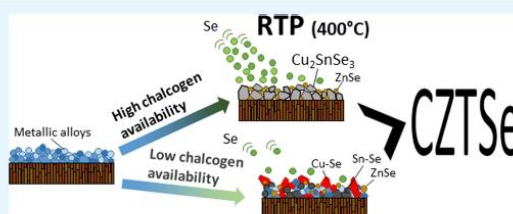
1. INTRODUCTION

Nowadays, the photovoltaic (PV) community is focusing more and more into obtaining maximum profit of sunlight via inexpensive, earth-abundant, readily available, and nontoxic materials. Thin film PV is one of the most promising technologies to fulfill those objectives. Recently, Cu(In,Ga)Se₂ (CIGS) solar cell has held a record efficiency of 22.6% and that for CdTe of 22.1%,[1] reinforcing the position of thin film technologies in the PV field. However, one of the main culprits of CIGS and CdTe technologies are the materials inside their structure. CIGS contains two critical raw materials (indium and gallium) and CdTe one (tellurium), which may develop into a shortage of supply in a relatively near future.[2]

In this scenario, a relatively new PV technology based on quaternary absorber compounds (Cu₂ZnSnS₄–CZTS or Cu₂ZnSnSe₄–CZTSe, or their corresponding solid solution Cu₂ZnSn(S,Se)₄–CZTSSe), is becoming one of the most promising ones to overpass raw materials scarcity limitations, because they only contain nontoxic earth-abundant elements, showing a very high light absorption coefficient of over 10⁴ cm⁻¹, an intrinsic p-type conductivity, and a direct band gap ranging from 1.0 to 1.5 eV depending on the S/Se content.[3,4]

Kesterites share with the other thin film PV chalcogenide technologies a high degree of flexibility for the synthesis of good quality absorbers. In fact, several chemical[5−9] and

A

Table 1. Summary of Some of the Most Relevant Papers Published in the Literature Analyzing the Formation Mechanisms of Kesterites

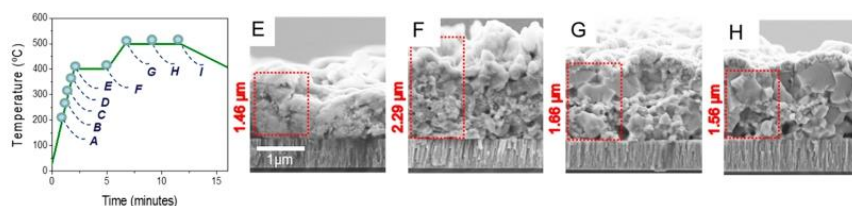| ref	material	process	precursor	annealing process	reaction pathway	T_F (°C)
15	CZTSSe	chemical: hydrazine based slurries	Cu_2S–$S/SnSe_2$–Se/Zn slurries, spin coating	hot plate at 540 °C	$Cu + Sn + Zn + X$ or alloys → binary chalcogenides → $Cu_2ZnX_3 + ZnX \rightarrow Cu_2ZnSnS_4$ $X = S, Se$	350
16	CZTS	physical: sputtering (metallic stacks)	$Sn/Cu/Zn$ metallic stacks	graphite box (S + Sn) at 550 °C	$[Cu_2S + SnS]_{(liq)} + ZnS + S_{2(gas)} \rightarrow Cu_2ZnSnS_4$	480
17	CZTSe	chemical: ethanol based inks	$Cu(II)$ and Zn nitrates, $Sn(IV)$ chloride; knife coating; Se top capping layer	graphite dome with enough Se at 550 °C	$(Cu, Zn, Sn) \xrightarrow{\sim 190\,°C} CuSe_x$ $\xrightarrow{\sim 340\,°C} Cu_2SnSe_3 + Cu_2ZnSnSe_4$ $\xrightarrow{\sim 420\,°C} Cu_2ZnSnSe_4$	340
18	CZTS	chemical: electrodeposition of metals	Cu and Zn metallic electrodeposited	graphite box with S and Sn at 550 °C as maximum T	$2ZnS_{(s)} + Cu_{2-x}S_{(s)} + SnS_{(g)} + (1/2)S_{2(g)}$ → $Cu_2ZnSnS_{4(s)} + ZnS_{(s)}$	>500
19	CZTS	physical: sputtering (sulfides)	ZnS, SnS_2, and Cu by sputtering	tubular furnace (95/5 N_2/H_2S (%)) at 550 °C as maximum T	$Cu_2S + SnS_2 \xrightarrow{350\,°C} Cu_2SnS_3$ $Cu_2SnS_3 + ZnS \xrightarrow{500\,°C} Cu_2ZnSnS_4$	500
20	CZTSe	physical: sputtering (metals)	Cu, Zn, and Sn metals by cosputtering	graphite box with elemental Se at a maximum T of 600 °C	$\alpha Cu + \beta Cu_xSn_y + Zn + 2Se_2$ → $Cu_2ZnSnSe_4$	>350
20	CZTSe	physical: sputtering (metals)	Cu, Zn, and Sn metals by cosputtering	three zones furnace using elemental Se with a cracking zone at a maximum T of 600 °C	$\alpha'Cu_{2-2z}Se + ZnSe + SnSe + \gamma'Se_2$ → $Cu_2ZnSnSe_4$	300

B

121

Figure 1. Temperature profile with the different points where the annealing was stopped for the break-off experiment (left side). Points A−E are the first temperatures in the annealing process, being 200, 250, 300, 350, and 400 °C, respectively. Points E−I are the different key points in the annealing process. Cross-section SEM images of devices from selected samples (right-hand panels E−H).

physical[3,10−12] based routes have been successfully applied to the synthesis of kesterites, where most of them can be classified as sequential synthetic processes. In these so-called sequential processes, during a first step a precursor is deposited by different techniques either from elemental sources, or binary, ternary, or multinary compounds; while in a second step the precursor is submitted to a thermal treatment normally under reactive conditions (with chalcogen in the atmosphere). During this reactive annealing, the desired compound is formed and then crystallized, so regularly both phenomena have to be controlled and optimized. In order to do that, it is quite common that reactive thermal annealing requires several stages at different temperatures and pressures, with the aim to decouple the synthesis process (that normally requires lower temperatures) and the crystallization process (that usually requires higher temperatures).[10,13,14] In this sense, and due to the multiple elements forming the material, together with the complexity of the synthesis/crystallization processes, the careful analysis of the formation mechanisms of kesterites has been of paramount importance from the beginning.[15,16] This is among others very relevant for understanding the role of the different possible secondary phases during the kesterite formation and in the properties of the resulting absorbers. Thus, Table 1 summarizes some of the most relevant works published in this subject,[15−20] where it is clear that, for the different possible materials and processes, relatively different pathways have been deduced.

Nowadays, there is a general agreement that the synthesis route of kesterites proceeds either via the previous formation of binary (Cu−X, Zn−X, and Sn−X binaries, X = S and/or Se) or ternary (mainly Cu−Sn−X phase, X = S and/or Se) compounds, which react at a given temperature to form the corresponding quaternary phase. The formation of the pure Se-based kesterite compound seems to proceed at lower temperatures (∼350 °C)[15,17,20] than the formation of the pure S counterpart (∼500 °C).[16,18,19] Nevertheless, there is no general indication of when or why the formation precedes either via the reaction of binary compounds, such as in refs 15, 17, and 19, or via the reaction of ternary Cu−Sn−X compounds with ZnSe, such as in refs 14, 16, and 18. In principle, as is clear from Table 1 this is fully independent of the chalcogen (S/Se).

Further analyzing the reported mechanisms of Table 1, it seems that when metallic precursors are used, the formation of kesterites preferably proceeds directly via the reaction of binary compounds and in general no ternary compounds are observed. On the contrary, if the chalcogen is already present in the precursor from the very beginning of the annealing, the reaction formation proceeds preferably including ternary compounds (Cu−Sn−X and Cu−Zn−X). This could be a clear advantage of this last pathway, because a simplified formation schema, with less number of molecules involved in the synthesis, can

represent a lower risk of secondary phases remaining after the end of the formation reaction. All this has been almost exclusively studied for conventional thermal processes (CTP), i.e., for annealing routes involving furnaces with radiative heating using electrical resistances. These processes are characterized for being slow with total synthesis/crystallization times in the range of 2−3 h or even longer and are ideal for research purposes but not for industrial applications.

Conversely, rapid thermal processes (RTPs), based in the fast heating of the annealing system using halogen lamps, is extensively used in the conventional PV industry, because of its substantial reduction of the time required for the synthesis and crystallization process, minimizing the processing time and energy consumption. In kesterites, RTP annealing has been barely studied. Some reports demonstrate its potential,[21−23] reducing the total duration of this critical step from hours to several minutes. Additionally, to the shorter process times, in this type of process higher chalcogen vapor pressures can be achieved from the very beginning. All these fundamental changes are expected to have a non-negligible impact in the formation mechanisms of kesterites.

Taking this into account, in this work we optimize and analyze an RTP annealing for the synthesis of CZTSe absorbers, using metallic stacks deposited by sputtering as precursors. Different parameters of the annealing are investigated. The phase evolution during the annealing process is analyzed in a break-off experiment, where the RTP process has been stopped at different stages. By combining advanced characterization techniques such as multiwavelength Raman spectroscopy, X-ray diffraction, X-ray fluorescence, and glow discharge optical emission spectroscopy (GDOES). The formation mechanisms are investigated and compared with standard thermal routes. We observe remarkable differences that open interesting new perspectives for the optimization of rapid thermal processes applied to the kesterite synthesis.

2. EXPERIMENTAL SECTION

For the synthesis of CZTSe by a sequential process, SLG/Mo/Cu/Sn/Cu/Zn metallic precursor stacks were deposited by DC-magnetron sputtering (Alliance Concept Ac-450) onto Mo coated soda-lime glass substrates. The compositions of the films were near the range of those reported as ideal for high-efficiency solar cell devices, namely, Cu-poor and Zn-rich: Cu/(Zn + Sn) = 0.77, Zn/Sn = 1.21, Cu/Zn = 1.41, and Cu/Sn = 1,71.

Precursors (2.5×2.5 cm^2 in area) were then selenized by RTP using an AnnealSys AS-ONE-100 furnace in a semiclosed system made up by a graphite box with a reaction volume of 3.8 cm^3. Approximately, 20 mg of elemental Se (Alfa Aesar, 99.999% purity) were placed into the box next to the substrates, and after two evacuate and purge cycles (base vacuum of 3×10^{-2} mbar), the Ar flow was increased until obtaining 1 mbar total pressure inside the furnace. Then, the reactive annealing was conducted in a two-step process: (1) heating from room

C

temperature to 400 °C (ramp, 180 °C/min; dwell time, 3 min) and (2) heating to 500 °C (ramp, 60 °C/min; dwell time, 5 min). The temperatures during all the process presented here were measured by a calibrated pyrometer located just below the sample holder, which consists of a specially designed graphite box. During the second step, the pressure was raised to 900 mbar. After the second step, the setup cooled to below 80 °C (also at 900 mbar). The whole annealing process takes only 12 min, with an additional 8 min approximately for the cool down. For the break-off experiment, the annealing process was interrupted at different temperatures and times as is shown in Figure 1, corresponding to different stages of the thermal treatment. The samples were then cooled quickly for further characterization.

Precursor stacks and annealed CZTSe films from the break-off experiment were characterized by X-ray fluorescence (XRF), for its compositions. In addition, a phase analysis was performed by combining X-ray diffraction (XRD) and Raman spectroscopy (RS). XRD measurements were performed using a PANalytical X'pert ProMPD diffractometer with Cu Kα radiation (λ = 1.54056 Å) monochromated and a secondary graphite monochromator. Multiwavelength Raman characterization has been carried out using 325, 442, 532, and 785 nm laser wavelengths as a source of excitation. Raman scattering measurements were performed in backscattering configuration using a Horiba Jobin Yvon fHR-640 spectrometer for the wavelengths 325, 442, and 532 nm and an iHR-320 spectrometer for the 785 nm wavelength. Spectrometers are coupled with Raman probes developed at IREC and a low-noise CCD detector cooled to −70 °C. Excitation and light collection were made using a macro-optic system with a laser spot diameter of the order of 50 μm. In order to avoid thermal effects in the spectra, the power density on the surface of samples was kept below 150 W/cm². The position of all spectra has been corrected by taking into account the first order Raman spectrum of monocrystalline silicon as a reference measured before each acquisition and imposing its position at 520 cm⁻¹. Cross-section images were obtained in selected samples by using scanning electron microscopy (SEM-ZEISS Series Auriga microscope) for its thickness calculation. A depth profiling analysis of some selected samples was performed by GDOES measurements using a Horiba Jobin Yvon GD Profiler 2 spectrometer, equipped with an anode diameter of 4 mm and 19 element channels.

Once the kesterite absorbers were synthesized and characterized, solar cell devices were fabricated with selected samples. First, and in order to remove the possible presence of secondary phases (mainly ZnSe and SnSe), the films were etched in H_2SO_4 + $KMnO_4$ and $(NH_4)_2S$ solutions.[24,25] Next, a CdS buffer layer was deposited via chemical bath deposition (CBD) with a thickness of approximately 50 nm.[26] Then, i-ZnO (50 nm) and In_2O_3:SnO_2 (ITO, 200 nm) layers were deposited by pulsed DC-magnetron sputtering (Alliance Concept CT100). Finally, 3 × 3 mm² cells were mechanically scribed to complete device fabrication and were optoelectronically characterized by measuring both the J–V characteristics under simulated AM1.5 illumination (AAA Abet 3000 Solar Simulator) and the external quantum efficiency (EQE; Bentham Instruments PV300 photovoltaic characterization system).

3. RESULTS

Figure 1 (left) shows the temperature profile used in this work, in which the different temperatures where the process was stopped in the break-off experiments are indicated (points from A to I), covering the full temperature and time ranges for the RTP annealing. The four right-hand panels of Figure 1 show the corresponding cross-section SEM images of selected samples.

We will focus on the evolution of morphology for the samples from point E on, i.e., from the point in which Se starts to be significantly incorporated into the precursor, as we will show later. At point E, the thickness of the precursor has increased almost twice with respect to the metallic stack one (see Figure S1a of the Supporting Information (SI)), suggesting that almost all the Se necessary for the synthesis of kesterite has been integrated into the precursor. In fact, XRF analysis

performed on all the samples (see the evolution of the concentration of the different elements determined by XRF in Figure S2 of the SI) confirms that the selenization of the metallic precursors is completed and only rather small quantities of Se are further incorporated later on and/or at higher temperatures. This is also confirmed by GDOES measurements that show nonsignificant variation of Se content in samples F, G, H, and I (see Figure S6 of the SI).

Following the steps of the RTP annealing (from point F up to point I) helps to clearly increase the grain size (first in the surface near region; afterward these grains grow toward the back interface) and to reduce the rough superficial structures. Compared to conventional thermal processes (with generally slower heating ramps, longer dwelling times, and lower Se partial vapor pressures), in the RTP annealing the chalcogen is incorporated much faster, but proper crystallization is only achieved during the second ramp at higher temperature, as is also characteristic for conventional processes.[16] Nevertheless, in the RTP case only 5 min at 500 °C are enough for the formation of large crystals, suggesting that the Se vapor pressure in the reaction chamber is still high enough to assist a fast crystallization. (See in Figure S1b a very well crystallized absorber made by the described RTP process.) Thus, compared to the conventional process, RTP annealing accelerates the incorporation thanks to the high Se vapor pressures present. This has a clear impact on the crystallization (large crystals are formed in shorter times), but probably this feature has an impact on phase evolution during kesterite formation, too.

In order to investigate this, XRD analysis was performed in the complete set of samples. Figure 2a shows the diffractograms evolution corresponding to all the samples, while Figure 3b shows the evolution of the relative XRD intensity for the different detected phases. This relative XRD intensity was normalized with respect to the (110) reflection of Mo, which is supposed to be constant for all the samples. It is important to remark that the main XRD peaks of the ZnSe, Cu_2SnSe_3 (CTSe), and $Cu_2ZnSnSe_4$ (CTZSe) phases almost coincide at room temperature, making the distinction extremely complicated.[27] While this impedes the detection of ZnSe/CuSnSe₃ secondary phases, there are several additional characteristic peaks with low intensity for the tetragonal kesterite phase with lower symmetry, which allow one to clearly identifying the latter. These are for example the peaks at 22.1°, 28.3°, 35.2°, and 36.1° corresponding to diffraction planes (110), (103), (202), and (121), respectively. In consequence and to our surprise, already in point E, i.e., at the very beginning of the first dwell time at 400 °C, we were able to detect peaks corresponding to the CZTSe tetragonal kesterites phase, along with SnSe. There is no evidence of other phases.

This contrasts with the samples prepared in our standard conventional thermal process at IREC with very similar conditions (see Figure S3 of the SI, point E), where no evidence of kesterite formation is found, although other groups have reported the possibility of forming kesterite at such low temperature with standard annealing.[28] We rather observe several secondary phases including, even, metallic ones. This implies that in the RTP process the formation of kesterite phases occurs faster, starting at lower temperatures and/or shorter times. Again, we relate this to the higher Se vapor pressures achievable with this setup. Beside this, the RTP process seems to produce kesterite with acceptable crystalline quality even at 400 °C.

The evolution of the diffractograms of the different samples describes the phase formation in the bulk during the

D
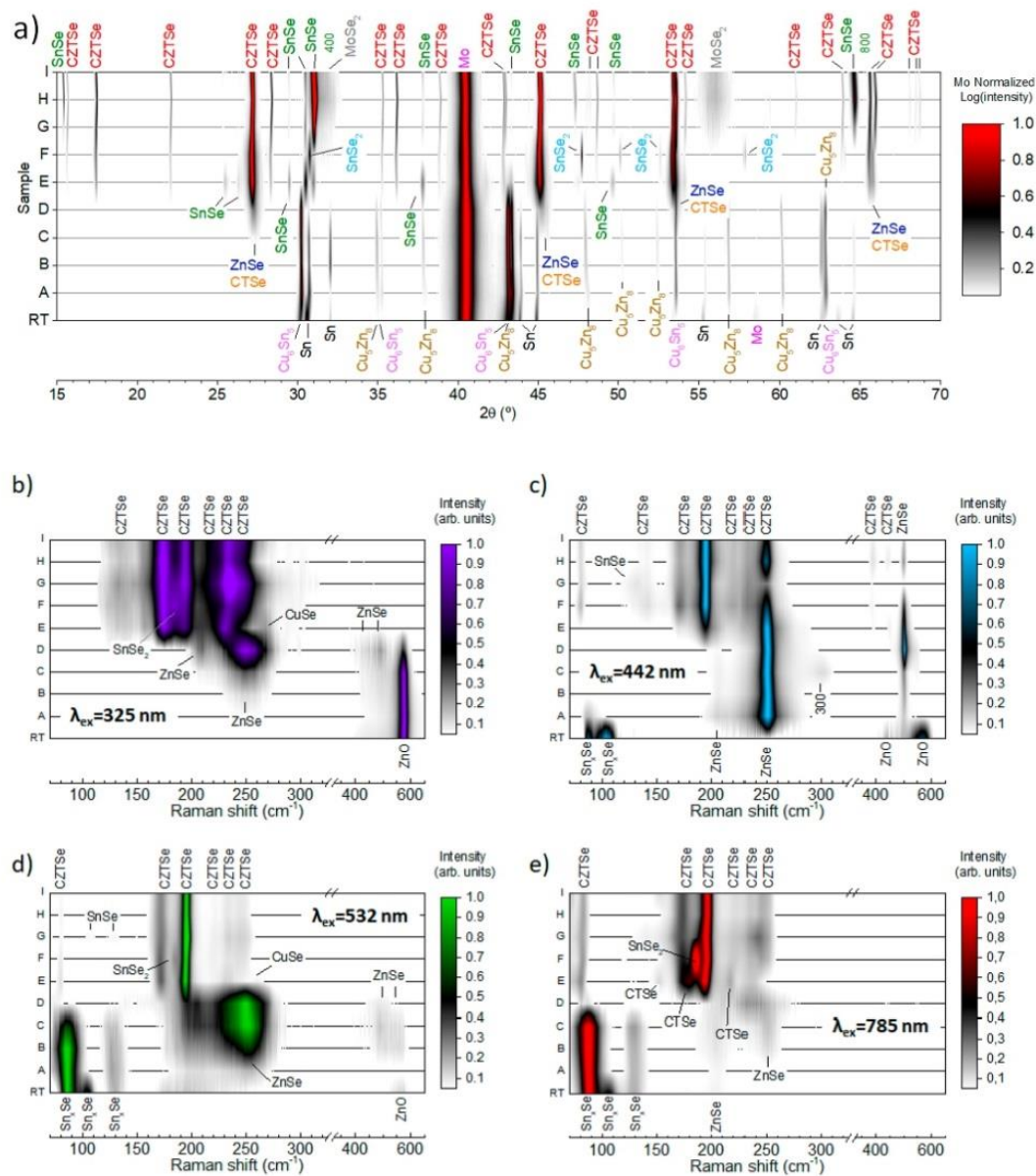
Figure 2. (a) XRD diffractogram and (b−e) Raman spectra using four different excitation wavelengths (325, 442, 532, and 785 nm) of the different samples produced in the break-off experiment (detailed diffractograms and Raman spectra are reported in Figures S3 and S4). Here and in the following, CTSe stands for the ternary Cu_2SnSe_3 compound.

annealing process. From room temperature (RT) to point D, we see transformation of the metallic phases from a highly textured Sn phase and Cu−Sn, Cu−Zn alloys toward a Cu−Sn alloy, accompanied by a reduction of the peaks of the Sn and Cu−Zn phases. The reduced intensities of the Zn related phases are attributed to the formation of ZnSe with low crystallinity. The diffractogram of point F is very similar to the one of point E, with a slightly increased intensity of the CZTSe peaks, while the peaks corresponding to SnSe are decreased in favor of increasing $SnSe_2$ peaks. We postulate that here SnSe formed during the

first dwell time gets further selenized to $SnSe_2$. Finally, for points G, H, and I (corresponding to different times during the second dwell time at 500 °C), the intensity and the full width at half-maximum (fwhm) of the characteristic CZTSe peaks remain practically constant. Additionally, a thin $MoSe_2$ layer is formed, as expected. Highly [400] textured and nontextured SnSe is detected, but its origin is most probably the condensation of remaining gaseous Sn−Se during the user-forced cooling process.[25] Following this line of arguments, the actual quaternary kesterite phase is already completely formed during

E

Figure 3. (a) Evolution of the absolute area of most relevant peaks detected by Raman spectroscopy (surface), corresponding to the different binary, ternary, and quaternary phases present in the system. (b) Evolution of the XRD diffraction peaks area corresponding to the different binary, ternary, and quaternary phases that have been normalized with respect to the total area of the 110 reflection of the Mo layer at 40.5°, extracted from Figure S3.

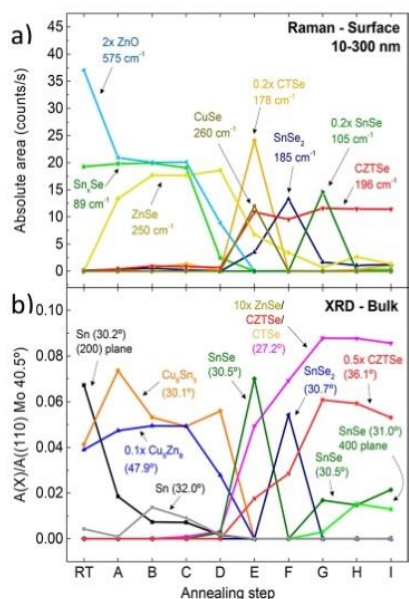the first dwell time at 400 °C, and the second dwell time at 500 °C is predominantly necessary for an improved crystallization of the absorber.

Raman spectroscopy with four different excitation wavelengths (325, 442, 532, and 785 nm) was performed in order to complement the previous analysis. The use of various excitation wavelengths leads to pre-resonant conditions for different compounds and enhances the ability to detect several secondary phases present.[29] Panels b−e of Figure 2 show the Raman spectra obtained in the different samples for the four excitation wavelengths. In particular, under UV excitation (325 nm) the ZnO phase signal is strongly enhanced,[30] together with a nonbandgap resonant enhancement of the CZTSe.[31] Under blue excitation (442 nm) we enhance the detection of ZnSe,[32,33] and with red excitation (785 nm), the detection of Sn−Se[34] and ternary Cu−Sn−Se phases[32] (CTSe). Figure 3a depicts the evolution of the absolute intensity for the Raman peaks recorded at the absorber surface (<300 nm) using the signal acquired with the most favorable excitation wavelength for each phase. During the first ramp (from point A up to point E), ZnO, ZnSe, SnSe, and Cu_2SnSe_3 are clearly detected, with CuSe traces only at point E. This is unexpected, as in literature CuSe(S) is found most frequently along with SnSe(S) or $SnSe(S)_2$ in the case in which the formation reaction proceeds via the reaction of binary compounds.[16] Alternatively, $Cu_2SnSe(S)_3$ is found when the formation of kesterites proceeds via the reaction of this ternary phase with ZnSe.[17] The intimate mixing of all these phases and the presence of both Sn−Se and Cu−Sn−Se coexisting in the bulk of the same absorber suggest that most probably these two reaction pathways are competing and contributing both to the formation of kesterites under the studied conditions. As is clear, somewhere

between point D (350 °C) and point E (400 °C) the kesterite starts to be formed, in good agreement with previously published data.[17,20] In our case, the heating ramp is 180 °C/min, i.e., to go from point D to point E only takes approximately 17 s. This implies that once the minimum formation temperature is reached, the precursor phases react very quickly with selenium in the RTP and form the kesterite almost immediately.

At point E, the selenization has not been completed yet. We find strong contributions from ternary Cu−Sn−Se compounds and ZnSe, and only a few quantities of Cu−Se and Sn−Se binary phases are left. At point F, we can consider that the reaction is almost finished, the kesterites are formed, and only some secondary phases remain: ZnSe due to the Zn-rich composition, and SnSe probably in the $MoSe_2$/CZTSe interface[32] and the surface due to condensation during the cooling process from pre-evaporated material.[25] Additionally, a clear contribution of the $SnSe_2$ (under resonant conditions with 785 nm excitation) is observed that is arguably correlated with the superficial structures observed in the corresponding SEM image (Figure 1). After point F, i.e., once the temperature is increased to 500 °C, no reduction of the Raman fwhm is observed for the CZTSe phase. This contrasts with conventional thermal processes where in the last step a clear improvement of the crystal quality with the annealing time has been reported.[35] On the order hand, an accurate analysis (using the Raman nonbandgap resonant conditions with 325 nm excitation) shows a clear modification with time of the bands at 175, 233, and 250 cm^{-1} (Figure 4). Modifications of these peak intensities have been
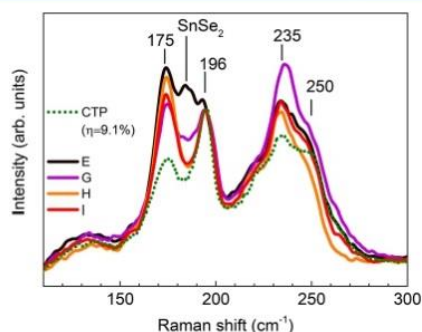
Figure 4. Raman spectra under UV nonbandgap resonant conditions (325 nm) for samples E−I together with a reference sample annealed using an optimized conventional thermal process.

attributed to changes in the V_{cu} and Zn_{Sn} point defect concentrations which have strong impact in the final optoelectronics properties.[31]

We now return to the possible formation mechanisms and compare the results obtained here with those reported in the literature. For low chalcogen vapor pressures and/or a low availability of chalcogen (e.g., no chalcogen in the precursors), the formation of kesterites proceeds mainly by the reaction of binary compounds (see refs 16−21), where the kesterite was synthesized under equivalent conditions. In this case a trimolecular reaction is required, enhancing the probability of formation and the presence of secondary phases at the end of the annealing.

On the other hand, under high chalcogen vapor pressure, such as in this work, or high availability of chalcogen from the very beginning of the annealing (such as the precursors already containing chalcogen in their composition), the reaction preferably proceeds via the formation of ternary Cu−Sn−Se

F

compounds (see refs 15−19). This implies that a bimolecular reaction between Cu−Sn−Se and Zn−Se is favored, minimizing the risk of secondary phases formation. Figure 5 summarizes the

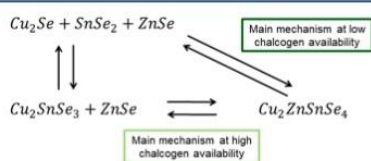**Figure 5.** Schematic representation of the two competing formation mechanisms.

pathways that are competing and contributing in this case to the formation of CZTSe:

In order to demonstrate the impact of the different stages on the properties and characteristics of the devices, solar cells were prepared with the most relevant samples. As was expected, devices prepared with absorbers from A up to F do not give any working solar cell. All of them where shunted, probably because the presence of very large amounts of secondary phases as is clear from the XRD and Raman spectroscopy analysis, together with the poor crystallization of the kesterite phase when present. On the contrary, samples G, H, and I lead to working devices as is presented in Figure 6. Additionally, in this figure, the short circuit current density (J_{sc}), open circuit voltage (V_{oc}), fill factor (FF), and efficiency (η) are presented with some statistics. The solar cell prepared with absorber G exhibit low efficiency mainly due to the low V_{oc} and FF. The differences of only 100 s and 100 °C between point F and point G seem therefore to be enough to go from no working devices to working ones. This means that the crystallization/defect reordering observed by Raman spectroscopy under 325 nm excitation wavelength (Figure 4) is also very fast for the RTP process with relatively high Se pressures. Nevertheless, at point G, the absorber properties (defects concentration and type, and presence of a residual $SnSe_2$ secondary phase) are still not good enough to ensure a high performance. Additionally, relatively small grains are observed in the SEM that can contribute to the low V_{oc} and FF. A large number of grain boundaries which are not well passivated leads to an increased density of defects. This could severely deteriorate the charge transport properties of the absorber and explain the bad performance.

After only 150 additional seconds at 500 °C, both the V_{oc} and the FF are largely improved (and in consequence the efficiency). The J_{sc} is also slightly increased. This large improvement is
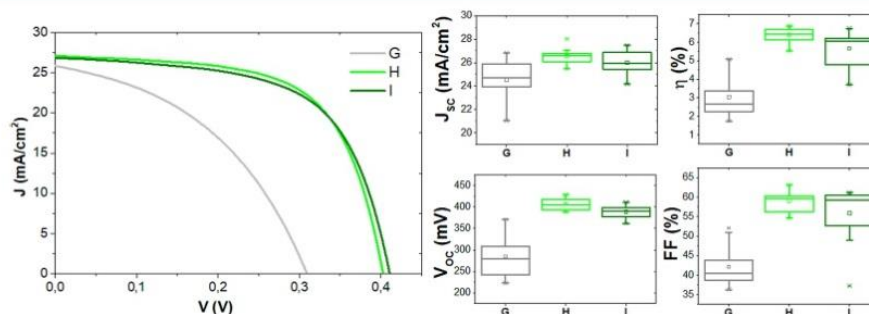
basically explained by the better crystalline quality of the absorber thanks to the fast grain size growth, as well as the complete consumption or minimization of secondary phases. Longer crystallization times seem to have a limited impact on the improvement of the performance of the devices, suggesting that times as short as 150 s at relatively high temperatures can be enough to crystallize the CZTSe absorber and fully exploit the potential of the RTP annealing.

Finally, with further optimization of the precursor composition and device preparation, via a fine-tuning of the cationic ratios and a better substrate cleaning, we prepared a device with 8.3% efficiency using the RTP thermal routine presented in Figure 1. Figure 7 shows the $J-V$ illuminated curve and the
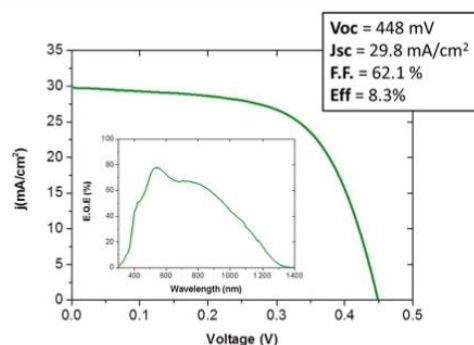
Figure 7. $J-V$ illuminated curve (under AM1.5G conditions, no anti-reflection coating or metallic grid) and external quantum efficiency of the champion cell.

corresponding external quantum efficiency of this champion device, obtained with an annealing process of only 12 min of total duration (20 min including the cooling process). If we compare this device with others previously reported by our group using the CTP annealing (10.1%, 10.6%, 8.2%, and 11.8%),[10,13,26,35] we can conclude that the V_{oc} is at the same level, and only J_{sc} and FF are slightly lower. Please note that these absorbers have been prepared without any additional Ge layer. The J_{sc} is somehow lower than expected. One plausible cause is the rather small absorber thickness (1.2 μm) for these absorbers; also, no antireflection coating was applied. The lower FF can be probably related to the necessity to adapt and optimize the back and front contacts for the characteristics of the absorbers obtained with this type of thermal treatment and the fact that no metallic grids were applied.

Figure 6. $J-V$ illuminated curve of devices obtained from absorbers produced during the break-off experiments (points G−I). Evolution of the different optoelectronic parameters of the same three points.

4. CONCLUSIONS

The formation pathways of CZTSe absorber by using a RTP annealing were investigated. The higher vapor pressures achieved with this rapid process have been shown to have a dramatic impact on the formation pathways of the kesterite absorber. While the selenization of metallic precursors in conventional thermal processes proceeds predominantly via binary compounds, this contrasts to what is observed for the RTP. A competing mechanism between the route implying binaries and the one implying the formation of CTSe ternary compound is observed here. We therefore present first evidence for the dependence of the reaction pathway on the selenium (or chalcogen) availability. A pathway involving binary selenides is preferred for relatively low Se availability during annealing, and a pathway involving the CTSe ternary compound predominates for relatively high Se availability. In between apparently both mechanisms can compete. The consequences on the devices show that nonworking solar cells are obtained for poorly crystallized absorbers, even if the formation reaction of the kesterite phase seems to be completed. During the crystallization at 500 °C, the J_{sc} of the corresponding devices is quickly raised during heat up, while the V_{oc} and FF improve rapidly during the first minutes together with the crystal quality. Through the optimization of this RTP annealing we report an 8.3% efficient device, prepared with an annealing time of only 12 min, demonstrating the compatibility of the materials with possible future industrial processes.

■ ASSOCIATED CONTENT

ⓢ Supporting Information

The Supporting Information is available free of charge on the ACS Publications website at DOI: 10.1021/acsaem.8b00089.

> Cross-sectional SEM images of kesterite precursors and absorbers, additional XRF and XRD data on the elemental and phase evolution, additional multiwavelength Raman spectra, and elemental depth profiles measured by glow-discharge optical emission spectroscopy (PDF)

■ AUTHOR INFORMATION

Corresponding Author

*Tel.: +34 933562615. Fax: +34 933563802. E-mail: ahernandez@irec.cat.

ORCID ⓘ

A. Hernández-Martínez: 0000-0002-0895-3864
S. Giraldo: 0000-0003-4881-5041

Notes

The authors declare no competing financial interest.

■ ACKNOWLEDGMENTS

■ ABBREVIATIONS

CIGS, $CuIn_{1−x}Ga_xSe_2$
CTP, conventional thermal processing
CZTSe, $Cu_2ZnSnSe_4$
fwhm, full width at half-maximum
GDOES, glow discharge optical emission spectroscopy
PV, photovoltaics
RS, Raman spectroscopy
RT, room temperature
RTP, rapid thermal processing
SEM, scanning electron microscopy
XRD, X-ray diffraction
XRF, X-ray fluorescence

■ REFERENCES

(1) Green, M. A.; Hishikawa, Y.; Warta, W.; Dunlop, E. D.; Levi, D. H.; Hohl-Ebinger, J.; Ho-Baillie, A. W. H. Solar Cell Efficiency Tables (Version 50). *Prog. Photovoltaics* **2017**, 25 (7), 668−676.

(2) Wadia, C.; Alivisatos, A. P.; Kammen, D. M. Materials Availability Expands the Opportunity for Large-Scale Photovoltaics Deployment. *Environ. Sci. Technol.* **2009**, 43 (6), 2072−2077.

(3) Fairbrother, A.; Fontané, X.; Izquierdo-Roca, V.; Espindola-Rodriguez, M.; López-Marino, S.; Placidi, M.; López-García, J.; Pérez-Rodríguez, A.; Saucedo, E. Single-Step Sulfo-Selenization Method to Synthesize $Cu_2ZnSn(S_ySe_{1-y})_4$ Absorbers from Metallic Stack Precursors. *ChemPhysChem* **2013**, 14 (9), 1836−1843.

(4) Siebentritt, S. Why Are Kesterite Solar Cells Not 20% Efficient? *Thin Solid Films* **2013**, 535 (1), 1−4.

(5) Todorov, T. K.; Reuter, K. B.; Mitzi, D. B. High-Efficiency Solar Cell with Earth-Abundant Liquid-Processed Absorber. *Adv. Mater.* **2010**, 22 (20), E156−E159.

(6) Carrete, A.; Shavel, A.; Fontane, X.; Montserrat, J.; Fan, J.; Ibañez, M.; Saucedo, E.; Pérez-Rodríguez, A.; Cabot, A. Antimony-Based Ligand Exchange To Promote Crystallization in Spray-Deposited $Cu_2ZnSnSe_4$ Solar Cells. *J. Am. Chem. Soc.* **2013**, 135, 15982−15985.

(7) Sutter-Fella, C. M.; Stückelberger, J. A.; Hagendorfer, H.; La Mattina, F.; Kranz, L.; Nishiwaki, S.; Uhl, A. R.; Romanyuk, Y. E.; Tiwari, A. N. Sodium Assisted Sintering of Chalcogenides and Its Application to Solution Processed $Cu_2ZnSn(S,Se)_4$ Thin Film Solar Cells. *Chem. Mater.* **2014**, 26 (3), 1420−1425.

(8) Larramona, G.; Levcenko, S.; Bourdais, S.; Jacob, A.; Chone, C.; Delatouche, B.; Moisan, C.; Just, J.; Unold, T.; Dennler, G. Fine-Tuning the Sn Content in CZTSSe Thin Films to Achieve 10.8% Solar Cell Efficiency from Spray-Deposited Water-Ethanol-Based Colloidal Inks. *Adv. Energy Mater.* **2015**, 5 (24), 1501404.

(9) Su, Z.; Tan, J. M. R.; Li, X.; Zeng, X.; Batabyal, S. K.; Wong, L. H. Cation Substitution of Solution-Processed Cu_2ZnSnS_4 Thin Film Solar Cell with over 9% Efficiency. *Adv. Energy Mater.* **2015**, 5 (19), 1500682.

(10) Giraldo, S.; Neuschitzer, M.; Thersleff, T.; López-Marino, S.; Sánchez, Y.; Xie, H.; Colina, M.; Placidi, M.; Pistor, P.; Izquierdo-Roca, V.; et al. Large Efficiency Improvement in $Cu_2ZnSnSe_4$ Solar Cells by Introducing a Superficial Ge Nanolayer. *Adv. Energy Mater.* **2015**, 5 (21), 1501070.

(11) Márquez, J.; Neuschitzer, M.; Dimitrievska, M.; Gunder, R.; Haass, S.; Werner, M.; Romanyuk, Y. E.; Schorr, S.; Pearsall, N. M.; Forbes, I. Systematic Compositional Changes and Their Influence on Lattice and Optoelectronic Properties of $Cu_2ZnSnSe_4$ Kesterite Solar Cells. *Sol. Energy Mater. Sol. Cells* **2016**, 144, 579−585.

(12) Sun, K.; Yan, C.; Liu, F.; Huang, J.; Zhou, F.; Stride, J. A.; Green, M.; Hao, X. Over 9% Efficient Kesterite Cu_2ZnSnS_4 Solar Cell

Fabricated by Using $Zn_{1-x}Cd_xS$ Buffer Layer. *Adv. Energy Mater.* **2016**, 6 (12), 1600046.

(13) Giraldo, S.; Thersleff, T.; Larramona, G.; Neuschitzer, M.; Pistor, P.; Leifer, K.; Pérez-Rodríguez, A.; Moisan, C.; Dennler, G.; Saucedo, E. $Cu_2ZnSnSe_4$ Solar Cells with 10.6% Efficiency through Innovative Absorber Engineering with Ge Superficial Nanolayer. *Prog. Photovoltaics* **2016**, 24 (10), 1359−1367.

(14) Malerba, C.; Valentini, M.; Mittiga, A. Title Cation Disorder In Cu_2ZnSnS_4 Thin Films: Effect On Solar Cell Performances. *Sol. RRL* **2017**, 1, 1700101.

(15) Hsu, W.-C.; Bob, B.; Yang, W.; Chung, C.-H.; Yang, Y. Reaction Pathways for the Formation of $Cu_2ZnSn(Se,S)_4$ Absorber Materials from Liquid-Phase Hydrazine-Based Precursor Inks. *Energy Environ. Sci.* **2012**, 5, 8564−8571.

(16) Fairbrother, A.; Fontané, X.; Izquierdo-Roca, V.; Espindola-Rodríguez, M.; López-Marino, S.; Placidi, M.; Calvo-Barrio, L.; Pérez-Rodríguez, A.; Saucedo, E. On the Formation Mechanisms of Zn-Rich Cu_2ZnSnS_4 Films Prepared by Sulfurization of Metallic Stacks. *Sol. Energy Mater. Sol. Cells* **2013**, 112, 97−105.

(17) Fella, C. M.; Uhl, A. R.; Hammond, C.; Hermans, I; Romanyuk, Y. E.; Tiwari, A. N. Formation Mechanism of $Cu_2ZnSnSe_4$ Absorber Layers during Selenization of Solution Deposited Metal Precursors. *J. Alloys Compd.* **2013**, 567, 102−106.

(18) Berg, D. M.; Crossay, A.; Guillot, J.; Izquierdo-Roca, V.; Pérez-Rodriguez, A.; Ahmed, S.; Deligianni, H.; Siebentritt, S.; Dale, P. J. Simplified Formation Process for Cu_2ZnSnS_4-Based Solar Cells. *Thin Solid Films* **2014**, 573, 148−158.

(19) Jung, H. R.; Shin, S. W.; Gurav, K. V.; Suryawanshi, M. P.; Hong, C. W.; Yang, H. S.; Lee, J. Y.; Moon, J. H.; Kim, J. H. Phase Evolution of Cu_2ZnSnS_4 (CZTS) Kesterite Thin Films during the Sulfurization Process. *Ceram. Int.* **2015**, 41, 13006−13011.

(20) Bodeux, R.; Mollica, F.; Delbos, S. Growth of $Cu_2ZnSnSe_4$ by Cosputtering and Reactive Annealing Atmosphere. *Sol. Energy Mater. Sol. Cells* **2015**, 132, 67−73.

(21) Olgar, M. A.; Klaer, J.; Mainz, R.; Ozyuzer, L.; Unold, T. Cu_2ZnSnS_4-Based Thin Films and Solar Cells by Rapid Thermal Annealing Processing. *Thin Solid Films* **2017**, 628, 1−6.

(22) Placidi, M.; Espindola-Rodriguez, M.; Lopez-Marino, S.; Sanchez, Y.; Giraldo, S.; Acebo, L.; Neuschitzer, M.; Alcobé, X.; Pérez-Rodríguez, A.; Saucedo, E. Effect of Rapid Thermal Annealing on the Mo Back Contact Properties for $Cu_2ZnSnSe_4$ Solar Cells. *J. Alloys Compd.* **2016**, 675, 158−162.

(23) Fairbrother, A.; Fourdrinier, L.; Fontane, X.; Izquierdo-Roca, V.; Dimitrievska, M.; Pérez-Rodríguez, A.; Saucedo, E. Precursor Stack Ordering Effects in $Cu_2ZnSnSe_4$ Thin Films Prepared by Rapid Thermal Processing. *J. Phys. Chem. C* **2014**, 118, 17291−17298.

(24) Lopez-Marino, S.; Sánchez, Y.; Placidi, M.; Fairbrother, A.; Espindola-Rodríguez, M.; Fontané, X.; Izquierdo-Roca, V.; López-García, J.; Calvo-Barrio, L.; Pérez-Rodríguez, A.; Saucedo, E. ZnSe Etching of Zn-Rich $Cu_2ZnSnSe_4$: An Oxidation Route for Improved Solar-Cell Efficiency. *Chem. - Eur. J.* **2013**, 19 (44), 14814−14822.

(25) Xie, H.; Sanchez, Y.; López-Marino, S.; Espíndola-Rodríguez, M.; Neuschitzer, M.; Sylla, D.; Fairbrother, A.; Izquierdo-Roca, V.; Pérez-Rodríguez, A.; Saucedo, E. Impact of Sn(S,Se) Secondary Phases in $Cu_2ZnSn(S,Se)_4$ Solar Cells: A Chemical Route for Their Selective Removal and Absorber Surface Passivation. *ACS Appl. Mater. Interfaces* **2014**, 6 (15), 12744−12751.

(26) Neuschitzer, M.; Sanchez, Y.; López-Marino, S.; Xie, H.; Fairbrother, A.; Placidi, M.; Haass, S.; Izquierdo-Roca, V.; Pérez-Rodríguez, A.; Saucedo, E. Optimization of CdS Buffer Layer for High-Performance $Cu_2ZnSnSe_4$ Solar Cells and the Effects of Light Soaking: Elimination of Crossover and Red Kink. *Prog. Photovoltaics* **2015**, 23, 1660−1667.

(27) Redinger, A.; Hönes, K.; Fontané, X.; Izquierdo-Roca, V.; Saucedo, E.; Valle, N.; Pérez-Rodríguez, A.; Siebentritt, S. Detection of a ZnSe Secondary Phase in Coevaporated $Cu_2ZnSnSe_4$ thin films. *Appl. Phys. Lett.* **2011**, 98 (10), 101907.

(28) Juškėnas, R.; Niaura, G.; Mockus, Z.; Kanapeckaitė, S.; Giraitis, R.; Kondrotas, R.; Naujokaitis, A.; Stalnionis, G.; Pakštas, V.;

Karpavičienė, V. XRD Studies of an Electrochemically Co-Deposited Cu−Zn−Sn Precursor and Formation of a $Cu_2ZnSnSe_4$ Absorber for Thin-Film Solar Cells. *J. Alloys Compd.* **2016**, 655, 281−289.

(29) Fontane, X.; Izquierdo-Roca, V.; Fairbrother, A.; Espindola-Rodriguez, M.; Lopez-Marino, S.; Placidi, M.; Jawhari, T.; Saucedo, E.; Perez-Rodriguez, A. Selective Detection of Secondary Phases in $Cu_2ZnSn(S,Se)_4$ Based Absorbers by Pre-Resonant Raman Spectroscopy. *Conf. Rec. IEEE Photovolt. Spec. Conf* **2013**, 2581−2584.

(30) Rousset, J.; Tsin, F.; Guc, M.; Vidal, J.; Le Bris, A.; Thomere, A.; Izquierdo-Roca, V.; Lincot, D. Perchlorate-Induced Doping of Electrodeposited ZnO Films for Optoelectronic Applications. *J. Phys. Chem. C* **2016**, 120, 18953−18962.

(31) Oliva, F.; Giraldo, S.; Dimitrievska, M.; Pistor, P.; Martinez-Perez, A.; Calvo-Barrio, L.; Saucedo, E.; Perez-Rodriguez, A.; Izquierdo-Rodríguez, V. Raman Scattering Assessment of Point Defects in Kesterite Semiconductors: UV Resonant Raman Characterization for Advanced Photovoltaics. IEEE 44th Photovoltaic Specialists Conference (PVSC-44), Washington, DC, USA, Jun. 25−30, 2017.

(32) Fairbrother, A.; Fontané, X.; Izquierdo-Roca, V.; Placidi, M.; Sylla, D.; Espindola-Rodríguez, M.; Lopez-Marino, S.; Pulgarín, F. A.; Vigil-Galán, O.; Perez-Rodriguez, A.; Saucedo, E. Secondary Phase Formation in Zn-Rich $Cu_2ZnSnSe_4$- Based Solar Cells Annealed in Low Pressure and Temperature Conditions. *Prog. Photovoltaics* **2014**, 22, 479−487.

(33) Dimitrievska, M.; Xie, H.; Jackson, A. J.; Fontané, X.; Espíndola-Rodríguez, M.; Saucedo, E.; Pérez-Rodríguez, A.; Walsh, A.; Izquierdo-Roca, V. Resonant Raman Scattering of ZnS_xSe_{1-x} Solid Solutions: The Role of S and Se Electronic States. *Phys. Chem. Chem. Phys.* **2016**, 18 (11), 7632−7640.

(34) Becerril-Romero, I.; Acebo, L.; Oliva, F.; Izquierdo-Roca, V.; López-Marino, S.; Espíndola-Rodríguez, M.; Neuschitzer, M.; Sánchez, Y.; Placidi, M.; Pérez-Rodríguez, A.; Saucedo, E.; Pistor, P. CZTSe Solar Cells Developed on Polymer Substrates: Effects of Low-Temperature Processing. *Prog. Photovoltaics* **2018**, 26, 55−68.

(35) Giraldo, S.; Saucedo, E.; Neuschitzer, M.; Oliva, F.; Placidi, M.; Alcobé, X.; Izquierdo-Roca, V.; Kim, S.; Tampo, H.; Shibata, H.; Perez-Rodriguez, A.; Pistor, P. How Small Amounts of Ge Modify the Formation Pathways and Crystallization of Kesterites. *Energy Environ. Sci.* **2018**, 11, 582−593.

Insights Into the Formation Pathways of Cu$_2$ZnSnSe$_4$ Using Rapid Thermal Processes

A. Hernández-Martínez[1], M. Placidi[1], L. Arqués[1], S. Giraldo[1], Y. Sánchez[1],*

V. Izquierdo-Roca[1], P. Pistor[1,2], M. Valentini[3,4], C. Malerba[4,5], E. Saucedo[1]

1Catalonia Institute for Energy Research (IREC), 08930, Sant Adrià de Besòs (Barcelona), Spain.

2Martin Luther University Halle-Wittenberg, Universitätsplatz 10, 06108 Halle (Saale), Germany.

3Rise Technology Srl, Lungomare Toscanelli 170, 00121 Roma, Italy

4ENEA, Casaccia Research Center, via Anguillarese 301, 00123 Roma, Italy

5DICAM, University of Trento, via Mesiano 77, 38123 Trento, Italy

*Jardins de les Dones de Negre 1, 08930 Sant Adrià de Besòs, Barcelona, Spain. Phone: +34 933562615, Fax: +34 933563802, e-mail: ahernandez@irec.cat

The change from Conventional Thermal Processing (CTP) to Rapid Thermal Processing (RTP) is not obvious at all since the system becomes kinetically controlled and the CZTSe formation mechanism can drastically change. In this work we present the transfer of our kesterite production baseline (Cu2ZnSnSe4: Ge) from CTP using a tubular furnace, towards a RTP process by studying the formation mechanisms as well as photovoltaic absorber properties.

S1. SEM
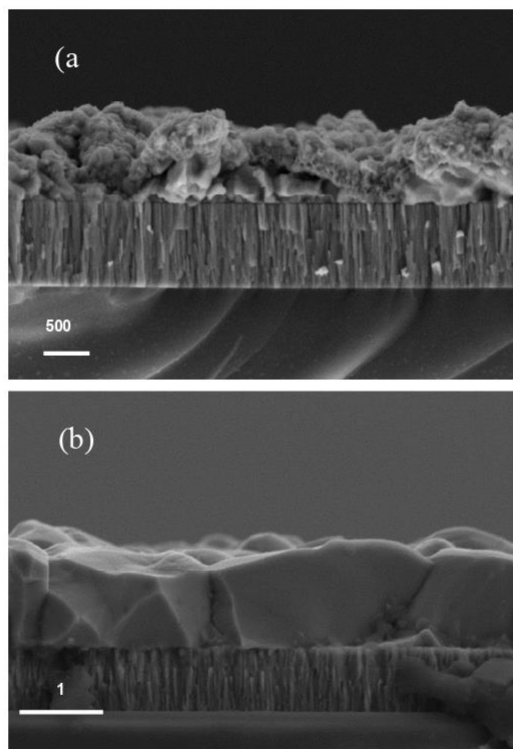
Figure S1. a) Cross Sectional image of a Kesterite Precursor obtained via Sputtering. b) Cross Sectional Image of a Kesterite Absorber obtained via RTP, using same precursor and identical conditions than in the champion cell.

S-2

S2. XRF
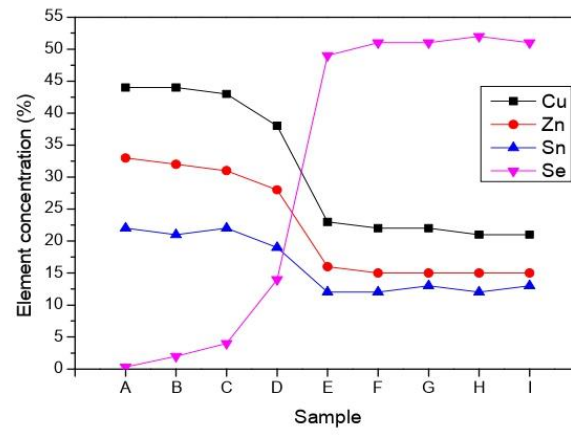
Figure S2. Evolution of the concentration of the different elements determined by X-Ray Fluorescence (XRF)

S3. XRD

Figure S3. XRD diffractogram.

Figure S3. shows the XRD diffractogram of the different samples studied in this experiment, ranging from room temperature up to 500ºC.

S4. Raman spectroscopy
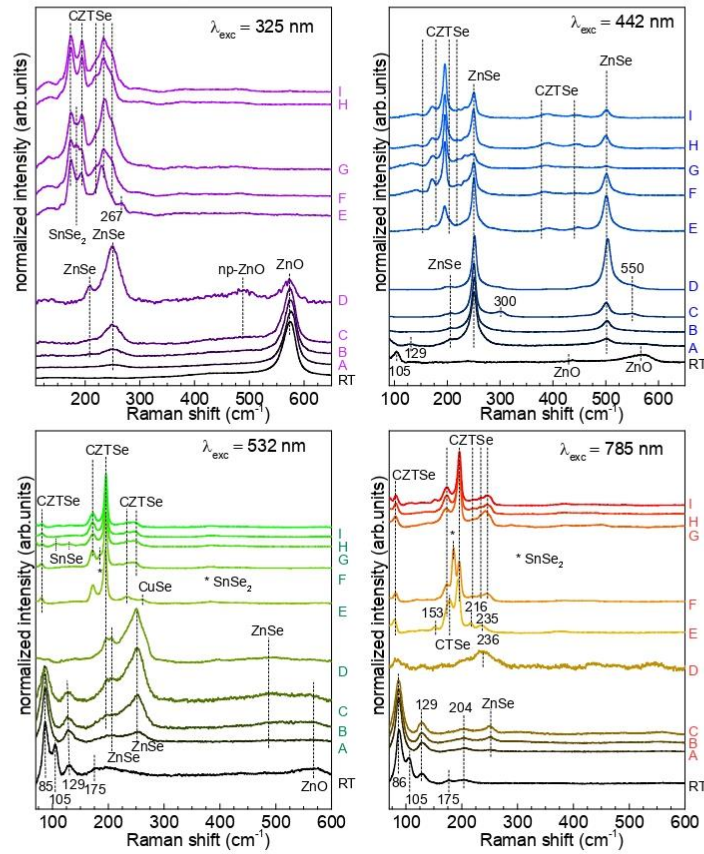
Figure S4. Raman analysis of the different samples produced in the break off experiment using 4 different excitation wavelengths (325 nm, 442 nm, 532 nm and 785 nm)

Figure S4 shows the Raman spectra obtained in the different samples for the four different wavelengths. In particular under UV excitation (325 nm) the ZnO phase. Under blue excitation (442 nm) the ZnSe is enhanced and with red excitation we are able to detect Sn-Se and quaternary

S5. Na GDOES profiles
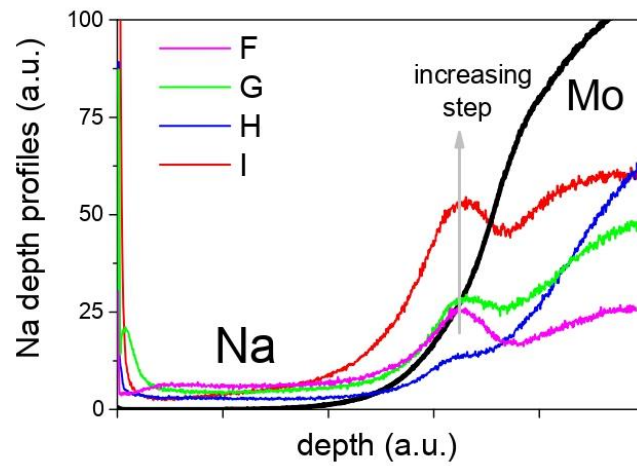
Figure S5. Sodium depth profile evolution through RTP processing

In FigureS5, the sodium depth profile evolution is shown. It can be observed that the typical sodium segregation at the interfaces (CZTSe/Mo and CZTSe/air) increases with increasing process steps. Sample H shows a sodium profile out of trend, probably due to an anomalous sodium content in the glass substrate.
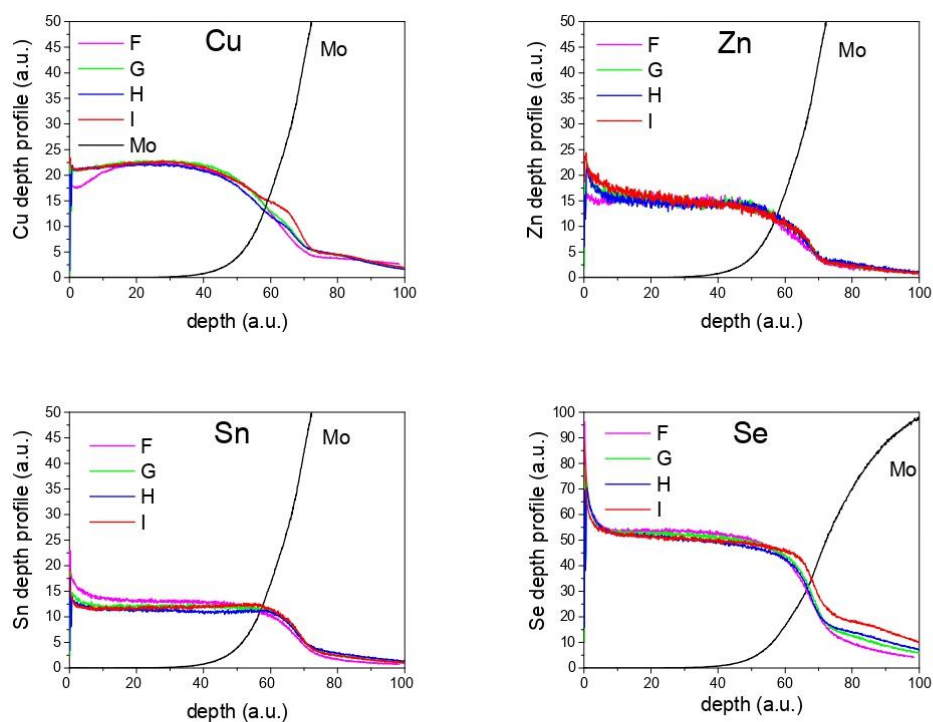
Figure S6. Comparison of Cu, Zn, Sn and Se depth profiles in different samples, measured after different RTP step processes

In Figure S6 the elements' depth profiles in samples F, G, H and I are reported. Similar compositions and homogeneous elements distribution are found in all the samples, showing that a thermal treatment of 5 minutes at 400 °C (sample F) is enough to obtain a homogeneous sample, despite the precursor is a metallic stack. This finding points out a very fast reaction kinetic (that could involve a liquid phase).

Other significant effects are the widening of the selenium depth profile, probably due to the molybdenum selenization, and the increasing of a shoulder in the Cu profile that should arise from a copper diffusion inside the molybdenum. It is also visible a change in the surface element distribution: while the Se content at the surface seems almost constant during the process (after the step 2), Cu and Zn concentration seem to increase whereas an opposite trend is found for Sn.

S-8

Cu$_2$ZnSnSe$_4$ based solar cells combining co-electrodeposition and rapid thermal processing

M. Valdés[a,b,*], A. Hernández-Martinez[b], Y. Sánchez[b], F. Oliva[b], V. Izquierdo-Roca[b], A. Perez Rodriguez[b,c], E. Saucedo[b]

[a] Electroquímica Aplicada, INTEMA, Facultad de Ingeniería, CONICET-Universidad Nacional de Mar del Plata, Av. Colón 10500, 7600 Mar del Plata, Argentina
[b] Catalonia Institute for Energy Research (IREC), Jardins de les Dones de Negre 1, 08930 Sant Adrià del Besòs-Barcelona, Spain
[c] IN2UB, Departament d' Electrònica, Universitat de Barcelona, C. Martí i Franquès 1, 08028 Barcelona, Spain

ABSTRACT

In this work, a fast two-step process combining co-electrodeposition of a CuZnSn precursor plus a reactive selenization step with a rapid thermal annealing to synthesize Cu$_2$ZnSnSe$_4$ thin films is presented. By tuning the electrochemical procedure is feasible to obtain with a short electrodeposition time (15 min) the precursor composition required for high efficiency solar cell devices. XRD characterization reveals that the precursor is mainly composed of binary Cu-Zn and Cu-Sn alloys that after thermal treatment completely react to form a kesterite thin film. Raman spectra and Raman mappings demonstrate that best quality kesterite films are obtained after selective chemical etching necessary to remove secondary phases, like ZnSe and SnSe, which are detrimental for solar cell performance. Best solar cells prototypes achieve efficiencies of 5% with a current density of 30.9 mA/cm^2, an open circuit potential of 327 mV and a fill factor of 51.5%. The low value of open circuit voltage is attributed to the presence of voids and partial delamination observed in the Mo/Cu$_2$ZnSnSe$_4$ interface.

1. Introduction

In the last decade, kesterite (Cu$_2$ZnSnSe$_4$ or CZTSe) has emerged as an excellent thin film absorber for photovoltaic devices. This material has excellent optical properties ($\alpha \geq 10^4$ cm^{-1} in the visible range) and a direct band gap energy value (E_{GAP}) that matches the solar spectrum ($E_{GAP} \sim 1$ eV) (Platzer-Björkman, 2017; Siebentritt, 2017). As opposed to Cu(In,Ga)Se$_2$ (CIGSe) technology, kesterite is more attractive due the earth abundance of its constituent elements which, from an industrial point of view, is a key aspect to ensure mass production compatible with several GW of production in the medium and long term (Almosni et al., 2018; Wallace et al., 2017). A world-record 12.6% power conversion efficiency has been achieved using a mixed CZTSSe absorber composition (Wang et al., 2014).

CZTSe films are usually obtained by "two-steps" or sequential processes, consisting on the deposition of a precursor, either composed by metallic stacks (Cu/Zn/Sn) or by metal-chalcogenides, followed by a reactive annealing in selenium containing atmosphere. Using sequential approaches, a record efficiency of 11.8% has been reported for a CZTSe solar cell, using an innovative approach based on the introduction of

very small Ge quantities (Giraldo et al., 2018).

In order to achieve real cost reductions and competitiveness, this sequential processes requires the development of cost-efficient methodologies. First, the precursor must be obtained with a low-cost technique that can be easily transferable to industrial scale. Electrodeposition meets this requirement and has been used for decades in coatings with applications in several fields (Djokić, 2014; Popov et al., 2016). Besides, electrolytes are prepared from low-cost and eco-friendly aqueous solution in contrast to other chemical routes that use highly toxic and more expensive solvent such as hydrazine (Wang et al., 2014). There are several electrodeposition routes that can be used to obtain a precursor that after a selenization/sulfurization treatment is converted into CZTSe or CZTS films. Detailed information on each of these routes can be found in reviewing article of Colombara et al. (2015). Record efficiencies of 8.2% for a pure selenide Cu$_2$ZnSnSe$_4$ (CZTSe) device (Vauche et al., 2016) and 8% for a pure-sulfide CZTS device (Jiang et al., 2014) were reported using electrodeposition. In these works, the electrodeposition of stacked layers of individual elements, also known as the SEL route, has been used to deposit a precursor material, followed by a treatment in Se or S atmosphere to
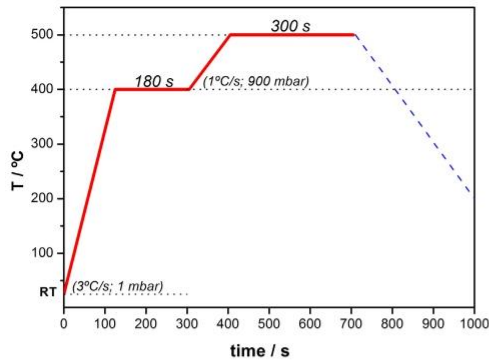

Fig. 1. Temperature – time profile used during RTP for selenization of CZT precursors. Heating rate and argon background pressure are indicated in brackets at each stage.

transform the precursor into a high quality CZTSe or CZTS film. Another route is based on the co-electrodeposition of a metallic CuZnSn precursor. In contrast to the SEL route where three separate electrolytes and three electrochemical steps are needed to obtain the metallic stack, this method is highly attractive because it involves a single electrolyte and one-electrodeposition step to form a precursor film. Despite this, certain disadvantages related to inhomogeneous deposition and problems with bath stability explain why co-electrodeposited kesterite devices have presented lower efficiencies than those prepared with the SEL route, in addition to the difficulties to accurately control the precursor metallic composition. Efficiencies in the range 2–6% are found in literature for the co-electrodeposition route followed by a selenization or sulfurization treatment (Gougaud et al., 2013; Khalil et al., 2017; Kim et al., 2015; Kondrotas et al., 2015; Li et al., 2014; Rakhshani et al., 2017; Zhang et al., 2013), but most reported efficiencies were only achieved when a low-temperature thermal treatment of the CZT precursor is carried out prior the Se or S annealing. A remarkable pure selenide (CZTSe) 8.0% power conversion efficiency has been achieved with a layer obtained by a single selenization of a co-electrodeposited CZT metallic precursor (Jeon et al., 2014), while 7.4% PCE solar cells of

pure sulfide (CZTS) composition has been recently reported also using co-electrodeposition (Ge and Yan, 2018).

The thermal treatment necessary to achieve high quality films can also be optimized by the use of rapid thermal processing (RTP). Prior work developed at IREC has demonstrated at lab scale the advantages of RTP systems in contrast to the most frequently used conventional thermal treatment (CTP) (Fairbrother et al., 2014). RTP is advantageous because processing times are much shorter than conventional thermal processes. By using RTP treatments, the total time of the selenized (sulfurized) stage can be reduced 5 times and even more, taking into account that an RTP takes minutes while a CTP takes hours of processing. Therefore, the incorporation of RTP treatments accomplish the premises that are sought for a large-scale process: speed, cost reduction and energy savings. RTP process has been mostly combined with kesterite precursors prepared by sputtering (He et al., 2014; Hwang et al., 2015; Olgar et al., 2017; Pawar et al., 2014; Placidi et al., 2016). On the side of electrochemical routes very little has been reported of the use of RTP processes. Vauche et al. have reported kesterites using electrodeposition of stacked layers (SEL method) followed by a RTP process (Vauche et al., 2014, 2015). It should be noted that the SEL method has significant experimental differences with the co-electrodeposition method (Colombara et al., 2015). On the side of the co-electrodeposition method.

In summary, this paper reports CZTSe thin films prepared by a sequential process combining a short-time co-electrodeposition of a CZT precursor and a selenization step with an RTP system. Selected films were tested in solar cell prototypes achieving a promising efficiency of 5.2% which is twice the efficiency of previous kesterite solar cells reported by the group using the co-electrodeposition route as a low cost approach (Kondrotas et al., 2015). To our best knowledge only one work has been published combining co-electrodeposition and RTP treatment, producing solar cells with 4.5% efficiency (Zhang et al., 2013). In contrast, the present work shows that even reducing 4 times the precursor electrodeposition time, solar cells with comparable (an even higher) efficiencies can be achieved.

2. Material and methods

CZTSe films were prepared by a sequential process onto Mo-coated soda lime glass substrates. First, a CuZnSn (CZT) precursor alloy was obtained by co-electrodeposition employing a three-electrode cell. Soda-lime glasses coated with a DC magnetron sputtered Mo layer were used as a working electrode. Prior to deposition, Mo substrates were
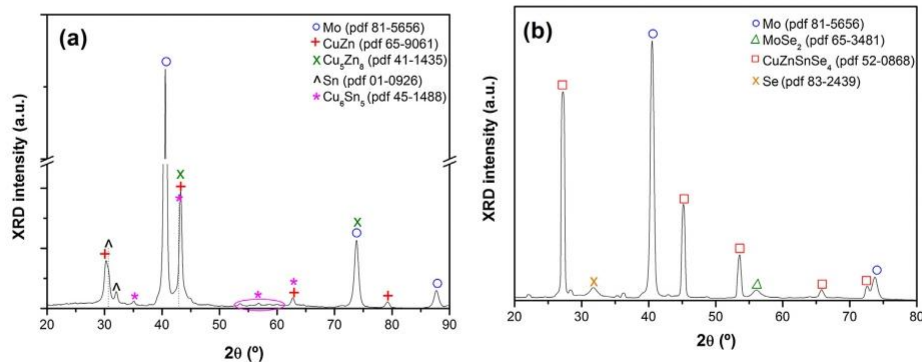

Fig. 2. XRD pattern of (a) CZT precursor electrodeposited at −1.2 V (vs. Ag/AgCl) during 15 min and (b) CZTSe thin film obtained after RTP treatment.

Table 1
Chemical composition and elements ratios in selected CZT and CZTSe films.[a]

Sample	Thickness [nm]	%Cu	%Zn	%Sn	%Se	Cu/(Zn + Sn)	Zn/Sn
CZT	480.5 ± 95.2	44.2 ± 1.1	27.9 ± 1.5	27.8 ± 1.1	–	0.79	1.00
Sample	**Thickness [μm]**	**%Cu**	**%Zn**	**%Sn**	**%Se**	**Cu/(Zn + Sn)**	**Zn/Sn**
CZTSe	1.65 ± 0.21	22.7 ± 1.2	14.1 ± 1.0	10.4 ± 0.3	52.8 ± 1.5	0.94	1.38
CZTSe + KMnO4	1.62 ± 0.15	22.5 ± 0.9	12.9 ± 0.6	12.5 ± 0.5	52.1 ± 1.0	0.88	1.03
CZTSe + KMnO4 + (NH4)S	1.55 ± 0.1	22.8 ± 0.6	13.2 ± 1.1	11.4 ± 0.4	52.6 ± 1.3	0.93	1.16
CZTSe + KMnO4 + (NH4)S + KCN[b]	1.53 ± 0.15	21.4 ± 0.8	13. 6 ± 0.8	11.2 ± 0.6	53.8 ± 1.8	0.86	1.21

[a] Chemical composition and film thicknesses were determined using XRF. For CZT and CZTSe films the mean value and the error were calculated from six individual point measurements, while for the etched films not less than four individual measurements were taken.
[b] Composition of the best device reported in this work.

immersed in 20% NH_4OH solution for 3 min to remove native molybdenum oxide. A platinum (purity 99.999%) mesh of much larger dimensions than that of the working electrode was used as auxiliary electrode and a silver chloride electrode (Ag/AgCl, KCl saturated) served as reference.

The electrolyte solutions were prepared using deionized water containing milli molar concentrations of $CuSO_4 \cdot 5H_2O$ (ACS reagent ≥ 98% Sigma-Aldrich); $ZnSO_4 \cdot 7H_2O$ (ReagentPlus®, ≥99.0% Sigma-Aldrich) and $SnSO_4$ (≥95% Sigma-Aldrich). Sodium citrate tribasic ($Na_3C_6H_5O_7$, ACS reagent, ≥99.0% Sigma-Aldrich) was used as complexing agent in the electrolyte solution for the co-deposition of CZT as it was previously reported (Valdés et al., 2017). The molar ratios of Cu:Zn:Sn:Na-cit in the electrolyte were fixed to 1.3:1.2:1:20 with a copper concentration of 13×10^{-3} mol/L. The final pH of the solution was close to 6 without any addition of acids or bases. CZT precursor films were co-electrodeposited at room temperature in potentiostatic mode applying a potential of −1.2 V (vs. Ag/AgCl) during 15 min employing a VSP Electrochemical Workstation (Biologic).

In a second step, CZT precursors were selenized with a RTP system (AS-One AnnealSys). Samples were placed in a graphite box together with 25 mg of selenium powder (99.999 purity). The temperature profile employed is shown in Fig. 1. The total process time (heating + selenization steps + cooling) takes less than 30 min in a very controlled way, enabling important energy savings at industrial scale considering that RTP is the preferred thermal process in the thin film chalcogenide industry. The elemental composition and thicknesses of CZT and CZTSe films were measured by XRF (Fisherscope XVD) which has been previously calibrated by Inductively Coupled Plasma Optical Emission Spectroscopy (ICP).

The crystalline structure of the as-deposited metallic CZT precursors as well as of the selenized films was analyzed by X-ray diffraction using an Advance D8 diffraction system (Bruker) employing Cu Kα radiation at 40 kV and 40 mA. The samples were scanned, in Bragg-Brentano θ/2θ geometry, between 15° and 80° with a step size of 0.01°. Scanning electron microscopy (SEM) images were obtained using a ZEISS Series Auriga microscope. Raman scattering measurements were made using a Raman probe developed at IREC coupled with an optical fiber to an iHR320 Horiba Jobin Yvon spectrometer. The measurements were made in backscattering configuration focusing the excitation laser spot directly on the surface of the samples (diameter 50 μm, excitation power density < 1 kW/cm²) with excitation wavelengths of 442 nm and 633 nm. Raman spectra were calibrated using a monocrystal Si reference sample before each measurement by imposing the position of the dominant Si peak at 520 cm^{-1}. Raman micro-mappings were performed using an Invia Reflex confocal Raman microprobe using a 50×

objective. Excitation was provided with the 514 nm emission line of an Ar^+ laser and 786 nm emission of IR-laser. The laser power on the sample was less than 2 mW measured with a silicon photodiode (Coherent Inc.). Maps were obtained scanning a square zone (100 × 100 μm) in the sample and recording a total of 25 spectra in the x and y directions. For both axes the step between spectra was set in 20 μm.

After a through characterization, the films were incorporated into solar cells. Selected films were etched in a series of electrolytes: in an acidic solution of $KMnO_4$, to remove superficially segregated ZnSe (López-Marino et al., 2013b), in NaS_2 solution to remove SnSe and passivate the surface region (Xie et al., 2014); and finally in 2 wt.%/v KCN solution to remove possible Cu_xSe secondary phases. An n-type buffer layer of CdS was deposited by chemical bath deposition to a thickness of approximately 50 nm as is published in (Neuschitzer et al., 2015). Immediately after the CdS growth, the solar cells were completed by DC-pulsed sputtering deposition (Alliance CT100) of i-ZnO (50 nm) and In:SnO_2 (ITO, 350 nm) as transparent window layer and front conductive layer, respectively. The CZTSe/CdS junction was not intentionally heated until the deposition of the ITO layer which is performed at 200 °C in the sputtering system. Afterwards, for the standard optoelectronic characterization, 3 × 3 mm² cells were mechanically scribed using a manual microdiamond scriber (MR200, OEG Optical Metrology). Dark and illuminated J–V curves were measured using a calibrated Sun 3000 class AAA solar simulator (Abet Technologies). Measurements were carried out at 25 °C, under AM1.5G 1-Sun illumination conditions. The spectral response was measured using a Bentham PVE300 system calibrated with Si and Ge photodiodes, in order to obtain the EQE of the solar cells.

3. Results and discussion

Fig. 2 presents the XRD diffractograms of a CZT precursor (Fig. 2a) and a CZTSe film after RTP selenization (Fig. 2b). The precursor is mainly composed of CuZn, zinc-rich Cu_5Zn_8 and Cu_6Sn_5 intermetallic compounds. Also, weak signals assigned to elemental Sn are also observed. These phases are frequently observed in co-electrodeposited CZT films, given that as confirmed by several authors (Gougaud et al., 2013; Hreid et al., 2015; Juškenas et al., 2012; Schurr et al., 2009), the co-electrodeposition route involves the formation of alloys instead of pure metals. The presence of intermetallic CuZn has been related to a Cu-poor composition of the CZT precursor (Schurr et al., 2009) and as it was reported by Hreid et al., the concentration of Cu ions regulates the formation of intermetallic compounds (Hreid et al., 2015).

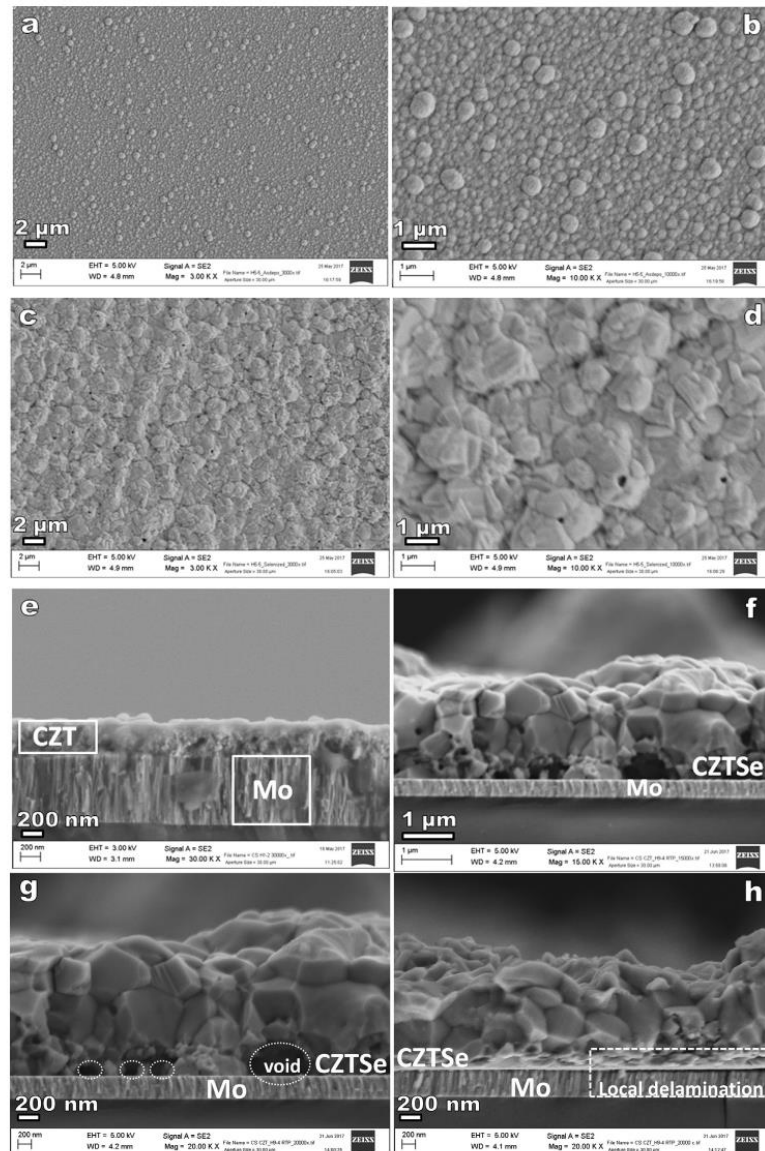After RTP (Fig. 2b), the film presents intense and sharp peaks of the

Fig. 3. Top-view FESEM pictures of (a-b) co-electrodeposited CZT precursor (c-d) CZTSe thin film obtained after RTP selenization. Cross section view of (e) CZT precursor and (f-h) CZTSe thin films (no etching). Pictures (g-h) show defects at Mo/CZTSe interface using higher magnification.

main crystallographic planes of the CZTSe phase. Minor signals of $MoSe_2$ and elemental Se are also observed. The former is attributed to the formation of a $MoSe_2$ layer during selenization. According to Wei et al, during the cooling down of the annealing process residual selenium on the samples can be deposit by condensation of Se vapor (Wei et al., 2018).

Further than the crystal structure, another important factor for

achieving working devices is the chemical composition, particularly the Cu/(Zn + Sn) and Zn/Sn ratios. It has been well established that highly efficient devices must present a Cu-poor and Zn-rich composition, and so must the precursor. Table 1 presents the chemical composition of the CZT precursor, of the CZTSe films after RTP and the composition after chemical etching. The composition of the precursor fulfills the pre-requisites of Cu-poor, and presents equal contents of zinc and tin atoms.
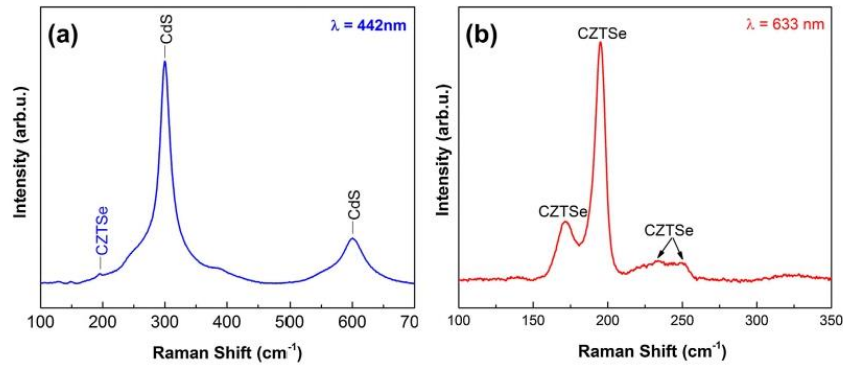
140

Fig. 4. Raman spectra of a finished solar cell under different excitation wavelengths: (a) 442 nm and (b) 633 nm.

The thickness of the CuZnSn precursor is close to 0.5 μm but the dispersion of this value, which is related to the thickness homogeneity, is relatively high. This is likely to be one of the main drawbacks of the co-electrodeposition approach (Colombara et al., 2015). Despite this, the deviation in the chemical composition of each element is less than 5%, which for a 2.5 × 2.5 cm² electrodeposited film indicates good uniformity. After RTP and selenium incorporation the composition is slightly Cu-poor and Zn-rich. The excess of selenium (above 50%) is attributed to the MoSe₂ layer during selenization and elemental selenium, in accordance with what was observed by XRD.

Table 1 also includes the change in the atomic composition of the CZTSe film after being etched in selected solutions to remove secondary phases like ZnSe, Sn-Se and Cu$_x$Se. After the etchings, the composition of the best CZTSe absorber gives a Cu/(Zn + Sn) ~ 0.85 and (Zn/Sn) ~ 1.2. The thickness of the CZTS film is in average three times higher than the precursor material. This expansion of the films is usually observed in reactive annealing, mainly, where the chalcogen is incorporated into the material during the thermal treatment (Ahmed et al., 2012; Jeon et al., 2014; Salomé et al., 2010; Scragg, 2011). Selected FESEM images are presented in Fig. 3. At low magnification (Fig. 3a) the films appear to be homogenously deposited and no voids or cracks are observed. Indeed, after co-electrodeposition, CZT precursors present specular reflectivity.

At higher magnification (Fig. 3b), round particles (or agglomerates) can be visualized in the nanometer range, with some dispersion of bigger agglomerates at the top surface. After the RTP treatment (Fig. 3c) the material continues to present a high degree of homogeneity but the morphology fully changes to planar particles with irregular shape. Now, CZTSe absorbers do not longer show a shiny specular surface and transform into to a grayish and opaque film. At higher magnification (Fig. 3d) small voids are observed on the surface of the CZTSe film. These could be produced by partial evaporation of volatile compounds formed at high temperatures like SnSe$_x$ (López-Marino et al., 2013a; Márquez et al., 2017; Redinger et al., 2011; Salomé et al., 2010). As it can be seen in Table 1, the increase of the Zn/Sn ratio from 1 to 1.38 after RTP is an indication of tin evaporation during RTP. In a recent work, Unveroglu et al. have reported a similar behavior of tin evaporation during sulfurization of co-electrodeposited CZT precursors quantifying the variation of the Zn/Sn ratio before and after the thermal treatment (Unveroglu and Zangari, 2016). Cross section pictures of CZT (Fig. 3e) and CZTSe films (Fig. 3f) corroborate the

XRF thickness measurements and, in fact, provide additional evidence of the volume expansion in the film after the RTP treatment. The CZT precursor shows compactness and high adherence to the Mo substrate while after RTP some voids in the Mo/CZTSe interface are present. Localized delamination (partial detachment of kesterite from the substrate) is highly detrimental for device performance because a low quality Mo/CZTSe interface strongly influences overall solar cell performance, especially decreases shunt resistance affecting the open circuit voltage.

The formation of voids or local delamination has been reported before in kesterite films synthesized from electrodeposited precursors (Guo et al., 2014; Kondrotas et al., 2015; Li et al., 2014; Vauche et al., 2014), but it is a common problem that extends to other fabrication techniques like sputtering (Malerba et al., 2016; Márquez et al., 2017) or chemical methods (Larramona et al., 2014; Todorov et al., 2013).

Raman spectra of a complete solar cell are presented in Fig. 4. Different laser wavelengths were used to identify potential secondary phases taking into account Raman resonant excitation. For CZTSe, resonant effects are frequently found in binary compounds like ZnSe and Sn-Se, at excitation laser wavelengths of 442 and 633 nm, respectively (Álvarez-García et al., 2016). After the chemical etchings of the CZTSe absorber, no traces of SnSe₂ and ZnSe secondary phases were observed. Fig. 4a presents a Raman spectrum of a complete device using 442 nm excitation wavelength. The spectrum is characterized by the dominant band at 300 cm⁻¹ identified as A₁(LO) of the CdS, and weaker contributions at around 195 and 600 cm⁻¹ identified as Se–Se vibrations of the CZTSe and the second order of the A₁ (LO) CdS mode. Resonant effects of CdS at this laser wavelength explain the remarkable difference in Raman intensities between CdS ad CZTSe layers (Oliva et al., 2016). On the other hand, the absence of contributions at 250 and 500 cm⁻¹ characteristics of ZnSe under resonant conditions (488 nm) suggest the absence of this phase in the CZTSe surface (Dimitrievska et al., 2016). With a laser excitation of 633 nm (Fig. 4b) only Raman signals coming from the CZTSe layer are present in the spectrum without interference of the upper layers (Oliva et al., 2016). The spectrum presents two main modes of CZTSe at 195 cm⁻¹ and at 170 cm⁻¹, both with A symmetry; and other two minor signals at 235 and 250 cm⁻¹ with E and B symmetry, as it is reported in the literature (Guc et al., 2013). Under these excitation conditions the absence of the Raman signals between 110 and 180 cm⁻¹ can be taken as an indication of the absence of Sn-Se related secondary phases on the surface film (Dimitrievska et al., 2016).
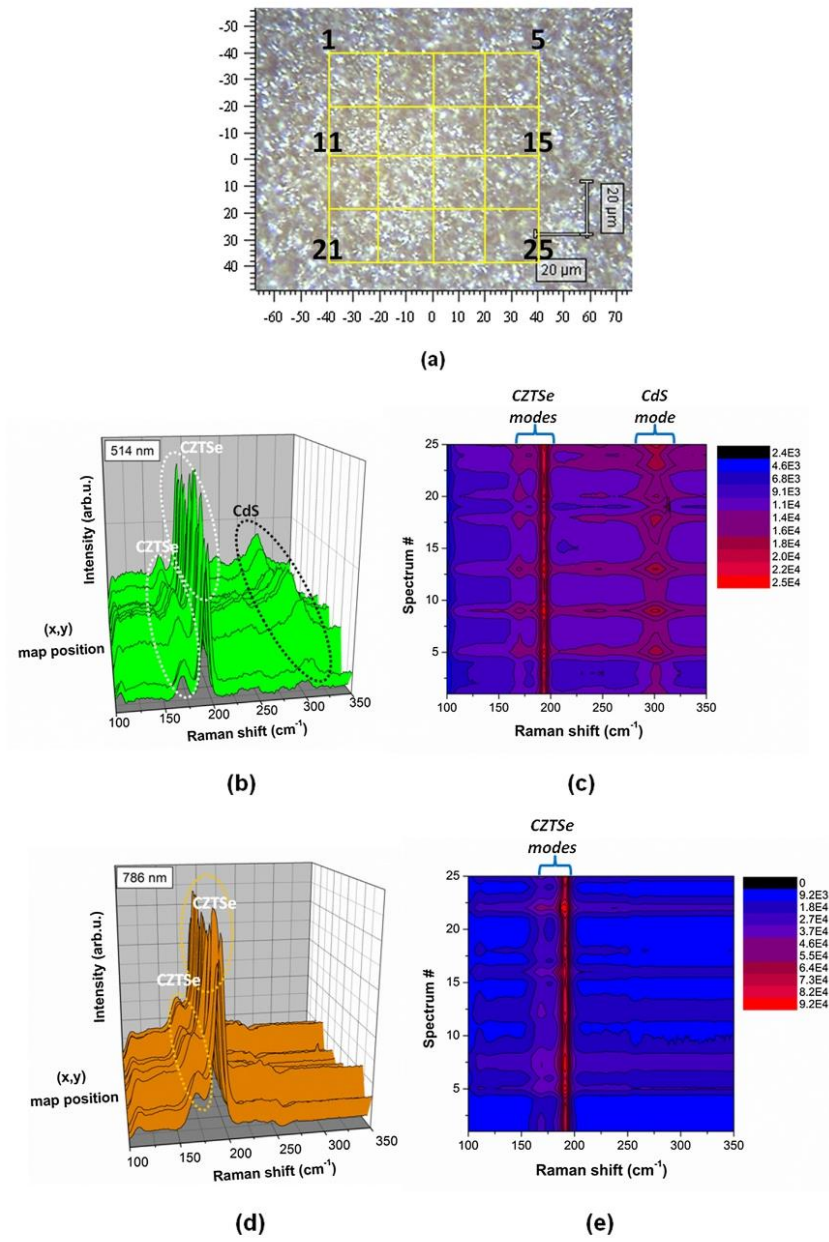
Fig. 5. Raman μ-maps of the best CZTSe sample reported in this work; (a) microscopy image and grid used to record the maps; (b) 514 nm Raman map; (c) 514 nm color contour of Raman intensity signals; (d) 786 nm Raman map and (e) 786 nm color contour of Raman intensity signals. (For interpretation of the references to colour in this figure legend, the reader is referred to the web version of this article.)
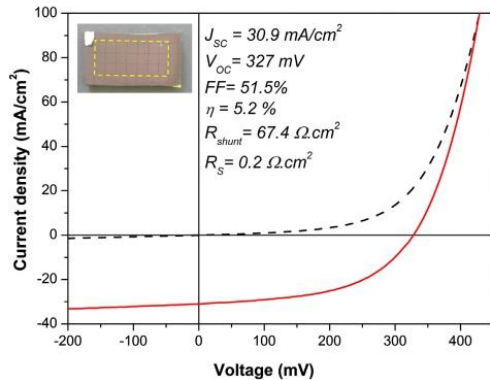
142

Fig. 6. Current-voltage curves recorded under simulated AM1.5G for the best CZTSe solar cells prototype. The insert shows an image of a full sample and the cells that were measured for the statistical values presented in Table 2.

Raman micro-mapping has emerged as powerful tool to study the homogeneity of thin films and their properties. Raman maps were recorded following the grid presented in Fig. 5a, using 20 μm steps in the x and y directions. Raman maps performed at excitation wavelengths of 532 (Fig. 5b and c) and 786 nm (Fig. 5d and d) show a homogeneous distribution of kesterite Raman signals along the analyzed area (80 × 80 μm) together with a small and broad signal of the CdS buffer layer, that is only visible when the excitation is made with the 514 nm (close to the resonant effect). The broadening of the CdS Raman mode is explained by its nanocrystalline dimensions. The even distribution of Raman signals and a more statistical representation can be visualized when the maps are shown in the form of colors contour. These are presented in Fig. 5c and d for each wavelength, respectively. In both figures can be observed narrows and high intensity color bands around the main A mode (195 cm^{-1}) of the CZTSe, which is an indication of high crystallinity and homogeneity of the CZTSe absorber throughout the whole sample.

I-V curves of the best device in the dark and in simulated AM1.5 solar radiation are shown in Fig. 6. Extracted solar cell parameters for the best cell, and statistical values for the full sample (see insert in Fig. 5), are presented in Table 2. A solar cell with a maximum efficiency (η) of 5.2% was achieved, which is twice the efficiency of previous devices reported by our group using co-electrodeposition (Kondrotas et al., 2015). Shunt and series resistance for the best cell were $R_{shunt} = 67.4 \, \Omega \, cm^2$ and $R_s = 0.2 \, \Omega \, cm^2$ respectively. As it was expected from the observation of the Mo/CZTSe interface, the R_{shunt} of the solar cell is very low compared to higher efficiency cells (typically 10

times higher) (Giraldo et al., 2015; Wang et al., 2014). The low R_{shunt} value is originated by the presence of defects in the Mo/CZTSe interface reducing the fill factor and V_{OC} of the cell. A soft pre-annealing of the CZT/Mo (Lin et al., 2014) or back contact modification (López-Marino et al., 2013a) could help to reduce these defects in the interface.

It is important to notice that there is no crossover between dark and illuminated I-V curves. The explanation of crossover of I-V curves in CZTSe solar cells has been ascribed mainly to photogenerated carrier trapping in the CdS layer (Ben Messaoud et al., 2015; Khadka et al., 2016; Neuschitzer et al., 2015). Therefore, the absence of a crossover can be taken as a proof of a proper CZTSe/CdS interface quality and band alignment.

An external quantum efficiency (EQE) spectrum of the best cell is depicted in Fig. 7. EQE reaches 70–80% between 500 and 800 nm indicating reasonably good carrier generation and collection in the p-n junction. Below 500 nm absorption of the CdS buffer layer reduces the EQE in this region. From 900 nm, the decay in EQE could be related to a low diffusion length of carrier generated at these wavelengths.

In comparison with the work previously published by the group (Kondrotas et al., 2015), in this work replacing (time consuming) conventional thermal treatment with RTP we have improved the quality of CZTSe films. This has led us to double the efficiency of the cells, improving the electrical parameters of the devices. The series resistance (R_s) of the cells has decreased an order of magnitude, increasing the Jsc and the FF. On the other hand, the shunt resistance (R_{shunt}) of our cells is still low compared to record devices limiting the V_{OC} of our cells. An improvement of the Mo/CZTSe interface is essential to achieve this objective and obtain greater efficiencies.

4. Conclusion

CZTSe thin films were synthesized combining the co-electrodeposition of a CuZnSn (CZT) precursor with a rapid thermal (selenization) process. CZT films mainly consisted in binary CuZn and CuSn phases. FESEM pictures revealed that the films were homogeneous and formed by round particles (or agglomerates) in the nanometer range. After the RTP treatment, the morphology fully changes to platelet-shaped grains. Cross-section FESEM pictures exposed different types of defects located in the Mo/CZTSe interface like voids and partial film delamination which act as recombination paths affecting device performance. Selected films were submitted to several etchings in order to remove detrimental secondary phases and adjust the chemical composition. The best device reported in this work achieved a 5.2% conversion efficiency, which doubles the solar cells efficiency previously reported by the group using co-electrodeposition. The main limitation of this device is the low open circuit (V_{OC}) potential of 327 mV in comparison with record CZTSe devices. The low V_{OC} value is highly related to the low quality of the Mo/CZTSe interface. A soft-annealing treatment prior the RTP (improving precursor quality) or introducing back contact modification can help to mitigate interface defects and improve device efficiency. Work in this direction is currently in progress.

Table 2
CZTS best device optoelectronic parameters.[a]

η (best) [%]	η (mean) [%]	RSD [%]	J_{sc} (best) [mA cm^{-2}]	J_{sc} (mean) [mA cm^{-2}]	RSD [%]	V_{oc} (best) [mV]	V_{oc} (mean) [mV]	RSD [%]	FF [%]	R_{SH} [Ω cm^2]	R_S [Ω cm^2]
5.2	4.5	11.7	30.9	30.8	4.7	327	309.9	5.4	46.7	48.5	0.8

RSD, relative standard deviation.

[a] Main optoelectronic parameters (η, V_{OC}, J_{SC}) are reported as best value at cell size (active area: 0.087 cm^2), average value for the full sample (21 cells, see insert in Fig. 5a), and its relative standard deviation. The reported values for fill factor (FF), series (R_S), and shunt resistance (R_{SH}) are average for the full sample.
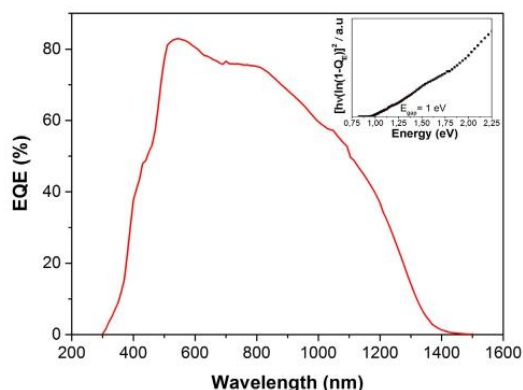
143

Fig. 7. External quantum efficiency (EQE) of the best device. The inset shows the calculated energy gap (E_{GAP}) of the CZTSe absorber from the EQE data.

References

Ahmed, S., Reuter, K.B., Gunawan, O., Guo, L., Romankiw, L.T., Deligianni, H., 2012. A high efficiency electrodeposited cu_2znsns_4 solar cell. Adv. Energy Mater. 2 (2), 253–259.

Almosni, S., Delamarre, A., Jehl, Z., Suchet, D., Cojocaru, L., Giteau, M., Behaghel, B., Julian, A., Ibrahim, C., Tatry, L., Wang, H., Kubo, T., Uchida, S., Segawa, H., Miyashita, N., Tamaki, R., Shoji, Y., Yoshida, K., Ahsan, N., Watanabe, K., Inoue, T., Sugiyama, M., Nakano, Y., Hamamura, T., Toupance, T., Olivier, C., Chambon, S., Vignau, L., Geffroy, C., Cloutet, E., Hadziioannou, G., Cavassilas, N., Rale, P., Cattoni, A., Collin, S., Gibelli, F., Paire, M., Lombez, L., Aureau, D., Bouttemy, M., Etcheberry, A., Okada, Y., Guillemoles, J.-F., 2018. Material challenges for solar cells in the twenty-first century: directions in emerging technologies. Sci. Technol. Adv. Mater. 19 (1), 336–369.

Álvarez-García, J., Izquierdo-Roca, V., Pistor, P., Schmid, T., Pérez-Rodríguez, A., 2016. In: Raman Spectroscopy on Thin Films for Solar Cells, Advanced Characterization Techniques for Thin Film Solar Cells. Wiley-VCH Verlag GmbH & Co. KGaA, pp. 469–499.

Ben Messaoud, K., Buffière, M., Brammertz, G., ElAnzeery, H., Oueslati, S., Hamon, J., Kniknie, B.J., Meuris, M., Amlouk, M., Poortmans, J., 2015. Impact of the Cd^{2+} treatment on the electrical properties of $Cu_2ZnSnSe_4$ and $Cu(In, Ga)Se_2$ solar cells. Prog. Photovolt: Res. Appl. 23 (11), 1608–1620.

Colombara, D., Crossay, A., Vauche, L., Jaime, S., Arasimowicz, M., Grand, P.P., Dale, P.J., 2015. Electrodeposition of kesterite thin films for photovoltaic applications: Quo vadis? Phys. Stat. Solidi A 88–102.

Dimitrievska, M., Fairbrother, A., Saucedo, E., Pérez-Rodríguez, A., Izquierdo-Roca, V., 2016. Secondary phase and Cu substitutional defect dynamics in kesterite solar cells: impact on optoelectronic properties. Sol. Energy Mater. Sol. Cells 149, 304–309.

Djokić, S.S., 2014. In: Electrodeposition and Surface Finishing, Modern Aspects of Electrochemistry. Springer-Verlag, New York, pp. pp. XIV 363.

Fairbrother, A., Fourdrinier, L., Fontané, X., Izquierdo-Roca, V., Dimitrievska, M., Pérez-Rodríguez, A., Saucedo, E., 2014. Precursor stack ordering effects in $Cu_2ZnSnSe_4$ thin films prepared by rapid thermal processing. J. Phys. Chem. C 118 (31), 17291–17298.

Ge, J., Yan, Y., 2018. Controllable multinary alloy electrodeposition for thin-film solar cell fabrication: a case study of kesterite Cu_2ZnSnS_4. iScience 1, 55–71.

Giraldo, S., Neuschitzer, M., Thersleff, T., López-Marino, S., Sánchez, Y., Xie, H., Colina, M., Placidi, M., Pistor, P., Izquierdo-Roca, V., Leifer, K., Pérez-Rodríguez, A., Saucedo, E., 2015. Large efficiency improvement in $Cu_2ZnSnSe_4$ solar cells by introducing a superficial Ge nanolayer. Adv. Energy Mater. 5 (21).

Giraldo, S., Saucedo, E., Neuschitzer, M., Oliva, F., Placidi, M., Alcobé, X., Izquierdo-Roca, V., Kim, S., Tampo, H., Shibata, H., Pérez-Rodríguez, A., Pistor, P., 2018. How small amounts of Ge modify the formation pathways and crystallization of kesterites. Energy Environ. Sci. 11 (3), 582–593.

Gougaud, C., Rai, D., Delbos, S., Chassaing, E., Lincot, D., 2013. Electrochemical studies

of one-step electrodeposition of Cu-Sn-Zn layers from aqueous electrolytes for photovoltaic applications. J. Electrochem. Soc. 160 (10), D485–D494.

Guc, M., Levcenko, S., Izquierdo-Roca, V., Fontané, X., Arushanov, E., Pérez-Rodríguez, A., 2013. Polarized Raman scattering analysis of $Cu_2ZnSnSe_4$ and $Cu_2ZnGeSe_4$ single crystals. J. Appl. Phys. 114 (19).

Guo, L., Zhu, Y., Gunawan, O., Gokmen, T., Deline, V.R., Ahmed, S., Romankiw, L.T., Deligianni, H., 2014. Electrodeposited $Cu_2ZnSnSe_4$ thin film solar cell with 7% power conversion efficiency. Prog. Photovolt: Res. Appl. 22 (1), 58–68.

He, J., Sun, L., Chen, Y., Jiang, J., Yang, P., Chu, J., 2014. Cu_2ZnSnS_4 thin film solar cell utilizing rapid thermal process of precursors sputtered from a quaternary target: a promising application in industrial processes. RSC Adv. 4 (81), 43080–43086.

Hreid, T., Li, J., Zhang, Y., Spratt, H.J., Wang, H., Will, J., 2015. Effects of metal ion concentration on electrodeposited CuZnSn film and its application in kesterite Cu_2ZnSnS_4 solar cells. RSC Adv. 5 (80), 65114–65122.

Hwang, S., Kim, D.H., Son, D.H., Yang, K.J., Nam, D., Cheong, H., Kang, J.K., In, S.I., 2015. Effects of a pre-annealing treatment (PAT) on $Cu_2ZnSn(S, Se)_4$ thin films prepared by rapid thermal processing (RTP) selenization. Sol. Energy Mater. Sol Cells 143, 218–225.

Jeon, J.-O., Lee, K.D., Seul Oh, L., Seo, S.-W., Lee, D.-K., Kim, H., Jeong, J.-h., Ko, M.J., Kim, B., Son, H.J., Kim, J.Y., 2014. Highly efficient copper–zinc–tin– selenide (CZTSe) solar cells by electrodeposition. ChemSusChem 7(4), 1073–1077.

Jiang, F., Ikeda, S., Harada, T., Matsumura, M., 2014. Pure Sulfide Cu_2ZnSnS_4 thin film solar cells fabricated by preheating an electrodeposited metallic stack. Adv. Energy Mater. 4 (7), 1301381.

Juškenas, R., Kanapeckaite, S., Karpavičiene, V., Mockus, Z., Pakštas, V., Selskiene, A., Giraitis, R., Niaura, G., 2012. A two-step approach for electrochemical d eposition of Cu-Zn-Sn and Se precursors for CZTSe solar cells. Sol. Energy Mater. Sol. Cells 101, 277–282.

Khadka, D.B., Kim, S., Kim, J., 2016. Effects of Ge alloying on device characteristics of kesterite-based CZTSSe thin film solar cells. J. Phys. Chem. C 120 (8), 4251–4258.

Khalil, M.I., Bernasconi, R., Pedrazzetti, L., Lucotti, A., Donne, A.L., Binetti, S., Magagnin, L., 2017. Co-electrodeposition of metallic precursors for the fabrication of CZTSe thin films solar cells on flexible Mo foil. J. Electrochem. Soc. 164 (6), D302–D306.

Kim, G.Y., Jo, W., Lee, K.D., Choi, H.S., Kim, J.Y., Shin, H.Y., Nguyen, T.T.T., Yoon, S., Joo, B.S., Gu, M., Han, M., 2015. Optical and surface probe investigation of secondary phases in Cu_2ZnSnS_4 films grown by electrochemical deposition. Sol. Energy Mater. Sol Cells 139, 10–18.

Kondrotas, R., Juškènas, R., Naujokaitis, A., Selskis, A., Giraitis, R., Mockus, Z., Kanapeckaitè, S., Niaura, G., Xie, H., Sánchez, Y., Saucedo, E., 2015. Characterization of $Cu_2ZnSnSe_4$ solar cells prepared from electrochemically co-deposited Cu–Zn–Sn alloy. Sol. Energy Mater. Sol. Cells 132, 21–28.

Larramona, G., Bourdais, S., Jacob, A., Choné, C., Muto, T., Cuccaro, Y., Delatouche, B., Moisan, C., Péré, D., Dennler, G., 2014. Efficient Cu_2ZnSnS_4 solar cells spray coated from a hydro-alcoholic colloid synthesized by instantaneous reaction. RSC Adv. 4 (28), 14655–14662.

Li, Y., Yuan, T., Jiang, L., Su, Z., Liu, F., 2014. Growth and characterization of Cu_2ZnSnS_4 photovoltaic thin films by electrodeposition and sulfurization. J. Alloys Compd. 610, 331–336.

Lin, Y., Ikeda, S., Septina, W., Kawasaki, Y., Harada, T., Matsumura, M., 2014. Mechanistic aspects of preheating effects of electrodeposited metallic precursors on structural and photovoltaic properties of Cu_2Zn SnS_4 thin films. Sol. Energy Mater. Sol. Cells 120 (PART A), 218–225.

López-Marino, S., Placidi, M., Pérez-Tomás, A., Llobet, J., Izquierdo-Roca, V., Fontané, X., Fairbrother, A., Espíndola-Rodríguez, M., Sylla, D., Pérez- Rodríguez, A., Saucedo, E., 2013a. Inhibiting the absorber/Mo-back contact decomposition reaction in $Cu_2ZnSnSe_4$ solar cells: the role of a ZnO intermediate nanolayer. J. Mater. Chem. A 1 (29), 8338–8343.

López-Marino, S., Sánchez, Y., Placidi, M., Fairbrother, A., Espindola-Rodríguez, M., Fontané, X., Izquierdo-Roca, V., López-García, J., Calvo-Barrio, L., Pérez- Rodríguez, A., Saucedo, E., 2013b. ZnSe etching of Zn-Rich $Cu_2ZnSnSe_4$: an oxidation route for improved solar cell efficiency. Chem. Eur. J. 19 (44), 14814–14822.

Malerba, C., Valentini, M., Azanza Ricardo, C.L., Rinaldi, A., Cappelletto, E., Scardi, P., Mittiga, A., 2016. Blistering in Cu_2ZnSnS_4 thin films: correlation with residual stresses. Mater. Des. 108, 725–735.

Márquez, J., Stange, H., Hages, C.J., Schaefer, N., Levcenko, S., Giraldo, S., Saucedo, E., Schwarzburg, K., Abou-Ras, D., Redinger, A., Klaus, M., Genzel, C., Unold, T., Mainz, R., 2017. Chemistry and dynamics of Ge in kesterite: toward band-gap-graded absorbers. Chem. Mater. 29 (21), 9399–9406.

Neuschitzer, M., Sanchez, Y., López-Marino, S., Xie, H., Fairbrother, A., Placidi, M., Haass, S., Izquierdo-Roca, V., Perez-Rodriguez, A., Saucedo, E., 2015. Optimization of CdS buffer layer for high-performance $Cu_2ZnSnSe_4$ solar cells and the effects of light soaking: elimination of crossover and red kink. Prog. Photovolt.: Res. Appl. 23 (11), 1660–1667.

Olgar, M.A., Klaer, J., Mainz, R., Ozyuzer, L., Unold, T., 2017. Cu_2ZnSnS_4-based thin films and solar cells by rapid thermal annealing processing. Thin Solid Films 628, 1–6.

Oliva, F., Kretzschmar, S., Colombara, D., Tombolato, S., Ruiz, C.M., Redinger, A., Saucedo, E., Broussillou, C., de Monsabert, T.G., Unold, T., Dale, P.J., Izquierdo-Roca, V., Pérez-Rodríguez, A., 2016. Optical methodology for process monitoring of chalcopyrite photovoltaic technologies: application to low cost Cu(In,Ga)(S,Se)2 electrodeposition based processes. Sol. Energy Mater. Sol. Cells 158 (Part 2), 168-183.

Pawar, S.M., Inamdar, A.I., Pawar, B.S., Gurav, K.V., Shin, S.W., Yanjun, X., Kolekar, S.S., Lee, J.H., Kim, J.H., Im, H., 2014. Synthesis of Cu_2ZnSnS_4 (CZTS) absorber by rapid thermal processing (RTP) sulfurization of stacked metallic precursor films for solar cell applications. Mater. Lett. 118, 76–79.

Placidi, M., Espíndola-Rodriguez, M., Lopez-Marino, S., Sanchez, Y., Giraldo, S., Acebo, L., Neuschitzer, M., Alcobé, X., Pérez-Rodríguez, A., Saucedo, E., 2016. Effect of rapid

thermal annealing on the Mo back contact properties for Cu$_2$ZnSnSe$_4$ solar cells. J. Alloys Compd. 675, 158–162.

Platzer-Björkman, C., 2017. Kesterite compound semiconductors for thin film solar cells. Curr. Opin. Green Sustain. Chem. 4, 84–90.

Popov, K.I., Djokić, S.S., Nikolić, N.D., Jović, V.D., 2016. Morphology of Electrochemically and Chemically Deposited Metals. Springer International Publishing.

Rakhshani, A.E., Bumajdad, A., Al-Sagheer, F., Thomas, S., Tharayil, P.H., 2017. One-step electrodeposition of CuZnSn metal alloy precursor film followed by the synthesis of Cu$_2$ZnSnS$_4$ and Cu$_2$ZnSnSe$_4$ light absorber films and heterojunction devices. Int. J. Electrochem. Sci. 12 (8), 7786–7794.

Redinger, A., Berg, D.M., Dale, P.J., Siebentritt, S., 2011. The consequences of kesterite equilibria for efficient solar cells. J Am. Chem. Soc. 133 (10), 3320–3323.

Salomé, P.M.P., Fernandes, P.A., Da Cunha, A.F., 2010. Influence of selenization pressure on the growth of Cu$_2$ZnSnSe$_4$ films from stacked metallic layers. Phys. Stat. Solidi (C) 7 (3–4), 913–916.

Scragg, J.J., 2011. Copper Zinc Tin Sulfide Thin Films for Photovoltaics. Springer, Berlin.

Schurr, R., Hölzing, A., Jost, S., Hock, R., Voß, T., Schulze, J., Kirbs, A., Ennaoui, A., Lux-Steiner, M., Weber, A., Kötschau, I., Schock, H.W., 2009. The crystallisation of Cu$_2$ZnSnS$_4$ thin film solar cell absorbers from co-electroplated Cu-Zn-Sn precursors. Thin Solid Films 517 (7), 2465–2468.

Siebentritt, S., 2017. High voltage, please!. Nat. Energy 2 (11), 840–841.

Todorov, T.K., Tang, J., Bag, S., Gunawan, O., Gokmen, T., Zhu, Y., Mitzi, D.B., 2013. Beyond 11% efficiency: characteristics of state-of-the-art Cu$_2$ZnSn(S, Se)$_4$ Solar Cells. Adv. Energy Mater. 3 (1), 34–38.

Unveroglu, B., Zangari, G., 2016. Towards phase pure kesterite CZTS films via Cu-Zn- Sn electrodeposition followed by sulfurization. Electrochim. Acta 219, 664–672.

Valdés, M., Di Iorio, Y., Castañeda, K., Marotti, R.E., Vázquez, M., 2017. Cu$_2$ZnSnS$_4$ films prepared by sulfurization of co-electrodeposited metallic precursors. J. Appl.

Electrochem. 47 (6), 755–765.

Vauche, L., Dubois, J., Laparre, A., Mollica, F., Bodeux, R., Delbos, S., Ruiz, C.M., Pasquinelli, M., Bahi, F., de Monsabert, T.G., Jaime, S., Bodnar, S., Grand, P.P., 2014. Cu$_2$ZnSnSe$_4$ thin film solar cells above 5% conversion efficiency from electro-deposited Cu Sn Zn precursors. Phys. Stat. Solidi (a) 211 (9), 2082–2085.

Vauche, L., Dubois, J., Laparre, A., Pasquinelli, M., Bodnar, S., Grand, P.-P., Jaime, S., 2015. Rapid thermal processing annealing challenges for large scale Cu$_2$ZnSnS$_4$ thin films. Phys. Stat. Solidi (a) 212 (1), 103–108.

Vauche, L., Risch, L., Sánchez, Y., Dimitrievska, M., Pasquinelli, M., Goislard De Monsabert, T., Grand, P.P., Jaime-Ferrer, S., Saucedo, E., 2016. 8.2% pure selenide kesterite thin-film solar cells from large-area electrodeposited precursors. Prog. Photovolt.: Res. Appl. 24 (1), 38–51.

Wallace, S.K., Mitzi, D.B., Walsh, A., 2017. The steady rise of kesterite solar cells. ACS Energy Lett. 2 (4), 776–779.

Wang, W., Winkler, M.T., Gunawan, O., Gokmen, T., Todorov, T.K., Zhu, Y., Mitzi, D.B., 2014. Device characteristics of CZTSSe thin-film solar cells with 12.6% efficiency. Adv. Energy Mater. 4 (7), 1301465.

Wei, Y., Zhuang, D., Zhao, M., Gong, Q., Sun, R., Zhang, L., Lyu, X., Peng, X., Ren, G., Wu, Y., Wei, J., 2018. Effects of selenium atmosphere on grain growth for CZTSe absor-bers fabricated by selenization of as-sputtered precursors. J. Alloys Compd. 755, 224–230.

Xie, H., Sánchez, Y., López-Marino, S., Espíndola-Rodríguez, M., Neuschitzer, M., Sylla, D., Fairbrother, A., Izquierdo-Roca, V., Pérez-Rodríguez, A., Saucedo, E., 2014. Impact of Sn(S, Se) secondary phases in C$_u$2ZnSn(S, S$_e$)4 solar cells: a chemical route for their selective removal and absorber surface passivation. ACS Appl. Mater. Interfaces 6 (15), 12744–12751.

Zhang, Y., Liao, C., Zong, K., Wang, H., Liu, J., Jiang, T., Han, J., Liu, G., Cui, L., Ye, Q., Yan, H., Lau, W., 2013. Cu$_2$ZnSnSe$_4$ thin film solar cells prepared by rapid thermal annealing of co-electroplated Cu–Zn–Sn precursors. Sol. Energy 94, 1–7.

145

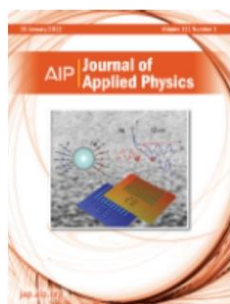## 8.4   Section 4 - Copyright permissions

Copyright Clearance Center   **RightsLink®**   Home | Account Info | Help | LIVE CHAT

Title:	Electronic and optical properties of Cu2ZnSnS4 and Cu2ZnSnSe4
Author:	Clas Persson
Publication:	Journal of Applied Physics
Volume/Issue	107/5
Publisher:	AIP Publishing
Date:	Mar 1, 2010
Page Count:	8

Rights managed by AIP Publishing.

Logged in as:
Alejandro Hernandez

LOGOUT

Order Completed

Thank you for your order.

This Agreement between Ronda Barcelo n59 2nd2a ("You") and AIP Publishing ("AIP Publishing") consists of your license details and the terms and conditions provided by AIP Publishing and Copyright Clearance Center.

Your confirmation email will contain your order number for future reference.

printable details

License Number	4654170081909
License date	Aug 22, 2019
Licensed Content Publisher	AIP Publishing
Licensed Content Publication	Journal of Applied Physics
Licensed Content Title	Electronic and optical properties of Cu2ZnSnS4 and Cu2ZnSnSe4
Licensed Content Author	Clas Persson
Licensed Content Date	Mar 1, 2010
Licensed Content Volume	107
Licensed Content Issue	5
Requestor type	Student
Format	Print and electronic
Portion	Figure/Table
Number of figures/tables	1
Requestor Location	Ronda Barcelo n59 2nd2a Ronda Barcelo n59 2nd2a
	Mataro, Barcelona 08302 Spain Attn: Ronda Barcelo n59 2nd2a
Total	0.00 EUR

ORDER MORE   CLOSE WINDOW

Copyright Clearance Center

RightsLink®

Home | Account Info | Help | LIVE CHAT

ACS Publications
Most Trusted. Most Cited. Most Read.

Title: Insights into the Formation Pathways of Cu2ZnSnSe4 Using Rapid Thermal Processes

Author: A. Hernández-Martínez, M. Placidi, L. Arqués, et al

Publication: ACS Applied Energy Materials

Publisher: American Chemical Society

Date: May 1, 2018

Copyright © 2018, American Chemical Society

Logged in as:
Alejandro Hernandez

LOGOUT

PERMISSION/LICENSE IS GRANTED FOR YOUR ORDER AT NO CHARGE

This type of permission/license, instead of the standard Terms & Conditions, is sent to you because no fee is being charged for your order. Please note the following:

- Permission is granted for your request in both print and electronic formats, and translations.
- If figures and/or tables were requested, they may be adapted or used in part.
- Please print this page for your records and send a copy of it to your publisher/graduate school.
- Appropriate credit for the requested material should be given as follows: "Reprinted (adapted) with permission from (COMPLETE REFERENCE CITATION). Copyright (YEAR) American Chemical Society." Insert appropriate information in place of the capitalized words.
- One-time permission is granted only for the use specified in your request. No additional uses are granted (such as derivative works or other editions). For any other uses, please submit a new request.

BACK | CLOSE WINDOW

147

Copyright
Clearance
Center

RightsLink®

Home | Account Info | Help | LIVE CHAT
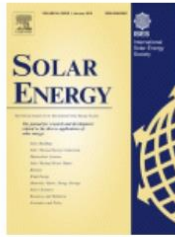
SOLAR ENERGY

Title:	Cu2ZnSnSe4 based solar cells combining co-electrodeposition and rapid thermal processing
Author:	M. Valdés,A. Hernández-Martinez,Y. Sánchez,F. Oliva,V. Izquierdo-Roca,A. Perez Rodriguez,E. Saucedo
Publication:	Solar Energy
Publisher:	Elsevier
Date:	October 2018

Logged in as:
Alejandro Hernandez

LOGOUT

BACK | CLOSE WINDOW

148

Copyright Clearance Center   **RightsLink®**   Home | Account Info | Help | LIVE CHAT

Title:	Electrodeposition of kesterite thin films for photovoltaic applications: Quo vadis?
Author:	P. J. Dale, P.-P. Grand, M. Arasimowicz, et al
Publication:	physica status solidi (a) applications and materials science
Publisher:	John Wiley and Sons
Date:	Dec 3, 2014

© 2015 WILEY-VCH Verlag GmbH & Co. KGaA, Weinheim

Order Completed

Thank you for your order.

This Agreement between Ronda Barcelo n59 2nd2a ("You") and John Wiley and Sons ("John Wiley and Sons") consists of your license details and the terms and conditions provided by John Wiley and Sons and Copyright Clearance Center.

Your confirmation email will contain your order number for future reference.

printable details

License Number	4654170594862
License date	Aug 22, 2019
Licensed Content Publisher	John Wiley and Sons
Licensed Content Publication	physica status solidi (a) applications and materials science
Licensed Content Title	Electrodeposition of kesterite thin films for photovoltaic applications: Quo vadis?
Licensed Content Author	P. J. Dale, P.-P. Grand, M. Arasimowicz, et al
Licensed Content Date	Dec 3, 2014
Licensed Content Volume	212
Licensed Content Issue	1
Licensed Content Pages	15
Type of use	Dissertation/Thesis
Requestor type	University/Academic
Format	Print and electronic
Portion	Figure/table
Number of figures/tables	1
Original Wiley figure/table number(s)	Table 5
Will you be translating?	No
Title of your thesis / dissertation	Development of RTP processing for kesterite solar cells
Expected completion date	Sep 2019
Expected size (number of pages)	130
Requestor Location	Ronda Barcelo n59 2nd2a

Ronda Barcelo n59 2nd2a

Mataro, Barcelona 08302
Spain
Attn: Ronda Barcelo n59 2nd2a

Publisher Tax ID	EU826007151
Total	0.00 EUR

Would you like to purchase the full text of this article? If so, please continue on to the content ordering system located here: Purchase PDF

If you click on the buttons below or close this window, you will not be able to return to the content ordering system.

ORDER MORE   CLOSE WINDOW